coatings

Special Issue Reprint

Advanced Alloy Degradation and Implants

Edited by
Jing’an Li

mdpi.com/journal/coatings

MDPI

Advanced Alloy Degradation and Implants

Advanced Alloy Degradation and Implants

Editor

Jing'an Li

MDPI

Basel • Beijing • Wuhan • Barcelona • Belgrade • Novi Sad • Cluj • Manchester

Editor
Jing'an Li
Zhengzhou University
Zhengzhou
China

Editorial Office
MDPI
St. Alban-Anlage 66
4052 Basel, Switzerland

This is a reprint of articles from the Special Issue published online in the open access journal *Coatings* (ISSN 2079-6412) (available at: https://www.mdpi.com/journal/coatings/special_issues/Degradation_Implants).

For citation purposes, cite each article independently as indicated on the article page online and as indicated below:

Lastname, A.A.; Lastname, B.B. Article Title. *Journal Name* **Year**, *Volume Number*, Page Range.

ISBN 978-3-7258-1113-7 (Hbk)
ISBN 978-3-7258-1114-4 (PDF)
doi.org/10.3390/books978-3-7258-1114-4

Contents

About the Editor

Jing’an Li

Dr. Jing’an Li is a professor at Zhengzhou University, China, and his research field include Biomaterials and Advanced Functional Materials. So far, he has published more than 100 academic papers on international academic journals as the first author or a corresponding author, including *Bioactive Materials*, *Journal of Magnesium and Alloys*, *Composites Part B: Engineering*, etc., and has also edited three books and written eight book chapters. He has served as the editorial board member of reputable journals, such as *Advanced Fiber Materials*, *Coatings*, and *Discover Applied Sciences* (as an Associate Editor), etc., and is also a invited reviewer of more than 130 academic journals, including *Advanced Materials*, etc. Till now, he has been honored with awards such as “IAAM Fellow” (FIAAM, 2020), “JMA CONTRIBUTION AWARD” (2022–2023), etc., and selected for the 2022 Top 2% Scientists (Biomedical Engineering, Elsevier) List.

Preface

Metals and their alloys are one of the oldest biomedical materials known to human beings. They still play an irreplaceable role in modern clinical treatment with excellent mechanical load-bearing properties, chemical stability, and good biocompatibility. In recent years, the R&D and design of metal implants and devices, the further exploration of their powerful functions, and the in-depth exploration of their interaction with the body microenvironment have made great progress. In particular, the design of biodegradable alloys, the elaboration of their degradation mechanism in different environments, the research on degradation behavior and degradation products, and the prospect of their advanced exclusive coating have attracted the attention of scholars.

The aim of this reprint, “Advanced Alloy Degradation and Implants”, is to publish full-length research articles, short communications, and review articles covering the latest studies, progress, and challenges on the design, fabrication, degradation, and surface modification of metal alloy implants for their future biomedical applications.

Jing’an Li
Editor

coatings

MDPI

Article

Fabrication and Characterization of LaF_3-Reinforced Porous HA/Ti Scaffolds

Xingping Fan * and Hao Zhang

School of Vanadium and Titanium, Panzhihua University, Panzhihua 617000, China; zhanghaozi25@163.com
* Correspondence: fanxingping123@163.com

Abstract: To improve the performance of porous hydroxyapatite/titanium (HA/Ti) composites, LaF_3 reinforced porous HA/Ti scaffolds with a porosity of approximately 60% were prepared via a powder metallurgical method, using NH_4HCO_3 as the pore-forming agent. The scaffolds induced HA formation and showed high bioactivity, and the compressive strength could be regulated by changing the LaF_3 dosage. When the LaF_3 dosage was 0.3%, the compressive strength of the porous scaffold was 65 MPa. Moreover, LaF_3 reinforced porous HA/Ti scaffolds can further induce the deposition of calcium phosphate after immersion in simulated body fluid (SBF) for 7 days, indicating that the corresponding scaffold is an ideal choice for spongy bone repair.

Keywords: lanthanum fluoride (LaF_3); porous; HA/Ti; scaffolds; biological activity in vitro

1. Introduction

Titanium is used as a biomaterial due to its excellent corrosion resistance and significant strength [1]. However, the Young's modulus is much higher than that of natural bone. The mismatch of the elastic modulus between titanium and the natural bone would lead to bone resorption and finally, to implant loosening [2]. In addition, due to the fact that the surface of titanium is usually covered with a dense oxide film, titanium exhibits biological inertness. When used as a bone repair material, the combination of this material with bone shows mechanical chimerism. The material is only mechanically integrated, rather than chemically osseointegrated, with the bone, resulting in poor adhesion between the implant material and bone tissue, often leading to implant failure [3]. There are various methods for modifying titanium to endow with biological activity [4–7]. These methods are all aimed at the surface of the material. This also inevitably leads to issues regarding the bonding strength between the modified layer and the matrix. Hydroxyapatite has been widely considered as an implant material because its mineral composition is very close to that of human bone. Hydroxyapatite offers not only good biocompatibility; it also exhibits osteoinductive properties. However, its mechanical properties are poor. Therefore, it can only be used for bone repair in nonbearing locations [8,9], which greatly limits the application of hydroxyapatite. In order to improve its mechanical properties, using the titanium and hydroxyapatite composite method has been considered for prepare new composite materials. However, most of the current reports on titanium/hydroxyapatite composites are based on hydroxyapatite, and titanium is only sintered as a reinforcing phase [10,11]. Its use has been limited to the improvement of the mechanical properties of the composite strength of the materials. In the studies regarding HA/Ti composites, researchers have extensively explored the preparation methods for hydroxyapatite and titanium. For example, Thian, ES et al. used Ti-6Al-4V and HA as raw materials and PVA as a binder to prepare green specimens with a certain shape using injection molding and then obtained composite materials with high mechanical properties through high-temperature sintering [12]. The biggest advantage of this method is that it can prepare products with complex shapes through the use of injection molding, which has great application prospects.

Citation: Fan, X.; Zhang, H. Fabrication and Characterization of LaF_3-Reinforced Porous HA/Ti Scaffolds. *Coatings* **2024**, *14*, 111. https://doi.org/10.3390/coatings14010111

Academic Editor: Alessandro Patelli

Received: 13 November 2023
Revised: 6 January 2024
Accepted: 13 January 2024
Published: 15 January 2024

Although thermal spraying and injection molding can be used to prepare HA/Ti composites with mechanical properties close to those of human bone and an elastic modulus of 10–30 GPa [13], its high processing costs, as well as its current product sizes and shapes, are still worthy of in-depth study. However, the above research mainly involves dense block-like composite materials, which do not have pore structures that facilitate the growth of bone tissue for "biological fixation". The pore structure plays an important role in the growth of bone tissue for the following reasons. (1) The volume density, strength, and elastic modulus of porous titanium can be adjusted by changing the porosity to achieve mechanical properties that match those of the replacement tissue. (2) The porous structure is conducive to the adhesion, differentiation, and growth of osteoblasts, promoting the growth of bone tissue into the pores, strengthening the connection between the implant and bone, achieving biological fixation [14]. Our previous research has shown that through the introduction of a porous structure, treated porous titanium can be implanted into the femurs of dogs. After 6 months of implantation, new bone tissue can be found in the pore, and the bonding strength between the implant and bone tissue is satisfactory [15]. Three-dimensional printing has emerged as a promising technique for fabricating porous hydroxyapatite scaffolds with controlled architecture and porosity. However, the development of biocompatible and bioactive 3D-printed hydroxyapatite scaffolds remains a challenge. In a recent study, Andrej Thurzo fabricated 3D-printed hydroxyapatite scaffolds using polyvinyl alcohol (PVA) as a thermoplastic binder. The scaffolds were found to be biocompatible and supported the adhesion and proliferation of mesenchymal stem cells (MSCs) [16]. However, the introduction of pores will reduce the mechanical strength of the composites. Research has shown that rare-earth elements play an important role in improving material properties. There are two main reasons for this phenomenon. Firstly, rare-earth elements can act as effective deoxidizers to extract oxygen from alloys; secondly, rare-earth elements can alleviate the instability of the alloy structure and surface, and improve the thermal stability of the alloy. Research has shown that adding rare-earth elements to titanium alloy composites can effectively refine the structure, as well as improve the room temperature performance, oxidation resistance, and thermal stability of the alloy [17]. For hydroxyapatite, the addition of rare-earth elements can alter the crystal structure of hydroxyapatite and generate new biological effects [18]. Tang et al. investigated the effect of the lanthanum content in hydroxyapatite coatings on the biological properties of cells attached on titanium surfaces. They found that hydroxyapatite coatings, with an appropriate amount of lanthanum added, exhibit good biocompatibility and can promote the early proliferation and differentiation of bone cells on the material surface. However, when the content of lanthanum is excessive, it can affect the proliferation of osteoblasts because the biological effects of rare-earth element ions are very similar to those of calcium ions, therefore exhibiting antagonistic effects affecting the calcium phosphorus ratio of hydroxyapatite. Another study has shown that strontium offers good compatibility at a concentration of 10% [19,20]. Therefore, adding an appropriate amount of rare-earth elements to Ti/HA composite materials can effectively improve the strength of the matrix and improve its biological properties. In order to further improve the mechanical properties of the strength of materials, this study intends to add appropriate rare-earth elements in Ti/HA composites to effectively improve the strength of the matrix and improve its biological properties.

2. Materials and Methods

2.1. Fabrication of LaF_3 Reinforced Porous HA/Ti Scaffolds

LaF_3 reinforced porous HA/Ti scaffolds were prepared using powder metallurgy through the process shown in Figure 1. Commercial pure titanium powders (purity: $\geq$99.9%, powder size $\leq$ 30.0 μm) and hydroxyapatite with a particle size of 1.0–3.0 μm (provided by Sichuan University) were mixed as raw materials in a mass ratio of 1:20. Ammonium bicarbonate with a particle size range of 100.0–300.0 μm was chosen as the spacer material, and the mass fractions of NH_4HCO_3 were 30.0%. LaF_3, with mass fractions of

0.1%, 0.3%, and 0.5%, respectively, were added. After the ingredients were homogeneously blended, powders obtained from the mixture were uniaxially pressed at a pressure of 100 MPa into cylindrical green pellets with the size of Φ10 mm × H15 mm. The specimens were then sintered in the vacuum sintering furnace (model: ZT-40-20Y, Suzhou Huolanxin Vacuum Technology Co., Ltd., Suzhou, China) in a vacuum. The heat-treatment process consisted of two steps, i.e., 150 °C for 1 h and 1200 °C for 3 h. The main purpose of holding the specimen at 150 °C for 1 h is to completely remove the spacer. According to the different amounts of LaF_3 added, the sintered samples are named HA/Ti, HA/Ti + 0.1% LaF_3, HA/Ti + 0.3% LaF_3, and HA/Ti + 0.5% LaF_3, respectively. The specific process is shown in Figure 1.

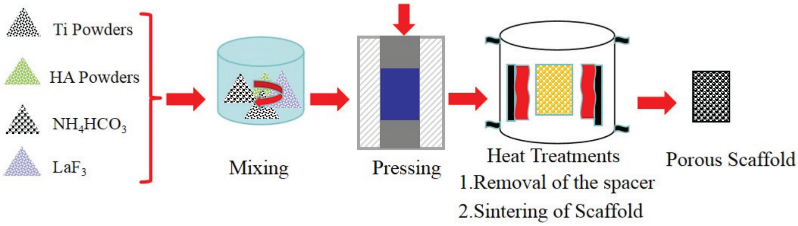

Figure 1. Graph showing the preparation process of the porous scaffold.

2.2. Immersion of Samples in the SBF

The bioactivity of the various samples was evaluated in terms of their apatite-forming abilities by immersing them in the SBF solution. The scaffold, with a diameter of 10.0 mm and a thickness of 2.0 mm, was soaked in a bionic mineralization SBF at 37 °C for 7 days. Afterwards, the bioactivity was tested. The SBF formulation was the same as that reported by Kokubo et al. [21]. Briefly, 8.035 g NaCl, 0.355 g $NaHCO_3$, 0.225 g KCl, 0.231 g $K_2HPO_4 \cdot 3H_2O$, 0.5 M-HCl, 0.292 g $CaCl_2$, 0.072 g Na_2SO_4, 6.118 g $CNH_2(CH_2OH)_3$, and 1M-HCl were added into 1 L deionized water to reach a pH of 7.4 at 36.5 °C.

2.3. Characterization

All the samples were analyzed using a scanning electron microscope (SEM). X-ray diffraction (XRD) was used to characterize the crystalline phase and chemical compositions, with the measurement scanning speed of 5°/min 2θ (10°–90°). The phase analysis was carried out with the Jade 6.5 software package, using the powder diffraction file (PDF) of the International Center for Diffraction Data. The compressive strength tests were carried out on an Instron mechanical testing machine (Instron 5567, Norwood, MA, USA) with a crosshead speed of 0.5 mm/min, employing three groups of sintered samples of each type, namely HA/Ti, HA/Ti + 0.1%LaF_3, HA/Ti + 0.3%LaF_3, and HA/Ti + 0.5%LaF_3, with three samples in each group for compressive testing. The porosity of the specimens was determined by measuring their surface areas and weights according to the following Equation (1):

$$P = 1 - \rho_{scaffold}/\rho_{material} \tag{1}$$

where P is total porosity, $\rho_{scaffold}$ is the apparent density of porous titanium measured by dividing the weight by the volume of the samples, and $\rho_{material}$ is the density of the material of which the scaffold is fabricated [22].

3. Results and Discussion

Figure 2 shows the morphology of the sintered samples of the porous composite materials before and after the addition of rare-earth LaF_3. Figure 2a,c shows the samples without the addition of the rare-earth element, and Figure 2b,d shows the samples after the addition of 0.3% LaF_3; the porosity of the porous scaffold is about 60%. From the figure, it can be seen that the shape of the pores somewhat circular, and the pore size is basically distributed between 100–300 μm. The shape and size of the pores are comparable to those of the added pore forming agent. The method of adding pore forming agents is used to prepare porous materials, and the formation of pores is significantly related to the shape of the pore forming agent. It is generally believed that adding pore forming agents to form pores results in a space left by the decomposition of the pore forming agent when heated. Most holes are interconnected with each other. In addition, the morphology of porous materials at high magnification shows the presence of micropores ranging in size from a few micrometers to several tens of micrometers on their macroscopic pore walls, as shown in Figure 2c,d. These pores are significantly smaller than those of the pore forming agent, so their formation mechanism is different from that of large pores. This is because during the pressing of green specimens, space is formed by the accumulation of raw material particles, such as titanium powder. After sintering, approximately circular micropores were formed due to shrinkage. These complex pore structures, interconnected by large and small pores, are conducive to the transport of nutrient solution and the growth of bone tissue.

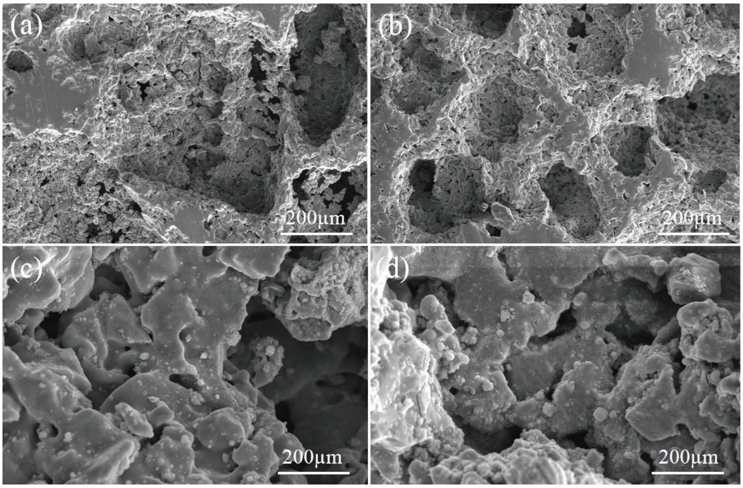

Figure 2. SEM photos of LaF_3 reinforced porous HA/Ti scaffolds. (**a**,**c**) 0.0% LaF_3; (**b**,**d**) 0.3% LaF_3.

Figure 3 shows the surface scan image of the porous material after adding 0.3% LaF_3. From this image, it can be seen that elements such as calcium and phosphorus are uniformly distributed on the titanium matrix, and the lanthanum element after adding rare-earth LaF_3 is also uniformly distributed on the matrix, which further improves the mechanical properties of the porous composite material. On the surface, this method can successfully prepare composite materials with uniform composition.

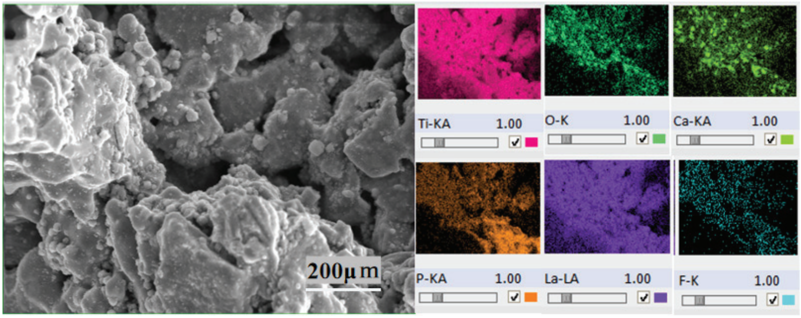

Figure 3. SEM photos of porous HA/Ti composites prepared with 0.3% Lanthanum trifluoride.

Figure 4 shows the XRD patterns of different porous HA/Ti scaffolds. The main phases of the composite are Ti, Ti_2O, Ti_3P, CaO, and $CaTiO_3$. During sintering, the formation of the Ti_2O phase is mainly due to the sintering process. Oxygen elements in the surrounding HA phase and the glass phase diffuse into Ti. When the concentration of the oxygen atoms in the interstitial gap of the Ti lattice reaches a certain level, titanium oxides will form. The type of oxide formed is closely related to the concentration of the oxygen atoms in the sintering atmosphere. This study used a vacuum sintering furnace for the sintering process. The oxygen concentration is very low; therefore, only Ti_2O can be generated, rather than oxides with a high oxygen content, such as TiO_2. The volume fraction of titanium in the composite materials is relatively high The main crystal phase is Ti. However, due to the diffusion of elements with smaller atomic radii, such as oxygen and phosphorus, into the Ti lattice, the formation of compounds such as Ti_3P, CaO, and $CaTiO_3$ occurs. The results are similar to those of Ning CQ et al. [23]. Research has shown that Ti_3P, CaO, and $CaTiO_3$ contributes to the formation of HA and improves the biological activity of materials. The increase in the concentration of Ca^{2+} in SBF leads to the supersaturation of Ca^{2+} on the surface of the composite, which reduces the minimum free energy required to cause apatite nucleation and growth [24]. There are two stable phases of calcium phosphate in an aqueous solution at room temperature. When the pH was lower than 4.2, the stable phase was $CaHPO_4{\cdot}2H_2O$, and when the pH was higher than 4.2, the stable phase was $Ca_{10}(PO_4)_6(OH)_2$(HA) [25]. In this experiment, the pH of SBF is 7.4, so HA is easily formed on the surface. However the dissolution of the CaO phase forms micropores on the surface, which also contributes to the nucleation of HA. Ti_2O-containing compounds can be prepared by sintering, and the results show that the presence of titanium oxides contributed to the formation of HA [10]. However, in this study, the content of LaF_3 is relatively small, so the presence of LaF_3 or La_2O_3 is not detected by XRD. From Figure 4, it can be seen that there is no diffraction peak of NH_4HNO_3. This indicates that the added pore forming agent (ammonium bicarbonate) has been completely removed after low temperature heating and high temperature sintering, and the sintered sample is not polluted, which ensures the biological safety of porous titanium implanted in the body.

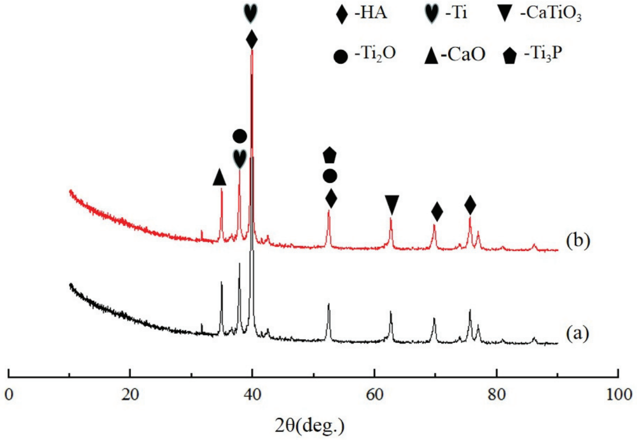

Figure 4. X-ray diffractogram of porous HA/Ti scaffolds before and after adding LaF_3. (**a**) 0.0% LaF_3; (**b**) 0.3% LaF_3.

Figure 5 shows the effect of LaF_3 addition on the compressive strength of the HA/Ti porous scaffolds. With the increase in rare-earth content, the compressive strength of the porous scaffolds increases first and then decreases. When LaF_3 is 0.3%wt, the compressive strength of the porous scaffolds is the largest, reaching 65 MPa. The addition of rare-earth elements can significantly improve the compressive strength of the HA/Ti composites, mainly because the rare-earth element as an effective deoxidizer can absorb the oxygen in the composite, purify the interface of the original particles, reduce the oxygen content of the matrix, and improve the sintering density of the sintered body [19]; the refinement of the structure by LaF_3 can also improve the compressive strength of the porous scaffolds. Figure 4 shows that when adding rare-earth LaF_3 to 0.3%, the diffraction peak corresponding to $CaTiO_3$ widens significantly, and the diffraction intensity decreases. This indicates that the entropy value of the system is large; that is, the lattice distortion of $CaTiO_3$ is severe, resulting in an increase in the compressive strength of the composite material, which is consistent with the XRD results shown in Figure 4. When adding rare-earth LaF_3 to 0.3%, the compressive strength is the highest. On the other hand, research has shown that one of the biggest obstacles in regards to the sintering density of titanium powder is the presence of an oxide film on the surface of the powder particles [26]. The affinity between rare-earth element La and oxygen is much greater than that between Ti and oxygen. Therefore, adding LaF_3 to the alloy can effectively activate the titanium powder. Adding a small amount of LaF_3 has a significant promoting effect on the sintering densification of the HA/Ti powder metallurgy. The La element carries oxygen on the surface of the Ti powder and diffuses into the matrix to form a Ti (La, O) solid solution, promoting the diffusion of elements between the titanium particles. As the amount of LaF_3 added increases, the surface of the activated Ti particles increases, and the densification effect is improved. However, due to the fact that the sintering process mainly occurs in the solid phase, excessive secondary particles will hinder the plastic and viscous flow of the sintering process, thereby reducing the sintering density. Therefore, when the amount of LaF_3 added is 0.5%, the relative density of the material decreases, and its compressive strength also decreases [18].

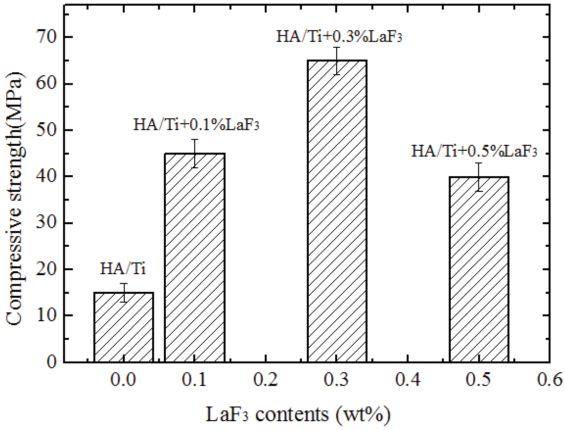

Figure 5. The effect of LaF_3 addition on the compressive strength of the porous HA/Ti scaffolds.

Figure 6 shows the surface morphology of the porous scaffolds after soaking in SBF for 7 days. It can be seen from the figure that the materials with 0.3% LaF_3 added exhibit more spherical coverings over the surface of the porous materials after soaking in SBF solution. The energy spectrum analysis results show that the coverage is mainly composed of calcium, phosphorus, and oxygen, and its composition ratio is similar to that of HA, which indicates that the addition of LaF_3 can further improve the biological activity of the composite.

Due to limited experimental conditions, this study demonstrates certain limitations. For example, if the sample size is small and only in vitro testing methods are used to evaluate biological activity, subsequent studies will be required to conduct cell culture experiments and related animal experiments using the material in order to exhaustively evaluate its comprehensive performance.

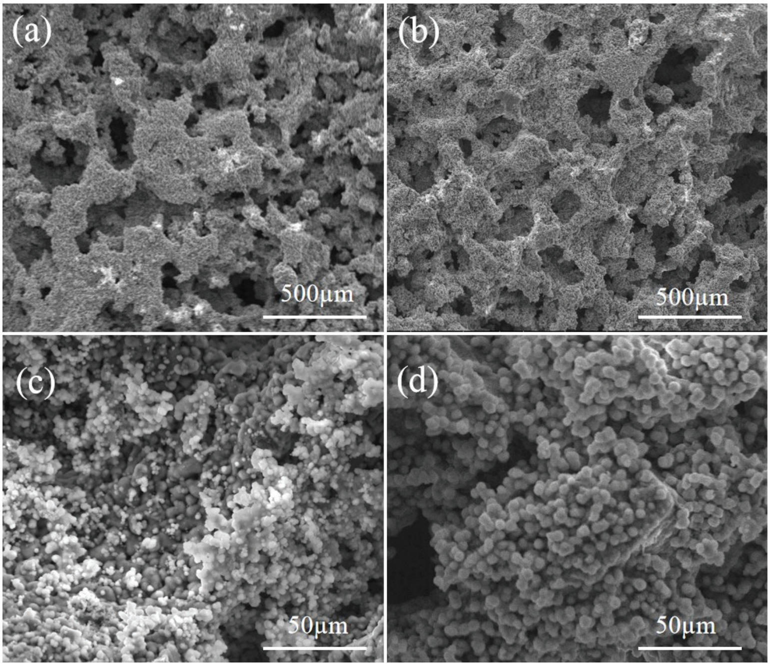

Figure 6. SEM morphology of different porous HA/Ti scaffolds after immersion in SBF for 7 days. (**a**,**c**) 0.0% LaF_3; (**b**,**d**) 0.3% LaF_3.

4. Conclusions

A porous HA/Ti scaffold with high porosity (60%) was prepared by adding pore forming agents. The pore structure of the scaffold is three-dimensional, with pore sizes mainly distributed between 100–300 μm, and there are micrometer sized micropores distributed on the pore walls, which are conducive to the growth of bone tissue and the achievement of biological fixation. The addition of LaF_3 can improve the biomechanical properties of porous HA/Ti scaffolds, and the HA/Ti scaffold exhibits the optimal mechanical performance when the amount of the addition is 0.3%. The compressive strength is 65 MPa, exhibiting mechanical properties similar to those of human bone, which is beneficial for reducing the stress shielding problem caused by the mismatch between the biomechanical properties of the implant and human bone. The rare-earth LaF_3 enhanced porous HA/Ti scaffold offers good pore structure and biomechanical compatibility, and it is expected to be employed as an ideal material for bone replacement and repair.

Author Contributions: Experiments, X.F.; writing, X.F.; editing and translation, H.Z. All authors have read and agreed to the published version of the manuscript.

Funding: This research was funded by the Sichuan Science and Technology Program, No: 2022YFSY0044.

Institutional Review Board Statement: Not applicable.

Informed Consent Statement: Not applicable.

Data Availability Statement: Data are contained within the article.

Conflicts of Interest: The authors declare no conflicts of interest.

References

1. Long, M.; Rack, H.J. Titanium alloys in total joint replacement-a materials science perspective. *Biomaterials* **1998**, *19*, 1621–1639. [CrossRef]
2. Pattanayak, D.K.; Fukuda, A.; Matsushita, T.; Takemoto, M.; Fujibayashi, S.; Sasaki, K.; Nishida, N.; Nakamura, T.; Kokubo, T. Bioactive Ti metal analogous to human cancellous bone: Fabrication by selective laser melting and chemical treatments. *Acta Biomater.* **2011**, *7*, 1398–1406. [CrossRef] [PubMed]
3. Tang, J.; Cui, Z.D.; Zhu, S.L.; Sang, X.M. Progress in the research of biomimetic modification on the surface of Ti and Ti alloy. *J. Funct. Mater.* **2005**, *1*, 19–22.
4. Wang, X.H.; Cao, Y.; Zhang, L. Alkali and thermal treatment of titanium and its effect on the bioactivity. *J. Funct. Mater.* **2013**, *2*, 275.
5. Kim, H.M.; Miyaji, F.; Kokubo, T.; Nakamura, T. Preparation of bioactive Ti and its alloys via simple chemical surface treatment. *J. Biomed. Mater. Res.* **1996**, *32*, 409–417. [CrossRef]
6. Filiaggi, M.J.; Coombs, N.A.; Pilliar, R.M. Characterization of the interface in the plasma-sprayed HA coating/Ti-6Al-4V implant system. *J. Biomed. Mater. Res.* **1991**, *25*, 1211–1229. [CrossRef] [PubMed]
7. Yan, Y.Y.; Sun, J.F.; Han, Y. Microstructure and bioactivity of Ca, P and Sr doped TiO_2 coating formed on porous titanium by micro-arc oxidation. *Surf. Coat. Technol.* **2010**, *205*, 1702–1713. [CrossRef]
8. Akao, H.; Aoki, H.; Kato, K. Mechanical properties of sintered hydroxyapatite for prosthetic application. *J. Mater. Sci.* **1981**, *16*, 809–812. [CrossRef]
9. Osborn, J.; Newesely, H. The material science of calcium phosphate ceramics. *Biomaterials* **1980**, *1*, 108–111. [CrossRef]
10. Ning, C.Q.; Zhou, Y. In vitro bioactivity of a biocomposite fabricated from HA and Ti powders by powder metallurgy method. *Biomaterials* **2002**, *23*, 2909–2915. [CrossRef]
11. Salman, S.; Gunduz, O.; Yilmaz, S. Sintering effect on mechanical properties of composites of natural hydroxyapatites and titanium. *Ceram. Int.* **2009**, *35*, 2965–2971. [CrossRef]
12. Thian, E.S.; Loh, N.H.; Khor, K.A. Ti-6A1-4V HA composite feedstock for injection molding. *Mater. Lett.* **2002**, *56*, 522–532. [CrossRef]
13. Egorov, A.; Smirnov, V.; Shvorneva, L. High-temperature hydroxyapatite-titanium interaction. *Inorg. Mater.* **2010**, *46*, 168–171. [CrossRef]
14. Zou, H.; Lu, Q.; Tian, W.D. Preparation and characterization of bio-medical porous titanium by unconventional powder metallurgy. *J. Funct. Mater. Devices* **2010**, *16*, 490–494.
15. Fan, X.P.; Feng, B.; Liu, Z.Y. Fabrication of TiO_2 nanotubes on porous titanium scaffold and biocompatibility evaluation in vitro and in vivo. *J. Biomed. Mater. Res. A* **2012**, *12*, 3422–3427. [CrossRef] [PubMed]
16. Thurzo, A.; Gálfiová, P.; Nováková, Z.V.; Polák, Š.; Varga, I.; Strunga, M.; Urban, R.; Surovková, J.; Leško, L'.; Hajdúchová, Z.; et al. Fabrication and in vitro characterization of novel hydroxyapatite scaffolds 3D printed using polyvinyl alcohol as a thermoplastic binder. *Int. J. Mol. Sci.* **2022**, *23*, 14870. [CrossRef] [PubMed]
17. Zhang, G.J.; Sun, Y.J.; Niu, R.M. The strenthening mechanism of rare earth lanthanum oxide doped molybdenum alloys. *Rare Met. Mater. Eng.* **2005**, *34*, 1926–1930.
18. Wang, B.; Liu, Y.; Liu, Y.B. Effects of LaH_2 and LaB_6 addition on microstructure and mechanical property of powder metallurgy Ti alloy. *Mater. Sci. Eng. Powder Metall.* **2011**, *16*, 136–142.
19. Shao, Z.Y.; Li, F.; Zhang, J.L. Research progress of various nano-materials reinforced and rare earth element doped Ti-HA composites. *Met. Funct. Mater.* **2017**, *24*, 13–24.
20. Lv, N.L.; Yin, P.; Xia, M. Sr-containing bioglass fabricated by sol-gel method and its solubility. *Fenmo Yejin Cailiao Kexue yu Gongcheng/Mater. Sci. Eng. Powder Metall.* **2015**, *20*, 296–303.
21. Kokubo, T.; Takadama, H. How useful is SBF in prediction in vivo bone bioactivity? *Biomaterials* **2006**, *27*, 2907–2915. [CrossRef]
22. Chen, Y.J.; Feng, B.; Zhu, Y.P. Fabrication of porous titanium implants with biomechanical compatibility. *Mater. Lett.* **2009**, *30*, 2659–2661. [CrossRef]
23. Ning, C.Q.; Zhou, Y.; Jia, D.C. Mechanical properties and biological behavior of titanium/hydroxyapatite biocomposites. *J. Chin. Ceram. Soc.* **2000**, *28*, 483–486.
24. Ohtsuki, C.; Kokubo, T.; Yamamuro, T. Mechanism of apatite formation on CaO-SiO_2-P_2O_5 glasses in a simulated body fliud. *J. Non-Cryst. Solids* **1992**, *143*, 84–92. [CrossRef]
25. De, G.K.; Klein, C.P.A.T.; Wolke, J.G.C. Chemistry of calcium phosphate bioceramics. In *Handbook of Bioactive Ceramics, II*; Yamamuro, T., Hench, L.L., Wilson, J., Eds.; CRC Press: Boca Raton, FL, USA, 1990; pp. 3–6.
26. Fujita, T.; Ogawa, A.; Ouchi, C. Microstructure and properties of titanium alloy produced in the newly developed blended elemental powder metallurgy process. *Mater. Sci. Eng. A* **1996**, *213*, 148–153. [CrossRef]

coatings

Article

Effect of Vacancy Defects and Hydroxyl on the Adsorption of Glycine on Mg(0001): A First-Principles Study

Zhe Fang [1,2], Wutao Wei [1,*], Huijie Qiao [1], Erjun Liang [2,*], Yu Jia [2,3] and Shaokang Guan [4]

[1] School of Materials and Chemical Engineering, Center for Advanced Materials Research, Zhongyuan University of Technology, Zhengzhou 450007, China
[2] International Laboratory for Quantum Functional Materials of Henan & School of Physics and Microelectronics, Zhengzhou University, Zhengzhou 450001, China
[3] Key Laboratory for Special Functional Materials of Ministry of Education, Henan University, Kaifeng 475004, China
[4] School of Materials Science and Engineering, Zhengzhou University, Zhengzhou 450001, China
* Correspondence: 9889@zut.edu.cn (W.W.); ejliang@zzu.edu.cn (E.L.)

Abstract: Glycine (Gly), as one of the fundamental components of biomolecules, plays a crucial role in functional biomolecular coatings. The presence of structural defects and hydroxyl-containing functional groups in magnesium (Mg) materials, which are commonly used as biomedical materials, significantly affects their biocompatibility and corrosion resistance performance. This study computationally investigates the influence of vacancy defects and hydroxyl groups on the adsorption behavior of Gly on Mg(0001) surfaces. All potential adsorption configurations are considered through first-principles calculations. The findings indicate that stronger chemisorption occurs when Gly is positioned at the edge of the groove, where the surface has a vacancy defect concentration of 1/3. Among the four adsorption locations, the fcc-hollow site is determined to be the most favorable adsorption site for hydroxyl. The adsorption energy of Gly on the Mg(0001) surface containing the hydroxyl (-1.11 eV) is 0.05 eV more than that of on the Mg(0001) surface (-1.16 eV). The adsorption energies, electronic properties, charge transfer, and stable configurations are calculated to evaluate the interaction mechanism between Gly and defective surfaces. Calculated results provide a comprehensive understanding of the interaction mechanism of biomolecules on defective Mg surfaces and also indicate the directions for future experimental research.

Keywords: glycine; Mg; defect; first-principles calculation; adsorption

Citation: Fang, Z.; Wei, W.; Qiao, H.; Liang, E.; Jia, Y.; Guan, S. Effect of Vacancy Defects and Hydroxyl on the Adsorption of Glycine on Mg(0001): A First-Principles Study. *Coatings* **2023**, *13*, 1684. https://doi.org/10.3390/coatings13101684

Academic Editor: Alessandro Patelli

Received: 30 August 2023
Revised: 19 September 2023
Accepted: 22 September 2023
Published: 26 September 2023

1. Introduction

The initial reactions of biological magnesium (Mg) alloy materials in the physiological environment of the human body depend on their surface properties [1–5]. Surface modification is one of the most commonly used methods to regulate the interaction between biomaterials and internal tissues, improving the biocompatibility and corrosion resistance of Mg alloys [6–12]. The optimal treatment and disease diagnosis are achieved through this method to better adapt to physiological environments and provide required clinical performance requirements.

Investigating the interaction between material surfaces with different microstructures and biomolecules has important clinical applications. It is difficult to obtain the perfect crystal surface with atoms arranged regularly and completely due to the influence of atoms (or ions and molecules), the formation conditions of crystals, cold or hot processing, and some crystal defects [13–15]. Crystal defects are mainly divided into vacancy defects, line defects, and surface defects according to the geometric characteristics, and common vacancy defects mainly include vacancy, interstitial particles, and foreign particles. Han et al. used the first-principles calculation method based on density functional theory and found that the presence of vacancy defects enhances the reaction activity of the Mg(0001) surface and reduces the diffusion barrier of hydrogen on the surface [16]. The calculated results by Zhou et al. through the first-principles calculation indicate that the addition of transition metals on the Mg surface makes a strong interaction between the transition metals and Mg atoms, and the diffusion process of the transition metal atoms is difficult to produce due to the higher potential barrier [17].

For the study of the adsorption of hydroxyl on the surface of Mg, the results of Williams et al. reported that the adsorption of hydroxyl on the surface of Mg is relatively stable in a neutral environment with a pH value of 7. The stable adsorption of hydroxyl reduced the work function of the Mg surface, which will be beneficial for the hydrogen release process [18]. Yuwono et al. found that the stability of the Mg surface is related to the concentration of hydroxyl adsorbed. A certain concentration of hydroxyl adsorbed on the Mg surface decreases the surface work function, which is conducive to the progress of chemical reactions [19]. Zhou et al. calculated the different bromine coverage on the Mg(0001) surface and found that the adsorption is most stable at the fcc-hollow site with the bromine coverage being 0.25–1.00 ML, and the adsorption energy decreases, and the work function increases with the increase of the coverage [20]. Li et al. modified the metal surface state by doping, introducing defects, or adsorbing other radicals to prompt the hydride formation and revealed the nature of this phenomenon in the Mg corrosion via the first-principles calculation [21].

Amino acids, as the fundamental units of proteins, are interesting adsorbents for studying the interaction between biomolecules and solid surfaces [22]. These organic molecules exhibit various charges, polarities, water interactions, and proton exchanges. A common feature is that they are composed of an amino group and a carboxyl group, but there is a unique functional group in the side chain. They are the fundamental units of complex biological molecules containing peptides and proteins. Gly is one of the basic components of biological molecules and a nonessential amino acid that exists in neutral and zwitterionic forms. A single carbon molecule is linked to an amino and a carboxyl group, making it the simplest amino acid among all amino acids [23,24]. The investigation of the surface structure and properties of Gly and biomaterials is not only a significant subject in the fields of life sciences and medicine but also a crucial scientific matter in the domains of chemistry, materials science, and the pharmaceutical industry [25–30]. Kumar et al. optimized the adsorption geometries of Gly and suggested covalent bonding between N and O atoms of the molecules and the surface Cu-atoms [24]. Madden et al. [31] carried out both experimental and computational investigations to shed light on the adsorption behavior of glycine on this specific Cu(311) surface and found that Gly adsorbs onto Cu(311) with the nitrogen atom and one or two oxygen atoms of the carboxylic acid group bonding to copper atoms in an adjacent row. These simulations helped explain the specific bonding arrangements observed in the experimental results.

The adsorption and reactivity of Gly on Mg and Mg-based alloy surfaces, as well as the interaction mechanism between biomolecules and different Mg surfaces, were investigated in our previous work [32–35]. In the present work, the influence of surface vacancy defects concentration (1/36, 1/6, 1/3, and 1/2) and hydroxyl on the adsorption characteristics of Gly on the Mg(0001) surface was systematically investigated and discussed based on the density functional theory (DFT). Our theoretical studies help us propose scenarios for the adsorption mechanism of Gly/Mg(0001) and elucidate their dependence on different surface vacancy concentrations. The anticipated computational results will provide a better understanding of the reactivity of Mg-defected crystal surfaces and hydroxyl groups during the adsorption process of glycine. This understanding will facilitate the design of Mg surfaces with enhanced performance.

2. Computational Methods

All DFT calculations were performed using the Vienna Ab initio Simulation Package (VASP) with the projector-augmented wave (PAW) method to characterize the interaction between ions and valence electrons [36–38]. The exchange-correlation function was dealing with GGA-PBE [39]. Dion et al. [40] and Klimeŝ et al. [41–43] have proposed the local van der Waals density functional scheme for the van der Waals contributions. Calculations of the present work were performed by the optB86b-vdW method [44]. The plane wave cut-off energy was set to 400 eV to describe the valance electrons. Six atomic layer thicknesses with four vacancy defect concentrations of 1/36, 1/6, 1/3, and 1/2 were chosen as the surface model, and the bottom two layers of Mg atoms were fixed throughout the optimization. The concentration of four vacancy defects is primarily distributed in the topmost atomic layer of the surface model. The bottom two layers of Mg atoms were fixed throughout the optimization with the vacuum of 20 Å, and the optimized glycine molecule was placed above the Mg(0001) surface. The ground state convergence criterion was set to 10^{-5} eV, and all atoms were allowed to fully relax until the Hellmann-Feynman forces were smaller than 0.02 eV/Å during the geometry optimization process.

The calculation of the adsorption energy (E_{ads}) of Gly on different substrates is as follows:

$$E_{ads} = E_{mol} + E_{sub} - E_{mol+sub} \tag{1}$$

where E_{mol}, E_{sub}, and $E_{mol+sub}$ represent the total energy of the optimized Gly, the energy of different substrates, and the energy of the stable adsorption systems, respectively.

3. Results and Discussion

Gly is primarily composed of an amino group and a carboxyl group, making it the simplest structure in the amino acid sequence. The interaction between amino acids and the surface mainly includes van der Waals and electrostatic interactions, and surface charges significantly affect the adsorption of amino acids [7]. The optimized structure of Gly is shown in Figure 1a, and the bond lengths of C1-N1, C2-O1, and C2-O2 are 1.45 Å, 1.21 Å, and 1.36 Å, respectively. The hexagonal close-packed crystal structure of Mg is depicted in Figure 1b, and the optimized lattice parameters of the bulk hcp Mg are a = b = 3.188 Å and c = 5.193 Å, which are in good agreement with the experimental results (a = b = 3.210 Å, c = 5.213 Å) [45] as well as the previously calculated results (a = b = 3.193 Å, c = 5.185 Å) [46]. For the adsorption of the isolated hydroxyl, four adsorption sites (bridge, top, fcc-hollow, and hcp-hollow sites) on the Mg(0001) surface are shown in Figure 1c.

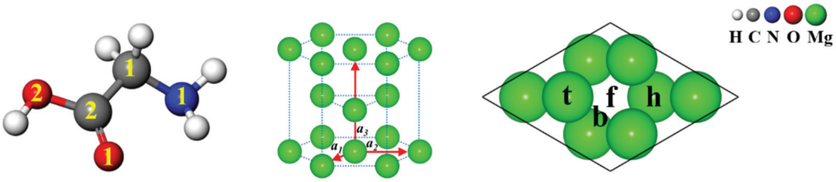

(a) Gly (b) Mg (c) Mg(2×2)

Figure 1. (**a**) Optimized structure of Gly. (**b**) The crystal structure of Mg. (**c**) Four adsorption sites (bridge, top, fcc-hollow, and hcp-hollow sites) on the surface of Mg(0001).

3.1. Adsorption of Gly on the Mg(0001) Surfaces with Different Defect Concentrations

The isolated adsorption behavior of Gly on the Mg(0001) surface was reported earlier, and the strongest interaction occurs when the amino and carboxyl groups in glycine adsorbed on the Mg(0001) surface simultaneously, according to the calculated results [32]. The electronic structural properties of the Mg surface are altered by the presence of a vacancy defect in the optimized defect-free cleaved Mg(0001) surface. In this study, the adsorption behavior of Gly on the Mg(0001) surface with four different surface vacancy defect concentrations (1/36, 1/6, 1/3, and 1/2) was investigated to establish a correlation between the electronic properties of Gly and the surfaces. The optimized surfaces of four energetically significant configurations with varying vacancy defect concentrations (1/36, 1/6, 1/3, and 1/2) are illustrated in Figure 2.

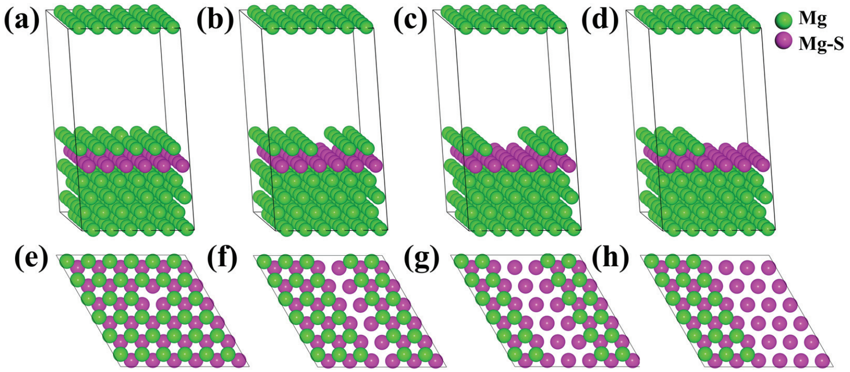

Figure 2. (**a**–**d**) provide side views, and (**e**–**h**) show top views of four different Mg(0001) surfaces with varying vacancy defect concentrations of (**a**) 1/36, (**b**) 1/6, (**c**) 1/3, and (**d**) 1/2. The Mg-S notation indicates the Mg atoms in the second layer.

As reported in Ref. [32] regarding the adsorption of Gly on the Mg(0001) surface, it is important to note that the N atom in the amino group and the O atom in the carboxyl group primarily interact with the surface Mg atoms. The coordination covalent bonds formed between N-Mg and O-Mg contribute to stronger interactions. To investigate the adsorption behavior of Gly on surfaces with vacancy defects, the adsorption energies of Gly on the Mg surface were calculated at the four different vacancy defect concentrations mentioned above. The adsorption energies of Gly on the Mg surface after reaching a stable adsorption state are listed in Table 1, and the adsorption configurations of Gly on the Mg(0001) surface are depicted in Figure 3.

Table 1. Adsorption energies of Gly on different vacancy defect concentrations of Mg(0001) surfaces.

Adsorption Energy	Vacancy Defect Concentrations			
	1/36	1/6	1/3	1/2
E_{ads} (eV)	−1.17	−1.26	−1.27; −1.40	−1.25; −1.15

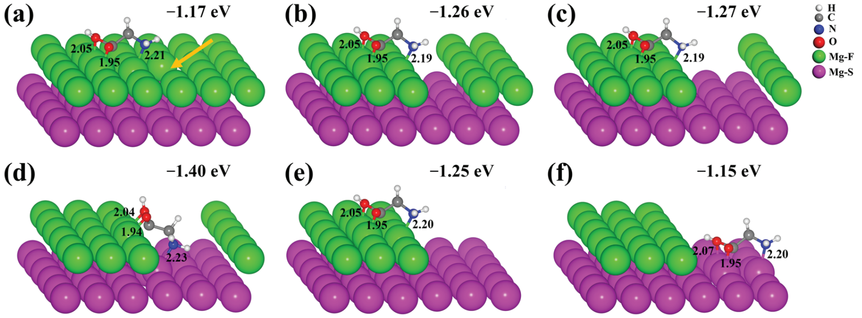

Figure 3. (**a**–**f**) are stable adsorption configurations of Gly on the Mg(0001) surfaces with the defect concentration of 1/36, 1/6, 1/3, 1/3, 1/2, and 1/2, respectively. Mg-F and Mg-S represent Mg atoms in the first and second layers, respectively.

The presence of defects has an impact on the electronic structure properties of the surface, which in turn affects the adsorption process of Gly. According to the calculated adsorption energy using Equation (1) in Table 1, it is observed that the presence of a single atomic vacancy defect on the Mg(0001) surface, as indicated by the arrow in Figure 3a, results in an adsorption energy of −1.17 eV for Gly on this surface. In comparison to the adsorption energy of Gly on the defect-free Mg(0001) surface (−1.16 eV), the presence of a vacancy defect with a concentration of 1/36 slightly influences the adsorption energy of Gly, resulting in an adsorption energy of −1.17 eV. Figure 3b illustrates the optimized adsorption configuration of Gly on the Mg(0001) surface with a vacancy defect concentration of 1/6. In this configuration, the adsorption energy is −1.26 eV, indicating a higher stability compared to the adsorption on the Mg(0001) surface with a vacancy defect concentration of 1/36.

For the adsorption of Gly on the Mg(0001) surface with a defect concentration of 1/3, the optimized adsorption configurations are shown in Figure 3c,d. Considering the adsorption near and at the edge of the groove, the calculated E_{ads} are −1.27 eV and −1.40 eV, respectively. In comparison to the other cases shown in Figure 3, the configurations presented in Figure 3c,d exhibit higher E_{ads}. Among the six different adsorption configurations, the most stable configuration is observed when Gly is adsorbed at the edge of the groove. Considering defect surfaces with a vacancy defect concentration of 1/2, the adsorption of Gly near the edge and at the bottom of grooves was investigated. The optimized results for these adsorption configurations are depicted in Figure 3e,f, and the calculated E_{ads} are −1.25 and −1.15 eV, respectively. When Gly was adsorbed at the bottom of the vacancy defect groove, its adsorption energy was nearly equivalent to that on the surface of a defect-free Mg(0001) surface.

From the calculated results, the adsorption configuration of Gly at the edge of the grooved Mg(0001) surface with the vacancy defect is the most stable adsorption structure. The sharing of electrons from the adsorbent to the surface of Mg(0001) leads to a decrease in the length of the interaction bond to its optimal distance, resulting in an increase in the adsorption interaction energy. The optimized bond lengths of N1-Mg, O1-Mg, and O2-Mg in the adsorption systems shown in Figure 3 are approximately 2.19–2.23 Å, 1.94–1.95 Å, and 2.04–2.07 Å, respectively. These optimized bond lengths in Figure 3 are in close agreement with the sum of the covalent radii (2.11 and 2.09 Å) of nitrogen (0.75 Å) and oxygen (0.73 Å) atoms with the Mg (1.36 Å) atom, as reported in Ref. [47]. This agreement between the calculated bond lengths and the expected values is consistent with the results presented in Ref. [48].

3.2. Effect of Hydroxyl on the Adsorption of Gly on the Mg(0001) Surfaces

Under physiological conditions, the surfaces of Mg and Mg alloys are susceptible to hydroxylation, resulting in the formation of hydroxyl (hydroxide anion) on their surfaces. This hydroxyl presence has an impact on the binding properties of biomolecular coatings to these surfaces. To investigate the adsorption behavior of Gly on the Mg(0001) surface with hydroxyl, it is essential to determine the most stable position of the hydroxyl on the Mg(0001) surface. The optimized adsorption configurations of the hydroxyl at the four adsorption sites' (bridge, top, fcc-hollow, and hcp-hollow sites, as shown in Figure 1c) on the Mg(0001) surfaces are displayed in Figure 4. The calculated E_{ads} of the four adsorption cases by Equation (1) are depicted in Table 2.

Table 2. Adsorption energies of hydroxyl on the Mg(0001) surfaces.

Adsorption Energy	**Adsorption Site of Hydroxyl**			
	Bridge	**Top**	**Fcc-Hollow**	**Hcp-Hollow**
E_{ads} (eV)	−5.4581	−5.4569	−5.5010	−5.5004

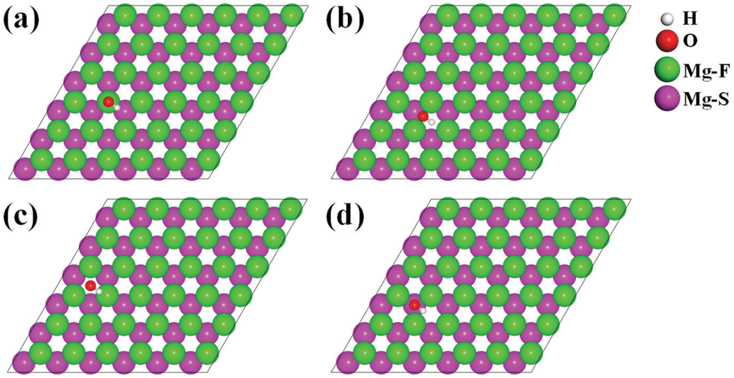

Figure 4. (**a**–**d**) correspond to the structures of hydroxyl adsorbed on the top, bridge, fcc, and hcp sites of Mg(0001) surface, respectively. The Mg-F and Mg-S labels indicate the Mg atoms in the first and second layers, respectively.

According to the optimized adsorption configurations of hydroxyl on the Mg(0001) surface in Figure 4 and the calculated E_{ads} by Equation (1) in Table 2, it can be seen that the E_{ads} of hydroxyl on the Mg(0001) surface for the four adsorption sites (bridge, top, fcc-hollow, and hcp-hollow sites) are −5.4581, −5.4569, −5.5010, and −5.5004 eV, respectively. The fcc-hollow site is the most favorable adsorption site among the four adsorption locations. Therefore, a Mg surface model with the hydroxyl adsorbed on the fcc-hollow site was selected as the surface for the adsorption of Gly. A hydroxylated Mg(0001) surface differs from the defect-free surface by the presence of a hydroxyl group (OH) that obtains some electrons from the surface. The optimized stable adsorption structure of Gly on the hydroxylated Mg(0001) surface, along with the selected bond lengths, is shown in Figure 5. The calculated E_{ads} of Gly on the Mg(0001) surface containing the hydroxyl is −1.11 eV, which is 0.05 eV more than the adsorption energy of Gly on the defect-free Mg(0001) surface (−1.16 eV) [32]. The presence of an additional OH group on the Mg(0001) surface leads to a slight decrease in the adsorption energy of Gly adsorption configurations. The sharing of electrons from the hydroxyl group to the Mg surface affects the overall binding energy between Gly and the Mg(0001) surface. This electron sharing leads to a decrease in the adsorption energy of Gly adsorption configurations.

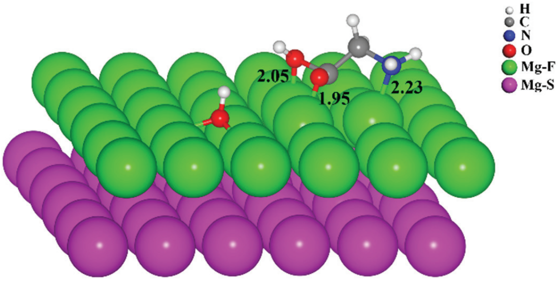

Figure 5. The optimized adsorption configuration of Gly on the hydroxylated Mg(0001) surface. The bond lengths (in Å) are also listed, and Mg-F and Mg-S represent Mg atoms in the first and second layers, respectively.

Based on the calculated results, it is observed that the adsorption of Gly on the hydroxylated Mg(0001) surface is accompanied by the release of a considerable amount of charge and energy. In the process of hydroxyl adsorption, some electrons are obtained from Mg atoms on the surface, resulting in corresponding changes in the electronic structure properties of the surface. After stable adsorption, the interaction between the Mg(0001) surface containing hydroxyl and Gly is weakened. The bond lengths of O1-Mg, O2-Mg, and N-Mg are 1.95, 2.05, and 2.23 Å, respectively, which are close to the theoretical bond lengths for forming covalent bonds [47], and this result is also in good agreement with the results in Ref. [48].

3.3. Electronic Properties of Gly on Different Mg(0001) Surfaces

In this section, the interaction mechanism between orbitals during the formation of Gly and the defected/hydroxylated Mg(0001) surfaces was explored. As the results of previous sections suggest, the favorable adsorption structure of Gly at the edge of the groove in the defected adsorption system was focused. To analyze the electronic properties, the projected density of states (PDOS) of the Gly adsorption configurations on the mentioned substrates was examined. Specifically, the orbitals of the covalently bonded atoms before and after the adsorption were analyzed, as depicted in Figure 6.

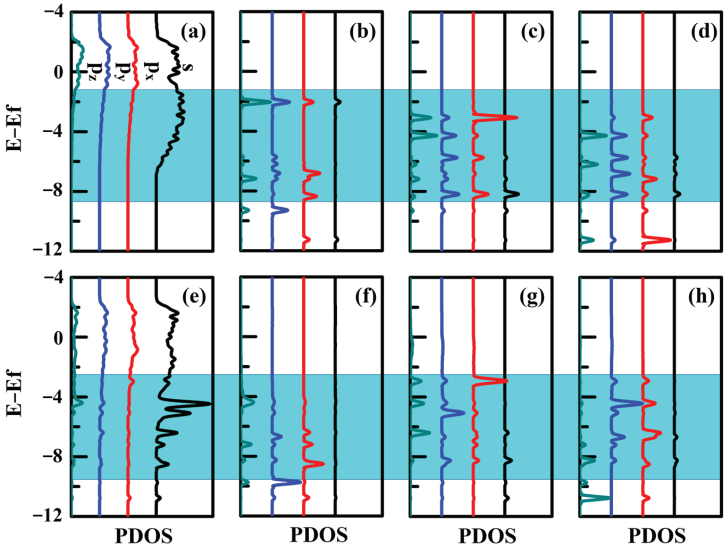

Figure 6. (**a**–**d**) are the PDOS of binding Mg atoms of the Mg(0001) surface, N1, O1, and O2 atoms of Gly before the adsorption; (**e**–**h**) are the PDOS of the corresponding atoms after adsorption, respectively. The Fermi level is set at 0 eV.

The calculated results in Figure 6 reveal that the electron localization of the binding atoms in isolated Gly decreases, and new peaks of the binding Mg atoms emerge after adsorption, in contrast to the results obtained before adsorption. A new peak overlap was observed between the N and Mg atoms at −4.30 eV in Figure 6e,f, which suggests the formation of a covalent bond between these atoms. This is evident from the shaded areas in the figure, where the PDOS curves of N and Mg atoms overlap, indicating the sharing of electrons and the formation of a chemical bond. The O1 atom that binds to the Mg atom on the surface exhibits overlapping peaks at −5.20 eV and −8.22 eV in Figure 6e,g. This indicates the formation of new covalent bonds between O1 and Mg. The shaded regions in the figure demonstrate this overlap, suggesting the sharing of electrons and the formation of chemical bonds between the O1 and Mg atoms. Indeed, it can be observed that the p-state electron localization of O1 is weakened after the surface adsorption of Gly, as compared to the results of Gly on the vacancy defect surface before adsorption. This can be seen in the PDOS curves of O1 in Figure 6g,h, where the peaks corresponding to the p-states of O1 become less pronounced after the adsorption of Gly on the Mg(0001) surface. This suggests a redistribution of electron density and a weakening of the electron localization of O1 upon adsorption. Overlapping peaks of O2 and Mg atoms appear at the positions of −3.00 and −5.00 eV, indicating that O2 forms a new bond with surface Mg atoms, as depicted in the shaded areas in Figure 6e,h. According to the bond length values of each stable adsorption configuration in Figure 3, the bond lengths of N-Mg and O-Mg are close to the theoretical bond length of the covalent bond formed by them. The binding reason is mainly that the N in the amino group and the O in the carboxyl group share the lone pair electrons with the surface Mg atoms. Therefore, a coordination covalent bond is also formed between them when the defective Mg surface adsorbs Gly.

Further, the PDOS of Gly on the Mg(0001) surface with the hydroxyl adsorbed is plotted, as shown in Figure 4. This is an important process as hydroxylated Mg surfaces are very common on biomimetic coating surfaces.

One significant observation is the distinct downward displacement of the sp states of N and O in Figure 7. This indicates that the adsorption of Gly onto the hydroxylated Mg(0001) surface leads to a substantial reduction in electron localization within Gly. This considerable weakening of electron localization arises from the strong interaction that occurs between the N and O atoms of Gly and the surface. New peaks of N1-Mg atoms appear at the positions of −4.02, −6.21, and −8.10 eV in Figure 7e,f. At the same time, the O1 and Mg atoms exhibit new overlapping peaks at the positions of −3.80 and −4.10 eV, and the broadening range of O1 increases. This is mainly caused by the strong interaction between the *p*-orbital electrons of O1 and the s- and p-orbital electrons of the Mg surface atoms, as shown in the shaded regions in Figure 7e,g. The overlapping peaks of O2-Mg in Figure 7e,h appear at −3.80 and −4.20 eV, respectively.

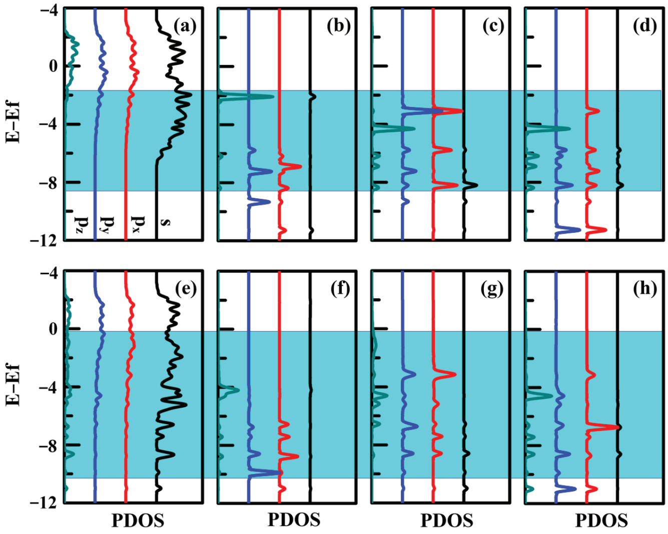

Figure 7. The PDOS of Gly on the hydroxylated Mg(0001) surface. (**a**–**d**) are the PDOS of Mg, N1, O1, and O2 atoms before adsorption, respectively; (**e**–**h**) are the PDOS of the corresponding atoms after adsorption, respectively.

The presence of overlapping peaks in the observed regions implies the formation of a novel chemical bond between Gly and the Mg surface atoms. The bonding process is mainly caused by the sharing of electrons between N and O atoms and Mg surface atoms. The bond lengths of N1-Mg, O1-Mg, and O2-Mg are close to the theoretical bond lengths for N/O and Mg to form a covalent bond. Therefore, Gly binds to the Mg surface containing defect/hydroxyl through coordinating covalent bonds.

4. Conclusions

In conclusion, the DFT calculations with the optb86b-vdw dispersion correction were utilized to investigate the impact of surface vacancy defects and hydroxyl on the adsorption characteristics of Gly on the Mg(0001) surface. All the possible adsorption configurations have been taken into account, and the interaction mechanism of Gly on different surface vacancy defect concentrations was also analyzed. Based on our analysis, the conclusions can be drawn as follows:

1. In the case of vacancy defects with varying concentrations, the most favorable adsorption mode of Gly on the Mg(0001) surface was found to involve the formation of coordination covalent bonds between the amino and carboxyl groups of Gly and the surface Mg atoms. Computational analysis revealed that the presence of defects facilitated a stronger adhesion of Gly to the surface compared to the defect-free surface. Specifically, the most stable configuration was observed when Gly was adsorbed at the edge of the grooved vacancy defect surface, with a defect concentration of 1/3.
2. Among the four adsorption sites, the fcc site is the most favorable adsorption site for the hydroxyl group. The adsorption of the hydroxyl group alters the electronic structure properties of the Mg(0001) surface, causing some electrons to transfer from the Mg(001) surface to the hydroxyl group, resulting in a slight decrease in the adsorption energy of Gly.
3. Different concentrations of vacancy defects can improve the adsorption of glycine on the Mg(0001) surface. The presence of the hydroxyl functional group weakens the adsorption of glycine on the Mg(0001) surface. These findings offer a theoretical foundation for the development of amino acid-based bio-coatings on material surfaces.

Author Contributions: Conceptualization, E.L.; Software, Y.J.; Writing—original draft, Z.F.; Writing—review & editing, S.G.; Visualization, H.Q.; Supervision, W.W. All authors have read and agreed to the published version of the manuscript.

Funding: The authors are very grateful for the financial support of the National Key Research and Development Program of China (2021YFC2400700), the Youth Fund Project of Zhongyuan University of Technology (K2022QN026), and the GHfund B 202302022245.

Institutional Review Board Statement: Not applicable.

Informed Consent Statement: Not applicable.

Data Availability Statement: Not applicable.

Conflicts of Interest: The authors declare no conflict of interest.

References

1. Kim, J.; Pan, H.B. Effects of magnesium alloy corrosion on biological response—Perspectives of metal-cell interaction. *Prog. Mater. Sci.* **2023**, *133*, 101039.
2. Farshid, S.; Kharaziha, M.; Atapour, M. A self-healing and bioactive coating based on duplex plasma electrolytic oxidation/polydopamine on AZ91 alloy for bone implants. *J. Magnes. Alloys* **2023**, *11*, 592–606.
3. Hou, R.Q.; Feyerabend, F.; Helmholz, H.; Garamus, V.M.; Willumeit-Roemer, R. Effects of proteins on magnesium degradation-static vs. dynamic conditions. *J. Magnes. Alloys* **2023**, *11*, 1332–1342.
4. Albaraghtheh, T.; Willumeit-Roemer, R.; Zeller-Plumhoff, B. In silico studies of magnesium-based implants: A review of the current stage and challenges. *J. Magnes. Alloys* **2022**, *10*, 2968–2996.
5. Kuah, K.X.; Wijesinghe, S.; Blackwood, D.J. Toward understanding in vivo corrosion: Influence of interfacial hydrogen gas build-up on degradation of magnesium alloy implants. *J. Biomed. Mater. Res. Part A* **2023**, *111*, 60–70. [CrossRef] [PubMed]
6. Mei, D.; Wang, C.; Lamaka, S.V.; Zheludkevich, M.L. Clarifying the influence of albumin on the initial stages of magnesium corrosion in Hank's balanced salt solution. *J. Magnes. Alloys* **2021**, *9*, 805–817.
7. Höhn, S.; Virtanen, S.; Boccaccini, A.R. Protein adsorption on magnesium and its alloys: A review. *Appl. Surf. Sci.* **2019**, *464*, 212–219.
8. Hou, R.Q.; Scharnagl, N.; Willumeit-Römer, R.; Feyerabend, F. Different effects of single protein vs. protein mixtures on magnesium degradation under cell culture conditions. *Acta Biomater.* **2019**, *98*, 256–268. [PubMed]

9. Cai, L.; Mei, D.; Zhang, Z.Q.; Huang, Y.D.; Cui, L.Y.; Guan, S.K.; Chen, D.C.; Kannan, M.B.; Zheng, Y.F.; Zeng, R.C. Advances in bioorganic molecules inspired degradation and surface modifications on Mg and its alloys. *J. Magnes. Alloys* **2022**, *10*, 670–688.
10. Hedberg, Y.S. Role of proteins in the degradation of relatively inert alloys in the human body. *npj Mater Degrad* **2018**, *2*, 1–5.
11. Rajan, S.T.; Arockiarajan, A. A comprehensive review of properties of the biocompatible thin films on biodegradable Mg alloys. *Biomed. Mater.* **2023**, *18*, 012002. [CrossRef]
12. Zhang, Z.Q.; Wang, H.Y.; Zeng, R.C. Protein conformation and electric attraction adsorption mechanisms on anodized magnesium alloy by molecular dynamics simulations. *J. Magnes. Alloys* **2022**, *10*, 3143–3155. [CrossRef]
13. Dai, J.H.; Xie, R.W.; Chen, Y.Y.; Song, Y. First principles study on stability and hydrogen adsorption properties of Mg/Ti interface. *Phys. Chem. Chem. Phys.* **2015**, *17*, 16594–16600. [CrossRef] [PubMed]
14. Savaedi, Z.; Motallebi, R.; Mirzadeh, H. A review of hot deformation behavior and constitutive models to predict flow stress of high-entropy alloys. *J. Alloys Compd.* **2022**, *903*, 163964. [CrossRef]
15. Li, Z.X.; Li, D.J.; Zhou, W.K.; Hu, B.; Zhao, X.F.; Wang, J.Y.; Qin, M.; Xu, J.K.; Zeng, X.Q. Characterization on the formation of porosity and tensile properties prediction in die casting Mg alloys. *J. Magnes. Alloys* **2022**, *10*, 1857–1867. [CrossRef]
16. Han, Z.Y.; Chen, H.P.; Zhou, S.X. Dissociation and diffusion of hydrogen on defect-free and vacancy defective Mg (0001) surfaces: A density functional theory study. *Appl. Surf. Sci.* **2017**, *394*, 371–377. [CrossRef]
17. Zhou, B.C.; Shang, S.L.; Wang, Y.; Liu, Z.K. Diffusion coefficients of alloying elements in dilute Mg alloys: A comprehensive first-principles study. *Acta Mater.* **2016**, *103*, 573–586. [CrossRef]
18. Williams, K.S.; Labukas, J.P.; Rodriguez-Santiago, V.; Andzelm, J.W. First Principles Modeling of Water Dissociation on Mg(0001) and Development of a Mg Surface Pourbaix Diagram. *Corrosion* **2014**, *71*, 209–223. [CrossRef]
19. Yuwono, J.A.; Birbilis, N.; Williams, K.S.; Medhekar, N.V. Electrochemical Stability of Magnesium Surfaces in an Aqueous Environment. *J. Phys. Chem. C* **2016**, *120*, 26922–26933. [CrossRef]
20. Zhou, W.L.; Liu, T.; Li, M.C.; Zhao, T.; Duan, Y.H. Adsorption of bromine on Mg(0001) surface from first-principles calculations. *Comput. Mater. Sci.* **2016**, *111*, 47–53. [CrossRef]
21. Li, B.X.; Xiao, C.C.; Harrison, N.M.; Fogarty, R.M.; Horsfield, A.P. Role of electron localisation in H adsorption and hydride formation in the Mg basal plane under aqueous corrosion: A first-principles study. *Phys. Chem. Chem. Phys.* **2023**, *25*, 5989–6001. [CrossRef]
22. Talha, M.; Ma, Y.C.; Kumar, P.; Lin, Y.H.; Singh, A. Role of protein adsorption in the bio corrosion of metallic implants—A review. *Colloids Surf. B Biointerfaces* **2019**, *176*, 494–506. [CrossRef]
23. Jackson, A.A. The Glycine story. *Eur. J. Clin. Nutr.* **1991**, *45*, 59–65.
24. Adeva-Andany, M.; Souto-Adeva, G.; Ameneiros-Rodriguez, E.; Fernandez-Fernandez, C.; Donapetry-Garcia, C.; Dominguez-Montero, A. Insulin resistance and glycine metabolism in humans. *Amino Acids* **2018**, *50*, 11–27. [CrossRef]
25. Yin, L.H.; Liu, X.P.; Yi, L.Y.; Wang, J.; Zhang, Y.J.; Feng, Y.F. Structural characterization of calcium glycinate, magnesium glycinate and zinc glycinate. *J. Innov. Opt. Health Sci.* **2016**, *10*, 1650052. [CrossRef]
26. Kanazawa, K.; Taninaka, A.; Takeuchi, O.; Shigekawa, H. What Orchestrates the Self-Assembly of Glycine Molecules on Cu(100)? *Phys. Rev. Lett.* **2007**, *99*, 216102. [CrossRef]
27. Pantaleone, S.; Rimola, A.; Ugliengo, P.; Sodupe, M. First-Principles Modeling of Protein/Surface Interactions. Polyglycine Secondary Structure Adsorption on the TiO_2 (101) Anatase Surface Adopting a Full Periodic Approach. *J. Chem. Inf. Model.* **2021**, *61*, 5484–5498. [CrossRef]
28. Xavier, N.F.; da Silva, A.M., Jr.; Sacchi, M.; Bauerfeldt, G.F. Decarboxylation of glycine on icy grain surfaces: A first-principle investigation. *Mon. Not. R. Astron. Soc.* **2022**, *517*, 5912–5920. [CrossRef]
29. Remko, M.; Rode, B.M. Effect of Metal Ions (Li^+, Na^+, K^+, Mg^{2+}, Ca^{2+}, Ni^{2+}, Cu^{2+}, and Zn^{2+}) and Water Coordination on the Structure of Glycine and Zwitterionic Glycine. *J. Phys. Chem. A* **2006**, *110*, 1960–1967. [CrossRef]
30. Zhu, C.; Wang, Q.; Huang, X.X.; Yun, J.N.; Hu, Q.L.; Yang, G. Adsorption of amino acids at clay surfaces and implication for biochemical reactions: Role and impact of surface charges. *Colloids Surf. B-Biointerfaces* **2019**, *183*, 110458. [CrossRef]
31. Madden, D.C.; Temprano, I.; Sacchi, M.; Jenkins, S.J. Spontaneous Local Symmetry Breaking: A Conformational Study of Glycine on Cu{311}. *J. Phys. Chem. C* **2015**, *119*, 13041–13049. [CrossRef]
32. Fang, Z.; Wang, J.F.; Yang, X.F.; Sun, Q.; Jia, Y.; Liu, H.R.; Xi, T.F.; Guan, S.K. Adsorption of arginine, glycine and aspartic acid on Mg and Mg-based alloy surfaces: A first-principles study. *Appl. Surf. Sci.* **2017**, *409*, 149–155. [CrossRef]
33. Fang, Z.; Wang, J.F.; Zhu, S.J.; Yang, X.F.; Jia, Y.; Sun, Q.; Jia, Y.; Guan, S.K. A DFT study of the adsorption of short peptides on Mg and Mg-based alloy surfaces. *Phys. Chem. Chem. Phys.* **2018**, *20*, 3602–3607. [CrossRef]
34. Fang, Z.; Zhao, Y.; Wang, H.Y.; Wang, J.F.; Zhu, S.J.; Jia, Y.; Cho, J.Y.; Guan, S.K. Influence of surface charge density on ligand-metal bonding: A DFT study of NH3 and HCOOH on Mg (0001) surface. *Appl. Surf. Sci.* **2019**, *470*, 893–898. [CrossRef]
35. Fang, Z.; Ding, H.L.; Li, P.; Qiao, H.J.; Liang, E.J.; Jia, Y.; Guan, S.K. Interaction Mechanism of RGD Tripeptide on Different Surfaces of Mg and Mg Alloys: A First-Principles Study. *Coatings* **2022**, *12*, 1814. [CrossRef]
36. Kresse, G.; Furthmüller, J. Efficient iterative schemes for ab initio total-energy calculations using a plane-wave basis set. *Phys. Rev. B* **1996**, *54*, 11169–11186. [CrossRef]
37. Kresse, G.; Furthmüller, J. Efficiency of ab-initio total energy calculations for metals and semiconductors using a plane-wave basis set. *Comput. Mater. Sci.* **1996**, *6*, 15–50. [CrossRef]
38. Blöchl, P.E. Projector augmented-wave method. *Phys. Rev. B* **1994**, *50*, 17953–17979. [CrossRef]

39. Perdew, J.P.; Burke, K.; Ernzerhof, M. Generalized Gradient Approximation Made Simple. *Phys. Rev. Lett.* **1996**, *77*, 3865–3868. [CrossRef]
40. Dion, M.; Rydberg, H.; Schröder, E.; Langreth, D.C.; Lundqvist, B.I. Van der Waals Density Functional for General Geometries. *Phys. Rev. Lett.* **2004**, *92*, 246401. [CrossRef]
41. Klimeš, J.; Bowler, D.R.; Michaelides, A. Chemical accuracy for the van der Waals density functional. *J. Phys. Condens. Matter* **2010**, *22*, 022201. [CrossRef]
42. Klimeš, J.; Michaelides, A. Perspective: Advances and challenges in treating van der Waals dispersion forces in density functional theory. *J. Chem. Phys.* **2012**, *137*, 120901. [CrossRef]
43. Klimeš, J.; Bowler, D.R.; Michaelides, A. Van der Waals density functionals applied to solids. *Phys. Rev. B* **2011**, *83*, 195131. [CrossRef]
44. Lüder, J.; Sanyal, B.; Eriksson, O.; Puglia, C.; Brena, B. Comparison of van der Waals corrected and sparse-matter density functionals for the metal-free phthalocyanine/gold interface. *Phys. Rev. B* **2014**, *89*, 045416. [CrossRef]
45. Swanson, H.E.; McMurdie, H.F.; Morris, M.C.; Evans, E.H. Standard X-ray Diffraction Powder Patterns. In *National Bureau of Standards Monograph 25—Section 6*; U.S. Department of Commerce, National Bureau of Standards: Gaithersburg, MD, USA, 1968.
46. Lei, H.P.; Wang, C.Z.; Yao, Y.X.; Wang, Y.G.; Hupalo, M.; McDougall, D.; Tringides, M.; Ho, K.M. Strain effect on the adsorption, diffusion, and molecular dissociation of hydrogen on Mg (0001) surface. *J. Chem. Phys.* **2013**, *139*, 224702. [CrossRef]
47. Sargent, W. *Table of Periodic Properties of the Elements*; Sargent-Welch Scientific: Skokie, IL, USA, 1980.
48. Hoffling, B.; Ortmann, F.; Hannewald, K.; Bechstedt, F. Single cysteine adsorption on Au(110): A first-principles study. *Phys. Rev. B* **2010**, *81*, 045407. [CrossRef]

coatings

Article

Fabrication of Zn^{2+}-Loaded Polydopamine Coatings on Magnesium Alloy Surfaces to Enhance Corrosion Resistance and Biocompatibility

Lingjie Meng [1,†], Xuhui Liu [2,†], Qingxiang Hong [1], Yan Ji [1], Lingtao Wang [1], Qiuyang Zhang [1], Jie Chen [1,*] and Changjiang Pan [1,*]

[1] Faculty of Mechanical and Material Engineering, Jiangsu Provincial Engineering Research Center for Biomaterials and Advanced Medical Devices, Huaiyin Institute of Technology, Huai'an 223003, China; mlj963555816@163.com (L.M.); 15715183778@163.com (Q.H.); jy18362965023@163.com (Y.J.); wjjswlt@126.com (L.W.); qyzhang@hyit.edu.cn (Q.Z.)

[2] The Affiliated Huai'an Hospital, Xuzhou Medical University, Huai'an 223003, China; liuxuhui_0221@163.com

* Correspondence: jiechen@hyit.edu.cn (J.C.); panchangjiang@hyit.edu.cn (C.P.)

† These authors contributed equally to this work.

Abstract: In this study, inspired by the adhesion protein of mussels, a Zn^{2+}-loaded polydopamine (PDA/Zn^{2+}) coating was prepared on an alkali–heat-treated magnesium alloy surface, through the chelating effect of PDA with metal ions, to improve anticorrosion and biocompatibility. The results of water contact angles show that the PDA/Zn^{2+} coatings with different Zn^{2+} contents had excellent wettability, which contributed to the selective promotion of the albumin adsorption. The corrosion degradation behaviors of the modified magnesium alloys were characterized using potentiodynamic scanning polarization curves, electrochemical impedance spectroscopy (EIS), and an immersion test, the results indicate that anticorrosion was significantly improved with the increase of Zn^{2+} content in the coating. Meanwhile, the PDA/Zn^{2+} coatings with different Zn^{2+} concentrations demonstrated improved hemocompatibility, confirmed by assays of the hemolysis rate and platelet adhesion behaviors. In addition, the results regarding the growth behaviors of endothelial cells (ECs) suggest that, due to the sustained release of Zn^{2+} from the coatings, the modified magnesium alloys could enhance the adhesion, proliferation, and upregulated expression of vascular endothelial growth factor (VEGF) and nitric oxide (NO) in endothelial cells, and that better cytocompatibility to ECs could be achieved as the Zn^{2+} concentration increased. Therefore, the PDA/Zn^{2+} coatings developed in this study could be utilized to modify magnesium alloy surfaces, to simultaneously impart better anticorrosion, hemocompatibility, and endothelialization.

Keywords: magnesium alloy; zinc ions; corrosion resistance; endothelialization; biocompatibility

Citation: Meng, L.; Liu, X.; Hong, Q.; Ji, Y.; Wang, L.; Zhang, Q.; Chen, J.; Pan, C. Fabrication of Zn^{2+}-Loaded Polydopamine Coatings on Magnesium Alloy Surfaces to Enhance Corrosion Resistance and Biocompatibility. *Coatings* **2023**, *13*, 1079. https://doi.org/10.3390/coatings13061079

Academic Editor: Maria Cristina Tanzi

Received: 18 May 2023
Revised: 2 June 2023
Accepted: 9 June 2023
Published: 11 June 2023

1. Introduction

Percutaneous coronary intervention (PCI) with stent implantation is an extensive and effective method for treating stenotic cardiovascular disease; however, the biocompatibility of traditional metal stents within current clinical practice is limited. The drugs released from the drug-eluting stents (DESs) can prevent excessive neointimal hyperplasia, to reduce the in-stent restenosis; however, it can also inhibit endothelial repair and regeneration, leading to clinical complications such as chronic inflammation, late thrombosis, and late in-stent restenosis [1,2]. The drawbacks of current vascular stents have pushed researchers to explore novel stents made from biodegradable materials. Magnesium (Mg) is the fourth trace element in the human body, and plays important roles in impeding abnormal nerve excitation, participating in protein synthesis, abating hypertension, treating acute MI (myocardial infarction), and preventing atherosclerosis [3]. Cardiovascular stents made from a magnesium alloy have better biodegradation and mechanical properties. These offer potential advantages in overcoming clinic complications caused by non-degradable metal stents, such as chronic inflammatory responses, late thrombosis, and long-term use of anticoagulants. In the past several years, many types of magnesium alloy with excellent mechanical properties have been developed. For example, Zhang et al. developed a Mg alloy with ultrahigh ductility (nearly 50%) by combining Er micro-alloying (0.3 at% Er) with the appropriate grain refinement (~8 μm) [4]. Zhao et al. [5] utilized super-defined wave-welding technology to achieve high-strength connections between two heterogeneous light alloys (magnesium alloy and copper alloy). However, most of these were quickly corroded in the complicated in vivo physiological environment, easily leading to the premature loss of mechanical support after implantation. Moreover, the limited bioactivities on the magnesium-based biomaterials' surfaces could not effectively regulate the physiological reactions of the ambient microenvironment after implantation, which may result in late endothelial healing and thrombosis. Therefore, when exploring new ways of maintaining good biocompatibility, concurrently controlling the degradation speed of magnesium-based alloys remains the primary focus, and represents the sticking-point in clinical practice regarding vascular stents made from magnesium and its alloys.

Given that corrosion resistance and biocompatibility are closely related to surface characteristics, surface modification is one of the operationally easy and effective approaches toward overcoming the clinical complications of magnesium alloys in cardiovascular stents. Currently, various methods have been explored to improve the anticorrosion and biocompatibility of magnesium alloys, including chemical and electrochemical treatments, the preparation of inorganic coatings (sol–gel coating, inorganic non-metallic coating, layered double hydroxide coating, etc.), the in-situ introduction of bioactive factors onto the surface, the construction of polymer coatings with or without biomolecules, etc. [6–12]. Although these methods can obviously reduce the biodegradation speed of magnesium and its alloys, and introduce chemical groups or bioactive factors onto the surface, as well as reducing the side effects after implantation to some degree, there are still shortcomings, including the complex preparation steps, the long time-consuming procedures, the short duration of action, the difficult performance control, and other issues.

It is well known that zinc is the second trace element in the human body, and has a significant impact on the biological behaviors of cells and tissues [13,14]. Zinc ions play a crucial role in preventing and treating various physiological diseases, such as preventing local ischemia and vascular infarction. Zinc ions have a cytoprotective effect that can accelerate the integrity of endothelial cells, thereby preventing atherosclerosis, and facilitating the regeneration of the damaged vascular endothelium [15], which plays an important role in maintaining the normal physiological function of the human vascular endothelium. In this study, polydopamine coatings containing different Zn^{2+} concentrations (PDA/Zn^{2+}) were prepared by a one-step process on the alkali–heat-treated magnesium alloy surface, and electrochemical degradation behaviors, blood compatibility, and endothelial cell growth behaviors were investigated in detail. The results indicate that the introduction of Zn^{2+} onto the magnesium alloy's surface can effectively enhance anticorrosion and anticoagulation, and promote endothelial cell growth for endothelialization.

2. Materials and Methods

2.1. Construction of PDA/Zn^{2+} Coatings

AZ31B magnesium alloy plates (12 mm diameter, 4 mm thickness) were polished to the point of displaying no scratches. The polished plates were ultrasonically cleaned for 10 min by acetone and ethanol, respectively. The cleaned Mg plates were immersed in a 3 M NaOH solution to be treated for 24 h at 75 °C. After being washed and dried, the alkali–heat-treated samples (Mg-OH) were dipped into the mixed solutions of 2 mg/mL dopamine and 1 mg/mL, 2 mg/mL, and 3 mg/mL $ZnSO_4.7H_2O$ (Tris-HCl buffer, pH 8.5, volume ratio 1:1), respectively, for 4 h at room temperature. The as-prepared samples were named as Mg-PDA/1Zn, Mg-PDA/2Zn, and Mg-PDA/3Zn, respectively.

2.2. Surface Characterization

The surface chemical structures of the different samples were characterized by attenuated total reflection–Fourier-transform infrared spectroscopy (ATR-FTIR, TENSOR27, Bruker of Germany, Mannheim, Germany) and X-ray photoelectron spectroscopy (XPS, Quantum 2000; PHI Co., Chanhassen, MN, USA). The surface morphologies were examined using scanning electron microscopy (SEM, FEI, Quata 250, Portland, OR, USA). The surface wettability was characterized by the water contact angles of three parallel samples; the average value for each sample was calculated and expressed as mean ± standard derivation (SD).

2.3. In Vitro Electrochemical Corrosion Degradation Behavior

2.3.1. Potentiodynamic Scanning Polarization Curves and EIS

The three-electrode system (with the sample as the working electrode, platinum wire as the auxiliary electrode, and Ag/AgCl as the reference electrode) was utilized to measure the potentiodynamic scanning polarization curves and electrochemical impedance spectra (EIS) of the different modified samples. The test was carried out using a CHi660D electrochemical workstation (CHI Instruments, Inc., Shanghai, China). The test solution was Hank's simulated body fluid (SBF). Before the test, the sample was immersed into SBF to obtain the stable open circuit potential, and then the scanning polarization was carried out, at a scan speed of 1 mV/s, to obtain the potentiodynamic scan polarization curves. The corrosion current density and potential were obtained using the Tafel method, and the corrosion depth per year was determined using the Equation (1) [16]:

$$d = 3.28 \times 10^{-3}\ (M/n\rho)I_{corr} \tag{1}$$

where d represents the corrosion depth per year (mm/y); M and ρ are equal to the gram atomic weight (24 g/mol) and the density (1.74 g/cm^3) of Mg; n represents the number of electrons lost by Mg ($n = 2$); and I_{corr} is the corrosion current density (μA/cm^2).

A sinusoidal alternating current with an amplitude of 10 mV was used to carry out the EIS measurement from high frequency to low frequency (10^5–0.1 Hz), and the impedance parameters of the equivalent circuit were fitted using the Zview software. The polarization resistance (R_p) was obtained from the EIS.

2.3.2. Immersion Experiment and pH Changes

The sealed sample with a 1 cm^2 exposed area was placed into 20 mL SBF solution (pH 7.4) for 1, 3, 7, and 14 days, respectively. The SBF solution was renewed every two days. The samples were rinsed using deionized water, and dried using compressed air flow. The corrosion morphologies and elemental compositions of the surface were examined by SEM and EDS (energy dispersive spectrometer), respectively. Meanwhile, the pH value for each sample solution was determined by a pH meter at predetermined times; three parallel specimens were measured, and the values were averaged.

2.4. Protein Adsorption

The bovine serum albumin (BSA) and fibrinogen (FIB) adsorption were evaluated using a BCA assay. The sealed magnesium alloy was first sterilized for 12 h under ultraviolet light, and then incubated for 2.5 h with 2 mL BSA and FIB solutions (1 mg/mL) at 37 °C, respectively. The sample was rinsed using phosphate buffer solution (PBS), followed by ultrasonically desorbing the adsorbed proteins for 30 min with 2 mL sodium dodecyl sulfate solution (1 wt% SDS). For each sample, 200 μL eluent was mixed with 100 μL BCA working solution (reagent A: reagent B = 50:1) in a 96-well plate, and absorbance at 562 nm was measured. The protein adsorption amount was deduced based on the standard curve.

2.5. Blood Compatibility

2.5.1. Hemolysis

Healthy human blood was centrifuged for 10 min at 1500 rpm to obtain red blood cells (RBCs). The 2% RBC suspension was prepared using physiological saline, and the 2 mL suspension was incubated for 3 h with the sample at 37 °C. For the negative control and the positive control, respectively, 2% RBCs suspensions diluted with normal saline, and distilled water, were used. A 1 mL amount of the culture solution was centrifuged for 5 min at 3000 rpm, and 200 μL supernatant was used to detect absorbance at 545 nm using a microplate reader (Bio-Tek Eons). Equation (2) was utilized to determine the hemolysis rate:

$$\text{Hemolysis (\%)} = (A - A_2)/(A_1 - A_2) \times 100\% \tag{2}$$

where A, A_1, and A_2 represent the absorbance of the sample, the positive control, and the negative control, respectively.

2.5.2. Platelet Adhesion

The anticoagulated human blood was centrifuged for 10 min at 1500 rpm/min to obtain platelet-rich plasma (PRP). A 200 μL amount of PRP was incubated for 2.5 h with the specimen at 37 °C. The specimens were washed thrice using PBS to remove the non-attached platelets, then the attached platelets were fixed for 3 h using 2.5% glutaraldehyde at 4 °C. The attached platelets on the surface were successively treated using 50%, 70%, 90%, and 100% ethanol solutions, for 15 min each. After being dried at room temperature, the sample surface was sprayed with a gold layer, and the platelets were observed using SEM. Five different SEM pictures (×3000) were randomly selected, and their total adhered platelets counted. This was expressed as the number of adhered platelets per unit area.

2.6. Growth Behaviors of Endothelial Cells

2.6.1. Cell Adhesion and Proliferation

The specimens were first placed into a 24-well culture plate and sterilized for 12 h using ultraviolet light. Into each well, 0.5 mL endothelial cell suspension (5×10^4 cells/mL, ECV304, Cobioer, Nanjing, China), and 1.5 mL culture medium were added, to incubate with the sample for 6 h and 24 h at 37 °C with 5% CO_2, respectively. After being rinsed using the normal saline solution, the adhered cells were fixed using 2.5% glutaraldehyde at 4 °C for 3 h. The attached cells were treated using 100 μL rhodamine (10 μg/mL) for 20 min and 100 μL 4,6-diamidino-2-phenylindole (DAPI, 500 ng/mL) for 10 min, respectively. The cell images were recorded using a fluorescent microscope (Carl Zeiss A2 inverted).

The CCK-8 method was used to characterize cell proliferation. The cells were incubated with the different specimens as described above for 6 h and 24 h, respectively. Subsequently, the specimens were transferred to a new plate, and 0.5 mL of CCK-8 solution (10% in cell culture solution with 10% fetal bovine serum) was added into each well, to incubate for 3.5 h. Finally, 200 μL culture solution was used for measuring the absorbance at 450 nm, three parallel specimens were measured, and the values were averaged.

2.6.2. Endothelial Growth Factor (VEGF) Expression

Endothelial cells (ECs) were incubated with the specimen as described above. An enzyme-linked immunosorbent assay was carried out to evaluate the VEGF concentration expressed by ECs on the surface. After the cell culture, for each sample, 40 μL diluent and 10 μL cell culture medium were mixed in a 96-well plate. The culture plate was sealed and incubated for 1 h at 37 °C. After rinsing five times, 50 μL enzyme-labeled reagent was added, to incubate for another 15 min, followed by the successive adding of 50 μL chromogenic reagent A, and 50 μL chromogenic reagent B, into each well, to incubate for 15 min in the dark at 37 °C. Finally, 50 μL stop solution was added, and absorbance at 450 nm was measured. The VEGF concentration was determined based on the standard curve. The values of the three parallel specimens were averaged.

2.6.3. Endothelial Nitric Oxide (NO) Expression

The NO expressed by the ECs was determined by the nitrate reductase method. Firstly, endothelial cells were inoculated on each surface to culture for 6 h and 24 h as described above, respectively, and then 50 μL supernatant was moved into the 96-well plate, followed by the successive adding of 50 μL Grignard reagent I and 50 μL Grignard reagent II. The absorbance value at 540 nm was determined, and the NO concentration was deduced based on the standard curve.

3. Results and Discussion

3.1. Surface Chemical Structure and Morphologies

Figure 1A shows the ATR-FTIR spectra of the different specimens. Obviously, no obvious infrared absorption peaks on the Mg surface can be detected. A strong absorption peak at 3700 cm^{-1} can be observed on Mg-OH, which belonged to the adsorption peak of -OH, indicating that NaOH treatment can produce a $Mg(OH)_2$ coating on the surface. The existence of the oxide layer can enhance anticorrosion to some degree. After constructing the PDA/Zn^{2+} coatings, the absorption peaks at 1530 cm^{-1} and 3200 cm^{-1}, belonging to the adsorption of the -NH and -NH_2 groups, respectively, can be detected, suggesting that the amino groups were introduced onto the surface. The adsorption peaks at 1450–1625 cm^{-1} for the C=C and N-H peak of the benzene ring [17], and the peak at 2980 cm^{-1} for the -CH_2 group, are clearly observed, demonstrating that the polydopamine coating was successfully constructed on the surface.

Figure 1B,C are the XPS survey spectra and high-resolution spectra, respectively, of the different specimens. Table 1 shows the surface atomic compositions of the different magnesium alloys. Since the unmodified magnesium alloys could be oxidized in the natural environment, and had some carbon contaminants [16], the peaks of Mg_{1s} (1305.91 eV), Mg_{2p} (346.59 eV), C_{1s} (284.72 eV), and O_{1s} (532.75 eV) could be detected on the Mg surface. For Mg-OH, the Mg_{1s} peak was weakened, and its content dropped from 47.3% to 9.6%; the O_{1s} and C_{1s} peaks were enhanced and their contents increased to 58.56% and 31.77%, respectively. According to the high resolution spectra of Mg_{1s}, the fitting peaks at 1304.65 eV and 1307.44 eV can be attributed to $MgCO_3$ and $Mg(OH)_2$, respectively, indicating that alkali–heat treatment can produce a $Mg(OH)_2$ passivation layer on the surface. The formation of $MgCO_3$ may be due to the fact that a small amount of CO_2 in the air diffused into the inner layer, and reacted with the magnesium substrate. For the PDA/Zn^{2+} modified sample, the occurrence of Zn_{2p} (1022 eV) and N_{1s} suggested that the Zn^{2+}-loaded polydopamine coating was successfully prepared on the surface. As the concentration of zinc ions in the solution increased, the Zn concentration in the coating augmented, while the Mg content decreased, which was beneficial to improving corrosion resistance. As dopamine concentration was constant (2 mg/mL) in the process of preparing the coatings, there was no significant change in N_{1s} content. The C_{1S} high-resolution spectrum of Mg-PDA/Zn^{2+} can be fitted into two peaks; i.e., C-O at 285.14 eV, and C-C at 284.75 eV. The two peaks of O_{1S} at 530.28 eV and 531.78 eV were mainly due to C=O and Zn·· O=C; the N_{1S} high-resolution spectrum shows that the absorption peaks of C-NH_2 and NH_3 appeared at 400.41 eV and 398.75 eV, respectively [18]; these results indicated that the Zn^{2+}-loaded polydopamine coating had been successfully constructed on the surface.

The surface morphologies of the different specimens characterized by SEM are exhibited in Figure 2. The surfaces of the Mg and Mg-OH (data not shown for Mg-OH) were relatively smooth. For Mg-PDA/Zn, white particles can be seen on the surface, and the surface became a little rough; this is because the self-polymerization of dopamine under an alkaline environment can cause PDA aggregates to precipitate on the surface, resulting in an increased surface roughness [19]. Therefore, it can be seen from Figure 2 that particle agglomeration appeared on all the Mg-PDA/Zn surfaces. The dopamine concentration was constant; more dopamine would be used for chelating Zn^{2+} with the increase in Zn^{2+} in the solution, leading to the decreased white particles, which contributed to the production of a denser coating to enhance anticorrosion.

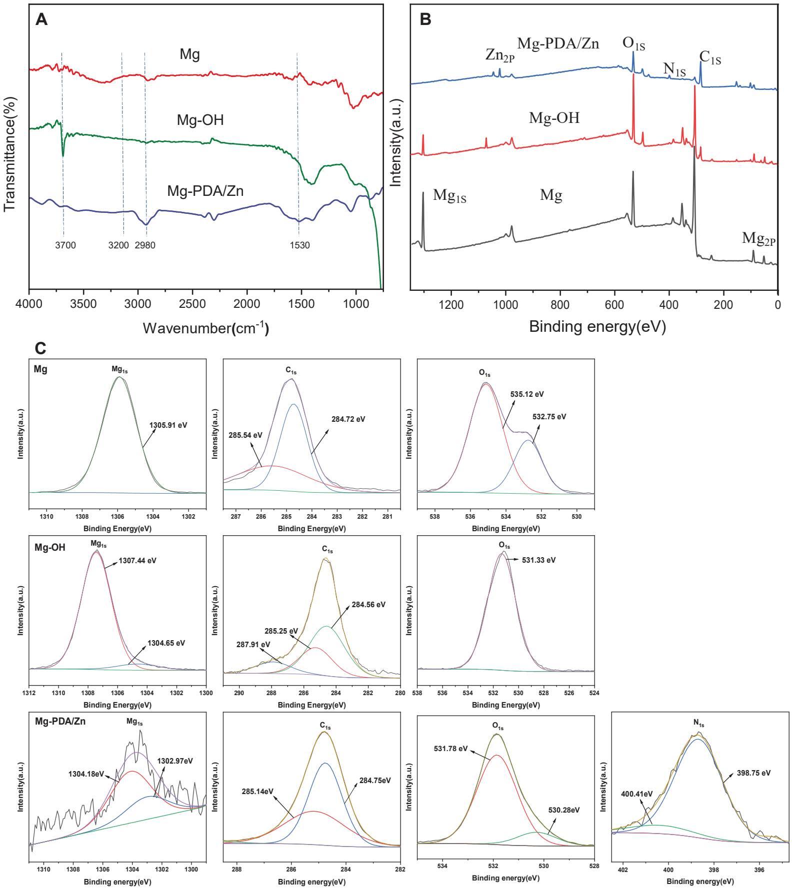

Figure 1. (**A**) ATR-FTIR, (**B**) XPS survey spectra, and (**C**) high-resolution XPS spectra of the different specimens.

Table 1. Atomic compositions of the different sample surfaces.

Samples	Mg	C	O	Zn	N
Mg	47.3	6.5	46.2	-	-
Mg-OH	9.6	31.8	58.6	-	-
Mg-PDA/1Zn	9.1	49.1	31.9	3.3	6.6
Mg-PDA/2Zn	7.3	53.3	28.5	5.2	5.7
Mg-PDA/3Zn	4.5	61.2	20.9	7.8	5.6

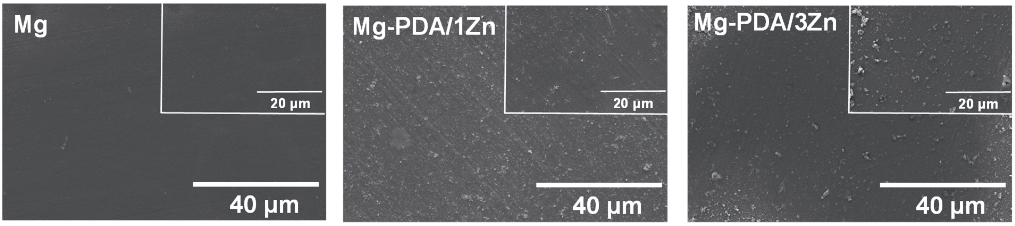

Figure 2. The representative SEM pictures of the different modified magnesium alloys.

3.2. Electrochemical Corrosion Degradation Behaviors

Potentiodynamic scanning polarization curves and EIS were used to investigate the electrochemical behaviors of the magnesium alloys, and the results are displayed in Figure 3A,B. The corresponding corrosion parameters of the different specimens, including the corrosion potential (E_{corr}), corrosion current density (I_{corr}), and annual corrosion depth of the different samples, are displayed in Table 2. In order to quantitatively describe the EIS graph response, equivalent circuit diagrams of the response were constructed, as shown in Figure 3B(b1,b2), respectively. Table 3 shows the EIS fitting parameters of the different magnesium alloys. Generally speaking, under the same corrosive environment, a larger E_{corr} represents more thermodynamic stability, and a smaller I_{corr} means a slower corrosion degradation rate [20]. The results shown in Figure 3A and Table 2 clearly indicate that the pristine magnesium alloy showed the largest corrosion current density (1.42×10^{-5} A·cm^{-2}) and corrosion depth per year (2.80×10^{-1} mm/y), as well as the lowest corrosion potential (−1.55V). Moreover, Figure 3B and Table 3 show that the Mg specimen had the smallest capacitive ring, and the lowest impedance value (5900 Ω·cm^2), suggesting that the blank Mg alloy had the worst anticorrosion properties. After alkali–heat treatment, the E_{corr} was elevated to −1.50 V, and the I_{corr} and annual corrosion depth were reduced to 1.47×10^{-6} A·cm^{-2}, and 7.95×10^{-2} mm/y, respectively, suggesting that alkali heat treatment could enhance anticorrosion properties to some degree. After the PDA/Zn^{2+} coating was constructed, the E_{corr} continued to shift positively, and the I_{corr} decreased by an order of magnitude compared with Mg-OH, indicating that the PDA/Zn coating can further improve anticorrosion properties. It can be concluded that a dense and compact coating on the surface can effectively prevent the penetration of corrosive ions, providing a better corrosion resistance. The polarization resistances of Mg-PDA/1Zn, Mg-PDA/2Zn, and Mg-PDA/3Zn were 16,161 Ω·cm^2, 18,095 Ω·cm^2, and 57,422 Ω·cm^2, respectively, indicating that the increase in zinc ions in the coating was helpful for improving corrosion resistance. On the one hand, the zinc-loaded polydopamine coating could completely cover the magnesium alloy surface; on the other hand, the higher content of Zn^{2+} could react with OH^- to form a stable and dense $Zn(OH)_2$ protective layer, to further enhance anticorrosion properties [21].

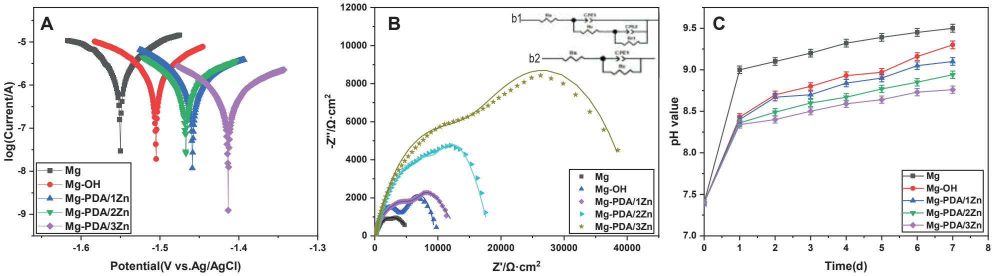

Figure 3. (**A**) Potentiodynamic scanning polarization curves and (**B**) Nyquist plots of the different specimens. For Nyquist plots, the scatter is the original values; the line is the calculative values; (b1) is equivalent circuits of Mg, Mg-OH, Mg-PDA/1Zn, and Mg-PDA/3Zn; and (b2) is equivalent circuits of Mg-PDA/2Zn. (**C**) pH changes in the different specimens immersed in SBF for 7 days.

According to the corrosion mechanism of the Mg alloy, plenty of OH^- may be generated after corrosion, resulting in the pH value increasing, which can reflect the degradation behavior of the magnesium alloy. Figure 3C shows the pH values of the different Mg alloys immersed in SBF solution for 7 days. Obviously, the pH values of all specimens increased during this period. The pH value of the unmodified magnesium alloy sample was always the highest. In contrast, the trend of rising pH in the modified samples was relatively slow, indicating that this modification (alkali–heat treatment and PDA/Zn coating) can effectively reduce the release of OH^- to a certain extent. Compared with PDA/Zn^{2+}-coated modified magnesium alloys, the pH of Mg-OH was relatively high, because the Cl^- in SBF can turn $Mg(OH)_2$ into soluble $MgCl_2$ after prolonged immersion, leading to the relatively fast degradation of the magnesium alloys. Notably, the pH value of Mg-PDA/3Zn was always the smallest during the 7 d immersion, demonstrating that it had the best anticorrosion properties and the slowest degradation rate, which can be attributed to the fact that the formation of $Zn(OH)_2$, and the robust PDA coating [22] were helpful for inhibiting the generation of OH^-, and reducing the pH value changes.

Table 2. Corrosion potential, corrosion current density, and annual corrosion depth of the different samples.

Samples	E_{corr}/(V)	i_{corr}/($A \cdot cm^{-2}$)	d/(mm/y)
Mg	−1.55	1.42×10^{-5}	2.8×10^{-1}
Mg-OH	−1.50	1.47×10^{-6}	7.95×10^{-2}
Mg-PDA/1Zn	−1.45	9.23×10^{-7}	4.63×10^{-2}
Mg-PDA/2Zn	−1.47	7.79×10^{-7}	4.30×10^{-2}
Mg-PDA/3Zn	−1.41	4.41×10^{-7}	2.32×10^{-2}

Table 3. EIS fitting values of the different magnesium alloys.

Samples	R_s/($\Omega \cdot cm^2$)	CPE_1/($\mu F \cdot cm^{-2}$)	R_{ct}/($\Omega \cdot cm^2$)	CPE_2/($\mu F \cdot cm^{-2}$)	R_c/($\Omega \cdot cm^2$)	R_p/($\Omega \cdot cm^2$)
Mg	70.9	5.47×10^{-5}	1608	2.17×10^{-4}	4292	5900
Mg-OH	89.3	4.90×10^{-5}	2568	3.14×10^{-4}	4153	6721
Mg-PDA/1Zn	55.3	1.61×10^{-5}	7362	1.06×10^{-4}	8799	16,161
Mg-PDA/2Zn	83.6	2.36×10^{-5}	18,095	-	-	18,095
Mg-PDA/3Zn	91.5	5.94×10^{-7}	20,374	3.14×10^{-5}	37,048	57,422

R_s is solution resistance; CPE_1, CPE_2 are constant phase elements; R_{ct} is coating resistance; R_c is charge transfer resistance.

The corrosion morphologies of the different magnesium alloys soaked in SBF for 1 d, 3 d, 7 d, and 14 d, respectively, are exhibited in Figure 4, and the surface elemental compositions after 14 d immersion determined by EDS are displayed in Table 4. After 1 d, cracks occurred on the Mg surface because of its poor anticorrosion properties; in contrast, no obvious cracks occurred on the other samples, indicating that the anticorrosion properties of the modified samples were improved to varying degrees. After 3 d, corrosion products could be observed on the Mg-OH surface, which could be due to the $Mg(OH)_2$ coating having been damaged to form the secondary corrosion products. For the PDA/Zn^{2+}-coated modified samples, the corrosion morphologies after 3 d immersion did not change obviously, compared to immersion of 1 d. It can be concluded that the zinc with positive potential was less likely to lose electrons in aqueous solution than Mg, which could provide better thermodynamic stability for the PDA/Zn^{2+} coatings. The zinc-loaded polydopamine coating could inhibit the corrosive chloride ions from reaching the magnesium substrate, and thus enhanced anticorrosion [23]. After 7 d, the corrosion of Mg and Mg-OH samples were further intensified; microcracks could be found on the surfaces of Mg-PDA/1Zn and Mg-PDA/2Zn. It was considered that the existence of microdefects might provide the way in which the corrosive medium could contact the surface to cause corrosion. After 14 d, significant corrosion occurred on all surfaces, with the emergence of white particles and accumulation of corrosion products on the Mg and Mg-OH surfaces. Conversely, the Mg-PDA/3Zn surface exhibited minimal white particles, thereby signifying its superior corrosion resistance. The EDS results shown in Table 4 indicate that P and Ca occurred on all surfaces. The severity of corrosion observed on the Mg surface was significant, presenting as a discernible reduction in the Mg content, and an increase in the contents of C, O, and P, suggesting that the main component of the corrosion products could be a mixture of carbides and phosphides. The appearance of phosphorus on the Mg-OH surface indicated that the $Mg(OH)_2$ layer was damaged, potentially resulting in the creation of the Ca-P compound. A small amount of Ca was found on the surfaces of the PDA/Zn^{2+} coatings, which was due to the slight dissolution of the zinc-loaded polydopamine coating on the local area of the sample surface. The combination of Zn^{2+} and $HPO_4{}^{2-}$ in the physiological environment could form Zn-based phosphates and oxides, which could reduce the chance of the magnesium substrate being directly exposed to aggressive solutions, and provide better corrosion protection for the magnesium substrate [22]. As displayed in Figure 4, as the concentration of zinc ions increased, the white particles on the surface decreased, and the Mg-PDA/3Zn surface was intact, with only a small amount of corrosion products. Taking all results into consideration, it can be concluded that Mg-PDA/3Zn had the highest coating integrity, and the best corrosion resistance.

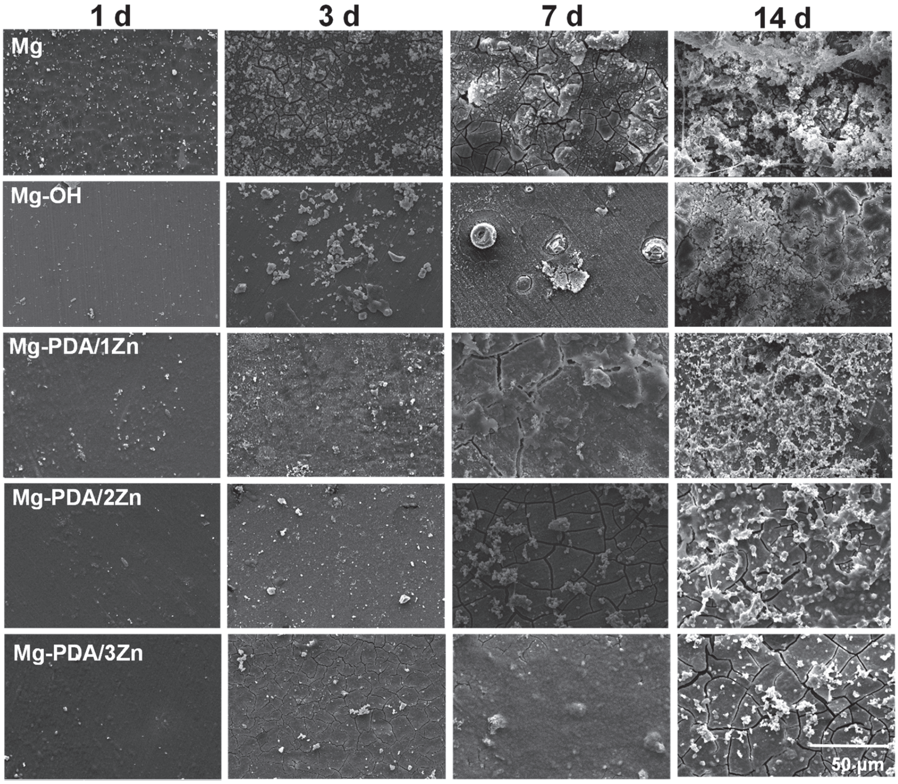

Figure 4. Representative SEM pictures of the different specimens incubated in SBF for 1 d, 3 d, 7 d, and 14 d, respectively.

Table 4. Surface element composition of the different specimens after 14 d immersion.

Samples	Mg	C	O	P	Ca
Mg	2.1	10.1	56.1	5.2	26.5
Mg-OH	1.5	26.8	39.2	15.0	17.5
Mg-PDA/Zn	3.3	27.7	53.6	6.8	8.6
Mg-PDA/2Zn	1.5	46.8	42.8	3.7	5.2
Mg-PDA/3Zn	1.1	37.1	44.5	7.6	9.7

3.3. Surface Wettability and Protein Adsorption Behaviors

Surface wettability has a key influence on protein adsorption and interactions between biomaterials and cells/blood. Protein adsorption is normally the first event for blood-contact biomaterials after implantation, which participates in mediating biological responses, such as blood compatibility and cell behaviors. Albumin and fibrinogen, as two important proteins in human plasma, play an important role in hemocompatibility. Generally, albumin adsorption can inhibit platelet adhesion and activation, leading to enhanced blood compatibility. However, fibrinogen adsorption and denaturation can cause platelet activation and aggregation, to form a thrombus [24]. Figure 5 shows the results for the water contact angle and protein adsorption of the different samples. The water contact angle of the blank Mg alloy was 49°, and it decreased to 25° after alkali–heat treatment, resulting in better wettability. It was considered that plenty of the hydrophilic -OH could be introduced onto the surface using the NaOH treatment, leading to improvements in the surface wettability and antifouling performance [25]. After the fabrication of the PDA/Zn^{2+} coatings, the water contact angle decreased significantly; this is because polydopamine with a large number of oxygen-containing groups can combine with hydrogen atoms in water to form a dense hydration layer, to achieve a better hydrophilic surface [26]. At the same time, zinc ions can also increase the hydrophilicity [27]. The hydrophilic surface exhibits a high capacity for water molecule absorption, which can minimize non-specific protein adsorption, and reduce platelet adhesion, which can contribute to improvement in the surface anticoagulant performance [28].

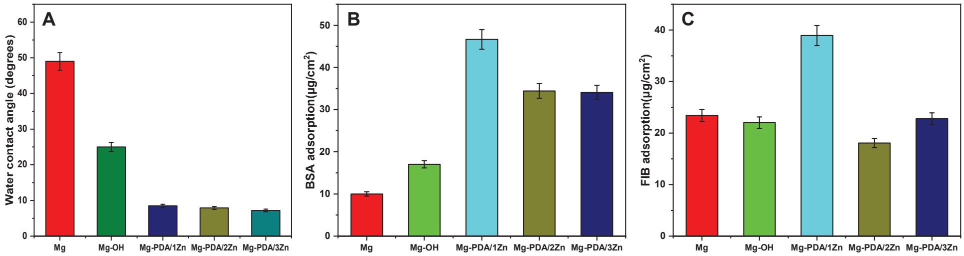

Figure 5. Water contact angle (**A**), albumin (**B**), and fibrinogen (**C**) adsorption amount of the different sample surfaces.

Compared with the unmodified magnesium alloys, the Mg-OH demonstrated excellent hydrophilicity, which contributed to BSA adsorption on the surface. In addition, fibrinogen has a strong affinity for hydrophobic surfaces [29], so the amount of fibrinogen adsorption on the Mg-OH surface decreased. Studies have indicated that polydopamine coating can significantly enhance protein adsorption, and Zn^{2+} can also selectively promote albumin adsorption and improve hemocompatibility [27]. Compared with the Mg-OH, the fibrinogen adsorption on the PDA/Zn^{2+} coating was higher. On the one hand, the hydroxyl groups on the surface could promote positively-charged fibrinogen adsorption [30]; on the other hand, the fibrinogen adsorption was more influenced by the surface roughness than the albumin adsorption was [31]. The surface became rougher after Zn^{2+} loading, leading to the increase in fibrinogen adsorption. The imine and quinine groups of the PDA coating would rapidly adsorb proteins [32], which may be the reason for the higher adsorption capacity of Mg-PDA/1Zn than of Mg-PDA/2Zn and Mg-PDA/3Zn. Although the PDA coating could simultaneously enhance albumin and fibrinogen adsorption, the increase in albumin adsorption was more obvious, which could inhibit the fibrinogen adsorption to some degree, thereby reducing the chance of platelet adhesion and thrombus formation [33].

3.4. Blood Compatibility

Platelet adhesion behaviors on the surfaces of biomaterials can lead to coagulation, and even thrombosis and atherosclerosis [34]. Therefore, platelet adhesion assays are usually utilized to examine the hemocompatibility of biomaterials. Figure 6A shows the adhesion and quantity of the platelets adhered to the different surfaces. Obviously, many platelets adhered to the Mg surface, accompanied by platelet aggregation and activation, suggesting that the hemocompatibility of the pristine Mg alloy was limited. This was related to its higher water contact angle, poor corrosion resistance, and a large amount of fibrinogen adsorption. The quantity of platelets on the Mg-OH surface decreased because the improved wettability was conducive to inhibiting the adsorption of plasma proteins and platelets; however, the quantity of platelets on the Mg-OH surface was still about 17,320/mm^2, suggesting that its anticoagulation properties needed to be further enhanced. For PDA/Zn^{2+}-coated modified magnesium alloy, due to its excellent hydrophilicity and characteristic of selectively promoting albumin adsorption, the quantity of attached platelets was further reduced, which contributed to a reduction in thrombus formation. The quantity of attached platelets on the Mg-PDA/3Zn surface was higher than that on the Mg-PDA/2Zn surface, which may be due to the high level of FIB adsorption on the Mg-PDA/3Zn surface (Figure 5C).

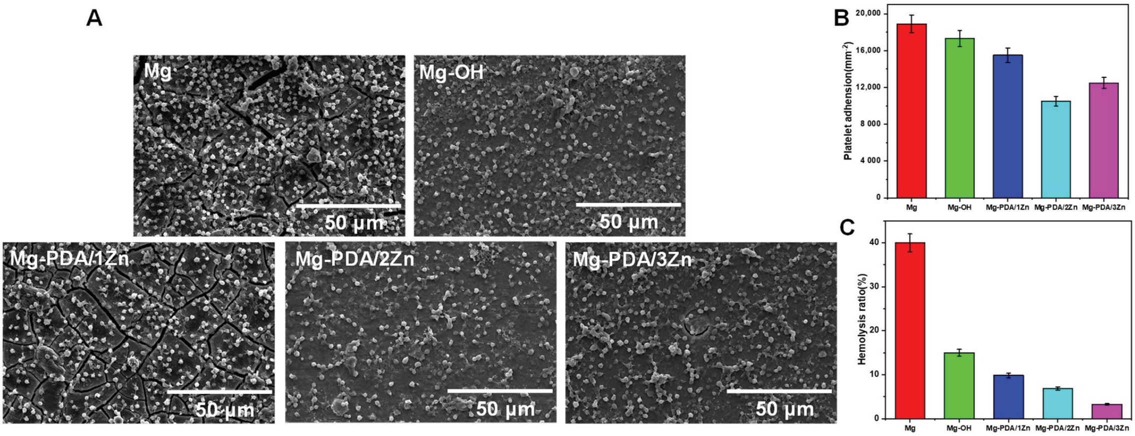

Figure 6. **(A)** Representative SEM pictures, and (**B**) quantity of platelets attached to the different specimens. (**C**) Hemolysis rates of the different specimens.

Figure 6C shows the hemolysis rates of the different Mg alloys. According to the standard of ISO 10,994.4: 2002, a hemolysis rate below 5% can be accepted in blood-contacting biomaterials. The released OH$^-$ caused by the corrosion of the pristine Mg alloy increased the pH value of the RBC suspension, thereby promoting the combination of hemoglobin and the cell membrane, which contributed to red blood cell rupture, with a hemolysis rate of 40%. This degree of hemolysis could potentially lead to severe complications. For Mg-OH, the hemolysis rate displayed a considerable reduction, due to the enhanced corrosion resistance; however, the value still exceeded 5%. After the preparation of the PDA/Zn^{2+} coatings, the further improvement in corrosion resistance could significantly reduce the release of OH$^-$ and Mg^{2+}; at the same time, zinc ions have a certain protective effect on red blood cells, which can reduce the fragility of red blood cells, and maintain enzyme activity [35]. As a result, the hemolysis rate of Zn^{2+}-loaded polydopamine coating was significantly reduced. The hemolysis rate of Mg-PDA/3Zn was only 4.9%, which met the requirement for blood-contacting biomaterials (<5%).

3.5. Endothelial Cell Growth Behaviors

The interaction of cells with their surrounding environment plays a major role in the performance of the implant. Cell adhesion represents the first cellular event when cells make contact with the implant; it is a key factor that determines the performance of an implant in a clinical application [36]. Figures 7 and 8A are the fluorescent images and the CCK-8 values, respectively, of attached cells on the different surfaces. It can be clearly seen that whether cultured for 6 h or 24 h, the number of cell adhesions, and the CCK-8 value on the Mg surface were the lowest, implying that the cells on the pristine Mg surface failed to differentiate and proliferate. On the one hand, the limited anticorrosion of the unmodified Mg alloys could lead to the formation of H_2 bubbles, and a rising pH environment, which are not helpful for cell adhesion and growth; on the other hand, the pristine Mg alloy surface had no bioactivities, and lacked cell adhesion sites to induce EC adhesion and spreading. The number of cells and the CCK-8 value for the Mg-OH increased slightly, and there was a greater increase at 24 h than at 6 h, which can be attributed to the enhanced anticorrosion properties and better hydrophilicity of the Mg-OH. After the preparation of the PDA/Zn^{2+} coatings on the surface, whether the culture time was 6 h or 24 h, the quantity of adhered cells and the CCK-8 value on the surfaces had increased compared with Mg and Mg-OH, indicating that cytocompatibility had been significantly improved. With the increase in Zn^{2+} concentration, the number of cell adhesions, and the CCK-8 value on the PDA/Zn^{2+} modified surfaces also increased. However, due to the lower content of zinc ions on Mg-PDA/1Zn, the CCK-8 values of 6 h and 24 h were always slightly lower than those of Mg-PDA/2Zn and Mg-PDA/3Zn, implying that the zinc ions released from the PDA/Zn^{2+} coatings could promote endothelial cell proliferation. There was no significant difference for the CCK-8 values between Mg-PDA/2Zn and Mg-PDA/3Zn, indicating that high concentrations of Zn^{2+} did not consistently promote endothelial cell proliferation [37]. Studies have shown that the polydopamine coating can introduce a large quantity of functional groups (amine and catechol) to combine with many biomolecules, thereby enhancing cell adhesion and proliferation [38]. Ku et al. [39] confirmed that the polydopamine layer can minimize the deformation of serum proteins by regulating the surface energy to promote cell adhesion and proliferation. In addition, zinc ions are important trace elements to maintain cell redox balance. When the concentration is lower than 80 μM, it can enhance EC growth [40]. It is worth noting that the concentration of Zn^{2+} in this study (3.4~10.4 μM, 1~3 mg/mL $ZnSO_4 \cdot 7H_2O$) was in this range. Therefore, better growth behavior of endothelial cells on the PDA/3Zn coating could be achieved.

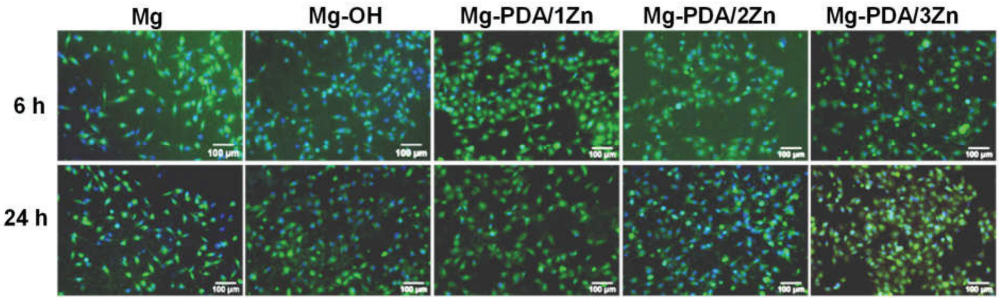

Figure 7. The fluorescence pictures of cells attached to the different surfaces for 6 h and 24 h, respectively.

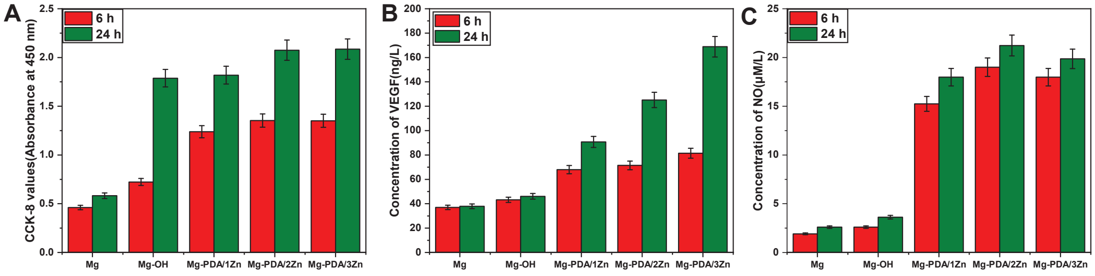

Figure 8. (**A**) CCK-8 values, (**B**) VEGF, and (**C**) NO expression of ECs cultured on the different specimens for 6 h and 24 h, respectively.

VEGF and NO are two key regulatory signaling molecules in the cardiovascular system, which can improve EC growth and proliferation, inhibit the migration and proliferation of smooth muscle cells, and prevent the adhesion and activation of platelets, reduce the formation of intravascular restenosis and intimal hyperplasia [41]. Endothelial cells in the human body can secrete VEGF and NO. The former can stimulate new angiogenesis, increase vascular permeability, and further enhance EC migration, proliferation, and differentiation; the latter can inhibit platelet aggregation, adhesion, and activation, regulate leukocyte adhesion and migration, and inhibit thrombosis and neointimal hyperplasia [42]. Figure 8B,C are the VEGF and NO expression of the ECs cultured on the different surfaces for 6 h and 24 h, respectively. It can be seen that the expression concentrations of VEGF (37 ng/L) and NO (2.5 μM/L) on the Mg surface were the lowest among all samples, indicating its poor endothelial growth performance. After alkali–heat treatment, the hydrophilicity and corrosion resistance were improved, which was beneficial to the adsorption and activity maintenance of proteins in plasma, leading to better endothelial cell adhesion. However, the VEGF and NO concentrations of Mg-OH were only increased to 46 ng/L and 3.9 μM/L, respectively. After constructing the PDA/Zn^{2+} coatings, the expression concentrations of VEGF and NO were significantly increased. With the prolongation of the culture time, the ECs can express more NO and VEGF, thereby promoting EC growth. On the one hand, a small amount of fibrinogen adsorbed on the PDA/Zn^{2+} coatings helped ECs to express more VEGF, and promoted endothelial cell proliferation [43]; on the other hand, the incorporation of Zn^{2+} improved the activity of NO enzymes inside cells, which contributed to the upregulated NO expression [44]. With the increase in zinc ion concentration, the increase in VEGF and NO expression had a significant effect on maintaining cell function and promoting endothelial cell differentiation, which was of great significance in improving the cytocompatibility of the Mg alloys. It is worth noting that from the perspective of NO expression (Figure 8C), Mg-PDA/1Zn was slightly lower than Mg-PDA/2Zn and Mg-PDA/3Zn, and there was no significant difference between Mg-PDA/2Zn and Mg-PDA/3Zn, suggesting that the continuous release of Zn^{2+} in the coating, to further improve EC differentiation, was difficult. Therefore, taking the results of cell behaviors into consideration, Mg-PDA/3Zn was the best at promoting EC adhesion, proliferation, and function expression.

4. Conclusions

In this paper, PDA/Zn^{2+} coatings containing different Zn^{2+} concentrations were successfully prepared on alkali–heat-treated magnesium alloys through the self-polymerization of dopamine, and its chelation to zinc ions. The properties and functions of the materials before and after the modification were studied, and the conclusions are as follows:

(1) The Zn^{2+}-loaded PDA coatings displayed superior characteristics with respect to corrosion. With the increase in Zn^{2+} in the coating, the anticorrosion properties of the Mg alloy were enhanced, and the Mg-PDA/3Zn had the best anticorrosion properties.
(2) The PDA/Zn^{2+} coatings not only displayed excellent hydrophilic properties and corrosion resistance, but could also release zinc ions, which could provide a favorable surface for selectively promoting albumin adsorption and significantly improving hemocompatibility.
(3) Due to the sustained release of Zn^{2+} from the PDA/Zn^{2+} coatings, the endothelial cell adhesion and proliferation, as well as the VEGF and NO expression, were enhanced.
(4) Due to the PDA coating's capability to further react with bioactive molecules with different functions, its use is expected in further enhancing the corrosion resistance and biocompatibility of the Mg alloys, by immobilizing bioactive molecules on the surface.

Author Contributions: Conceptualization, L.M. and C.P.; methodology, L.M.; software, L.M., Y.J. and L.W.; validation, Q.Z.; formal analysis, L.M. and J.C.; investigation, L.M. and Q.H.; resources, Q.Z. and C.P.; data curation, X.L.; writing—original draft preparation, L.M. and C.P.; writing—review and editing, J.C., Q.Z. and C.P.; visualization, Q.H. and J.C.; supervision, J.C. and C.P.; funding acquisition, C.P. All authors have read and agreed to the published version of the manuscript.

Funding: This work was financially supported by the National Natural Science Foundation of China (31870952) and the Natural Science Foundation of the Jiangsu Higher Education Institutions of China (No. 21KJB430013).

Data Availability Statement: Not applicable.

Conflicts of Interest: The authors declare no conflict of interest.

References

1. Erne, P.; Schier, M.; Resink, T.J. The Road to Bioabsorbable Stents: Reaching Clinical Reality? *Cardiovasc Interv. Radiol* **2006**, *29*, 11–16. [CrossRef]
2. Qi, P.; Yang, Y.; Maitz, F.M.; Huang, N. Current Status of Research and Application in Vascular Stents. *Chin. Sci. Bull.* **2013**, *58*, 4362–4370. [CrossRef]
3. Zhang, N.; Wang, W.; Zhang, X.; Nune, K.C.; Zhao, Y.; Liu, N.; Misra, R.D.K.; Yang, K.; Tan, L.; Yan, J. The Effect of Different Coatings on Bone Response and Degradation Behavior of Porous Magnesium-Strontium Devices in Segmental Defect Regeneration. *Bioact. Mater.* **2021**, *6*, 1765–1776. [CrossRef]
4. Zhang, Z.; Zhang, J.; Xie, J.; Liu, S.; Fu, W.; Wu, R. Developing a Mg Alloy with Ultrahigh Room Temperature Ductility via Grain Boundary Segregation and Activation of Non-Basal Slips. *Int. J. Plast.* **2023**, *162*, 103548. [CrossRef]
5. Zhao, D.; Jiang, C.; Zhao, K. Ultrasonic Welding of AZ31B Magnesium Alloy and Pure Copper: Microstructure, Mechanical Properties and Finite Element Analysis. *J. Mater. Res. Technol.* **2023**, *23*, 1273–1284. [CrossRef]
6. Yang, Y.-X.; Fang, Z.; Liu, Y.-H.; Hou, Y.-C.; Wang, L.-G.; Zhou, Y.-F.; Zhu, S.-J.; Zeng, R.-C.; Zheng, Y.-F.; Guan, S.-K. Biodegradation, Hemocompatibility and Covalent Bonding Mechanism of Electrografting Polyethylacrylate Coating on Mg Alloy for Cardiovascular Stent. *J. Mater. Sci. Technol.* **2020**, *46*, 114–126. [CrossRef]
7. Chen, Y.; Song, Y.; Zhang, S.; Li, J.; Zhao, C.; Zhang, X. Interaction between a High Purity Magnesium Surface and PCL and PLA Coatings during Dynamic Degradation. *Biomed. Mater.* **2011**, *6*, 025005. [CrossRef]
8. Johnson, I.; Akari, K.; Liu, H. Nanostructured Hydroxyapatite/Poly(Lactic- *Co* -Glycolic Acid) Composite Coating for Controlling Magnesium Degradation in Simulated Body Fluid. *Nanotechnology* **2013**, *24*, 375103. [CrossRef] [PubMed]
9. Pan, C.; Zhao, Y.; Yang, Y.; Yang, M.; Hong, Q.; Yang, Z.; Zhang, Q. Immobilization of Bioactive Complex on the Surface of Magnesium Alloy Stent Material to Simultaneously Improve Anticorrosion, Hemocompatibility and Antibacterial Activities. *Colloids Surf. B Biointerfaces* **2021**, *199*, 111541. [CrossRef] [PubMed]
10. Fan, X.-L.; Huo, Y.-F.; Li, C.-Y.; Kannan, M.B.; Chen, X.-B.; Guan, S.-K.; Zeng, R.-C.; Ma, Q.-L. Corrosion Resistance of Nanostructured Magnesium Hydroxide Coating on Magnesium Alloy AZ31: Influence of EDTA. *Rare Met.* **2019**, *38*, 520–531. [CrossRef]
11. Guo, Y.; Su, Y.; Jia, S.; Sun, G.; Gu, R.; Zhu, D.; Li, G.; Lian, J. Hydroxyapatite/Titania Composite Coatings on Biodegradable Magnesium Alloy for Enhanced Corrosion Resistance, Cytocompatibility and Antibacterial Properties. *J. Electrochem. Soc.* **2018**, *165*, C962–C972. [CrossRef]
12. Cui, L.-Y.; Zeng, R.-C.; Guan, S.-K.; Qi, W.-C.; Zhang, F.; Li, S.-Q.; Han, E.-H. Degradation Mechanism of Micro-Arc Oxidation Coatings on Biodegradable Mg-Ca Alloys: The Influence of Porosity. *J. Alloys Compd.* **2017**, *695*, 2464–2476. [CrossRef]
13. Su, Y.; Cockerill, I.; Wang, Y.; Qin, Y.-X.; Chang, L.; Zheng, Y.; Zhu, D. Zinc-Based Biomaterials for Regeneration and Therapy. *Trends Biotechnol.* **2019**, *37*, 428–441. [CrossRef]
14. O'Neill, E.; Awale, G.; Daneshmandi, L.; Umerah, O.; Lo, K.W.-H. The Roles of Ions on Bone Regeneration. *Drug Discov. Today* **2018**, *23*, 879–890. [CrossRef] [PubMed]
15. Xu, Z.; Kim, S.; Huh, J. Zinc Plays a Critical Role in the Cardioprotective Effect of Postconditioning by Enhancing the Activation of the RISK Pathway in Rat Hearts. *J. Mol. Cell. Cardiol.* **2014**, *66*, 12–17. [CrossRef]
16. Bakhsheshi-Rad, H.R.; Hamzah, E.; Daroonparvar, M.; Saud, S.N.; Abdul-kadir, M.R. Bi-Layer Nano-TiO2/FHA Composite Coatings on Mg–Zn–Ce Alloy Prepared by Combined Physical Vapour Deposition and Electrochemical Deposition Methods. *Vacuum* **2014**, *110*, 127–135. [CrossRef]
17. Zhang, L.; Mohammed, E.A.A.; Adriaens, A. Synthesis and Electrochemical Behavior of a Magnesium Fluoride-Polydopamine-Stearic Acid Composite Coating on AZ31 Magnesium Alloy. *Surf. Coat. Technol.* **2016**, *307*, 56–64. [CrossRef]
18. Wang, Y.; Chen, J. Preparation and Characterization of Polydopamine-Modified Ni/Carbon Nanotubes Friction Composite Coating. *Coatings* **2019**, *9*, 596. [CrossRef]
19. Hong, S.; Kim, J.; Na, Y.S.; Park, J.; Kim, S.; Singha, K.; Im, G.-I.; Han, D.-K.; Kim, W.J.; Lee, H. Poly(Norepinephrine): Ultrasmooth Material-Independent Surface Chemistry and Nanodepot for Nitric Oxide. *Angew. Chem. Int. Ed.* **2013**, *52*, 9187–9191. [CrossRef]
20. Yang, Q.; Yuan, W.; Liu, X.; Zheng, Y.; Cui, Z.; Yang, X.; Pan, H.; Wu, S. Atomic Layer Deposited ZrO2 Nanofilm on Mg-Sr Alloy for Enhanced Corrosion Resistance and Biocompatibility. *Acta Biomater.* **2017**, *58*, 515–526. [CrossRef]

21. Li, H.; Pang, S.; Liu, Y.; Sun, L.; Liaw, P.K.; Zhang, T. Biodegradable Mg–Zn–Ca–Sr Bulk Metallic Glasses with Enhanced Corrosion Performance for Biomedical Applications. *Mater. Des.* **2015**, *67*, 9–19. [CrossRef]
22. Li, J.; Li, J.; Li, Q.; Zhou, H.; Wang, G.; Peng, X.; Jin, W.; Yu, Z.; Chu, P.K.; Li, W. Titania-Zinc Phosphate/Nanocrystalline Zinc Composite Coatings for Corrosion Protection of Biomedical WE43 Magnesium Alloy. *Surf. Coat. Technol.* **2021**, *410*, 126940. [CrossRef]
23. Yao, H.-L.; Yi, Z.-H.; Yao, C.; Zhang, M.-X.; Wang, H.-T.; Li, S.-B.; Bai, X.-B.; Chen, Q.-Y.; Ji, G.-C. Improved Corrosion Resistance of AZ91D Magnesium Alloy Coated by Novel Cold-Sprayed Zn-HA/Zn Double-Layer Coatings. *Ceram. Int.* **2020**, *46*, 7687–7693. [CrossRef]
24. Baumgartner, J.N.; Cooper, S.L. Influence of Thrombus Components in Mediatingstaphylococcus Aureus Adhesion to Polyurethane Surfaces. *J. Biomed. Mater. Res.* **1998**, *40*, 660–670. [CrossRef]
25. Wang, S.; Chen, Y.; Gu, C.; Sai, Q.; Lei, T.; Williams, J. Antifouling Coatings Fabricated by Laser Cladding. *Coatings* **2023**, *13*, 397. [CrossRef]
26. Kuo, Y.-Y. Hydrothermal Crystallization and Modification of Surface Hydroxyl Groups of Anodized TiO2 Nanotube-Arrays for More Efficient Photoenergy Conversion. *Electrochim. Acta* **2012**. [CrossRef]
27. Pan, C.; Hu, Y.; Gong, Z.; Yang, Y.; Liu, S.; Quan, L.; Yang, Z.; Wei, Y.; Ye, W. Improved Blood Compatibility and Endothelialization of Titanium Oxide Nanotube Arrays on Titanium Surface by Zinc Doping. *ACS Biomater. Sci. Eng.* **2020**, *6*, 2072–2083. [CrossRef]
28. Gray-Munro, J.E.; Strong, M. The Mechanism of Deposition of Calcium Phosphate Coatings from Solution onto Magnesium Alloy AZ31. *J. Biomed. Mater. Res.* **2009**, *90A*, 339–350. [CrossRef]
29. Roach, P.; Farrar, D.; Perry, C.C. Interpretation of Protein Adsorption: Surface-Induced Conformational Changes. *J. Am. Chem. Soc.* **2005**, *127*, 8168–8173. [CrossRef]
30. Hu, Y.; Zhou, H.; Liu, T.; Yang, M.; Zhang, Q.; Pan, C.; Lin, J. Construction of Mussel-Inspired Dopamine–Zn2+ Coating on Titanium Oxide Nanotubes to Improve Hemocompatibility, Cytocompatibility, and Antibacterial Activity. *Front. Bioeng. Biotechnol.* **2022**, *10*, 884258. [CrossRef] [PubMed]
31. Rechendorff, K.; Hovgaard, M.B.; Foss, M.; Zhdanov, V.P.; Besenbacher, F. Enhancement of Protein Adsorption Induced by Surface Roughness. *Langmuir* **2006**, *22*, 10885–10888. [CrossRef] [PubMed]
32. Wei, Q.; Li, B.; Yi, N.; Su, B.; Yin, Z.; Zhang, F.; Li, J.; Zhao, C. Improving the Blood Compatibility of Material Surfaces via Biomolecule-Immobilized Mussel-Inspired Coatings. *J. Biomed. Mater. Res.* **2011**, *96A*, 38–45. [CrossRef]
33. Huo, K.; Zhang, X.; Wang, H.; Zhao, L.; Liu, X.; Chu, P.K. Osteogenic Activity and Antibacterial Effects on Titanium Surfaces Modified with Zn-Incorporated Nanotube Arrays. *Biomaterials* **2013**, *34*, 3467–3478. [CrossRef]
34. Li, G.; Yang, P.; Qin, W.; Maitz, M.F.; Zhou, S.; Huang, N. The Effect of Coimmobilizing Heparin and Fibronectin on Titanium on Hemocompatibility and Endothelialization. *Biomaterials* **2011**, *32*, 4691–4703. [CrossRef]
35. Zhang, Y.; Xu, J.; Ruan, Y.C.; Yu, M.K.; O'Laughlin, M.; Wise, H.; Chen, D.; Tian, L.; Shi, D.; Wang, J.; et al. Implant-Derived Magnesium Induces Local Neuronal Production of CGRP to Improve Bone-Fracture Healing in Rats. *Nat. Med.* **2016**, *22*, 1160–1169. [CrossRef] [PubMed]
36. Wang, J.; Li, B.; Li, Z.; Ren, K.; Jin, L.; Zhang, S.; Chang, H.; Sun, Y.; Ji, J. Electropolymerization of Dopamine for Surface Modification of Complex-Shaped Cardiovascular Stents. *Biomaterials* **2014**, *35*, 7679–7689. [CrossRef]
37. Cortese, M.M.; Suschek, C.V.; Wetzel, W.; Kröncke, K.-D.; Kolb-Bachofen, V. Zinc Protects Endothelial Cells from Hydrogen Peroxide via Nrf2-Dependent Stimulation of Glutathione Biosynthesis. *Free Radic. Biol. Med.* **2008**, *44*, 2002–2012. [CrossRef]
38. Wang, J.-L.; Ren, K.-F.; Chang, H.; Jia, F.; Li, B.-C.; Ji, Y.; Ji, J. Direct Adhesion of Endothelial Cells to Bioinspired Poly(Dopamine) Coating Through Endogenous Fibronectin and Integrin $\alpha_5 \beta_1$: Direct Adhesion of Endothelial Cells to Bioinspired Poly(Dopamine). *Macromol. Biosci.* **2013**, *13*, 483–493. [CrossRef] [PubMed]
39. Ku, S.H.; Ryu, J.; Hong, S.K.; Lee, H.; Park, C.B. General Functionalization Route for Cell Adhesion on Non-Wetting Surfaces. *Biomaterials* **2010**, *31*, 2535–2541. [CrossRef]
40. Krones, C.J.; Klosterhalfen, B.; Butz, N.; Hoelzl, F.; Junge, K.; Stumpf, M.; Peiper, C.; Klinge, U.; Schumpelick, V. Effect of Zinc Pretreatment on Pulmonary Endothelial Cells in Vitro and Pulmonary Function in a Porcine Model of Endotoxemia. *J. Surg. Res.* **2005**, *123*, 251–256. [CrossRef]
41. Orlando, A.; Re, F.; Sesana, S.; Rivolta, I.; Panariti, A.; Brambilla, D.; Nicolas, J.; Couvreur, P.; Andrieux, K.; Masserini, M.; et al. Effect of Nanoparticles Binding ß-Amyloid Peptide on Nitric Oxide Production by Cultured Endothelial Cells and Macrophages. *Int. J.Nanomed.* **2013**, 1335. [CrossRef]
42. Kim, J.; Lee, Y.; Singha, K.; Kim, H.W.; Shin, J.H.; Jo, S.; Han, D.-K.; Kim, W.J. NONOates–Polyethylenimine Hydrogel for Controlled Nitric Oxide Release and Cell Proliferation Modulation. *Bioconjugate Chem.* **2011**, *22*, 1031–1038. [CrossRef]
43. Yang, Z.; Tu, Q.; Wang, J.; Huang, N. The Role of Heparin Binding Surfaces in the Direction of Endothelial and Smooth Muscle Cell Fate and Re-Endothelialization. *Biomaterials* **2012**, *33*, 6615–6625. [CrossRef] [PubMed]
44. Nosrati, R.; Kheirouri, S.; Ghodsi, R.; Ojaghi, H. The Effects of Zinc Treatment on Matrix Metalloproteinases: A Systematic Review. *J. Trace Elem. Med. Biol.* **2019**, *56*, 107–115. [CrossRef] [PubMed]

coatings

MDPI

Article

Interaction Mechanism of RGD Tripeptide on Different Surfaces of Mg and Mg Alloys: A First-Principles Study

Zhe Fang [1,2,3,*], Huili Ding [2], Ping Li [2], Huijie Qiao [2], Erjun Liang [1,*], Yu Jia [1,4] and Shaokang Guan [3,*]

[1] International Laboratory for Quantum Functional Materials of Henan & School of Physics and Microelectronics, Zhengzhou University, Zhengzhou 450001, China
[2] School of Materials and Chemical Engineering, Zhongyuan University of Technology, Zhengzhou 450007, China
[3] School of Materials Science and Engineering, Zhengzhou University, Zhengzhou 450001, China
[4] Key Laboratory for Special Functional Materials of Ministry of Education, Henan University, Kaifeng 475004, China
* Correspondence: zhefang@zut.edu.cn (Z.F.); ejliang@zzu.edu.cn (E.L.); skguan@zzu.edu.cn (S.G.)

Highlights:

- The adsorption models of RGD on different surfaces of Mg and Mg alloys were set up.
- Alloying elements promoted the adsorption of RGD on different Mg surfaces.
- The ligand covalent bond between RGD and substrate was formed.
- The pronounced localization of electrons of Mg(11$\bar{2}$0) and Mg(10$\bar{1}$1) surfaces improved the adsorption.

Abstract: Functional Arg-Gly-Asp (RGD) tripeptide has a tremendous potential in clinical applications to accelerate the endothelialization of Magnesium (Mg) alloy vascular stent surface. The interaction mechanism of RGD on different surfaces of Mg and Mg alloy is important for promoting the development of Mg alloy vascular stent, yet still unclear. In the present work, first-principles calculation within density functional theory (DFT) was performed to investigate the interaction mechanism. The electron redistribution, effect of alloying elements and changes in the density of states of the adsorption systems were studied. The results revealed that RGD interacted with different surfaces of Mg (0001), Mg(11$\bar{2}$0) and Mg(10$\bar{1}$1) through ligand covalent bond; the pronounced localization of electrons of Mg(11$\bar{2}$0) and Mg(10$\bar{1}$1) surfaces promoted the adsorption of RGD tripeptide compared with that on the Mg(0001) surface; Zn/Y/Nd alloying elements improved the adsorption of RGD. Calculated results could provide insight for the interaction mechanism of biomolecule on the Mg and Mg-based alloy surfaces, and point out some directions for the future experimental efforts.

Keywords: RGD; Mg alloy; different surfaces; first-principles calculation; interaction mechanism

Citation: Fang, Z.; Ding, H.; Li, P.; Qiao, H.; Liang, E.; Jia, Y.; Guan, S. Interaction Mechanism of RGD Tripeptide on Different Surfaces of Mg and Mg Alloys: A First-Principles Study. *Coatings* **2022**, *12*, 1814. https://doi.org/10.3390/coatings12121814

Academic Editor: Vincent Ji

Received: 21 October 2022
Accepted: 21 November 2022
Published: 24 November 2022

1. Introduction

Magnesium (Mg) alloys with good biodegradability, biocompatibility and mechanical compatibility have become a research hotspot in biodegradable vascular stent materials in recent years [1–3]. In the physiological environment, the slow endothelialization process of the endothelial cell on Mg alloys surfaces could lead to inflammation, thrombosis and vascular restenosis, which limits the clinical application of Mg alloys vascular stent [4–6]. In the past decades, the construction of functional biomolecular coatings, such as Arg-Gly-Asp (RGD), Arg-Glu-Asp-Val (REDV) and Tyr–Ile–Gly–Ser–Arg (YIGSR), on the Mg alloys surfaces were considered as an effective strategy to improve the endothelialization process [7–9]. RGD tripeptide sequence was existing in a variety of extracellular matrices and containing specific binding sites with integrin receptors on the surface of endothelial cells (ECs). It had been extensively used for surface modification to promote the adhesion of ECs and inhibit the blood coagulation [10,11]. Kou et al. [12] pointed out that covalent bonding between carboxyl group and amine group was a preferable method in immobilizing bioactive molecules on the materials' surfaces and developed the PDA/CA-RGD multilayers on Mg-Zn-Y-Nd alloy surface. The in vitro cytocompatibility experiments indicated that the PDA/(CA-RGD)$_2$ coating not only displayed excellent performance in promoting surface endothelialization, but also provided sustained inhibition effects on SMCs adhesion and proliferation. Schieber et al. [13] concluded that RGD-coated CoCr surfaces induced a significant increase in ECs' adhesion without significantly enhancing SMCs' adhesion. Wang et al. [14] reported that various density combinations of RGD tripeptide and YIGSR in a quantitative and high-throughput manner to obtain surfaces on which ECs exhibited preponderant adhesion over SMCs.

The functional RGD tripeptide coating could significantly improve the endothelialization process, while the interaction mechanism of RGD tripeptide on the different Mg alloys surfaces was still unclear. With the help of the computational simulation, some detailed information about the interaction process of RGD tripeptide on the other material (rather than Mg alloys) surfaces at the atomic scale was obtained. Deguchi et al. [15] noted that RGD tripeptide was the most stable state when two oxygen atoms of carboxyl group in Asp were located very close to the atop sites of Au surface. Höffling et al. [16] reported that the two-coordinate covalent bond between the dipeptide Arg–Cys and Au(111) surface led to a strong interaction via the first-principles study. The amino acids and short peptides preferred to lie flat on the surface with the N and O anions in their functional groups (carboxyl, amine and guanidyl) binding to the Mg atoms [17,18]. Structural and electronic characteristics of RGD tripeptide and cyclophosphamide anticancer drugs were reported and the results indicated the effect of strong hydrogen bond interactions by using density functional theory (DFT) calculations and molecular dynamics (MD) simulations [19].

Another important factor affecting RGD tripeptide adsorption was the properties of different material surfaces, as different processes and surface treatment methods made the material have a polycrystalline surface distribution. The calculated results showed that RGD tripeptide had a higher binding energy on anatase (001) and rutile (010) than the other corresponding surfaces through MD simulations [20]. Zhang et al. [21] concluded that the interaction of RGD tripeptide on the anatase (101) surfaces was stronger than that on the rutile (110) surfaces through the energy analysis. In terms of different Mg surfaces, most studies focused on hydrogen storage properties and mechanical properties of the Mg basal, prismatic and pyramidal surfaces [22–25]. However, the research on the interaction mechanism of RGD tripeptide with different surfaces of Mg and Mg alloys has not been reported in the previous literature.

Based on the above background and the authors' previous studies about the interaction between biomolecules and Mg(0001) surface [17,18,26], the interaction mechanism of RGD with different surfaces of Mg and Mg alloys by the first-principles calculation was proposed in this study. Firstly, the properties of different surfaces (basal (0001), prismatic $(10\bar{1}0)$, $(11\bar{2}0)$, $(21\bar{3}0)$ and pyramidal $(10\bar{1}1)$ surfaces) of pure Mg were investigated. Secondly, the adsorption of RGD tripeptide on the pure Mg(0001), Mg$(11\bar{2}0)$ and $(10\bar{1}1)$ surfaces were calculated, and the effect of alloying elements on the adsorption of RGD tripeptide on different surfaces were analyzed. Finally, the interaction mechanism of RGD tripeptide on different surfaces of Mg and Mg alloys were proposed after studying the electronic properties. The calculated results could provide theoretical support for the selection of surface texture processing methods of biomedical Mg alloys.

2. Computational Methods

The DFT calculations were carried out using the Vienna *Ab initio* Simulation Package (VASP) with the projected augmented wave (PAW) method [27–29]. The exchange-correlation energy was dealing with the Perdew–Burke–Ernzerhof (PBE) functional with the framework of the generalized gradient approximation (GGA) [30]. The optB86b method proposed by Klimesis was adopted for van der Waals (vdW) correction [31,32]. The surface energy (E_{surf}) and work functions of basal (0001), prismatic (10$\bar{1}$0), (11$\bar{2}$0), (21$\bar{3}$0) and pyramidal (10$\bar{1}$1) surfaces of Mg were obtained using periodic boundary conditions with the energy cutoff of 400 eV. A 1 × 1 supercell with a certain atomic layer thickness in the z-direction was chosen as the surface model, and the thickness of the vacuum layer was 40 Å to ensure the same symmetry between the upper and lower surfaces. The k-point in the Brillouin zone in the direction of the vacuum layer was chosen as 1 and the k-point of atomic layer direction was taken as at least 25. The convergence accuracy of the total energy of the system was 10^{-8} eV, and the convergence criterion of the force was 10^{-4} eV/Å. When calculating the interaction of RGD tripeptide on the Mg surfaces, six atomic layer thickness with the vacuum of 20 Å were chosen as the surface model. The convergence criterion of the force and the electron relaxation energy for the adsorption system were set at 0.02 eV/Å and 10^{-5} eV, respectively. The bottom two layers of Mg atoms were fixed and the remaining Mg atoms and RGD were fully relaxed to the convergence criterion during the optimization of the adsorption systems. The E_{surf} for different number of layers were obtained by using the following equation.

$$E_{surf} = \frac{1}{2A}(E_{slab} - N_{slab}E_{bulk}) \tag{1}$$

where A is the area of the surface; E_{slab} is the energy of the optimized surface; N_{slab} is the number of atoms in the selected surface model; and E_{bulk} is the energy of per atom in the bulk.

The adsorption energy (E_{ads}) of molecules on the substrates were expressed as follows.

$$E_{ads} = E_{mol+sub} - (E_{mol} + E_{sub}) \tag{2}$$

where E_{mol}, E_{sub} and $E_{mol+sub}$ represent the total energy of the optimized RGD, the energy of the substrates and the energy of the stable adsorption systems, respectively.

3. Results and Discussion

3.1. Properties of Different Surfaces of Pure Mg

The surface energy is an important parameter to determine the surface stability of the materials. The thickness of the constructed surface model, which was at least 10 Å, was obtained by adjusting the number of selected Mg atomic layer. The topmost and bottommost surfaces were the same. Configurations of the basal (0001), prismatic (10$\bar{1}$0), (11$\bar{2}$0), (21$\bar{3}$0) and pyramidal (10$\bar{1}$1) surfaces of pure Mg were fully relaxed at the convergence criterion set, as shown in Figure 1.

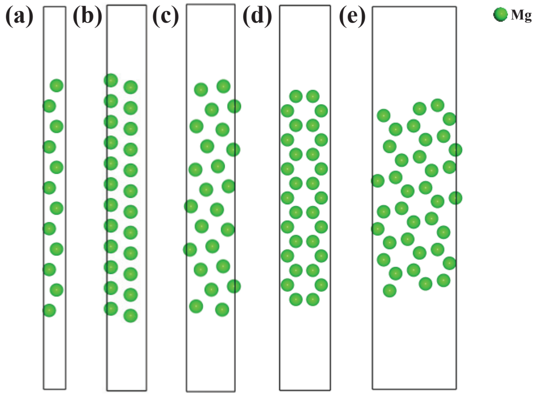

Figure 1. Configurations of different Mg surfaces: (**a**) basal (0001); (**b**–**d**) prismatic (11$\bar{2}$0), (21$\bar{3}$ 0), (10$\bar{1}$ 0); and (**e**) pyramidal (10$\bar{1}$ 1).

The surfaces with different Miller indices presented different properties due to the orientation of the atomic arrangement. For the configurations of Mg surfaces, six models with gradually increasing thicknesses were selected for each surface, and the E_{surf} of Mg surfaces at different layer thicknesses were calculated according to equation (1), as shown in Figure 2.

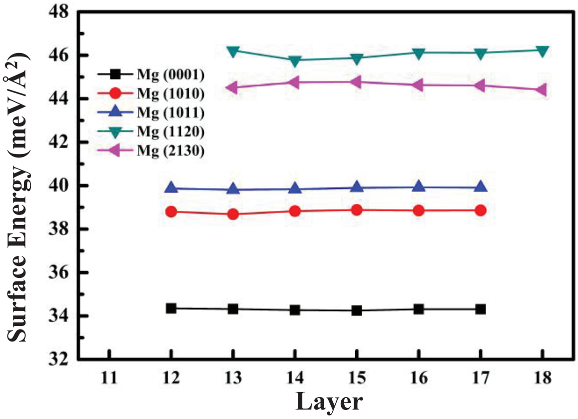

Figure 2. Surface energies of Mg basal (0001), prismatic $(10\bar{1}0)$, $(11\bar{2}\ 0)$, $(21\bar{3}\ 0)$ and pyramidal $(10\bar{1}\ 1)$ surfaces.

As seen in Figure 2, the fluctuations in surface energy are small as the thickness gradually increases, which shows a good convergence. Mg(0001) and Mg$(11\bar{2}0)$ surfaces had the lowest and the highest E_{surf}, respectively. The order of E_{surf} for the above different surfaces was $(11\bar{2}0) > (21\bar{3}0) > (10\bar{1}1) > (10\bar{1}0) > (0001)$. Work function was the required energy to move an electron from the Fermi energy level to vacuum at 0 K, and it was also investigated by Equation (3). The calculated work function of different Mg surfaces was depicted in Table 1.

$$\Phi = V_{vacuum} - E_{fermi} \tag{3}$$

where V_{vacuum} is the vacuum electrostatic potential; and E_{fermi} is the Fermi energy level.

Table 1. Surface energy and work function of different surfaces of Mg.

Surface	Surface Energy(meV/Å^2)		Work Function (eV)	
	This Work	Other Works	This Work	Other Works
0001	34.30	34.37 [33], 34.61 [34]	3.69	3.70 [34], 3.80 [35]
$10\bar{1}0$	38.81	39.90 [34]	3.61	3.60 [34], 3.64 [36]
$10\bar{1}1$	39.87	40.90 [34]	3.69	3.80 [34], 3.70 [34]
$11\bar{2}0$	45.94	45.70 [34]	3.66	4.00 [34]
$21\bar{3}0$	44.61	46.62 [36]	3.49	3.49 [36]

As seen in Table 1, the E_{surf} and Φ of Mg(0001) surface were 34.30 meV/Å^2 and 3.69 eV, respectively, which were in good agreement with the Refs. [33,34]. Compared with other Mg surfaces $(10\bar{1}0)$, $(11\bar{2}0)$, $(21\bar{3}0)$ and $(10\bar{1}1)$, Mg(0001) surface had the smallest E_{surf} and the largest work function, which means this surface was the most stable one. With the larger surface energy and lower work function, the prismatic $(10\bar{1}0)$, $(11\bar{2}0)$, $(21\bar{3}0)$ and pyramidal $(10\bar{1}1)$ surfaces were more electronically active and were prone to chemical reactions once stimulated by external conditions.

3.2. *Adsorption of RGD on Different Surfaces of Pure Mg and Mg Alloy*

3.2.1. Adsorption of RGD on Different Surfaces of Pure Mg

From the optimized stable adsorption structures of biomolecules in Refs. [17,18], it was clear that the strongest interaction occurred when the biomolecules were adsorbed in a flat lying manner on the Mg(0001) surfaces of Mg and Mg alloys. RGD had three potential metal-binding groups: guanidyl (–CN_3H_4), amino (–NH_2), and carboxyl (–COOH). These functional groups could be used as monodentate or bidentate ligands to make RGD more easily adsorbed on the surfaces. Many adsorption configurations of RGD on the (0001), ($11\bar{2}0$) and ($10\bar{1}1$) surfaces were optimized. The adsorption regularity showed that the most stable configurations occurred when functional groups bounded to the surface as much as possible. In addition, the stabilities of the most stable configurations at room temperature were checked by using ab initio molecular dynamics simulations [18], and the results showed that they were stable. The most stable adsorption configurations of RGD on the Mg(0001), Mg($11\bar{2}0$) and Mg($10\bar{1}1$) surfaces were shown in Figure 3.

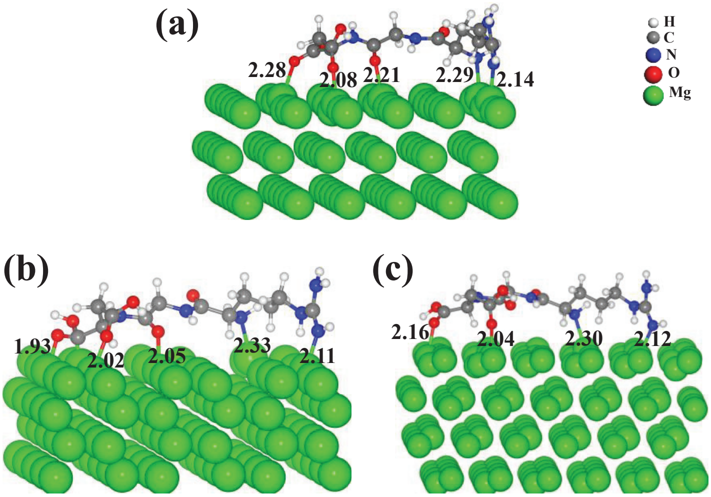

Figure 3. Stable adsorption configurations of RGD on the surfaces: (**a**) Mg(0001), (**b**) Mg($11\bar{2}0$) and (**c**) Mg($10\bar{1}$ 1).

According to equation (2), the E_{ads} of RGD on the Mg(0001), Mg($11\bar{2}0$) and Mg($10\bar{1}1$) surfaces were −3.24 eV,−4.44 eV and−3.32 eV, respectively. As shown in Figure 3, RGD was anchored to the Mg(0001), Mg($11\bar{2}0$) and Mg($10\bar{1}1$) surfaces via amino, carboxyl and guanidinium functional groups. The calculated E_{ads} of RGD on the Mg($11\bar{2}0$) and Mg($10\bar{1}1$) surfaces were 1.20 eV and 0.08 eV higher than that of on the Mg(0001) surface (−3.24 eV) [25], respectively. It was much easier for RGD to be adsorbed on the Mg($11\bar{2}0$) and Mg($10\bar{1}1$) surfaces compared with that on the Mg(0001) surface. For the stable adsorption configurations, the O-Mg and N-Mg bond lengths ranges of RGD on the pure Mg surfaces were 1.93~2.16 Å and 2.11~2.33 Å, respectively. The optimized O-Mg and N-Mg bond lengths were very close to the theoretical bond lengths of the formation of covalent bonds of N-Mg and O-Mg (2.11 Å and 2.09 Å) [37], indicating a ligand covalent bond of RGD on the pure Mg surfaces.

3.2.2. Effect of Zn, Y and Nd Alloying Elements on the Adsorption of RGD on Different Mg Alloys Surfaces

To analyze the effects of Zn, Y and Nd alloying elements, the adsorption of RGD on the (0001), ($11\bar{2}0$) and ($10\bar{1}1$) surfaces of Mg alloys were further calculated. Mg-Zn (1%, 2% and 3%), Mg-Y (1%) and Mg-Nd (1%) were considered in the present calculations. Note that the alloy concentrations should be connected with the number of Zn, Y and Nd in the respective supercells as well as on the symmetry of the primitive cells [38]. The substitution alloying elements were located at the first-topmost layer of Mg alloys surfaces to make the influence of alloying elements more evident. The initial configurations of RGD on the Mg alloys surfaces were the same as that of RGD on the pure Mg(0001), Mg(11$\bar{2}$0) and (10$\bar{1}$1) surfaces, as shown in Figure 3. The stable adsorption configurations of RGD on different surfaces of Mg alloys were fully optimized to the convergence criterion set. From the optimized structures, the surface charge redistribution was influenced by the addition of alloying elements which affected the following adsorption process. It was noticed that RGD tripeptide was attracted toward Y/Nd but repelled by Zn element as the electronegativity of Y (1.22) is smaller than that of Mg (1.31) while the electronegativity of Zn (1.65) was greater than that of Mg [17,39]. Figure 4 shows the optimized adsorption configurations of RGD on the Zn-, Y- and Nd-doped surfaces.

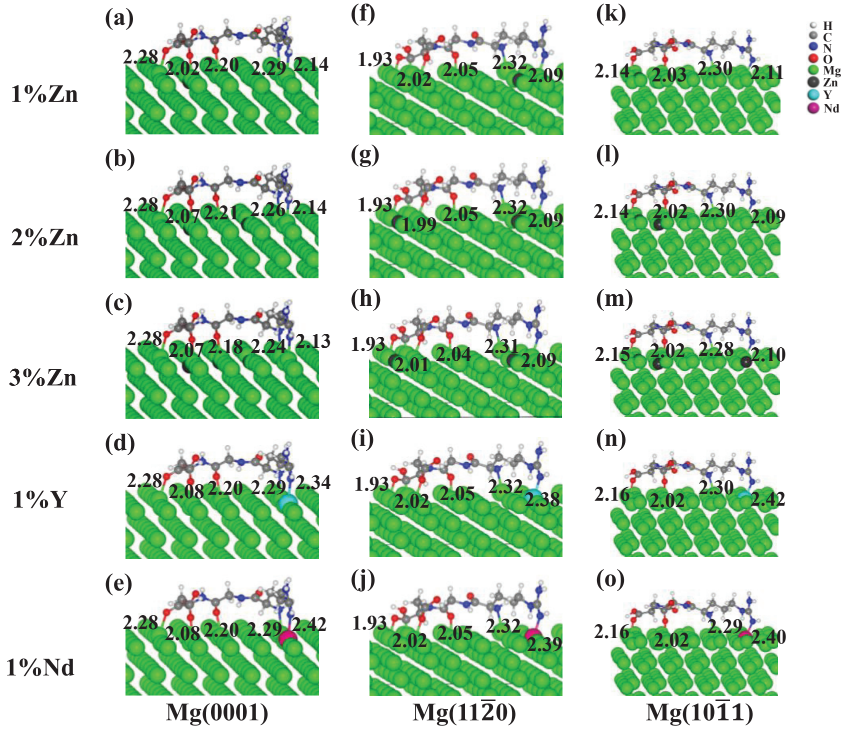

Figure 4. Optimized adsorption configurations of RGD on the Zn-, Y- and Nd-doped surfaces: (**a**–**e**) Mg(0001) surfaces, (**f**–**j**) Mg(11$\bar{2}$0) surfaces and (**k**–**o**) Mg(10$\bar{1}$ 1) surfaces. The bond lengths (in Å) are also listed.

For the Zn-doped surfaces, RGD preferred to be adsorbed on the Mg atom around the Zn atom; while for Y- and Nd-doped cases, RGD preferred to be adsorbed on the Y or Nd atom, as shown in Figure 4. It was easier for RGD tripeptide to be adsorbed on the neighbor site of the Zn-doped position, and on the top site of Y-/Nd-doped atom rather than the neighbor site of Y/Nd atom. The corresponding bond lengths on the Zn-doped Mg alloys surfaces were about 0.01~0.03 Å lower than that on the pure Mg surfaces. For Y- and Nd-doped Mg alloy surfaces, the range of bond lengths were 2.34~2.40 Å and 2.39~2.42 Å, respectively, which were very close to the sum of the theoretical covalent radii bond lengths of 2.40 Å and 2.43 Å [37].

Table 2 shows the E_{ads} of RGD on the (0001), $(11\bar{2}0)$ and $(10\bar{1}1)$ surfaces of Mg alloys. Compared with the calculated results of RGD on the clean Mg(0001), Mg$(11\bar{2}0)$ and Mg$(10\bar{1}1)$ surfaces, the addition of the alloying elements enhanced the adsorption process. The E_{ads} of RGD on the 1%, 2% and 3% Zn-doped Mg alloys surfaces increased about 0.29~0.49 eV, 0.03~0.11 eV and 0.19~0.22 eV, respectively. The promoting effect of Zn alloying element was enhanced with the increase of Zn content. For Y-/Nd-doped Mg alloys surfaces, The E_{ads} of RGD on different surfaces of Mg alloys were significantly increased due to the more active extranuclear electrons. The rank of the E_{ads} for different surfaces was $(11\bar{2}0) > (10\bar{1}1) > (0001)$. With the addition of Zn/Y/Nd alloying elements, new ligand covalent bonds between RGD tripeptide and Mg alloys' surfaces were formed, and alloying elements improved the adsorption process.

Table 2. E_{ads} of RGD on the Mg and Mg alloys surfaces (eV).

Mg Surfaces	Pure	1%Y	1%Nd	1%Zn	2%Zn	3%Zn
Mg(0001)	−3.24	−3.89	−4.03	−3.53	−3.64	−3.73
Mg$(11\bar{2}0)$	−4.44	−5.09	−4.91	−4.47	−4.49	−4.55
Mg$(10\bar{1}1)$	−3.32	−3.56	−3.47	−3.51	−3.52	−3.54

3.3. Electronic Properties of RGD on Mg and Mg-Based Alloy Surfaces

To further understand the interaction properties of the RGD tripeptide on different surfaces of Mg and Mg alloys surfaces, the electronic structure properties of different Mg surfaces were firstly investigated. The projected density of states (PDOS) of the most superficial atoms in the different Mg surfaces, as well as the individual Mg atoms in the bulk structure, are shown in Figure 5.

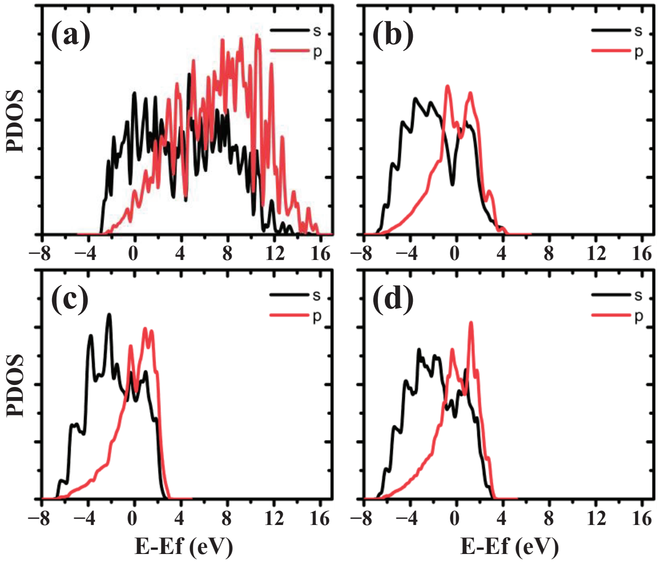

Figure 5. PDOS of a single Mg atom in the (**a**) Mg bulk structure, (**b**) the topmost layer of Mg(0001) surface, (**c**) the topmost layer of Mg$(11\bar{2}0)$ surface, and (**d**) the topmost layer of Mg$(10\bar{1}1)$ surface. The Fermi level is set at 0 eV.

Figure 5a shows that the PDOS of the bulk Mg atom is mainly distributed in the range −4.90~15.90 eV. The PDOS of the most superficial Mg atoms were mainly distributed in the range of −7.10~4.40 eV for the (0001), $(11\bar{2}0)$ and $(10\bar{1}1)$ surfaces, as depicted in Figure 5b–d. The variation of the electronic density of states of the most superficial Mg atoms in the (0001), $(11\bar{2}0)$ and $(10\bar{1}1)$ surfaces was essentially the same compared with the bulk structure. The most noticeable difference between the bulk and surfaces were the downward shift of the *sp* states to the lower energies due to the redistribution of the electrons during surface optimization. Figure 6 shows the charge density distributions of different Mg surfaces. It could be observed that the surface charge density distribution was relatively uniform for the Mg(0001) surface, while the surface charge density distribution of Mg$(11\bar{2}0)$ and Mg$(10\bar{1}1)$ surfaces were more localized. Mg$(11\bar{2}0)$ surface had the most pronounced localization of electrons, and it was relatively active to adsorb RGD. This was one of the reasons that for its larger surface energy and larger E_{ads} of RGD.

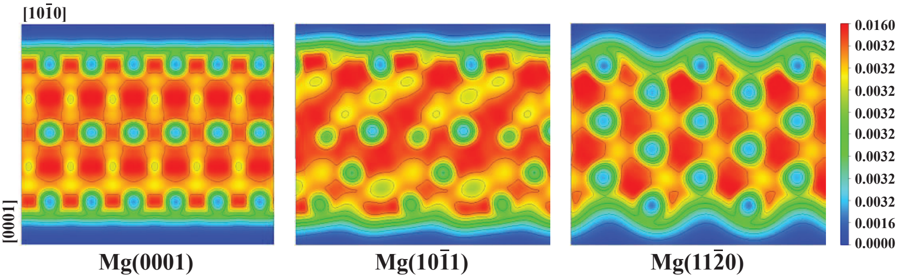

Figure 6. Surface charge density distribution of Mg(0001), Mg$(10\bar{1}1)$ and Mg$(11\bar{2}\,0)$.

To analyze the interaction mechanism of RGD on the Mg$(11\bar{2}0)$ and Mg$(10\bar{1}1)$ surfaces, the changes of electronic structures (see Figures 7 and 8) were investigated through PDOS, and the charge density difference ($\Delta\rho$) was calculated by Equation (4). It should be pointed out that the interaction mechanism of RGD on the Mg(0001) was proposed by our previous paper [17].

$$\Delta\rho = \rho_{mol+surf} - \left(\rho_{mol} + \rho_{surf}\right) \tag{4}$$

where $\rho_{mol+surf}$ is the total charge density of the optimized adsorbate–substrate systems, ρ_{mol} is the charge density of RGD without surface, and ρ_{surf} is the charge density of different Mg and Mg alloy surfaces, respectively.

As displayed in Figure 7, the highest occupied molecular orbital (HOMO) and the lowest unoccupied molecular orbital (LUMO) were attributed to the *p* orbitals of the N and O atoms in the functional groups of RGD, which were the active sites for adsorption. The most noticeable difference between the before (Figure 7a–c) and after adsorptions (Figure 7d–f) was the downward shift of the *sp* states of the O and N atoms. After adsorptions, the intensity of O and N states became weaker, as shown in Figure 7d,e, respectively. For the Mg atoms bound with O atoms, the Mg(s) states simultaneously showed a new peak at the −4.60 eV position, indicating the formation of a new chemical bond between RGD and the Mg surface, as shown in Figure 7e,f. For the Mg atoms bound with N atoms, the Mg(s) states appeared at the energy about −4.60 and −6.10 eV, indicating the lone pair electrons of N(p) donating to the Mg, as shown in Figure 7e,f.

Significant changes were investigated for the PDOS of RGD tripeptide on the Mg $(10\bar{1}1)$ surface, comparing the before adsorption in Figure 8a–c with the corresponding adsorption state in Figure 8d–f. A new peak appeared at the −5.20 eV position for the chemical bond formation of O-Mg atoms. The new peak appeared at −4.30 eV position for the binding process of N-Mg atoms, and electrons in *py* and *pz* orbits had also been redistributed to obtain a more stable state. Interactions of N-Mg atoms was slightly weakened compared with the results of RGD tripeptide on the Mg$(11\bar{2}0)$ surface.

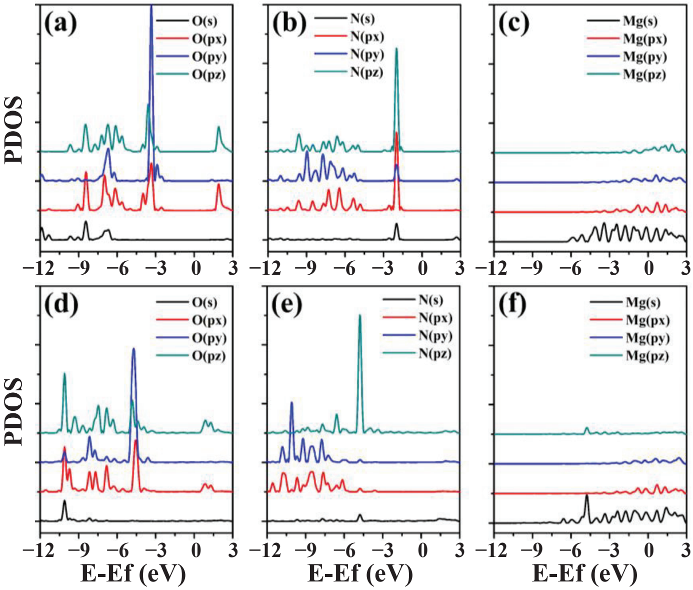

Figure 7. PDOS of the binding atoms on the Mg (11$\bar{2}$0) surface: (**a**) three O atoms, (**b**) two N atoms, and (**c**) five Mg atoms before adsorption; (**d**–**f**) are the PDOS of the corresponding atoms after adsorption. The energy zero is set to the Fermi level.

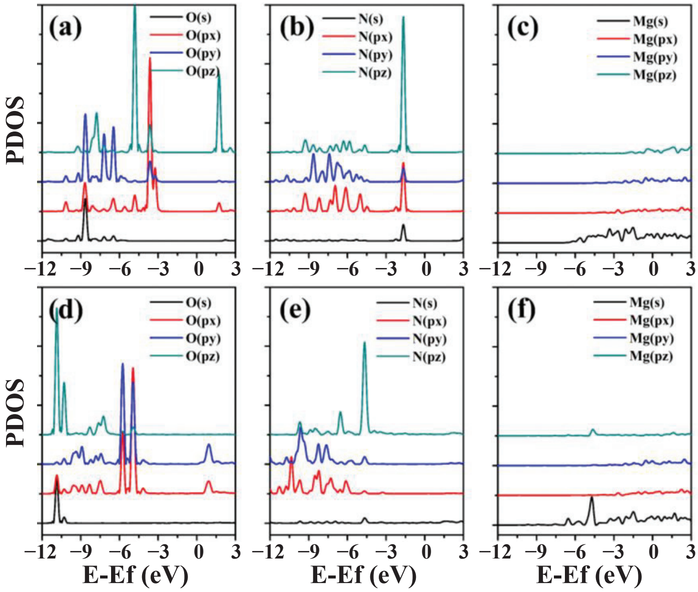

Figure 8. PDOS of the binding atoms on the Mg (10$\bar{1}$1) surface: (**a**) two O atoms, (**b**) two N atoms, and (**c**) four Mg atoms before adsorption; (**d**–**f**) are the PDOS of the corresponding atoms after adsorption. The energy zero is set to the Fermi level.

For a clear description of the charge redistribution after the adsorption, the charge density differences for the adsorptions of RGD on the Mg(0001), Mg(11$\bar{2}$0) and Mg(10$\bar{1}$1) surface were calculated to investigate the interactions, as depicted in Figure 9. The yellow and light cyan regions indicated the interactions between RGD and different surfaces due to the rearrangement of electrons. A significant accumulation of charge density occurred between RGD and different Mg surfaces, as shown in the yellow regions of O-Mg and N-Mg binding atoms in Figure 9. The new chemical bonds were described from the 2D and 3D coordinates according to the PDOS analysis and charge density differences.

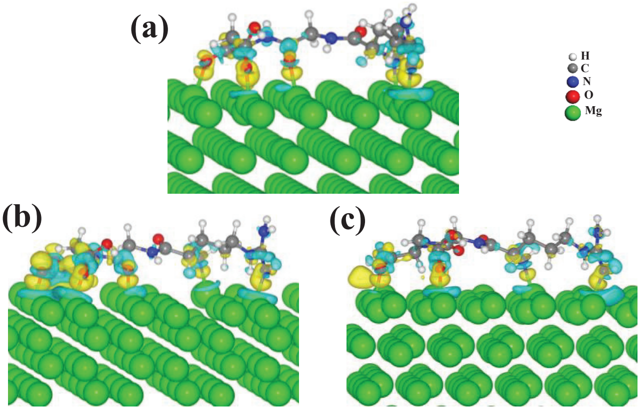

Figure 9. Charge density difference of RGD on the (**a**) Mg(0001), (**b**) Mg $(11\bar{2}0)$ and (**c**) Mg $(10\bar{1}\ 1)$ surfaces. The values of the isosurfaces are ±0.03 e/Å^3, and the yellow and light cyan isosurfaces indicate the accumulation and depletion of charge density.

The PDOS and charge density differences of RGD tripeptide on different surfaces of Mg alloys showed a similar regularity. The intensity of the binding peak was influenced by the addition of the Zn/Y/Nd alloying elements, while the bonding nature was still the ligand covalent bond. Electron redistribution was the driving force behind the changes observed in the structure of RGD tripeptide on different surfaces of Mg and Mg alloys. The calculated results concluded that this driving force made it easy for the lone pair of electrons of N/O to share bonding with the Mg atom to form the ligand covalent bond.

4. Conclusions

In this study, the influences of different surfaces and different alloying elements were investigated, and the interaction mechanism of RGD tripeptide on different surfaces of Mg and Mg alloys surfaces were analyzed. The conclusions can be drawn as follows.

(1) The order of E_{surf} for the above different surfaces was $(11\bar{2}0) > (21\bar{3}0) > (10\bar{1}1) > (10\bar{1}0) > (0001)$. The higher surface energy made it much easier to interact with RGD, and the order of E_{ads} was $\Delta E(11\bar{2}0) > \Delta E(10\bar{1}1) > \Delta E(0001)$.

(2) For Mg alloys surfaces, the addition of Zn/Y/Nd alloying elements improved the association of RGD tripeptide with the different Mg alloys surfaces. The E_{ads} also gradually increased with the increase of alloying element Zn content.

(3) RGD tripeptide was bonded to the (0001), $(11\bar{2}0)$ and $(10\bar{1}1)$ surfaces of Mg through the ligand covalent bond. The pronounced localization of electrons of Mg$(11\bar{2}0)$ and Mg$(10\bar{1}1)$ surfaces promoted the adsorption of RGD tripeptide compared with that on the Mg(0001) surface. The calculated results provide insight for the interaction mechanism of RGD tripeptide on the Mg and Mg-based alloy surfaces, and also point out some directions for the design of functional biomolecular coatings.

Author Contributions: Conceptualization, Z.F. and H.D.; methodology, P.L.; software, Z.F.; formal analysis, H.D.; resources, S.G.; data curation, P.L.; writing—original draft preparation, Z.F.; writing—review and editing, Y.J.; visualization, H.Q.; supervision, Y.J. and E.L.; funding acquisition, S.G. All authors have read and agreed to the published version of the manuscript.

Funding: The authors are very grateful for the financial support including the National Key Research and Development Program of China (2021YFC2400700), the Key Projects of the Joint Fund of the National Natural Science Foundation of China (U1804251) and Youth Fund Project of Zhongyuan University of Technology (K2022QN026).

Institutional Review Board Statement: Not applicable.

Informed Consent Statement: Not applicable.

Data Availability Statement: Not applicable.

Acknowledgments: The calculations were supported by National Supercomputing Center in Zhengzhou.

Conflicts of Interest: The authors declare no conflict of interest.

References

1. Zhang, Z.-Q.; Yang, Y.-X.; Li, J.-A.; Zeng, R.-C.; Guan, S.-K. Advances in coatings on magnesium alloys for cardiovascular stents–A review. *Bioact. Mater.* **2021**, *6*, 4729–4757. [CrossRef]
2. Wang, H.; Bai, M.; Yuan, H.; Hou, Y.; Liu, Y.; Fang, Z.; Sun, Y.; Wang, J.; Zhu, S.; Guan, S. Zn content mediated fibrinogen adsorption on biodegradable Mg-Zn alloys surfaces. *J. Magnes. Alloy.* **2021**, *9*, 2145–2154. [CrossRef]
3. Li, M.; Jiang, M.; Gao, Y.; Zheng, Y.; Liu, Z.; Zhou, C.; Huang, T.; Gu, X.; Li, A.; Fang, J.; et al. Current status and outlook of biodegradable metals in neuroscience and their potential applications as cerebral vascular stent materials. *Bioact. Mater.* **2022**, *11*, 140–153. [CrossRef]
4. Cheon, K.-H.; Park, C.; Kang, M.-H.; Park, S.; Kim, J.; Jeong, S.-H.; Kim, H.-E.; Jung, H.-D.; Jang, T.-S. A combination strategy of functionalized polymer coating with Ta ion implantation for multifunctional and biodegradable vascular stents. *J. Magnes. Alloy.* **2021**, *9*, 2194–2206. [CrossRef]
5. Wang, P.; Liu, J.; Luo, X.; Xiong, P.; Gao, S.; Yan, J.; Li, Y.; Cheng, Y.; Xi, T. A tannic acid-modified fluoride pre-treated Mg–Zn–Y–Nd alloy with antioxidant and platelet-repellent functionalities for vascular stent application. *J. Mater. Chem. B* **2019**, *7*, 7314–7325. [CrossRef]
6. Zong, J.; He, Q.; Liu, Y.; Qiu, M.; Wu, J.; Hu, B. Advances in the development of biodegradable coronary stents: A translational perspective. *Mater. Today Bio* **2022**, *16*, 100368. [CrossRef]
7. Wang, P.; Xiong, P.; Liu, J.; Gao, S.; Xi, T.; Cheng, Y. A silk-based coating containing GREDVY peptide and heparin on Mg–Zn–Y–Nd alloy: Improved corrosion resistance, hemocompatibility and endothelialization. *J. Mater. Chem. B* **2018**, *6*, 966–978. [CrossRef]
8. Liu, J.; Wang, P.; Chu, C.-C.; Xi, T. A novel biodegradable and biologically functional arginine-based poly(ester urea urethane) coating for Mg–Zn–Y–Nd alloy: Enhancement in corrosion resistance and biocompatibility. *J. Mater. Chem. B* **2017**, *5*, 1787–1802. [CrossRef] [PubMed]
9. Yao, S.; Cui, J.; Chen, S.; Zhou, X.; Li, J.; Zhang, K. Extracellular Matrix Coatings on Cardiovascular Materials—A Review. *Coatings* **2022**, *12*, 1039. [CrossRef]
10. Li, Y.; McRobb, L.S.; Khachigian, L.M. Inhibition of intimal thickening after vascular injury with a cocktail of vascular endothelial growth factor and cyclic Arg-Gly-Asp peptide. *Int. J. Cardiol.* **2016**, *220*, 185–191. [CrossRef] [PubMed]
11. Tugulu, S.; Silacci, P.; Stergiopulos, N.; Klok, H.-A. RGD—Functionalized polymer brushes as substrates for the integrin specific adhesion of human umbilical vein endothelial cells. *Biomaterials* **2007**, *28*, 2536–2546. [CrossRef] [PubMed]
12. Kou, F.; Liu, C.; Wang, L.; Yasin, A.; Li, J.; Guan, S. Fabrication of Citric Acid/RGD Multilayers on Mg-Zn-Y-Nd Alloy via Layer-by-Layer Self-Assembly for Promoting Surface Biocompatibility. *Adv. Mater. Interfaces* **2021**, *8*, 2002241. [CrossRef]
13. Schieber, R.; Mas-Moruno, C.; Lasserre, F.; Roa, J.J.; Ginebra, M.-P.; Mücklich, F.; Pegueroles, M. Effectiveness of Direct Laser Interference Patterning and Peptide Immobilization on Endothelial Cell Migration for Cardio-Vascular Applications: An In Vitro Study. *Nanomaterials* **2022**, *12*, 1217. [CrossRef]
14. Wang, C.; Hao, H.; Wang, J.; Xue, Y.; Huang, J.; Ren, K.; Ji, J. High-throughput hyaluronic acid hydrogel arrays for cell selective adhesion screening. *J. Mater. Chem. B* **2021**, *9*, 4024–4030. [CrossRef]
15. Deguchi, S.; Hakamada, M.; Mabuchi, M. Adsorption of RGD Tripeptide on Au (111) Surface. *Mater. Trans.* **2019**, *60*, 1711–1715. [CrossRef]
16. Höffling, B.; Ortmann, F.; Hannewald, K.; Bechstedt, F. Single cysteine adsorption on Au(110): A first-principles study. *Phys. Rev. B* **2010**, *81*. [CrossRef]
17. Fang, Z.; Wang, J.; Zhu, S.; Yang, X.; Jia, Y.; Sun, Q.; Guan, S. A DFT study of the adsorption of short peptides on Mg and Mg-based alloy surfaces. *Phys. Chem. Chem. Phys.* **2018**, *20*, 3602–3607. [CrossRef]
18. Fang, Z.; Wang, J.; Yang, X.; Sun, Q.; Jia, Y.; Liu, H.; Xi, T.; Guan, S. Adsorption of arginine, glycine and aspartic acid on Mg and Mg-based alloy surfaces: A first-principles study. *Appl. Surf. Sci.* **2017**, *409*, 149–155. [CrossRef]
19. Nikfar, Z.; Shariatinia, Z. The RGD tripeptide anticancer drug carrier: DFT computations and molecular dynamics simulations. *J. Mol. Liq.* **2019**, *281*, 565–583. [CrossRef]

20. Zhang, H.-P.; Lu, X.; Fang, L.-M.; Weng, J.; Huang, N.; Leng, Y. Molecular dynamics simulation of RGD peptide adsorption on titanium oxide surfaces. *J. Mater. Sci. Mater. Electron.* **2008**, *19*, 3437–3441. [CrossRef]
21. Zhang, H.-P.; Lu, X.; Leng, Y.; Watari, F.; Weng, J.; Feng, B.; Qu, S. Effects of aqueous environment and surface defects on Arg-Gly-Asp peptide adsorption on titanium oxide surfaces investigated by molecular dynamics simulation. *J. Biomed. Mater. Res. Part A* **2011**, *96A*, 466–476. [CrossRef] [PubMed]
22. Ouyang, L.; Tang, J.; Zhao, Y.; Wang, H.; Yao, X.; Liu, J.; Zhu, M. Express penetration of hydrogen on Mg(10(1)over-bar3) along the close-packed-planes. *Sci. Rep.* **2015**, *5*, 10776. [CrossRef] [PubMed]
23. Tang, J.J.; Ye, J.H.; Fang, Y.X.; Lin, Z.; Zhao, Y.J. Transition metal substitution on Mg(10$\bar{1}$3) and Mg(0001) surfaces for improved hydrogenation and dehydrogenation: A systematic first-principles study. *Appl. Surf. Sci.* **2019**, *479*, 626–633. [CrossRef]
24. Wang, Z.; Guo, X.; Wu, M.; Sun, Q.; Jia, Y. First-principles study of hydrogen dissociation and diffusion on transition metal-doped Mg(0001) surfaces. *Appl. Surf. Sci.* **2014**, *305*, 40–45. [CrossRef]
25. Banerjee, S.; Pillai, C.G.S.; Majumder, C. First-principles study of the H2 interaction with transition metal (Ti, V, Ni) doped Mg(0001) surface: Implications for H-storage materials. *J. Chem. Phys.* **2008**, *129*, 174703. [CrossRef] [PubMed]
26. Fang, Z.; Zhao, Y.; Wang, H.; Wang, J.; Zhu, S.; Jia, Y.; Cho, J.-H.; Guan, S. Influence of surface charge density on ligand-metal bonding: A DFT study of NH3 and HCOOH on Mg (0 0 0 1) surface. *Appl. Surf. Sci.* **2019**, *470*, 893–898. [CrossRef]
27. Kresse, G.; Furthmüller, J. Efficiency of ab-initio total energy calculations for metals and semiconductors using a plane-wave basis set. *Comput. Mater. Sci.* **1996**, *6*, 15–50. [CrossRef]
28. Kresse, G.; Furthmuller, J. Efficient iterative schemes for ab initio total-energy calculations using a plane-wave basis set. *Phys. Rev. B* **1996**, *54*, 11169–11186. [CrossRef] [PubMed]
29. Blöchl, P.E. Projector augmented-wave method. *Phys. Rev. B Condens. Matter Mater. Phys.* **1994**, *50*, 17953–17979. [CrossRef] [PubMed]
30. Perdew, J.P.; Burke, K.; Ernzerhof, M. Generalized gradient approximation made simple. *Phys. Rev. Lett.* **1996**, *77*, 3865. [CrossRef] [PubMed]
31. Klimes, J.; Bowler, D.; Michaelides, A. Van der Waals density functionals applied to solids. *Phys. Rev. B* **2011**, *83*, 195131. [CrossRef]
32. Lüder, J.; Sanyal, B.; Eriksson, O.; Puglia, C.; Brena, B. Comparison of van der Waals corrected and sparse-matter density functionals for the metal-free phthalocyanine/gold interface. *Phys. Rev. B* **2014**, *89*, 045416. [CrossRef]
33. Lee, J.-Y.; Punkkinen, M.; Schönecker, S.; Nabi, Z.; Kádas, K.; Zólyomi, V.; Koo, Y.; Hu, Q.-M.; Ahuja, R.; Johansson, B.; et al. The surface energy and stress of metals. *Surf. Sci.* **2018**, *674*, 51–68. [CrossRef]
34. Lautar, A.K.; Kopač, D.; Rejec, T.; Bančič, T.; Dominko, R. Morphology evolution of magnesium facets: DFT and KMC simulations. *Phys. Chem. Chem. Phys.* **2018**, *21*, 2434–2442. [CrossRef] [PubMed]
35. Wachowicz, E.; Kiejna, A. Bulk and surface properties of hexagonal-close-packed Be and Mg. *J. Physics: Condens. Matter* **2001**, *13*, 10767–10776. [CrossRef]
36. Ji, D.-P.; Zhu, Q.; Wang, S.-Q. Detailed first-principles studies on surface energy and work function of hexagonal metals. *Surf. Sci.* **2016**, *651*, 137–146. [CrossRef]
37. Sargent, W. *Table of Periodic Properties of the Elements*; Sargent-Welch Scientific: Skokie, IL, USA, 1980.
38. Evtimova, J.; Drioli, E.; De Luca, G. A density functional theory study of hydrogen occupation in VNiTi alloys used for dense metal membranes. *J. Alloys Compd.* **2016**, *665*, 225–230. [CrossRef]
39. Allred, A. Electronegativity values from thermochemical data. *J. Inorg. Nucl. Chem.* **1961**, *17*, 215–221. [CrossRef]

coatings

Article

Regulation of Macrophage Behavior by Chitosan Scaffolds with Different Elastic Modulus

Jiawei Xu [1,2,3], Wenchao Guan [1,2,3], Yan Kong [1,2,3], Fang Liu [1,2,3], Yahong Zhao [1,2,3], Guicai Li [1,2,3,*] and Yumin Yang [1,2,3,*]

[1] Key Laboratory of Neuroregeneration of Jiangsu and Ministry of Education, Nantong University, Nantong 226001, China
[2] Co-Innovation Center of Neuroregeneration, Nantong University, Nantong 226001, China
[3] NMPA Key Lab for Research and Evaluation of Tissue Engineering Technology Products, Nantong University, Nantong 226001, China
* Correspondence: gcli1981@ntu.edu.cn (G.L.); yangym@ntu.edu.cn (Y.Y.)

Abstract: Increasing evidence shows that the physical properties of biomaterials play an important role in regulating cell behavior and function, especially the mechanical properties of biomaterials. Macrophages can also be multidirectionally regulated by mechanical factors in the microenvironment, which simultaneously mediate biomaterials response that triggered by foreign body reactions (FBR). However, how the stiffness of biomaterials regulates macrophages and the underlying mechanisms are still not well understood. Our study demonstrates that chitosan freeze-dried scaffolds with different elastic modulus can modulate the proliferative capacity, growth morphology and polarization behavior of macrophages. The compression tests and morphology observation confirmed that the prepared lyophilized chitosan scaffolds possessed varied stiffness. The fluorescence staining experiments showed that the RAW macrophage cell lines exhibited differences in proliferation and morphology on the freeze-dried scaffolds with different stiffness. Macrophages in the 5% group (elastic modulus of 106.7 kPa) had the largest number and mean cell area. Furthermore, ELISA and qPCR results illustrated that macrophage polarization towards the M1/M2 phenotype was strongly influenced by the stiffness of the lyophilized scaffolds. The study may provide new insights and references for designing the elastic moduli of biomaterials for regulating immune responsiveness.

Keywords: chitosan; lyophilized scaffolds; elasticity; macrophages; polarization

Citation: Xu, J.; Guan, W.; Kong, Y.; Liu, F.; Zhao, Y.; Li, G.; Yang, Y. Regulation of Macrophage Behavior by Chitosan Scaffolds with Different Elastic Modulus. *Coatings* **2022**, *12*, 1742. https://doi.org/10.3390/coatings12111742

Academic Editor: Devis Bellucci

Received: 13 October 2022
Accepted: 11 November 2022
Published: 14 November 2022

1. Introduction

The biocompatibility of material is one of the important indicators of the tissue repair effect. Once the material is implanted in the body, it will cause a series of cellular activities, initiate the body's immune response and lead to the formation of inflammation [1,2]. Firstly, the implanted material rapidly adsorbs proteins (such as fibrinogen, albumin and immunoglobulin G) in the blood, forming a protein coating on the surface of the material [3]. Among them, the adsorbed fibrinogen stimulates mast cells to release histamine and promotes the recruitment of macrophages to the implantation site, causing an acute inflammatory response [4]. In addition, the newly formed protein interface activates the complement system, platelets and coagulation proteins, etc., and forms blood clots around the implant, which further activate and recruit macrophages and exacerbate the inflammatory response [5,6]. Macrophages are the main phagocytic cells in the human immune system which are derived from the monocytes in bone marrow [7]. They are white blood cells with a wide range of guards in the human body. In the process of wound repair in the body, macrophages mainly play two roles. On the one hand, macrophages secrete a variety of biologically active substances and enzymes, such as polypeptide transforming growth factor and interleukin, to promote wound repair in the process of body injury. On the other hand, macrophages play a role in phagocytosis to remove tissue, cell debris and pathogens from the damaged body, which promotes the repair and healing of damage in the inflammatory stage. Macrophages are divided into many phenotypes, and different phenotypes have different or even opposite effects. Classically activated macrophages are proinflammatory phenotypes (M1 macrophages) that secrete the additional proinflammatory cytokines TNF-α, IL-1β and nitric oxide synthase (INOS) after chemokine recruitment to kill bacteria and other microorganisms [8–10], while M2 macrophages do not deliver antigens to T cells. They are activated alternately by IL-4 and IL-13 and secrete the anti-inflammatory factors IL-4 and IL-10 which have anti-inflammatory effects [11–13]. At the same time, M2 macrophages secrete the vascular endothelial growth factor (VEGF) and transforming growth factor β (TGF-β), etc., to promote the reconstruction of the extracellular matrix and tissue regeneration [13,14]. Although it is too simple to classify macrophages into M1/M2 phenotypes which cannot truly express the dynamic process of macrophages in vivo, this classification allows us to quickly understand the functions and changes in macrophages in an in vivo niche [15]. Therefore, an appropriate ratio of M1 and M2 macrophages is beneficial to obtain an appropriate immune response from the biomaterials, which not only resists the risk of infection but also promotes tissue repair and regeneration.

Mechanical cues, including physical and chemical properties, affect cell adhesion, migration, proliferation and function, such as the material mechanical properties, biodegradability, magnetic properties, surface topography, etc. [16–19]. Among them, the mechanical properties are a factor that cannot be ignored in the design of biomaterials, which refers to the performance of materials when bearing various external loads (tensile, compressive, bending, torsion, impact, alternating stress) under different environments (temperature, medium, humidity) [20]. The elastic modulus is an index of particular concern in the mechanical properties in the process of the tissue engineering of biomaterials. When a cell is in contact with a material, the elastic deformation of the material imparts stress to the cell, causing the cell to deform, thus changing the cytoskeleton and transmitting biological signals to the genetic material, ultimately presenting different biological effects. In recent years, many studies have confirmed the effect of material elasticity on cell and tissue regeneration [21,22]. Stem cells, as a kind of cell with strong proliferation and differentiation ability, have great differences in their differentiation behavior with the change in the elasticity of the extracellular matrix. [23]. Oh et al. successfully prepared a PVA/HA matrix with a gradient elastic modulus and confirmed that human bone marrow mesenchymal stem cells tend to differentiate into different types of cells on different elastic matrices through in vitro cell culture experiments (about 20 kPa for nerve cells, about 40 kPa for muscle cells, about 80 kPa for chondrocytes and about 190 kPa for osteoblasts) [24]. Although macrophages do not possess a differentiation capacity, they show diversity in the elasticity of the matrix. The elasticity of the substrate leads to the reorganization of the cytoskeleton through contact, spreading and adhesion which accounts for the differences in morphology and function [25,26]. Studies have shown that macrophages display different surface clearance and phagocytosis capabilities for submicron particles with different stiffness [27]. In addition, macrophages are more prone to polarization towards the M1 type in the condition of a high stiffness matrix [25]. However, how biomaterials with different elastic modulus affect the morphology and function of macrophages and the underlying mechanisms is rarely studied.

There are many mature biomaterial mechanical property control systems at present. The elastic modulus of material can be adjusted to the value we desire by changing the ratio of the crosslinking monomers or the degree of the crosslinking [28,29]. For example, the mechanical properties of hydrogels can be easily changed using different types and concentrations of crosslinking agents [30]. Chitosan is one of the biomaterials with safe and excellent biological properties, which is approved by the FDA and widely used in the field of tissue repair and regeneration [31]. It is the only natural cationic polysaccharide found in nature and the most abundant polymer, second only to cellulose [32]. Chitosan is obtained by the partial deacetylation of chitin and shows good biocompatibility, biodegradability, non-antigenicity and antibacterial activity [33–39]. Chitosan is not bioactive by itself;

however, blending it with bioactive ceramic, bioglasses, other bioactive polymers such as gelatin and the loading of bioactive molecules can make it the ideal composite for different tissue engineering applications [40,41]. It has been studied that the elastic modulus of chitosan gel can be altered by adjusting the degree of acetylation [42]. There have been studies involving chitosan scaffolds or gels with different mechanical properties for regulating cell growth, but there are few reports on their effects on macrophages.

In this study, chitosan scaffolds with different elasticity were prepared by freeze-drying chitosan solutions of different concentrations. The rheological properties, elastic modulus, surface morphology, water uptake and wettability of the scaffolds were measured to analyze the differences in the physicochemical properties of the scaffolds with different elastic modulus. Then, the morphological changes, polarization directions and cell viability differences of the macrophages on the chitosan scaffolds with different elastic modulus were observed using in vitro cell culture experiments. Following a morphological analysis, the proteins and molecules of the macrophages related to the polarization behavior were determined and analyzed using an enzyme-linked immunosorbent assay (ELISA) experiment, Western blot and a qPCR experiment. We tried to elucidate the differential growth behavior of the macrophages on the chitosan scaffolds with different elastic modulus as well as the intrinsic mechanism of the phenomenon through this experiment.

2. Materials and Methods

2.1. Materials and Reagents

Pharmaceutical grade chitosan (Xingcheng, Nangtong, China) was obtained from Alaskan snow crab with a deacetylation degree of about 90% and a viscosity of about 60cP. Then, chitosan was dissolved in 2% (*v*/*v*) acetic acid solution which was obtained from Honeywell. RAW 264.7 was obtained from Cell Bank of Chinese Academy of Sciences. Mouse IL-6 ELISA Kit and Mouse IL-10 ELISA Kit were both obtained from Linktech in China. In addition, 1640 medium, fetal bovine serum and penicillin–streptomycin were all obtained from Gibco. Phalloidin-iFluor 488 Reagent and DAPI were both obtained from Abcam.

2.2. Preparation of Freeze-Dried Chitosan Scaffolds with Different Elasticity

Different weights of chitosan powder were dissolved in 2% (*v*/*v*) acetic acid solution and evenly stirred to prepare chitosan solutions with different concentrations (1%, 3%, 5% and 7%). Chitosan solutions of different concentrations were added to a 24-well plate at 500 μL per well with 1 mL injections and were left for 24 h to eliminate air bubbles. After the samples were frozen at −20 °C for 12 h, they were placed in a freeze dryer (Bilang, Shanghai, China) for 24 h. Then, the freeze-dried scaffolds were soaked with 4% (*w*/*v*) NaOH solution for 4 h at a volume ratio of 1:10 to neutralize the acetic acid in the scaffolds. The samples were then washed with distilled water until neutral so that the unreacted NaOH was completely removed. Finally, freeze-dried chitosan scaffolds with different elasticity were obtained (Figure 1). Then, the scaffolds were immersed in PBS at 37 °C for reservation for the following experiments.

2.3. Characterization of Freeze-Dried Chitosan Scaffolds with Different Elasticity

2.3.1. The Rheological Analysis

First, 1 mL of 1%, 3%, 5% and 7% chitosan solutions were placed on the rheometer sample stage (Thermo Fisher Scientific, RheoWin MARS 40, Waltham, MA, USA) at room temperature, and the shear rate was set from 0 to 50 (1/s) in order that changes in viscosity of chitosan solution with the shear rate increasing could be observed.

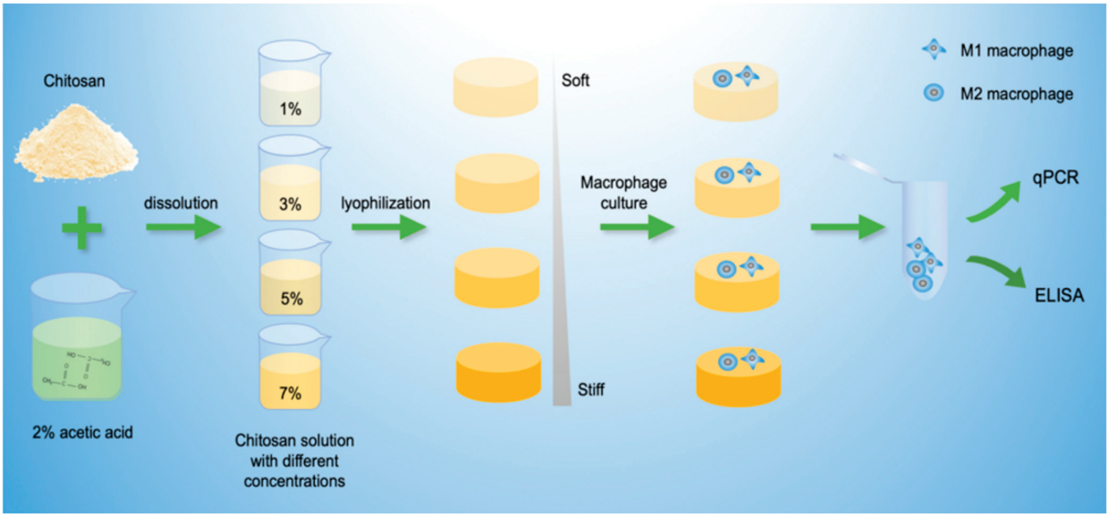

Figure 1. Schematic diagram of preparation of freeze-dried scaffolds with different elastic chitosan and study on the regulation of elasticity on macrophages.

2.3.2. Modulus of Elasticity

The freeze-dried chitosan scaffolds with diameter of 10 mm and thickness of 2 mm were placed on the sample stage of the universal electronic stretching machine (Fengtuo, Shanghai, China), and the program was set under compression mode with loading force of 100 N. The parameters of the stretching machine were set to measure the stress–strain curve of the samples. The elasticity modulus of the samples was obtained by calculating the slope of the stress–strain curve in elastic deformation stage.

2.3.3. Morphology

Next, the chitosan scaffolds were freeze-dried for 48 h in order to remove water. The secondary freeze-dried chitosan scaffolds were fixed on the stage with conductive glue, and a gold layer was sprayed on the surface of the sample. Then, scanning electron microscope (SEM, JEOL, Tokyo, Japan) was used to observe and photograph the morphology of freeze-dried chitosan scaffolds with different concentrations at high magnification.

2.3.4. Water Uptake

The freeze-dried chitosan scaffolds with diameter of 10 mm and thickness of 2 mm were freeze-dried on filter paper for a second time to remove water. Three parallel samples were taken for each concentration. The weights of the samples under the freeze-dried state were recorded as W0, and the weights of the freeze-dried scaffolds after being soaked in water for 5, 10, 20 and 30 min, and 1, 2, 4 and 8 h were recorded as W1. The formula for calculating water uptake is as follows:

$$\text{Water uptake (\%)} = (W1 - W0)/W0 \times 100$$

2.3.5. Contact Angle

Excess water of the samples was absorbed with filter paper. Then, the samples were placed on the sample stage of the contact angle measuring instrument (JY-PHA, Chengdejinhe, Chengde, China), and the microinjector with the same scale was rotated to make water droplets of the same volume. The contact angle was measured when the droplets dropped onto the surface of the scaffolds.

2.4. Biological Evaluation of Freeze-Dried Chitosan Scaffolds with Different Elasticity

2.4.1. Sterilization of Materials

The samples were soaked in 75% (v/v) ethanol for 30 min and then irradiated with a UV lamp for 30 min. Afterwards, the samples were washed with sterile water three times and rinsed with 1640 medium for use. The sterilized materials were subsequently used in cell culture experiments.

2.4.2. Cell Viability Assay

The freeze-dried scaffolds with different concentrations of chitosan were extracted with 1640 medium for 24 h at a volume ratio of 1:10 to prepare a complete medium (containing 10% fetal bovine serum, 1% penicillin–streptomycin). Mouse mononuclear macrophage leukemia cells (RAW 264.7) were seeded at 3000 cells per well in 96-well plates. After 4 h, the original medium was trashed, and 200 μL of complete medium prepared with chitosan extracts of different concentrations and normal medium as controls were added to 96-well plates. After incubation for 1 and 3 d, the culture medium in the well plates was discarded, and 200 μL of Cell Counting Kit-8 (CCK-8) solution was added to the experimental wells and blank wells and incubated in the dark for 4 h [43,44]. Then, the absorbance at 450 nm was measured with a microplate reader (Bio-Tek, Winooski, VT, USA), and the cell viability was calculated as follows:

$$\text{Cell viability (\%)} = [\text{OD(experiment)} - \text{OD(blank)}]/[\text{OD(control)} - \text{OD(blank)}] \times 100$$

2.4.3. Cell Fluorescence Staining

The RAW 264.7 cells were seeded on the sterilized scaffolds in 24-well plate at the number of 50,000 per well. After culturing for 1 and 3 days, the medium was discarded, and 500 μL of 4% paraformaldehyde was added to each well to fix cells for 1 h. Then, the paraformaldehyde was discarded, and the materials were washed three times with phosphate buffered saline (PBS). Next, 500 μL of immunofluorescence blocking solution was added to each well to block for 2 h at room temperature. Then, 200 μL of Phalloidin-iFluor 488 Reagent (Abcam, Cambridge, UK) was added at 1/1000 dilution in PBS to each well and incubated at room temperature for 90 min [45]. The materials were washed three times with PBS. Subsequently, 200 μL of DAPI (Sigma, St. Louis, MO, USA) at 1/1000 dilution in PBS was added to each well and incubated at room temperature for 10 min. The materials were washed three times with PBS, and 500μLof fluorescent mounting fluid was added per well. Then, the cells were observed and photographed under a confocal microscope (SP5; Leica, Heerbrugg, Germany).

2.4.4. ELISA

The RAW 264.7 cells were seeded on the sterilized 24-well plate at the number of 50,000 per well. Subsequently, the cell culture medium was collected after culturing for 1 and 3 days. Interleukin-6 (IL-6) and interleukin-10 (IL-10) in the culture medium were extracted and quantified according to the steps of the IL-6 and IL-10 ELISA kit (Multiscience, Hangzhou, China). The absorbance at 450 nm and 570 nm was measured using a microplate reader to determine the concentration of IL-6 and IL-10 in the culture medium.

2.4.5. Real-Time Polymerase Chain Reaction (RT-PCR) Analysis

The RAW 264.7 cells were seeded on sterilized material in a 24-well plate at a density of 100,000 per well. Then, the medium was discarded after 1 and 3 days, and 250 μL of TRI Reagent (Sigma, St. Louis, MO, USA) was added to each well to extract RNA. First strand complementary DNA (cDNA) was synthesized by reverse transcription of extracted RNA using PrimeScript RT reagent kit (Takara, Tokyo, Japan). Interleukin-1 (IL-1) was evaluated with GAPDH used as the house keeping gene. The relative expression level for each gene (fold change) was calculated usingLivak method with $2^{-\Delta\Delta Ct}$ and normalized to that of the reference gene GAPDH. The primers for RT-PCR are listed in Table 1. Relative expression was quantified using the comparative threshold method.

Table 1. Primer sequences.

Gene	Forward Primer Sequences (5′-3′)	Reverse Primer Sequences (3′-5′)
GAPDH	GCTCAGGCCTCTGCGCCCT	CCTACTCTCTTGAATACC
IL-1	GAAATGCCACCTTTTGACAGG	TGGATGCTCTCATCAGGACAG

2.5. Data Analysis

All data are expressed as means ± SEM. The *t*-test and one-way analysis of variance (ANOVA) were used to statistically analyze the data via GraphPad Prism 8. A probability (p) value less than 0.05 ($p < 0.05$) was considered as significant difference.

3. Results

3.1. The Rheological Analysis

Chitosan is a water-insoluble powder that can only be dissolved in organic or inorganic acids. Therefore, a 2% acetic acid solution was used to dissolve chitosan in this experiment, and the solutions with a chitosan concentration of 1%, 3%, 5% and 7% were successfully prepared. The rheological properties of the solutions also changed with the increase inthe chitosan content. The viscosity of the chitosan solution was characterized using a rheometer (Figure 2). In the 1% and 3% groups, the viscosity of the solution hardly changed with the change inthe shear rate (Figure 2a,b). Therefore, the viscosity of these two groups was a constant, and the solution viscosity of the 1% group and the 3% group was about 0.47 and 1.05 Pas. In the 5% and 7% groups, the viscosity of the solution significantly decreased with the increase in the shear rate which resulted from the fact that the viscosity of the solution increased with the increased content of chitosan, and the solution gradually became a non-Newtonian fluid whose viscosity was no longer a constant which meant the viscosity changed with the change in the shear rate (Figure 2c,d). However, under the same shear rate of 40 (1/s), the solution viscosity of the 5% and 7% groups was 6.78 and 22.12 Pas, respectively. Notably, the solution viscosity of the 7% group was the highest among all the groups. In general, the viscosity of the chitosan acetate solution increased with the increase in the chitosan concentration.

3.2. Modulus of Elasticity

The freeze-dried scaffolds prepared with various concentrations of chitosan solutions had different internal structures as a function of the volume ratios of chitosan and water. The internal structure of thescaffolds was directly related to the elastic modulus. The stress–strain curves of the different experimental groups in the elastic deformation stage showed that the freeze-dried scaffolds could withstand greater stress within the same strain range, which indicated that the scaffolds had a higher elastic modulus as the concentration of chitosan increased (Figure 3a). The slope of the stress–strain curves in the elastic deformation stage was calculated as the elastic modulus of the freeze-dried chitosan scaffolds (Figure 3b). The average elastic modulus of the 1%, 3%, 5% and 7% groups was 5.5, 40, 107 and 223 kPa, respectively. Therefore, the freeze-dried chitosan scaffolds with different concentrations exhibited various elastic properties and provided elastic reaction forces to the cells, which laid a foundation for the subsequent study of the effects of the elasticity of scaffolds on cell behavior and function.

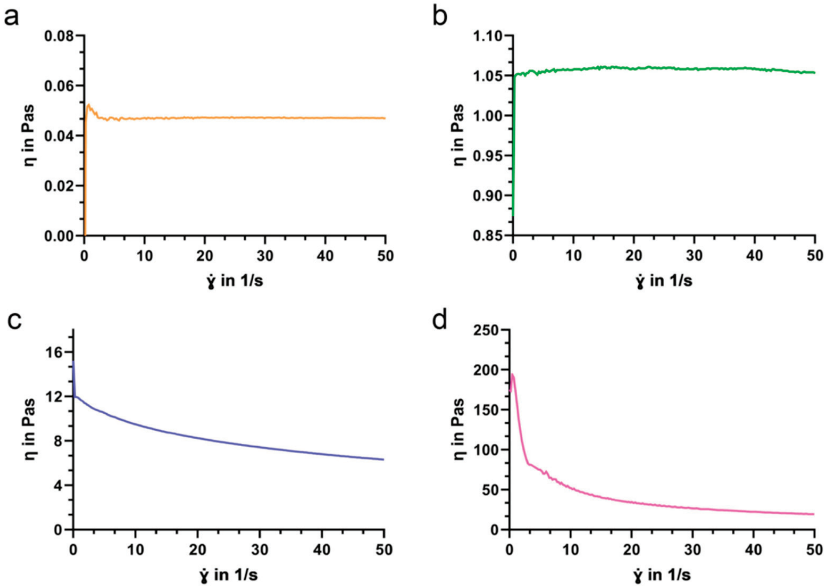

Figure 2. Rheological properties of chitosan solutions with different concentrations. (**a**–**d**) Viscosity–shear rate curve of chitosan solution with different concentrations. (**a**) 1%, (**b**) 3%, (**c**) 5%, (**d**) 7%.

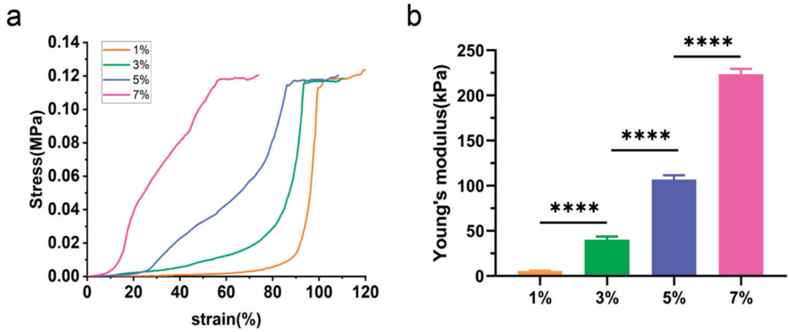

Figure 3. Stress–strain curves (**a**) and elastic modulus statistics (**b**) of freeze-dried chitosan scaffolds with different concentrations, $n = 6$, **** $p < 0.0001$.

3.3. Morphology of Freeze-Dried Scaffolds with Different Concentrations of Chitosan

Freeze-dried scaffolds are loose porous scaffolds prepared by directly subliming the water in them in a low-temperature vacuum environment after liquid freezing. The chitosan scaffolds with different concentrations have different microstructures due to their different water content. The surface and internal morphology of the freeze-dried scaffolds were observed using scanning electron microscopy (SEM) in order to explore the differences in the internal structure of the freeze-dried scaffolds (Figure 4a). The SEM images show that the chitosan freeze-dried scaffolds formed a uniform and dense pore structure inside, which satisfied the needs of the nutrient supply and material exchange for the cells. In addition, the pore size gradually became smaller, and the pore structure became more compact with the increase in the chitosan concentration (Figure 4b). The average pore size of 1%, 3%, 5% and 7% groups was 182, 148, 103 and 71 μm, respectively. The difference in the internal pore size and porosity results in the changes in the elastic modulus of the lyophilized scaffolds, which provides different sizes of support force for the macrophages.

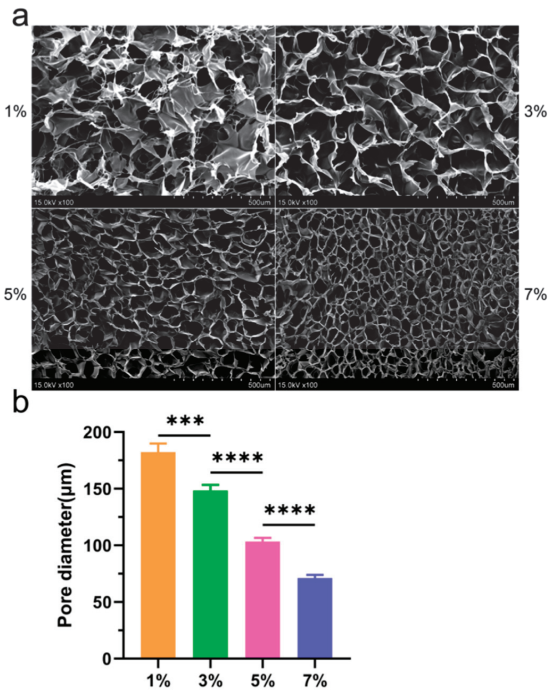

Figure 4. Cross-sectional SEM (**a**) and pore size statistics (**b**) of freeze-dried chitosan scaffolds at different concentrations, $n = 30$, *** $p < 0.001$, **** $p < 0.0001$.

3.4. Water Uptake of Freeze-Dried Scaffolds with Different Concentrations of Chitosan

The change in the internal pore size and porosity in the material will directly lead to the variation of the water uptake of the material. All freeze-dried scaffolds reached a water-saturated state after being soaked in water for ten minutes, indicating that the freeze-dried scaffolds possessed a sufficiently porous structure to provide nutrient support and substance exchange for the cells rapidly (Figure 5a). The quantitative statistics of the water uptake rate showed that the 1% group absorbed the most water and had the strongest water holding capacity under the same conditions (Figure 5b) due to its loose pore structure. The average water uptake of 1%, 3%, 5% and 7% was 3032%, 1836%, 775% and 634%, respectively, which was consistent with the previous analysis of the internal structure of lyophilized scaffolds.

3.5. Contact Angle of Freeze-Dried Scaffolds with Different Concentrations of Chitosan

The hydrophilicity of materials is one of the important aspects for the biological evaluation of biomedical materials. An appropriate surface hydrophilicity is beneficial for cell adhesion and migration. The contact angle is strong evidence that indicates the hydrophilicity status of the material. The surface contact angles of lyophilized chitosan scaffolds were measured and quantitatively analyzed in Figure 6, and the results indicate that there was no significant difference in the contact angles among the four experimental groups. Therefore, the different concentrations of chitosan in each experimental group did not affect the surface hydrophilicity of the freeze-dried scaffolds. The contact angles for all groups were in the range from 30° to 40°, confirming that the hydrophilicity may provide good interface conditions for cell adhesion and migration (Figure 6b).

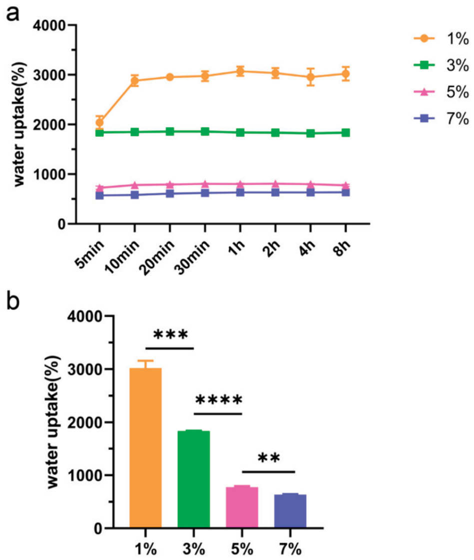

Figure 5. (**a**) Variation curve of water uptake rate of freeze-dried chitosan scaffolds with different concentrations over time, $n = 3$; (**b**) Statistical chart of water uptake rate after water saturation of freeze-dried scaffolds with different concentrations of chitosan, $n = 3$, ** $p < 0.01$, *** $p < 0.001$, **** $p < 0.0001$.

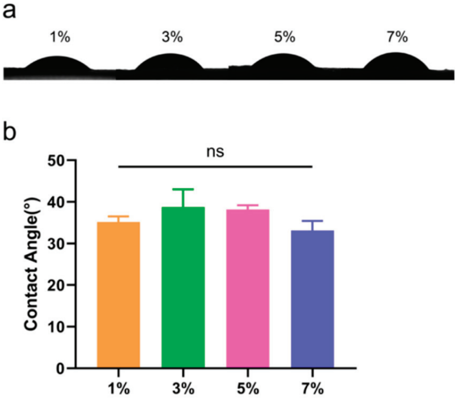

Figure 6. Hydrophilic analysis of different elastic chitosan lyophilized scaffolds. (**a**) Contact angle images of different elastic freeze-dried chitosan scaffolds; (**b**) Quantitative analysis of contact angles of different elastic freeze-dried chitosan scaffolds, $n = 6$, ns represents $p > 0.05$.

3.6. Cell Viability Assay

The freeze-dried chitosan scaffolds with various concentrations of chitosan are not only different in their physical properties but may also release soluble components into the medium which affects cell viability. Thence, the extract of the scaffolds was prepared to culture RAW cells. The CCK-8 results in Figure 7a show that there was no significant difference in the cell viability among the experimental groups at 1 or 3 days, respectively. Meanwhile the RAW cells stained with toluidine blue O (TBO) exhibited similar shapes and quantities in different groups at 1 or 3 days, respectively (Figure 7b). On the first day, most cells maintained a round shape, and the number of cells was low. By the third day, the number of cells expanded to a larger scale, and some cells became polarized with individual cells sticking out with distinct protrusions. Regardless of day 1 or 3, the cells exhibited similar cell numbers and cell morphology in the experimental groups. Therefore, the lysates of the different concentrations of the lyophilized chitosan scaffolds in the medium did not show a significant effect on cell viability and morphology. The cell viability of all experimental groups could reach more than 70% compared with the control group, indicating that the prepared chitosan scaffolds in all groups have an excellent biocompatibility.

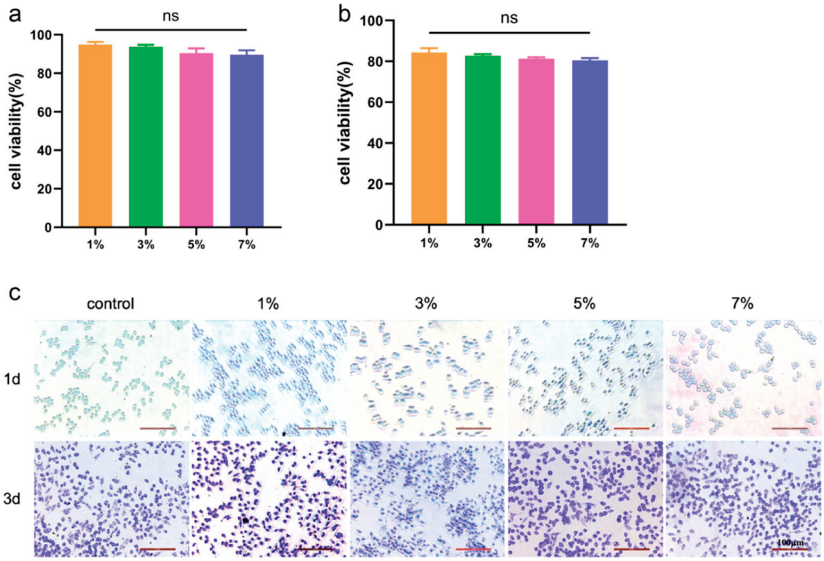

Figure 7. Effect of chitosan concentration on cell viability. RAW264.7 cells were cultured with different concentrations of chitosan freeze-dried scaffold extract, and the cell viability was measured using CCK-8 method at 1d (**a**) and 3d (**b**), $n = 8$, ns represents $p > 0.05$. Then, RAW264.7 cells were stained with TBO (**c**).

3.7. Cell Morphology

Macrophages are myeloid cells involved in the innate immune response, originating from monocyte precursors in the blood and play a key role in tissue homeostasis under normal physiological conditions as well as after tissue injury. Phagocytosis, exogenous antigen presentation and immune regulation through cytokine and growth factor secretion are its three key features. The microenvironment where macrophages are located is vital for their proliferation and migration. The chitosan freeze-dried scaffolds provide different specifications of support for the macrophages growing on the surface due to their different porosity to regulate the behavior and function of the macrophages.

On the first day of culture, the macrophages showed a differential affinity for different groups of materials (Figure 8a). The number of cells in the 5% group was significantly larger than the other three groups, while the number of cells in the 1% group was the smallest. In addition, cells in the 5% group grew in small flakes, close to the state of the cells in a Petri dish. Most of the cells in the 1% group independently grew and did not touch each other. On the third day, the cells in each group increased, and the spreading area of the cells enlarged. A few RAW cells showed obvious polarization behavior with stretching-out protrusions. Among them, the 5% group had the largest number of cells and the largest average area of cells (Figure 8b). In addition, a lot of the cells spread out in irregular shapes. Although the number of cells was more than that in day 1 in the 1% group, it was the least among the four groups, and most of the cells were spherical. Interestingly, as the chitosan concentration increased, the number and area of RAW cells decreased in the 7% group. The RAW cells showed the best proliferation and migration ability in the 5%

group, and the number and volume of cells were also the largest, while, vice versa, the 1% group was the worst.

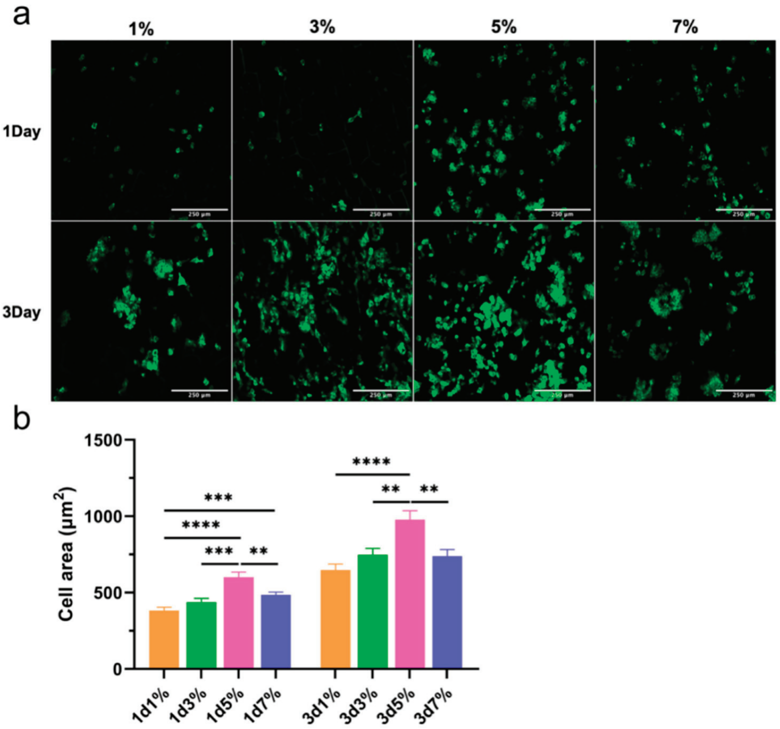

Figure 8. (**a**) RAW264.7 cells were cultured on different concentrations of chitosan freeze-dried scaffolds and stained with phalloidin. (**b**) Quantitative statistics of cell area, n = 30, ** $p < 0.01$, *** $p < 0.001$, **** $p < 0.0001$.

3.8. Pro- or Anti-Inflammatory Factors Secreted by Cells

The activation of macrophages plays a crucial role in tissue homeostasis as well as in inflammation and disease progression [46]. Macrophages can change their phenotype in response to many different stimuli, which is dynamic. In general, macrophages can be divided into classically activated M1 macrophages and alternatively induced M2 macrophages according to their function and activation. In the early stage of inflammation, classically activated M1 macrophages secrete factors, such as IL-6, which play a pro-inflammatory role. In the late stage of inflammation, alternately activated M2 macrophages secrete factors, such as IL-10, which play an anti-inflammatory role. The ELISA results show that the concentration of IL-6 decreased with the increasing stiffness of the lyophilized scaffolds on the first day. On the third day, the expression of IL-6 in the 1% group was still the highest, while it was the lowest in the 5% group (Figure 9a). The concentration of IL-6 in each group gradually increased over time. The concentration of IL-10 was generally lower than that of IL-6, and the overall trend was the opposite to that of IL-6. The 5% group had the highest IL-10 concentration on both the first and third days. When the concentration of chitosan was 1%–5%, the concentration of IL-10 increased with the elevation in the hardness of the freeze-dried scaffolds; when the concentration of chitosan was 5%–7%, the concentration of IL-10 decreased with the elevation in the hardness of the freeze-dried scaffolds (Figure 9b). Hence, the RAW cells have different polarization trends on the lyophilized scaffolds with different elasticity.

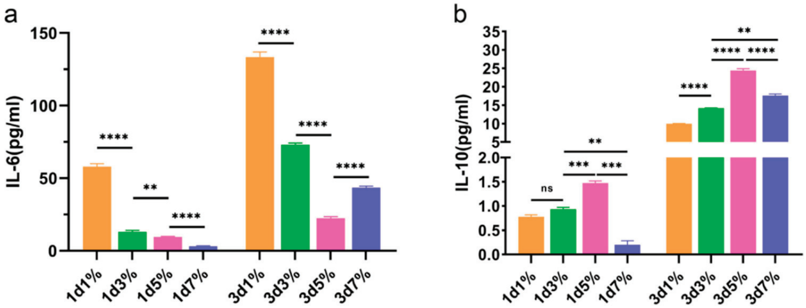

Figure 9. Concentrations of IL-6 (**a**) and IL-10 (**b**) in medium of RAW cells cultured on scaffolds at 1 and 3 days tested using ELISA, $n = 3$, ** $p < 0.01$, *** $p < 0.001$, **** $p < 0.0001$.

3.9. Gene Expression

Next, we verified the typing of the RAW macrophages in each group at the genetic level. The results of the qPCR experiment show that no matter whether it was the first or third day, the expression level of the marker IL-1 of the M1 macrophages had a gradually decreasing trend in the 1%, 3% and 5% groups, while it showed an upward trend in the 5% and 7% groups (Figure 10). The experimental results of the qPCR and ELISA show the same trend, as the IL-6 secreted by the M1 phenotype was also much higher than the IL-10 secreted by the M2 phenotype measured usingthe ELISA. Therefore, the regulation rules of the different elastic chitosan freeze-dried scaffolds on the RAW macrophages were further elaborated.

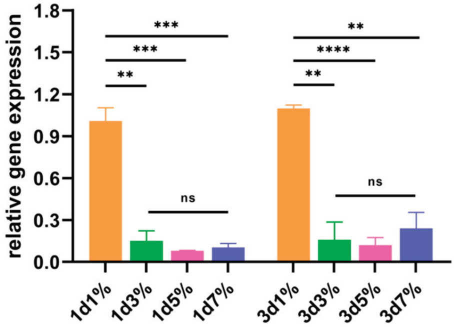

Figure 10. Real-time PCR analysis of the gene expression of the IL-1, $n = 3$, ns represents $p > 0.05$, ** $p < 0.01$, *** $p < 0.001$, **** $p < 0.0001$.

4. Discussion

The physical properties of biomaterials are increasingly becoming one of the important factors to consider when designing implants [47,48]. Cells are highly plastic, so the microenvironment created by the mechanical properties of the implant, especially the elasticity, has a profound influence on cell growth and development. Simultaneously, macrophages, as key immune cells that mediate FBR, can respond to the cellular microenvironment created by the materials and produce different degrees of inflammatory responses to the M1/M2 macrophages' polarization. The activity of macrophages against different biomaterials yields different biocompatibility outcomes. Our study intended to construct chitosan freeze-dried scaffolds with different elasticity to study the effects of biomaterials with different interface elasticity on the behavior and function of macrophages. To sum up, chitosan freeze-dried scaffolds can stimulate RAW cells to polarize in the M1/M2 direction, and the amount of polarization to the M1 type was greater than that of the M2 type. In the lower hardness range, the greater the elastic modulus of the material, the smaller the ratio of cells polarized to the M1 type and the greater the ratio of polarization to the M2 type. Conversely, in the higher hardness range, the ratio of cells polarized to the M1 type increased, while the ratio of cells polarized to the M2 type decreased.

We have built a kind of material system with a controllable elastic modulus based on chitosan because of the excellent biological properties of chitosan [35–39,49]. As a naturally occurring polysaccharide, chitosan has excellent biocompatibility and antibacterial properties and is also one of the FDA-approved biomaterials [31]. Thus, when we focus on the effects of the physical properties of the material on the cells, the cells are in a relatively healthy state so that the differences in cell behavior and function will not be masked. The CCK8 results also prove that there was no significant difference in the cell viability and proliferation ability of the leaching solution of the lyophilized scaffolds. Due to the different ratios of chitosan and water in the scaffolds prepared by freeze-drying, micropores and porosity of different sizes were produced inside the scaffolds after water sublimation (Figure 4). The freeze-dried scaffolds processed with different concentrations of chitosan are like nets woven with ropes of different thicknesses. The low concentration is a loose mesh of holes woven from thinner ropes, while the high concentration is much more like a dense mesh woven from thicker ropes. Hence, higher concentrations of chitosan lyophilized scaffolds can provide greater support to cells due to their compact structure and thicker hole walls [50–52]. These microscopic supporting forces are superimposed to the elastic modulus of the material macroscopically (Figure 3b). Consequently, the chitosan freeze-dried scaffolds give cells an interface environment with different elasticity, meanwhile other conditions keep the same. This differs from conventional hydrogel matrices because the monomer ratio or crosslinking concentration in the hydrogel is changed in order to adjust the stiffness of the hydrogel [53–55].

The experimental results show that the elasticity of the interface material plays an important role in regulating the growth of macrophages, especially the polarization behavior of macrophages. The results of the ELISA show that most cells were mainly polarized to the M1 type on the scaffold, and a few cells were polarized to the M2 type (Figure 9). The original RAW cells were mainly the M0 type, with a round or nearly round shape, while the polarized cells became larger in size and protruded several pseudopodia [56,57]. The process of cell polarization from M0 to M1 and M2 on the scaffold is similar to the physiological process of macrophages when inflammation occurs in vivo. After the material was implanted in vivo, M0 macrophages were chemotactically recruited to the implantation site through the blood circulation [57]. In the early stage of inflammation, cells are classically activated to M1 macrophages, which release various pro-inflammatory factors to kill pathogens, clean up tissue debris at the injury site and promote scar formation [11–13]. In the late stage of inflammation, macrophages are alternately activated to M2 macrophages, which release various anti-inflammatory factors, inhibit the further development of inflammation and promote extracellular matrix reconstruction and tissue regeneration [58–61]. While days 1–3 were in the early stage of inflammation, most cells on the scaffolds expressed the M1 phenotype. In particular, the degree of M1 phenotype polarization first decreased and then increased with the increase in the matrix hardness, while the M2 phenotype polarization first decreased and then increased with the increase in the matrix hardness, and the turning points were all in the 5% group. It has been reported that stiffness similar to that of collagen fibers promotes the M1 phenotype polarization, and the cells appear round. Stiffness similar to that of bone is more favorable for the M2 phenotype polarization, and the cells have a long and spindle-like shape [62]. When the elastic modulus of the Eucommiaulmoides gum (EUG)-based scaffold was reduced to the Mpa level, the RAW 264.7 increased the secretion of inflammatory cytokines which may suggest a different mechanism for macrophages in harder tissues such as articular cartilage [63]. We therefore propose that the polarizing effect of the matrix stiffness on macrophages is biphasic.

The elasticity of the matrix acts as a physical cue through the contact between cells and the matrix. When cells come into contact with the interface, integrin receptors bind to the material, forming cell–substrate anchor points [64]. Forces are transmitted from the integrin anchored at the cell–substrate sites into the cell, forming focal adhesions (FA) within the cell. Subsequently, the force is transmitted into the cell and alters the arrangement of the cellular actin skeleton through a signaling cascade. The chromatin structure in the nucleus changes accordingly and regulates the expression of genes which eventually changes the shape and function of the cell [65]. Chitosan freeze-dried scaffolds with various concentrations impart different forces to cells. The force that is delivered into cells offers intracellular forces, which are key factors in the regulation of cellular behavior and function by physical cues [66,67]. When the provided force is too small, a firm bond cannot be formed between the cells and the matrix, which reduces the intracellular force and affects the adhesion and proliferation of cells. As the hardness increases, the force provided to the cell elevates, the intracellular force becomes larger, and the function of the cell is improved. In addition to the difference in the elastic modulus, the pore size of freeze-dried scaffolds also affects cells as a topological clue [68]. When the chitosan concentration of the scaffold continues to increase, the pore size of the stent also decreases. The too-small pore size acts as a micropattern and inhibits the extension of the skeleton through spatial constraints and limiting intracellular forces. Thereby, the number and area of the RAW cells decreased in the 7% group as the restriction of the cytoskeletal stretch inhibited cell proliferation and migration (Figure 8).

Macrophages differentiated into different subtypes secrete pro-inflammatory or anti-inflammatory factors, which have profound implications for tissue repair and regeneration [11–13]. The ELISA assay shows that macrophages secreted the M1-type characteristic cytokine IL-6 and the M2-type characteristic cytokine IL-10 (Figure 9). The results of the qPCR also prove that the trend of the M1 phenotype-related gene IL-1 was also consistent with the results of the ELISA (Figure 10). That is to say, in the 1%–5% group, the pro-inflammatory factors secreted by the RAW cells gradually increased, and the anti-inflammatory factors gradually decreased. Conversely, the 5%–7% group showed the opposite trend. From this, we were inspired that the amount of pro- or anti-inflammatory factors secreted by macrophages can be modulated by controlling the stiffness of the freeze-dried scaffolds, thereby reducing the inflammatory response of the biomaterials.

5. Conclusions

In this study, we successfully developed chitosan freeze-dried scaffolds with different elastic modulus to study the effect of matrix elasticity on the behavior and function of macrophages. Through experiments, we found that the 5% concentration of the chitosan scaffold had the best effect on promoting cell proliferation. In addition, the 5% group can maximize the polarization of the macrophages to the M2 phenotype and inhibited the polarization of the macrophages to the M1 phenotype, thereby inhibiting FBR and improving the biocompatibility of the chitosan scaffolds. In addition, we found that the polarization regulation of the macrophages by the matrix stiffness was bidirectional. In the low elastic modulus range, high stiffness promotes the differentiation of macrophages towards the M2 phenotype, whereas in the high elastic modulus range, high stiffness promotes the differentiation of macrophages towards the M1 phenotype. Thus, our study may provide new insights and references for designing the elastic moduli of biomaterials for regulating immune responsiveness.

Author Contributions: Conceptualization, J.X., W.G. and Y.K.; methodology, F.L.; software, J.X.; validation, J.X., Y.K. and W.G.; formal analysis, J.X.; investigation, J.X.; resources, Y.Z.; data curation, J.X.; writing—original draft preparation, J.X.; writing—review and editing, G.L.; visualization, J.X.; supervision, Y.Y.; project administration, Y.Y.; funding acquisition, Y.Y. All authors have read and agreed to the published version of the manuscript.

Funding: The authors gratefully acknowledge the financial support of the National Natural Science Foundation of China (32230057, 32171352), the Open Project of the State Key Laboratory of Polymer Materials Engineering (Sichuan University) (sklpme2022-4-01), the Guangxi Key Laboratory of Regenerative Medicine (Guizaizhongkai202101) and the National Engineering Laboratory for Modern Silk, Soochow University (SDGC2147). 226 High-level Talent Training Project (2ndlevel, 2022).

Institutional Review Board Statement: Not applicable.

Informed Consent Statement: Not applicable.

Data Availability Statement: Not applicable.

Conflicts of Interest: The authors declare no conflict of interest.

References

1. Chen, H.; Agrawal, D.K.; Thankam, F.G. Biomaterials-Driven Sterile Inflammation. *Tissue Eng. Part B-Rev.* **2022**, *28*, 22–34. [CrossRef] [PubMed]
2. Wang, Y.J. Bioadaptability: An Innovative Concept for Biomaterials. *J. Mater. Sci. Technol.* **2016**, *32*, 801–809. [CrossRef]
3. Anderson, J.M.; Rodriguez, A.; Chang, D.T. Foreign body reaction to biomaterials. *Semin. Immunol.* **2008**, *20*, 86–100. [CrossRef] [PubMed]
4. Zdolsek, J.; Eaton, J.W.; Tang, L. Histamine release and fibrinogen adsorption mediate acute inflammatory responses to biomaterial implants in humans. *J. Transl. Med.* **2007**, *5*, 31. [CrossRef]
5. Ibrahim, M.M.; Medina, M.A.; Bond, J.; Chen, L.; Quiles, C.; Kokosis, G.; Bashirov, L.; Selim, A.; Klitzman, B.; Levinson, H. Foreign body reaction to commonly used surgical biomaterials. *Wound Repair Regen.* **2016**, *24*, A12–A13.
6. Zhou, G.Y.; Groth, T. Host Responses to Biomaterials and Anti-Inflammatory Design—A Brief Review. *Macromol. Biosci.* **2018**, *18*, 1800112. [CrossRef]
7. Wu, Y.L.; Zhang, C.H.; Teng, Y.; Pan, Y.; Liu, N.C.; Liu, P.X.; Zhu, X.; Su, X.L.; Lin, J. Propionate and butyrate attenuate macrophage pyroptosis and osteoclastogenesis induced by CoCrMo alloy particles. *Mil. Med. Res.* **2022**, *9*, 46. [CrossRef]
8. Klopfleisch, R.; Jung, F. The pathology of the foreign body reaction against biomaterials. *J. Biomed. Mater. Res. Part A* **2017**, *105*, 927–940. [CrossRef]
9. Abumaree, M.H.; Al Harthy, S.; Al Subayyil, A.M.; Alshabibi, M.A.; Abomaray, F.M.; Khatlani, T.; Kalionis, B.; El-Muzaini, M.F.; Al Jumah, M.A.; Jawdat, D.; et al. Decidua Basalis Mesenchymal Stem Cells Favor Inflammatory M1 Macrophage Differentiation In Vitro. *Cells* **2019**, *8*, 173. [CrossRef]
10. Veremeyko, T.; Yung, A.W.Y.; Anthony, D.C.; Strekalova, T.; Ponomarev, E.D. Early Growth Response Gene-2 Is Essential for M1 and M2 Macrophage Activation and Plasticity by Modulation of the Transcription Factor CEBPbeta. *Front. Immunol.* **2018**, *9*, 2515. [CrossRef]
11. Shrivastava, R.; Shukla, N. Attributes of alternatively activated (M2) macrophages. *Life Sci.* **2019**, *224*, 222–231. [CrossRef]
12. Wang, Q.; He, Z.; Huang, M.; Liu, T.; Wang, Y.; Xu, H.; Duan, H.; Ma, P.; Zhang, L.; Zamvil, S.S.; et al. Vascular niche IL-6 induces alternative macrophage activation in glioblastoma through HIF-2alpha. *Nat. Commun.* **2018**, *9*, 559. [CrossRef] [PubMed]
13. Alvarado-Vazquez, P.A.; Bernal, L.; Paige, C.A.; Grosick, R.L.; Moracho Vilrriales, C.; Ferreira, D.W.; Ulecia-Moron, C.; Romero-Sandoval, E.A. Macrophage-specific nanotechnology-driven CD163 overexpression in human macrophages results in an M2 phenotype under inflammatory conditions. *Immunobiology* **2017**, *222*, 900–912. [CrossRef]
14. Xu, X.W.; Gu, S.C.; Huang, X.; Ren, J.Y.; Gu, Y.H.; Wei, C.J.; Lian, X.; Li, H.Z.; Gao, Y.S.; Jin, R.; et al. The role of macrophages in the formation of hypertrophic scars and keloids. *Burn. Trauma* **2020**, *8*, tkaa006. [CrossRef] [PubMed]
15. Bonito, V.; de Kort, B.J.; Bouten, C.V.C.; Smits, A.I.P.M. Cyclic Strain Affects Macrophage Cytokine Secretion and Extracellular Matrix Turnover in Electrospun Scaffolds. *Tissue Eng. Part A* **2019**, *25*, 1310–1325. [CrossRef] [PubMed]
16. Di Cio, S.; Gautrot, J.E. Cell sensing of physical properties at the nanoscale: Mechanisms and control of cell adhesion and phenotype. *Acta Biomater.* **2016**, *30*, 26–48. [CrossRef] [PubMed]
17. Ye, K.; Cao, L.P.; Li, S.Y.; Yu, L.; Ding, J.D. Interplay of Matrix Stiffness and Cell-Cell Contact in Regulating Differentiation of Stem Cells. *ACS Appl. Mater. Interfaces* **2016**, *8*, 21903–21913. [CrossRef]
18. Feng, P.; Wu, P.; Gao, C.D.; Yang, Y.W.; Guo, W.; Yang, W.J.; Shuai, C.J. A Multimaterial Scaffold With Tunable Properties: Toward Bone Tissue Repair. *Adv. Sci.* **2018**, *5*, 1700817. [CrossRef]
19. Fan, D.Y.; Wang, Q.; Zhu, T.J.; Wang, H.F.; Liu, B.C.; Wang, Y.F.; Liu, Z.J.; Liu, X.Y.; Fan, D.W.; Wang, X. Recent Advances of Magnetic Nanomaterials in Bone Tissue Repair. *Front. Chem.* **2020**, *8*, 745. [CrossRef]
20. Whitehead, A.K.; Barnett, H.H.; Caldorera-Moore, M.E.; Newman, J.J. Poly (ethylene glycol) hydrogel elasticity influences human mesenchymal stem cell behavior. *Regen. Biomater.* **2018**, *5*, 167–175. [CrossRef]
21. Deng, M.; Lin, J.; Nowsheen, S.; Liu, T.Z.; Zhao, Y.C.; Villalta, P.W.; Sicard, D.; Tschumperlin, D.J.; Lee, S.; Kim, J.; et al. Extracellular matrix stiffness determines DNA repair efficiency and cellular sensitivity to genotoxic agents. *Sci. Adv.* **2020**, *6*, eabb2630. [CrossRef] [PubMed]

22. Zeng, Y.Y.; Yi, J.Y.; Wan, Z.P.; Liu, K.; Song, P.; Chau, A.; Wang, F.; Chang, Z.; Han, W.D.; Zheng, W.J.; et al. Substrate stiffness regulates B-cell activation, proliferation, class switch, and T-cell-independent antibody responses in vivo. *Eur. J. Immunol.* **2015**, *45*, 1621–1634. [CrossRef] [PubMed]
23. Lv, H.W.; Wang, H.P.; Zhang, Z.J.; Yang, W.; Liu, W.B.; Li, Y.L.; Li, L.S. Biomaterial stiffness determines stem cell fate. *Life Sci.* **2017**, *178*, 42–48. [CrossRef] [PubMed]
24. Oh, S.H.; An, D.B.; Kim, T.H.; Lee, J.H. Wide-range stiffness gradient PVA/HA hydrogel to investigate stem cell differentiation behavior. *Acta Biomater.* **2016**, *35*, 23–31. [CrossRef] [PubMed]
25. He, X.T.; Wu, R.X.; Xu, X.Y.; Wang, J.; Yin, Y.; Chen, F.M. Macrophage involvement affects matrix stiffness-related influences on cell osteogenesis under three-dimensional culture conditions. *Acta Biomater.* **2018**, *71*, 132–147. [CrossRef] [PubMed]
26. Adlerz, K.M.; Aranda-Espinoza, H.; Hayenga, H.N. Substrate elasticity regulates the behavior of human monocyte-derived macrophages. *Eur. Biophys. J. Biophys. Lett.* **2016**, *45*, 301–309. [CrossRef]
27. Lee, A.; Septiadi, D.; Taladriz-Blanco, P.; Almeida, M.; Haeni, L.; Spuch-Calvar, M.; Abdussalam, W.; Rothen-Rutishauser, B.; Petri-Fink, A. Particle Stiffness and Surface Topography Determine Macrophage-Mediated Removal of Surface Adsorbed Particles. *Adv. Healthc. Mater.* **2021**, *10*, 2001667. [CrossRef]
28. Seidlits, S.K.; Khaing, Z.Z.; Petersen, R.R.; Nickels, J.D.; Vanscoy, J.E.; Shear, J.B.; Schmidt, C.E. The effects of hyaluronic acid hydrogels with tunable mechanical properties on neural progenitor cell differentiation. *Biomaterials* **2010**, *31*, 3930–3940. [CrossRef]
29. Zhao, X.H. Multi-scale multi-mechanism design of tough hydrogels: Building dissipation into stretchy networks. *Soft Matter* **2014**, *10*, 672–687. [CrossRef]
30. Denisin, A.K.; Pruitt, B.L. Tuning the Range of Polyacrylamide Gel Stiffness for Mechanobiology Applications. *ACS Appl. Mater. Interfaces* **2016**, *8*, 21893–21902. [CrossRef]
31. Munteanu, B.S.; Paslaru, E.; Zemljic, L.F.; Sdrobis, A.; Pricope, G.M.; Vasile, C. Chitosan Coatings Applied to Polyethylene Surface to Obtain Food-Packaging Materials. *Cellul. Chem. Technol.* **2014**, *48*, 565–575.
32. Negm, N.A.; Hefni, H.H.H.; Abd-Elaal, A.A.A.; Badr, E.A.; Abou Kana, M.T.H. Advancement on modification of chitosan biopolymer and its potential applications. *Int. J. Biol. Macromol.* **2020**, *152*, 681–702. [CrossRef] [PubMed]
33. Liu, X.; Ma, L.; Mao, Z.W.; Gao, C.Y. Chitosan-Based Biomaterials for Tissue Repair and Regeneration. In *Chitosan for Biomaterials II*; Jayakumar, R., Prabaharan, M., Muzzarelli, R.A.A., Eds.; Advances in Polymer Science; Springer: Berlin/Heidelberg, Germany, 2011; Volume 244, pp. 81–127.
34. Li, J.H.; Zhuang, S.L. Antibacterial activity of chitosan and its derivatives and their interaction mechanism with bacteria: Current state and perspectives. *Eur. Polym. J.* **2020**, *138*, 109984. [CrossRef]
35. Kong, Y.; Tang, X.X.; Zhao, Y.H.; Chen, X.L.; Yao, K.; Zhang, L.L.; Han, Q.; Zhang, L.Z.; Ling, J.; Wang, Y.J.; et al. Degradable tough chitosan dressing for skin wound recovery. *Nanotechnol. Rev.* **2020**, *9*, 1576–1585. [CrossRef]
36. Li, G.C.; Xiao, Q.Z.; Zhang, L.Z.; Zhao, Y.H.; Yang, Y.M. Nerve growth factor loaded heparin/chitosan scaffolds for accelerating peripheral nerve regeneration. *Carbohydr. Polym.* **2017**, *171*, 39–49. [CrossRef] [PubMed]
37. Li, G.C.; Zhao, X.Y.; Zhang, L.Z.; Wang, C.P.; Shi, Y.W.; Yang, Y.M. Regulating Schwann Cells Growth by Chitosan Micropatterning for Peripheral Nerve Regeneration In Vitro. *Macromol. Biosci.* **2014**, *14*, 1067–1075. [CrossRef]
38. Li, G.C.; Zhao, X.Y.; Zhao, W.X.; Zhang, L.Z.; Wang, C.P.; Jiang, M.R.; Gu, X.S.; Yang, Y.M. Porous chitosan scaffolds with surface micropatterning and inner porosity and their effects on Schwann cells. *Biomaterials* **2014**, *35*, 8503–8513. [CrossRef]
39. Zhang, L.Z.; Dou, S.F.; Li, Y.; Yuan, Y.; Ji, Y.W.; Wang, Y.L.; Yang, Y.M. Degradation and compatibility behaviors of poly(glycolic acid) grafted chitosan. *Mater. Sci. Eng. C-Mater. Biol. Appl.* **2013**, *33*, 2626–2631. [CrossRef]
40. Genasan, K.; Mehrali, M.; Veerappan, T.; Talebian, S.; Raman, M.M.; Singh, S.; Swamiappan, S.; Mehrali, M.; Kamarul, T.; Raghavendran, H.R.B. Calcium-Silicate-Incorporated Gellan-Chitosan Induced Osteogenic Differentiation in Mesenchymal Stromal Cells. *Polymers* **2021**, *13*, 3211. [CrossRef]
41. Hasany, M.; Talebian, S.; Sadat, S.; Ranjbar, N.; Mehrali, M.; Wallace, G.G.; Mehrali, M. Synthesis, properties, and biomedical applications of alginate methacrylate (ALMA)-based hydrogels: Current advances and challenges. *Appl. Mater. Today* **2021**, *24*, 101150. [CrossRef]
42. Sacco, P.; Cok, M.; Asaro, F.; Paoletti, S.; Donati, I. The role played by the molecular weight and acetylation degree in modulating the stiffness and elasticity of chitosan gels. *Carbohydr. Polym.* **2018**, *196*, 405–413. [CrossRef] [PubMed]
43. Huang, T.T.; Zhou, Z.H.; Li, Q.Y.; Tang, X.X.; Chen, X.L.; Ge, Y.F.; Ling, J. Light-Triggered Adhesive Silk-Based Film for Effective Photodynamic Antibacterial Therapy and Rapid Hemostasis. *Front. Bioeng. Biotechnol.* **2022**, *9*, 820434. [CrossRef] [PubMed]
44. Tang, X.X.; Chen, X.L.; Zhang, S.M.; Gu, X.Y.; Wu, R.H.; Huang, T.T.; Zhou, Z.H.; Sun, C.; Ling, J.; Liu, M.; et al. Silk-Inspired In Situ Hydrogel with Anti-Tumor Immunity Enhanced Photodynamic Therapy for Melanoma and Infected Wound Healing. *Adv. Funct. Mater.* **2021**, *31*, 2101320. [CrossRef]
45. Li, G.C.; Li, S.J.; Zhang, L.L.; Chen, S.Y.; Sun, Z.D.; Li, S.Q.; Zhang, L.Z.; Yang, Y.M. Construction of Biofunctionalized Anisotropic Hydrogel Micropatterns and Their Effect on Schwann Cell Behavior in Peripheral Nerve Regeneration. *ACS Appl. Mater. Interfaces* **2019**, *11*, 37397–37410. [CrossRef] [PubMed]
46. Chen, Y.; Zhang, X. Pivotal regulators of tissue homeostasis and cancer: Macrophages. *Exp. Hematol. Oncol.* **2017**, *6*, 23. [CrossRef]
47. Zhou, H.Q.; Xue, Y.Z.B.; Dong, L.; Wang, C.M. Biomaterial-based physical regulation of macrophage behaviour. *J. Mater. Chem. B* **2021**, *9*, 3608–3621. [CrossRef] [PubMed]

48. Evans, N.D.; Gentleman, E. The role of material structure and mechanical properties in cell-matrix interactions. *J. Mater. Chem. B* **2014**, *2*, 2345–2356. [CrossRef]
49. Kong, Y.; Wang, D.; Wei, Q.F.; Yang, Y.M. Nerve Decellularized Matrix Composite Scaffold with High Antibacterial Activity for Nerve Regeneration. *Front. Bioeng. Biotechnol.* **2022**, *9*, 840421. [CrossRef]
50. Kumar, A.; Negi, Y.S.; Choudhary, V.; Bhardwaj, N.K.; Han, S.S. Morphological, mechanical, and in vitro cytocompatibility analysis of poly(vinyl alcohol)-silica glass hybrid scaffolds reinforced with cellulose nanocrystals. *Int. J. Polym. Anal. Charact.* **2017**, *22*, 139–151. [CrossRef]
51. Kumar, A.; Negi, Y.S.; Choudhary, V.; Bhardwaj, N.K. Fabrication of poly (vinyl alcohol)/ovalbumin/cellulose nanocrystals/nanohydroxyapatite based biocomposite scaffolds. *Int. J. Polym. Mater. Polym. Biomater.* **2016**, *65*, 191–201. [CrossRef]
52. Offeddu, G.S.; Ashworth, J.C.; Cameron, R.E.; Oyen, M.L. Multi-scale mechanical response of freeze-dried collagen scaffolds for tissue engineering applications. *J. Mech. Behav. Biomed. Mater.* **2015**, *42*, 19–25. [CrossRef] [PubMed]
53. Chen, S.; Shi, J.; Xu, X.; Ding, J.; Zhong, W.; Zhang, L.; Xing, M.; Zhang, L. Study of stiffness effects of poly(amidoamine)-poly(n-isopropyl acrylamide) hydrogel on wound healing. *Colloids Surf. B-Biointerfaces* **2016**, *140*, 574–582. [CrossRef] [PubMed]
54. Fadeev, M.; Davidson-Rozenfeld, G.; Biniuri, Y.; Yakobi, R.; Cazelles, R.; Aleman-Garcia, M.A.; Willner, I. Redox-triggered hydrogels revealing switchable stiffness properties and shape-memory functions. *Polym. Chem.* **2018**, *9*, 2905–2912. [CrossRef]
55. Wang, C.; Liu, X.; Wulf, V.; Vazquez-Gonzalez, M.; Fadeev, M.; Willner, I. DNA-Based Hydrogels Loaded with Au Nanoparticles or Au Nanorods: Thermoresponsive Plasmonic Matrices for Shape-Memory, Self-Healing, Controlled Release, and Mechanical Applications. *ACS Nano* **2019**, *13*, 3424–3433. [CrossRef]
56. Sun, Y.L.; Kuang, Y.Y.; Zuo, Z.; Zhang, J.; Ma, X.L.; Xing, X.Y.; Liu, L.Y.; Miao, Y.C.; Ren, T.; Li, H.; et al. Cellular processes involved in RAW 264.7 macrophages exposed to NPFF: A transcriptional study. *Peptides* **2021**, *136*, 170469. [CrossRef] [PubMed]
57. Shapouri-Moghaddam, A.; Mohammadian, S.; Vazini, H.; Taghadosi, M.; Esmaeili, S.A.; Mardani, F.; Seifi, B.; Mohammadi, A.; Afshari, J.T.; Sahebkar, A. Macrophage plasticity, polarization, and function in health and disease. *J. Cell. Physiol.* **2018**, *233*, 6425–6440. [CrossRef] [PubMed]
58. Baptista, D.; Teixeira, L.; van Blitterswijk, C.; Giselbrecht, S.; Truckenmuller, R. Overlooked? Underestimated? Effects of Substrate Curvature on Cell Behavior. *Trends Biotechnol.* **2019**, *37*, 838–854. [CrossRef]
59. Barbucci, R.; Lamponi, S.; Borzacchiello, A.; Ambrosio, L.; Fini, M.; Torricelli, P.; Giardino, R. Hyaluronic acid hydrogel in the treatment of osteoarthritis. *Biomaterials* **2002**, *23*, 4503–4513. [CrossRef]
60. Barth, K.A.; Waterfield, J.D.; Brunette, D.M. The effect of surface roughness on RAW 264.7 macrophage phenotype. *J. Biomed. Mater. Res. Part A* **2013**, *101*, 2679–2688. [CrossRef]
61. Martin-Cofreces, N.B.; Sanchez-Madrid, F. Sailing to and Docking at the immune Synapse: Role of Tubulin Dynamics and Molecular Motors. *Front. Immunol.* **2018**, *9*, 1174. [CrossRef]
62. Hersel, U.; Dahmen, C.; Kessler, H. RGD modified polymers: Biomaterials for stimulated cell adhesion and beyond. *Biomaterials* **2003**, *24*, 4385–4415. [CrossRef]
63. Jansen, L.E.; Amer, L.D.; Chen, E.Y.T.; Nguyen, T.V.; Saleh, L.S.; Emrick, T.; Liu, W.F.; Bryant, S.J.; Peyton, S.R. Zwitterionic PEG-PC Hydrogels Modulate the Foreign Body Response in a Modulus-Dependent Manner. *Biomacromolecules* **2018**, *19*, 2880–2888. [CrossRef] [PubMed]
64. Sit, S.T.; Manser, E. Rho GTPases and their role in organizing the actin cytoskeleton. *J. Cell Sci.* **2011**, *124*, 679–683. [CrossRef] [PubMed]
65. Hou, Y.; Xie, W.Y.; Yu, L.X.; Camacho, L.C.; Nie, C.X.; Zhang, M.; Haag, R.; Wei, Q. Surface Roughness Gradients Reveal Topography-Specific Mechanosensitive Responses in Human Mesenchymal Stem Cells. *Small* **2020**, *16*, 1905422. [CrossRef]
66. Yanakieva, I.; Erzberger, A.; Matejcic, M.; Modes, C.D.; Norden, C. Cell and tissue morphology determine actin-dependent nuclear migration mechanisms in neuroepithelia. *J. Cell Biol.* **2019**, *218*, 3272–3289. [CrossRef]
67. Yao, X.; Peng, R.; Ding, J.D. Cell-Material Interactions Revealed Via Material Techniques of Surface Patterning. *Adv. Mater.* **2013**, *25*, 5257–5286. [CrossRef]
68. Liu, W.; Sun, Q.; Zheng, Z.L.; Gao, Y.T.; Zhu, G.Y.; Wei, Q.; Xu, J.Z.; Li, Z.M.; Zhao, C.S. Topographic Cues Guiding Cell Polarization via Distinct Cellular Mechanosensing Pathways. *Small* **2022**, *18*, 2104328. [CrossRef]

coatings

MDPI

Article

Selective Detection of Fe^{3+} by Nitrogen–Sulfur-Doped Carbon Dots Using Thiourea and Citric Acid

Heng Zhou †, Ying Ren *,†, Zheng Li, Weichun He and Zhengxin Li *

Engineering and Technology Research Center of Diamond Composite Materials of Henan, School of Materials Science and Engineering, Henan University of Technology, Zhengzhou 450001, China; zhouheng19980428@163.com (H.Z.); li_2863925189@163.com (Z.L.); weichun_he@haut.edu.cn (W.H.)
* Correspondence: ying_ren@haut.edu.cn (Y.R.); zhengxin_li@haut.edu.cn (Z.L.)
† These authors contributed equally to this work.

Abstract: The quantum yield and fluorescence properties of carbon dots are key issues for environmental detection. In this study, nitrogen–sulfur-doped carbon dots (N,S-CDs) were prepared hydrothermally by adding thiourea to provide the N source. By adjusting the ratio of citric acid (CA) to thiourea (N,S) and adding anhydrous ethanol, blue fluorescent doped carbon dots with a quantum yield of up to 53.80% were obtained. The particle morphology and crystalline organization of the N,S-CDs were analyzed using transmission electron microscopy (TEM) and X-ray diffraction (XRD). Fourier transform infrared (FTIR) spectroscopy was used to illuminate distinct functional units through the recording of typical vibration bands. The luminescence properties of the N,S-CDs were investigated using ultraviolet–visible (UV-vis) absorption spectroscopy and steady-state fluorescence spectroscopy (PL). In addition, the fluorescence stability of the N,S-CDs was studied in detail. The results showed that the functional groups of the N,S-CDs chelate Fe^{3+} ions to quench the fluorescence of carbon dots. This shows that the N,S-CDs exhibit high selectivity for Fe^{3+} ions. With the addition of Fe^{3+} in the concentration of 0–100 μM, the fluorescence intensity of the N,S-CDs exhibited distinct and linear dependence upon the Fe^{3+} concentration ($R^2 = 0.9965$), and the detection limit ($D = 3\sigma/m$) was measured as 0.2 μM. The excellent optical properties and Fe^{3+} selectivity of the N,S-CDs provide a huge boost for application in the field of environmental monitoring.

Keywords: nitrogen and sulfur doping; fluorescence intensity; carbon dots; fluorescence probe; Fe^{3+} detection

Citation: Zhou, H.; Ren, Y.; Li, Z.; He, W.; Li, Z. Selective Detection of Fe^{3+} by Nitrogen–Sulfur-Doped Carbon Dots Using Thiourea and Citric Acid. *Coatings* **2022**, *12*, 1042. https://doi.org/10.3390/coatings12081042

Academic Editor: Ana-Maria Lepadatu

Received: 3 June 2022
Accepted: 18 July 2022
Published: 22 July 2022

1. Introduction

Iron, one of the essential trace elements for all living organisms, has little toxicity to humans and animals, but an excess amount of Fe^{3+} will lead to imbalanced human homeostasis and cause symptoms such as chronic poisoning, which seriously affect the healthy development of the human body [1–3]. In the water system, Fe^{3+} accumulates in organisms through the food chain and cannot be directly degraded. In vivo, Fe^{3+} can be transformed into a more toxic form or can directly interfere with metabolic processes [4–7]. When the concentration of Fe^{3+} in water is 0.1–0.3 mg/L [8], it will affect the color, smell, and taste of the water. Moreover, some special industries have higher requirements for iron content in water, such as the textile [9], paper [10], brewing [11], and food industries [12]. Therefore, under the condition of strictly controlling the Fe^{3+} content, researchers need to strictly detect Fe^{3+} in water resources [4–7].

Therefore, how to quickly and accurately detect Fe^{3+} in the environment has always attracted much attention [13]. At present, there are many detection methods for Fe^{3+}, including potential voltammetry [14], atomic absorption spectrometry [15], and colorimetric methods [16]. However, most of these testing methods require expensive tools or instruments, and the more complex testing processes also put forward higher technical requirements for sample processing and operation. In recent years, with the maturity of fluorescent carbon dot detection technology, it has been widely applied to detect the concentration of Fe^{3+} due to its advantages of simple and low-cost preparation [17,18], high sensitivity [19], instantaneous response, and the specific recognition of metal ion [20–22].

As new carbon nanomaterials, carbon dots have a large number of hydrophilic functional groups on the surface, which allow them to have good water solubility and excellent fluorescence properties. At present, there are two commonly used methods for the synthesis of carbon dots, namely microwave-based synthesis and hydrothermal synthesis. For microwave-assisted methods, the advantage is that they can quickly synthesize carbon dots. For example, Chen et al. [23] rapidly synthesized 12.45% QY carbon dots in 4 min utilizing a mixture of glutamic acid and ethylenediamine, which specifically responds to Fe^{3+} in the linear range of 8–80 μM. It has been successfully applied to the detection of Fe^{3+} in fungal cells due to its detection limit of 3.8 μM and its good water solubility. However, compared to the hydrothermal method, the linear range and detection limit can be further improved by using a simpler hydrothermal method to synthesize doped carbon dots, as reported in references [24–28].

Muhammad et al. [24] used cranberry beans to prepare carbon dots with a detection limit of 9.55 μM in the linear range of 30–600 μM Fe^{3+}, and Fe^{3+} ion detection could be achieved in a short time. The carbon dots prepared by Zhu et al. presented a detection limit of 0.45 μM in the concentration range of 0–60 μM [25]. These carbon dots that were synthesized using a hydrothermal method have a better detection range and detection limit than the microwave method. On the basis of these studies, a great deal of effort is devoted to improving the detection limit and range by changing the raw materials. Pu et al. [26] used phenylalanine as a nitrogen source and a common carbon source to prepare carbon dots. The results showed that Fe^{3+} combined with oxygen-containing functional groups outside of carbon dots formed static quenching, and Fe^{3+} combined with the induced carbon dots performed selective quenching. The carbon dots have a linear relationship with relative strength in the detection range of 5–500 μM, and the detection limit is as low as 0.720 μM. However, on the original basis, by using an environmentally friendly carbon source, that is, changing the type of carbon source, carbon dots with a QY of 28.6% and a lower detection limit of 0.398 μM were successfully prepared [27]. Through the analysis of the quenching mechanism, it was found that the carbon dots have an obvious selective quenching effect on Fe^{3+}, and they also showed a good linear relationship in the range of 0–100 μM. Huang et al. reported the preparation of 8.6% QY copper nanocarbon dots (Cu-NCs) using glutathione as a stabilizer [28]. The nanocarbon dots were in the Fe^{3+} concentration range of 1–100 μM, the fluorescence of Cu-NCs was linearly quenched, the detection limit was 0.3 μM, and the nanocarbon dots were available for the detection of Fe^{3+} in real water samples. All of this proves that the detection of Fe^{3+} by carbon dots has the characteristics of high efficiency, reliability, and high selectivity, which can make it widely used in the field of environmental monitoring. However, due to the high detection limit and low-fluorescence quantum yield, carbon dots still cannot be widely used as sensors for the detection of ions in food and production.

In this work, we aimed to synthesize nitrogen–sulfur-doped carbon dots (N,S-CDs) with high fluorescence intensity and fluorescence quantum yield using a hydorthermal method (as shown in Figure 1) and utilizing a mixed citric acid, thiourea, and ethanol solution that can provide heteroatomic sulfur, amino, and hydroxyl functional groups during the synthesis process. The synthesized carbon dots had good water solubility, photostability, a high quantum yield, a specific response to Fe^{3+} ions, and high selectivity, which enable the carbon dots to be successfully applied in the field of environmental monitoring.

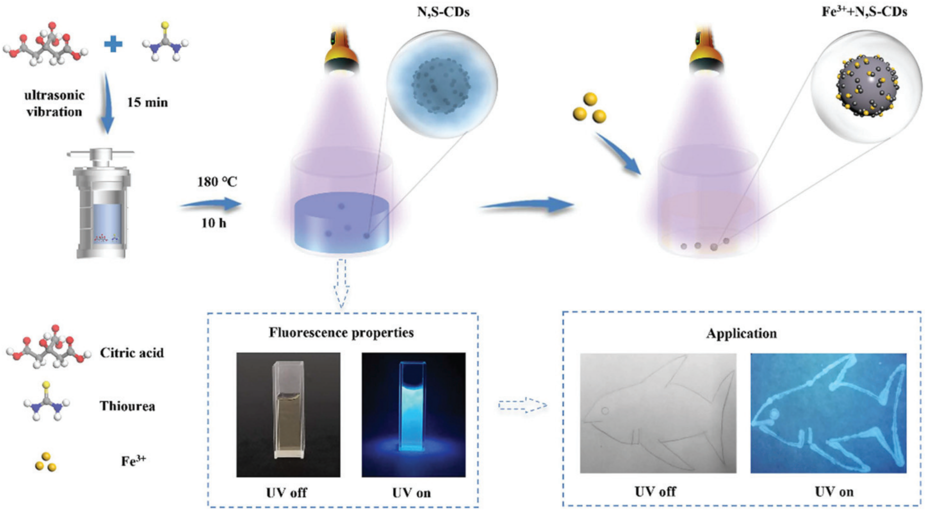

Figure 1. Schematic diagram of the preparation and application of N,S-CDs and their application in Fe^{3+} sensing.

2. Experimental Section

2.1. Materials

All metal ion salts were analytically pure, including NaCl, KCl, $Ba(NO_3)_2$, $Bi(NO_3)_2$, $ZnCl_2$, $MgCl_2$, $Al(NO_3)_3$. The compounds $9H_2O$, $Co(NO_3)_2$, $AgNO_3$, $FeCl_3$, $Pb(NO_3)_2$, and $CuSO_4$ were all obtained from Aladdin. Citric acid monohydrate, thiourea, dialysis membrane (MWCO 1000 Da), and quinine sulfate (98%) were purchased from Aladdin (Shanghai, China). The water used in all experiments was deionized water.

2.2. Instruments

The fluorescence and UV spectra were determined by using a fluorescence spectrometer (Hitachi, Tokyo, Japan) and a UVprobe2.70 UV-Vis spectrophotometer (Shimadzu Corporation, Shimadzu, Japan). The FTIR spectra were determined by using an IS20 Fourier Transform Infrared Spectrometer (Thermo Fisher Scientific, Shanghai, China). A drop of an aqueous solution containing N,S-CDs was dropped into the KBr particles, and after the water had evaporated, the particles were used to measure the FTIR spectrum (Thermo Fisher Scientific, Shanghai, China). XRD pictures were obtained using a MINIFLEX 600 benchtop X-ray diffractometer (Rigaku MiniFlex, Jiangsu, China). Transmission electron microscopy (TEM, Thermo Fisher, Shanghai, China) graphics were acquired on a FEI Tecnai G2 F20 high-resolution transmission electron microscope.

2.3. Preparation of N,S-CDs

Citric acid (CA) and thiourea (N,S) were first dissolved in a 10 mL absolute ethanol solution with the different substance ratios (2:1, 1:1, 1:2, 1:3, 1:4) and then were treated via ultrasonic dispersion for 10 min. The mixture was then added to the liner of a 50 mL Teflon reactor and heated at 180 °C for 12 h. The product obtained from the reaction was placed at room temperature for a period of time. The room temperature product was placed in a centrifuge (10,000 rpm, 30 min) to obtain the supernatant, and the filtrate containing the N,S-CDs was collected by filtration through a 0.22 μm syringe filter 2–3 times. Finally, the filtrate was put into a bag with a dialysis function (Mw = 1000 Da) for 3 days; the water was changed every 5 h to remove impurities; and the N,S-doped carbon dot products were acquired. In order to meet the needs of characterization, e.g., XRD, the sample needed to be prepared as a solid, and the method was as follows: the solution was placed in the cold trap of a freeze dryer to freeze, and freeze-drying was performed to obtain a solid powder product.

2.4. Fluorescence Quantum Yield Determination

The fluorescence quantum yield was calculated using the reference method in [29,30]. Quinine sulfate was dissolved in 0.1 M sulfuric acid to obtain a quinine sulfate solution as a standard solution. The quantum yield was 0.54 at excitation wavelengths of 340 nm and 360 nm. The quantum yield of doped carbon dots is calculated as

$$QY_S = QY_R \times (F_S/F_R) \times (A_R/A_S) \times (N_S^2/N_R^2)$$

where QY indicates the fluorescence quantum yield, F indicates the fluorescence integral area at the excitation wavelength, A represents the absorbance (required to be kept at 0.05 or below), N indicates the refractivity of the solution, and the subscripts of S and R represent the carbon point solution and the quinine sulfate solution, respectively.

2.5. Detection of Fe^{3+} Ions

$FeCl_3$ was used as the ion detection source, and differently weighted volumes were used. A 10 mL volumetric flask had 1 mM of Fe^{3+} solution and 2 mL of carbon dot dialysate. Ultrapure water was used to dilute the solution to the calibration line. The final concentrations of diluted Fe^{3+} were 0, 10, 20, 30, 40, 50, 60, 70, 80, 90, 100, 200, 300, 400, 500, and 600 μM. After shaking the volumetric flask up and down, the fluorescence intensity was measured at room temperature, and the process was repeated.

2.6. Selective Detection of Metal Ions

Under the same conditions as Fe^{3+} ion detection, 12 kinds of 1 mM metal ion solutions (Ag^+, Ba^{2+}, Bi^{2+}, Co^{2+}, Cu^{2+}, Fe^{3+}, Pb^{2+}, Na^+, Zn^{2+}, Al^{3+}, K^+, Mg^{2+}) and 1 mL of carbon dot solution were mixed to prepare the test stock solution with a metal ion concentration of 500 μM. The metal ion selectivity experiments were performed at room temperature with 11 replicates for each set of experiments, and standard deviation error bars were calculated. In addition, after the determination of ion selectivity, stability testing was carried out. For example, under the premise of the same concentration of N,S-CDs, the addition of different concentrations of NaCl solution and pH was conducted to explore the stability of the N,S-CDs. Relative ratio (F/F_0) of the fluorescence emission intensities of the N,S-CDs in the presence and absence of metal ions was used to indirectly indicate the stability of the N,S-CDs.

2.7. Real Samples Measurement

To evaluate the feasibility of Fe^{3+} carbon spot detection in real samples, tap water samples obtained in our laboratory were analyzed using this method. All water samples were spiked with different concentrations of Fe^{3+} without any pretreatment, including the real samples and the N,S-CD probes. To examine the practical application of carbon dots, we analyzed the tap water samples obtained in our laboratory using spiked recovery. The collected water samples were treated with 0.22 μm filter membrane, and different concentrations of Fe^{3+} were added to the real samples and the N,S-CD probes. Finally, the fluorescence emission spectra were recorded at the excitation wavelength of 360 nm for all samples.

3. Results and Discussion

3.1. Structure and Characterization of Carbon Dots

Using citric acid as a carbon source and thiourea as a nitrogen and sulfur source, high-QY fluorescent N,S-CDs were prepared by a one-step hydrothermal reaction. The morphology and particle size of the synthesized carbon dots were characterized by TEM. The TEM image in Figure 2a shows that the N,S-CDs are uniform in size, approximately spherical, and have good dispersion. As can be seen from the inset of Figure 2a, the size distribution of the N,S-CDs is between 5 and 7 nm. As shown in Figure 2c, the XRD diagram exhibits a peak trend of the carbon dots, with a peak at $2\theta = 26.3^{\circ}$, which corresponds to the (002) graphitic carbon diffraction curve and also corresponds to the lattice spacing of 0.21 nm (Figure 2b) [31,32]. Moreover, infrared spectroscopy (FTIR) was used to analyze the surface functional groups of the N,S-CDs to determine their water solubility. As shown in Figure 2d, which is from the perspective of the infrared spectrogram, the stretching vibration peak of C=S at 2064 cm^{-1} increases with the decrease in the CA:NS ratio [33], and the stretching vibration peak of C=C [10–12] at 1412 cm^{-1} also increases with the decrease in the ratio. Both functional groups are chromogenic groups, which affect the fluorescence emission of carbon dots. Moreover, the stretching vibration of O−H [15–17] at 3451 cm^{-1}, the stretching vibration of N–H [15–17] in –NH$_2$ at 3162 cm^{-1}, and the stretching vibration of C−N [22,26] at 1224 cm^{-1} all provide the basis for the fluorescence properties of the auxochrome-based carbon dots. These are hydrophilic groups, which provide the carbon dots with good water solubility [21]. The change in the amide C=O's [27] bending vibration peak at 1715 cm^{-1} gradually changed from a single peak to a double peak, which may be due to the structural changes caused by the changes in the amide reaction during product synthesis and may affect the fluorescence properties of the carbon dots. Combined with infrared spectroscopic analysis, it was shown that the N and S atoms were co-doped in the carbon dots in the form of functional groups, and functional groups such as hydroxyl, carboxyl, and amide groups existed on the surface of the N,S-CDs. These results are similar to those of many other reported CDs [18–27] and demonstrate that the prepared fluorescent products are CDs and have good water solubility.

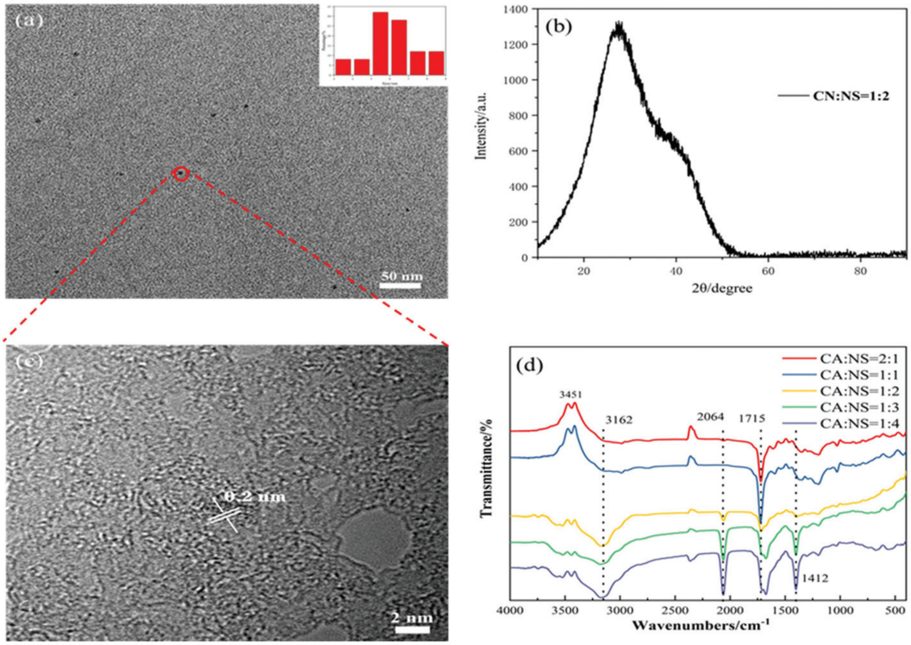

Figure 2. TEM and particle size distribution (**a**), XRD (**b**), lattice spacing (**c**), and IR spectrum (**d**) of N,S-CDs.

3.2. Optical Properties of Carbon Dots

The optical properties of the N,S-CDs were studied using UV-vis and fluorescence spectra. From the UV-Vis absorption spectrum in Figure 3b, the shoulder peak around 245 nm is due to the $\pi \rightarrow \pi^{*}$ energy transition of conjugated C=C hybridization, which confirmed the formation of a ring reaction and the formation of heterocyclic structure in the amidation process [24]. The peak around 345 nm is related to the n→π* energy transition of C=O/C−O generated by the "surface band". This peak produces strong fluorescence emissions due to the electron holes (surface states) on the surface of the carbon dots that capture and release the excited-state energy [24].

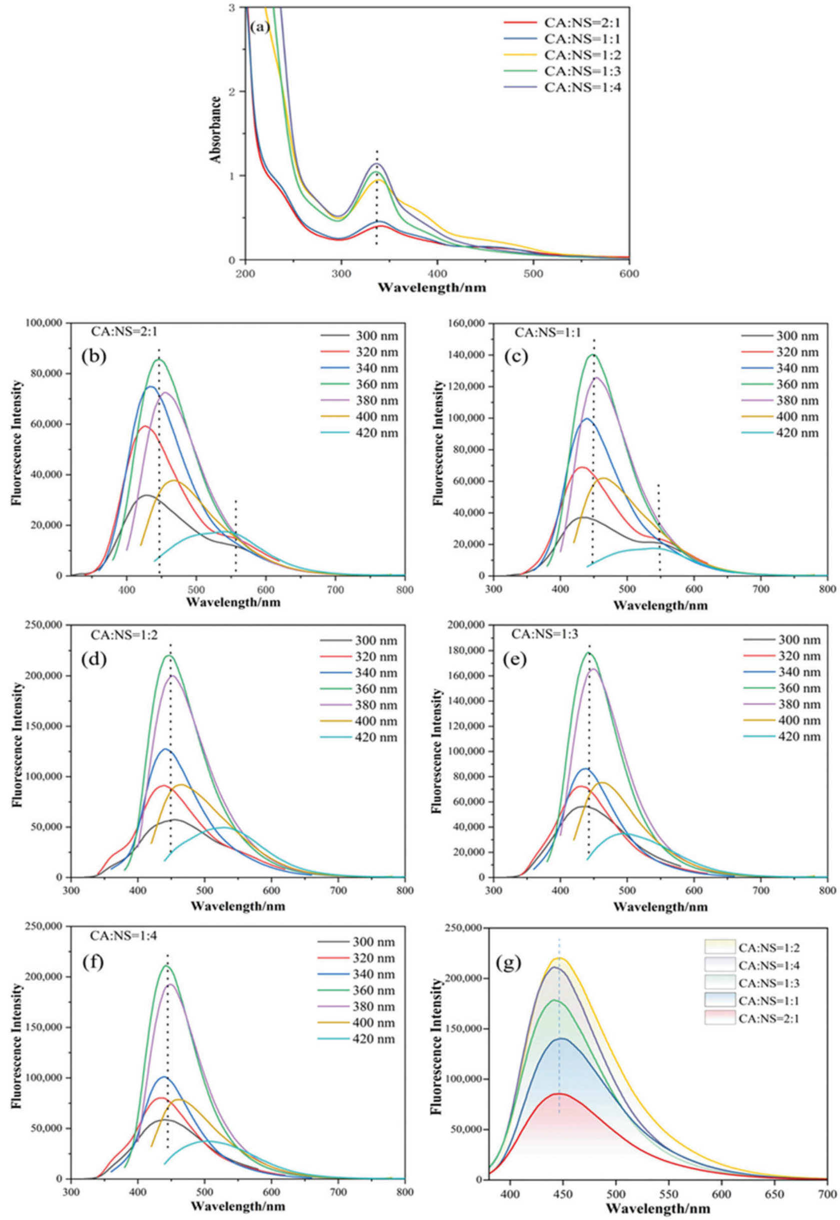

Figure 3. UV-Vis absorption spectra of different components of N,S-CDs (**a**), fluorescence emission spectra (**b**–**f**) at different excitation wavelengths from 300 to 420 nm, and emission spectra of each component at the optimal excitation wavelength of 360 nm (**g**).

In this experiment, the optical properties of the N,S-CDs were further characterized by measuring the fluorescence spectra of the N,S-CDs. The results of the fluorescence spectra of the N,S-CDs with different CA:NS ratios are shown in Figure 3b–f. It can be seen from the figure that with the change in the excitation wavelength from 300 nm to 400 nm, the fluorescence emission intensity first goes up and then comes down, and the characteristic emission peak of the N,S-CDs is obviously red-shifted. This indicates that different proportions of the N,S-CDs have obvious excitation light dependence. As can be seen in Figure 3b–f, different N,S-CDs all have the same optimal excitation wavelength, which is 360 nm. At the excitation wavelength of 360 nm, their corresponding emission peaks (445 nm, 447 nm, 450 nm, 445 nm, and 443 nm) are all in the blue emission range. Furthermore, in Figure 2b,c, there is a weak peak at 550 nm, which appears as a green fluorescence emission. However, at this time, the maximum emission peak of the N,S-CDs is around 450 nm, corresponding to the blue fluorescence emission, which overlays the green fluorescence emission, eventually leading to the blue fluorescence emission of the carbon dots. From the conclusions in these figures, it is inferred that the position of the starting emission peak is related to the excitation wavelength, and the emission peak has a red-shift phenomenon at different excitation wavelengths. These phenomena are induced by specific surface defects of the NS-CDs near the Fermi level, which can be illustrated by the IR spectra [26,34].

The optimal excitation wavelength of the N,S-CDs was determined to be 360 nm in Figure 3b–f. Figure 3g demonstrates the emission spectra of carbon dots with different doping ratios at the excitation wavelength of 360 nm. It was found that when the ratio of CA:NS was 1:2, the fluorescence intensity of the N,S-CDs was the highest. This is due to the unsaturated bond chromophore groups on the surface of the N,S-CDs, namely C=C and C=O, which lead the N,S-CDs to emit fluorescence under ultraviolet and visible light, and the fluorescence intensity is under the joint influence of the auxochrome group and the chromophore group. This resulted in the best fluorescence intensity at the ratio of 1:2.

3.3. Fluorescence Quantum Yield of Carbon Dots

It can be seen from the graph of the yield variation in each component in Figure 4 that with the decrease in the CA:NS ratio, the yield does not increase linearly, but presents an arched bridge trend, which first increased and then decreased with the increase in NS content. The maximum yield was achieved when the CA:NS ratio was 1:2, which was 53.80% (when the excitation wavelength was 360 nm), corresponding to the fluorescence emission intensity map in Figure 3g. The reason for this is that during the reaction of citric acid and thiourea, a large number of chromophore groups and auxochrome groups were generated on the surface of the carbon dots, and the surface oxidation degree was high, which affected the change in the fluorescence yield.

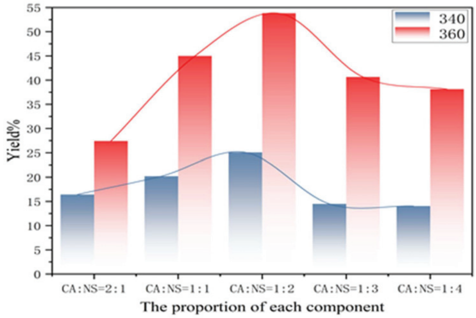

Figure 4. Variation in fluorescence yield in each component at excitation wavelengths of 340 and 360 nm.

3.4. Stability of Carbon Dots

For the purpose of exploring the stability of carbon dots, the carbon dots were first mixed with NaCl standard solution to make the final concentration of 0–2 mol/L. The influence of the NaCl standard solution concentration on the fluorescence intensity of the N,S-CDs is displayed in Figure 5a. F and F_0 represent the fluorescence emission intensities of the N,S-CDs in the presence and absence of metal ions, respectively. With the increase in the solution concentration, the fluorescence intensity of the N,S-CDs did not change much, which indicated that the N,S-CDs could exist stably in a high-concentration ionic environment. In addition, to further understand the stability of the carbon dots, the carbon dot solution was placed in different pH buffer solutions of pH 2–12, as shown in Figure 5b, which is the altered trend of the pH on the fluorescence intensity. From this, we can see that the fluorescence intensity of the N,S-CDs is about two times higher when the pH values are 6 and 7 than it is at pH 2 and pH 8–12. With the decrease in the pH value from 7 to 2 and the increase in acidity, the fluorescence intensity of the carbon dots weakened; as the pH increased from 7 to 12 and the alkalinity increased, the fluorescence intensity decreased significantly between 7 and 8 and then decreased slowly with the increase in the pH, demonstrating that the N,S-CDs have good fluorescence in neutral and weakly acidic environments. The luminescence intensity at the excitation wavelength of 360 nm was recorded as the photostability of the N,S-CDs under long-term storage at room temperature. As displayed in Figure 5c, with the passage of time at room temperature, the luminescence intensity of the carbon dots fluctuated up and down very little, demonstrating that the carbon dots have good photostability. In summary, the experiments show that the N,S-CDs have good stability.

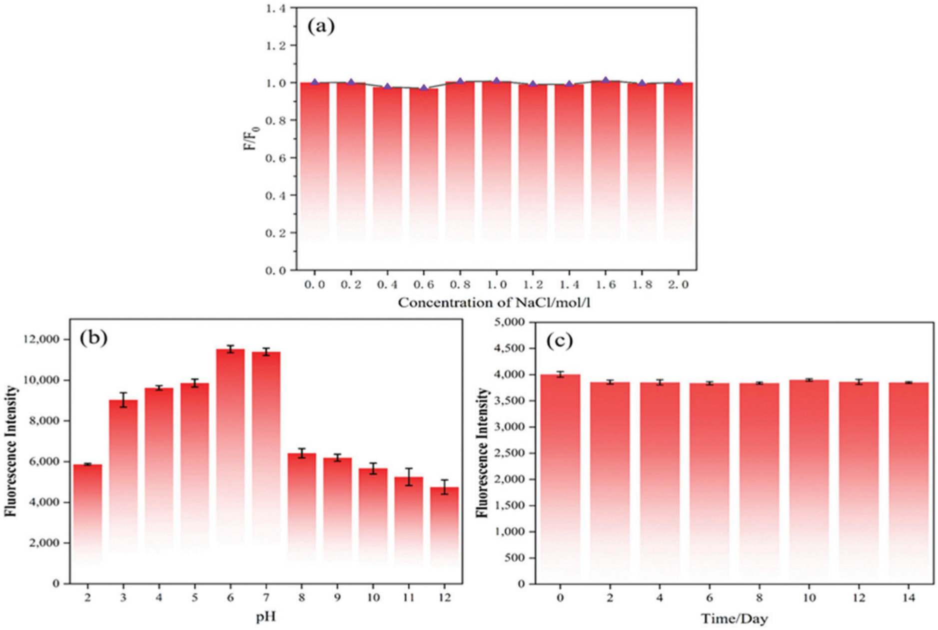

Figure 5. Effects of pH (**a**), NaCl solution concentration (**b**), and time (**c**) on fluorescence intensity of nitrogen–sulfur-doped carbon dots.

3.5. Metal Ion Selectivity

In order to evaluate the selective sensing ability and anti-interference ability of the N,S-CDs regarding metal ion selectivity, the fluorescence emission intensities of the N,S-CDs in the presence of different metal ions were investigated. Figure 6a illustrates the relative luminescence emission intensity (F/F_0) of the metal ions at a concentration of 500 μM when the excitation wavelength is 360 nm. F and F_0 are the fluorescence emission intensities of the N,S-CDs in the presence and absence of metal ions. Different metal ions have different effects on the fluorescence intensity of the N,S-CDs. From the bar chart of the N,S-CDs mixed with metal ions (Figure 6a), it can be seen that the addition of Fe^{3+} resulted in a significant decrease in the luminous intensity of the carbon dots and that the quenching was as high as 80%. Because the fluorescence intensity of other metal ions experienced no change or little change, the influence can be ignored. This shows that the prepared N,S-CDs have a stronger affinity for Fe^{3+} and can have good selectivity to Fe^{3+}. Figure 6b indicates the effect of adding Fe^{3+} on the relative fluorescence emission intensity (F/F_0) of the mixture system of metal ions and N,S-CDs. It can be seen from the bar chart (Figure 6b) that the addition of Fe^{3+} into the mixed system can still reduce the fluorescence intensity of the N,S-CDs to the greatest extent and that other metal ions cannot affect the quenching effect of Fe^{3+} on the N,S-CDs. This proves that the prepared N,S-CDs have good ionic anti-interference ability.

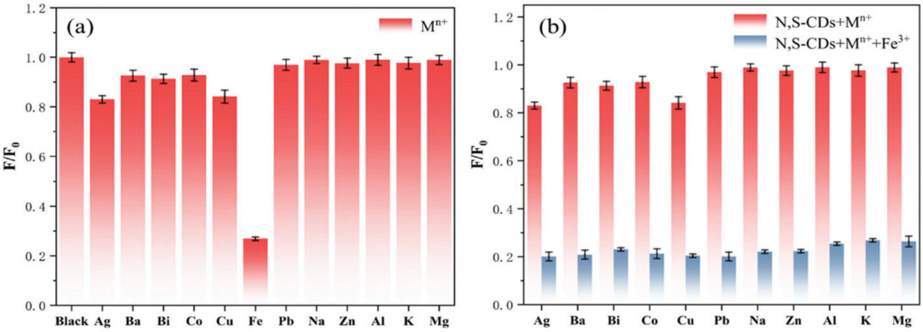

Figure 6. Selectivity (**a**) and anti-interference ability (**b**) of nitrogen–sulfur-doped carbon dots for different ions.

3.6. Linear Analysis of Carbon Dots on Fe^{3+}

The linear analysis of Fe^{3+} can be continued by using the stability of the N,S-CDs mentioned above. As displayed in Figure 7a,b, the relative fluorescence intensity changes and fluorescence intensity diagrams of the nitrogen–sulfur-doped carbon dots with various concentrations of Fe^{3+} (0, 10, 20, 30, 40, 50, 60, 70, 80, 90, 100, 200, 400, 500, and 600 μM) are described. This can clearly show that when the concentration of Fe^{3+} increases, the intensity of the N,S-CDs also decreases. As displayed in Figure 7c, in the range of 0–100 μM, the relative fluorescence intensity (F/F_0) displayed a good linear relationship, with an Fe^{3+} concentration ($R^2 = 0.9965$). According to the formula $D = 3\sigma/m$ [19,23,26–28], the detection limit (D) was obtained as 0.20 μM (about 0.11 mg/L). Compared to the detection limits in the literature (Table 1), the carbon dots prepared in this paper have higher quantum yields and lower detection limits, which can be used for actual sample detection.

Table 1. Performance comparison of the different detection ranges and detection limits of carbon dots in the literature.

Sensing Platform	Linear Range (μM)	Quantum Yield	LOD (μM)	Reference
Cu-NCs	1–100	8.6%	0.3	[28]
N-CDs	0.002–8	30.2%	0.138	[19]
C-dots	10–100	28.6%	0.398	[27]
N-CDs	8–80	No report	3.8	[23]
N-CDs	5–500	No report	0.720	[26]
N,S-CDs	0–100	53.80%	0.2	This Work

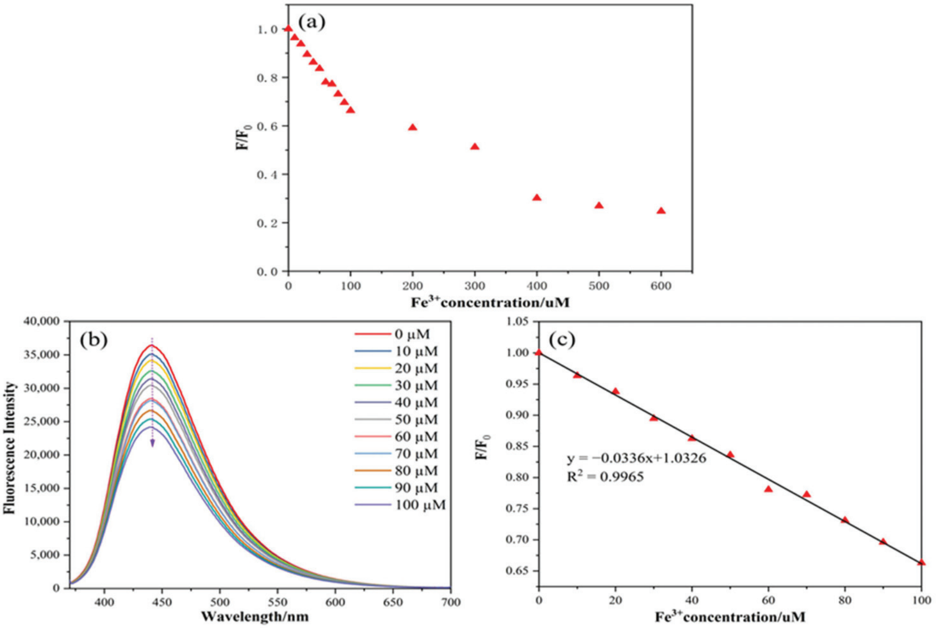

Figure 7. Relative fluorescence intensity changes in N,S-CDs under different concentrations of Fe^{3+} (**a**), fluorescence intensity spectra of N,S-CDs under different concentrations of Fe^{3+} (**b**), and linear relationship between Fe^{3+} concentration and fluorescence intensity of the N,S-CDs (**c**).

Finally, the quenching mechanism of Fe^{3+} on the N,S-CDs was briefly explored through the infrared and ultraviolet absorption spectra of the N,S-CDs and N,S-CDs+Fe^{3+}. Figure 8a displays the UV absorption spectrum in the mixed system of N,S-CDs+Fe^{3+}, and an absorption curve that is different from that of single N,S-CDs appeared. The curve has absorption peaks centered at 300 nm and 365 nm, and the peaks are higher than those in the N,S-CDs alone. In the infrared spectrum as displayed in Figure 8b, it can be observed that the stretching vibration peak of O–H of the hydroxyl group at 3451 cm^{-1} in the mixed system of N,S-CDs+Fe^{3+} is significantly weakened compared to that of the N,S-CDs alone, while the other peaks remain unchanged. This explains that when Fe^{3+} is added, the hydroxyl functional groups on the surface of the N,S-CDs are complexed with them to form ground-state complexes, which are attached to the surfaces of the carbon dots, affecting the luminescence properties of the N,S-CDs and resulting in the quenching effect of Fe^{3+}.

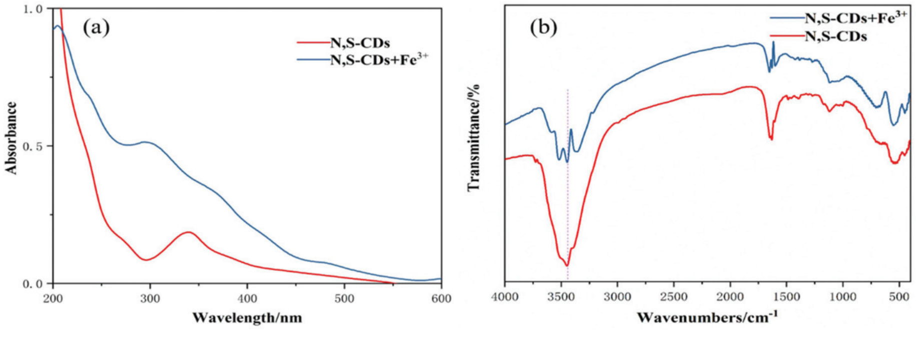

Figure 8. UV spectra (**a**) and infrared spectra (**b**) of N,S-CDs+Fe^{3+} system and N,S-CDs.

3.7. Real Sample Analysis

To further prove the effectiveness of N,S-CDs in detecting Fe^{3+}, three groups of Fe^{3+} with different concentrations were injected into a solution mixed with carbon dots and local tap water, and the data were recorded three times. The conclusion is displayed in Table 2, where the recovery rate of Fe^{3+} in tap water is 97.3%–110.1%, and the relative standard deviation is not more than 4%. The conclusion indicates that the N,S-CDs prepared in this paper had sufficient reliability and sensitivity and that the iron content indicated in the national sanitary standard for drinking water (GB 5749-2006) was 0.3 mg/L (5 μM) [8], which was higher than the detection limit in this paper, proving that the N,S-CDs could be used to measure the iron ion concentration in drinking water.

Table 2. The recovery rate of standard addition of Fe^{3+} in tap water.

Number	Added (μM)	Found (μM)	Recover (%)	RSD (%, n = 3)
1	1	0.99	97.3	3.28
2	5	5.56	110.1	1.91
3	10	10.23	101.8	1.05

4. Conclusions

In this study, co-doped nitrogen–sulfur carbon dots (N,S-CDs) were synthesized hydrothermally by employing thiourea and citric acid as precursors. By changing the ratio of citric acid and thiourea, blue fluorescent N,S-CDs with a quantum yield of 53.80% were synthesized. In weakly acidic, neutral, and high-concentration ionic environments, the N,S-CDs have a highly selective quenching response to Fe^{3+}. When the concentration is 0–100 μM, the fluorescence intensity of the N,S-CDs has a linear relationship with the concentration of Fe^{3+} ($R^2 = 0.9965$), and the measured detection limit ($D = 3\sigma/m$) is 0.2 μM. The results reported in this paper demonstrates the prospective potential application of carbon dots in the field of environmental analysis and monitoring.

Author Contributions: Project administration, Z.L. (Zhengxin Li); Supervision, W.H.; Writing—original draft, H.Z.; Writing—review & editing, Y.R.; Help experiment, Z.L. (Zheng Li). All authors have read and agreed to the published version of the manuscript.

Funding: This work was financially supported by the Innovative Funds Plan of Henan University of Technology (No. 2021ZKCJ06) and supported by the Project of Henan Science and Technology Research Program in 2022 (No.222102230040) and the Cultivation Programme for Young Backbone Teachers in Henan University of Technology (No. 21420117).

Institutional Review Board Statement: Not applicable.

Informed Consent Statement: Not applicable.

Data Availability Statement: The supporting data are available in Henan University of Technology and can be availed upon reasonable request. The data sets generated during this study are available from the corresponding author upon reasonable request.

Conflicts of Interest: The authors declare no conflict of interest.

References

1. Yan, Z.; Hu, L.; You, J. Sensing materials developed and applied for bio-active Fe^{3+} recognition in water environment. *Anal. Methods.* **2016**, *8*, 5738–5754. [CrossRef]
2. Roth-Walter, F.; Pacios, L.F.; Bianchini, R.; Jensen-Jarolim, E. Linking iron-deficiency with allergy: Role of molecular allergens and the microbiome. *Met. Integr. Biometal Sci.* **2017**, *9*, 1676–1692. [CrossRef]
3. Bischof, H.; Burgstaller, S.; Waldeck-Weiermair, M. Live-Cell Imaging of Physiologically Relevant Metal Ions Using Genetically Encoded FRET-Based Probes. *Cells* **2019**, *8*, 492. [CrossRef] [PubMed]
4. Qi, D.; Chen, L.; HaiJun, W. Electrochemical detection of heavy metal ions in water. *Chem. Commun.* **2021**, *57*, 7215–7231.
5. Malik, L.A.; Bashir, A.; Qureashi, A.; Pandith, A.H. Detection and removal of heavy metal ions: A review. *Environ. Chem. Lett.* **2019**, *17*, 1495–1521. [CrossRef]

6. Rao, K.M.; Raagala, V.; Kasula, N. Fabrication of Polyelectrolyte Membranes of Pectin Graft-Copolymers with PVA and Their Composites with Phosphomolybdic Acid for Drug Delivery, Toxic Metal Ion Removal, and Fuel Cell Applications. *Membranes* **2021**, *11*, 792.
7. Sugumari, V.; Karthikeyan, R.; Remya, R.R. Recent developments in magnetic nanoparticles and nano-composites for wastewater treatment. *J. Environ. Chem. Eng.* **2021**, *7*, 106553.
8. *GB 5749–2006*; Standards for Drinking Water Quality. National Standards of the People's Republic of China: Beijing, China, 2006.
9. Reddy, D.R.; Dinesh, G.K.; Anandan, S. Sonophotocatalytic treatment of Naphthol Blue Black dye and real textile wastewater using synthesized Fe doped TiO_2. *Chem. Eng. Process. Process Intensif.* **2016**, *99*, 10–18. [CrossRef]
10. Shi, D.; Ouyang, Z.; Zhao, Y.; Xiong, J.; Shi, X. Catalytic Reduction of Hexavalent Chromium Using Iron/Palladium Bimetallic Nanoparticle-Assembled Filter Paper. *Nanomaterials* **2019**, *9*, 1183. [CrossRef]
11. Wietstock, P.C.; Kunz, T.; Waterkamp, H.; Methner, F.J. Uptake and Release of Ca, Cu, Fe, Mg, and Zn During Beer Production. *J. Am. Soc. Brew. Chemists.* **2015**, *73*, 179–184. [CrossRef]
12. Deckers, M.; Deforce, D.; Fraiture, M.A.; Roosens, N.H.C. Genetically Modified Micro-Organisms for Industrial Food Enzyme Production: An Overview. *Foods* **2020**, *9*, 326. [CrossRef] [PubMed]
13. Juan, Z.; LiHui, X.; QingNan, L. Metal chelator EGCG attenuates Fe(III)-induced conformational transition of α-synuclein and protects AS-PC12 cells against Fe(III)-induced death. *J. Neurochem.* **2017**, *143*, 136–146.
14. Mittal, S.K.; Kumar, S.; Kaur, N. Enhanced Performance of CNT-doped Imine Based Receptors as Fe(III) Sensor Using Potentiometry and Voltammetry. *Electroanalysis* **2019**, *31*, 1229–1237. [CrossRef]
15. Adolfo, F.R.; Nascimento, P.D.; Leal, G.C. Simultaneous determination of iron and nickel as contaminants in multimineral and multivitamin supplements by solid sampling HR-CS GF AAS. *Talanta* **2019**, *159*, 745–751. [CrossRef]
16. Jalili, R.; Khataee, A.; Rashidi, M.R. Dual-colored carbon dot encapsulated metal-organic framework for ratiometric detection of glutathione. *Sens. Actuators B Chem.* **2019**, *297*, 126775. [CrossRef]
17. Kim, K.W.; Choi, T.Y.; Yong, M.K. Simple synthesis of photoluminescent carbon dots from a marine polysaccharide found in shark cartilage. *Electron. J. Biotechnol.* **2020**, *47*, 36–42. [CrossRef]
18. Thomas, C.W.; Piergiorgio, G.; Anh, N.P. Biomass-Based Carbon Dots: Current Development and Future Perspectives. *ACS Nano.* **2021**, *15*, 15471–15501.
19. Hashemi, N.; Mousazadeh, M.H. Preparation of fluorescent nitrogen-doped carbon dots for highly selective on-off detection of Fe^{3+} ions in real samples. *Opt. Mater.* **2021**, *121*, 111515. [CrossRef]
20. Lu, X.; FengYun, W.; Lei, W. The synthesis and modification of highly fluorescent carbon quantum dots for reversible detection of water-soluble phosphonate-1-hydroxyethane-1,1-diphosphonic acid by fluorescence spectroscopy. *J. Biol. Chem. Lumin.* **2021**, *36*, 200–209. [CrossRef]
21. Gorakh, B.D.; Garje, S.S. Nitrogen and Phosphorus Co-Doped Carbon Dots for Selective Detection of Nitro Explosives. *ACS Omega* **2020**, *5*, 2710–2717.
22. Dong, Y.; Zhang, Y.; Zhi, S. Green Synthesized Fluorescent Carbon Dots from Momordica charantia for Selective and Sensitive Detection of Pd^{2+} and Fe^{3+}. *ChemistrySelect* **2021**, *6*, 123–130. [CrossRef]
23. Chen, Y.; Sun, X.; Pan, W. Fe^{3+}-Sensitive Carbon Dots for Detection of Fe^{3+} in Aqueous Solution and Intracellular Imaging of Fe^{3+} Inside Fungal Cells. *Front. Chem.* **2020**, *7*, 911. [CrossRef] [PubMed]
24. Zulfajri, M.; Gangaraju, G.; Chang, C.J. Cranberry Beans Derived Carbon Dots as a Potential Fluorescence Sensor for Selective Detection of Fe^{3+} Ions in Aqueous Solution. *ACS Omega* **2019**, *4*, 15382–15392. [CrossRef] [PubMed]
25. Zhu, X.; Zhang, Z.; Xue, Z. Understanding the Selective Detection of Fe^{3+} based on Graphene Quantum Dots as Fluorescent Probes: The K_{sp} of a Metal Hydroxide-Assisted Mechanism. *Anal. Chem.* **2017**, *89*, 12054–12058. [CrossRef] [PubMed]
26. Pu, Z.F.; Wen, Q.L.; Yang, Y.J. Fluorescent carbon quantum dots synthesized using phenylalanine and citric acid for selective detection of Fe^{3+} ions. *Spectrochim. Acta Part A Mol. Biomol. Spectrosc.* **2020**, *229*, 117944. [CrossRef]
27. Nair, S.; Kottam, N.; Prasanna, K. Green Synthesized Luminescent Carbon Nanodots for the Sensing Application of Fe^{3+} Ions. *J. Fluoresc.* **2020**, *30*, 357–363.
28. Huang, H.; Li, H.; Feng, J.; Feng, H.; AiJun, W. One-pot green synthesis of highly fluorescent glutathione-stabilized copper nanoclusters for Fe^{3+} sensing. *Sens. Actuator B Chem.* **2017**, *241*, 292–297. [CrossRef]
29. Mei, S.; Wei, X.; Hu, Z. Amphipathic carbon dots with solvent-dependent optical properties and sensing application. *Opt. Mater.* **2019**, *89*, 224–230. [CrossRef]
30. Crista, D.; Mragui, A.E.; Algarra, M. Turning Spent Coffee Grounds into Sustainable Precursors for the Fabrication of Carbon Dots. *Nanomaterials* **2020**, *10*, 1209. [CrossRef]
31. Ra, A.; Tnjie, A.; Sp, B. Green synthesized multiple fluorescent nitrogen-doped carbon quantum dots as an efficient label-free optical nanoprobe for in vivo live-cell imaging. *J. Photochem. Photobiol. A: Chem.* **2019**, *372*, 99–107.
32. Atchudan, R.; Nesakumar, J.; Perumal, S. Indian Gooseberry-Derived Tunable Fluorescent Carbon Dots as a Promise for In Vitro/In Vivo Multicolor Bioimaging and Fluorescent Ink. *ACS Omega* **2018**, *3*, 17590–17601. [CrossRef]
33. Miao, X.; Yan, X.; Qu, D. Red emissive S, N codoped carbon dots and their application in ion detection and theraonostics. *Acs Appl. Mater. Interfaces* **2017**, *77*, 99–107.
34. ChenLong, S.; Qing, L.; ChongXin, S. Near-Infrared Chemiluminescent Carbon Nanodots and Their Application in Reactive Oxygen Species Bioimaging. *Adv. Sci.* **2020**, *7*, 1903525.

coatings

Review

Vascularization Reconstruction Strategies in Craniofacial Bone Regeneration

Jiping Chen, Yu Da, Jing Yang, Guirong Zhu and Haiyan Qin *

Department of Stomatology, Drum Tower Hospital, The Affiliated Hospital of Nanjing University Medical School, Nanjing 210000, China; chenjiping@smail.nju.edu.cn (J.C.); rain_da@126.com (Y.D.); jinyang19961104@163.com (J.Y.); 15250968551@163.com (G.Z.)
* Correspondence: haiyanandrew@163.com

Abstract: Craniofacial bone defects are usually secondary to accident trauma, resection of tumor, sever inflammation, and congenital disease. The defects of craniofacial bones impact esthetic appearance and functionality such as mastication, pronunciation, and facial features. During the craniofacial bone regeneration process, different osteogenic cells are introduced, including primary osteoblasts or pluripotent stem cells. However, the defect area is initially avascular, resulting in the death of the introduced cells and failed regeneration. Thus, it is vital to establish vascularization strategies to build a timely and abundant blood vessel supply network. This review paper therefore focuses on the reconstruction of both osteogenesis and vasculogenesis. The current challenges, various strategies, and latest efforts applied to enhance vascularization in craniofacial bone regeneration are discussed. These involve the application of angiogenic growth factors and cell-based vascularization strategies. In addition, surface morphology, porous characters, and the angiogenic release property of scaffolds also have a fundamental effect on vasculogenesis via cell behavior and are further discussed.

Keywords: craniofacial bone; osteogenesis; vasculogenesis; bone tissue engineering; blood vessel; angiogenesis growth factor; biocompatible materials

Citation: Chen, J.; Da, Y.; Yang, J.; Zhu, G.; Qin, H. Vascularization Reconstruction Strategies in Craniofacial Bone Regeneration. *Coatings* **2024**, *14*, 357. https://doi.org/10.3390/coatings14030357

Academic Editor: Jun-Beom Park

Received: 18 November 2023
Revised: 10 March 2024
Accepted: 13 March 2024
Published: 18 March 2024

1. Introduction

Craniofacial bone provides support for adjacent craniofacial soft tissues (especially the attachments of mastication-related muscles) and anchorage for dental structures [1]. The defects of craniofacial bones, secondary to accident trauma, congenital disease, tumor resection, and inflammation [2–5], impact esthetic appearance and functionality of the craniofacial complex, such as mastication, pronunciation, and facial features. Furthermore, craniofacial bone is highly vascularized, and its functions depend a lot on an unobstructed and well-organized vascular network. With the intact vessels, sufficient oxygen and nutrients can be supplied, guaranteeing the proliferation and viability of cells [6]. At the same time, the metabolic waste of cells can be taken away [7]. Therefore, it is well-recognized that the prompting of vasculogenesis is beneficial for reinforced bone functions. After the craniofacial bone defect occurs, osteogenic cells such as primary osteoblasts or pluripotent stem cells are recruited in order to generate neobones. However, the defect area is initially avascular, resulting in the death of the recruited cells and failed regeneration [6]. Thus, it is vital to establish vascularization strategies to build a timely and abundant blood vessel supply network [8].

Clinically, the damaged craniofacial bone can be reconstructed with a series of surgical operations. More than 90% of grafts used are autologous or allogenic transplantations, which are recognized as the “gold standards” [9]. However, challenges, such as donor site morbidity, pain, infection, and additional economic burden, are still unmet [10]. More importantly, vasculogenesis in the depth of the defect also cannot be well-established, which leads to the necrosis of transplanted grafts [11–13].

Rapid developments in bone tissue engineering bring new hope for solving the urgent problems and provide more strategies for neovascular networks and craniofacial bone tissue regeneration. During the past decades, numerous studies have been accomplished, introducing different angiogenic cells and growth factors based on biocompatible scaffolds for rebuilding vessel networks in craniofacial bone defects [9,14,15]. This work, presenting a first-time comprehensive review of recent advances of vascularization strategies in craniofacial bone tissue regeneration, overviews the current challenges, various strategies, and the latest efforts applied to enhancing vascularization in craniofacial bone regeneration.

2. Challenges of Vascularization in Craniofacial Bone Regeneration

Vasculogenesis and angiogenesis are two well-known approaches by which embryonic blood vessels develop. Vasculogenesis means that new blood vessels are formed in suit by endothelial progenitor cells and then coalesce with elongating vessels. In contrast, angiogenesis, assumed as the more prevalent way of vascularization, is related to new capillaries by budding, branching, and elongation of existing vessels [16–18]. While the specific angiogenesis mechanism during craniofacial bone defect regeneration remains unexplicit, some inspirations can be obtained from the craniofacial bone formation. Unlike the endochondral ossification pattern of the appendicular skeleton, most craniofacial bones display an intramembranous ossification pattern (Figure 1) [3,19–21]. Under this pattern, osteogenic cells derived from mesenchymal stem cells (MSCs) directly secrete osteoid and then mineralize as bone tissue [14]. Recent research has reported that capillary-like structures can be observed invading the avascular MSC layer prior to mineralization [21,22]. This indicates that ingrowth angiogenesis of the defect area is essential for craniofacial bone regeneration.

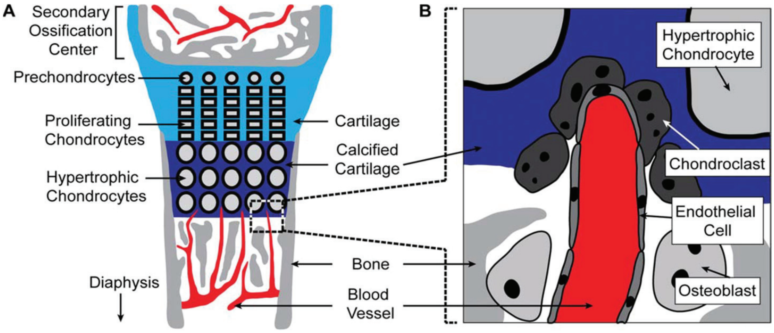

Figure 1. Schematic of the epiphyseal ossification of endochondral long bones, with emphasis on the process of capillary growth into calcified epiphyseal cartilage and subsequent trabecular ossification. (**A**) Chondrocytes differentiate from proliferating prechondrocytes within the growth plate. The chondrocytes are pushed toward the diaphysis by this continuous process and then enlarge under hypoxia, leading to mineralization of surrounding cartilage and the attraction of blood vessels required for bone formation. (**B**) Magnified view of bracketed zone from “A” showing capillaries, in association with chondroclasts, growing towards hypertrophic chondrocytes as a precursor to osteoblast activity and bone growth at the epiphysis. Reprinted with permission from Ref. [21], 2013, John Wiley and Sons.

However, there are still challenges in building a mature craniofacial neovascular system in the bone defect site. First of all, the defects of craniofacial bone, secondary to tumor resection or congenital craniofacial diseases, are usually critical-sized and the depth of defects is often thicker than 1 cm. The maximum cell–vessel distance to gain adequate oxygen supply and nutrition support is 200 µm [23,24], which means the transplanted or recruited cells may not survive, as minimal oxygen and nutrition can be obtained from host blood vessels, leading to the failure of new bone formation. Thus, how to establish a well-organized and functional neovascular network within a short time to support cell proliferation and bone formation is the main challenge in craniofacial revascularization. Furthermore, the final functionalization of the neovascular vessel relies on the extent of anastomosis between neo and host vasculature [7]. Thus, therapeutic approaches for achieving successful anastomosis with resident vasculature is another issue that should be urgently addressed.

Furthermore, current studies demonstrate that blood vessels can be further classified as two different types. Type H vessels are characterized by high and positive expressions of CD31 and Endomucin. In contrast, type L vessels are characterized by low or negative expressions of CD31 and Endomucin. Type H vessels are reported to be located near the periosteum and endosteum of the diaphysis, while type L vessels are located in the bone marrow [25,26]. Evidence indicates that type H vessels can promote the proliferation and differentiation of osteoprogenitors and stimulate direct bone formation [27,28]. Therefore, how to increase the type H vessel ratio of neovascular network formation to promote craniofacial bone defect regeneration becomes another issue that should be further explored.

3. Various Vascularization Strategies in Craniofacial Bone Regeneration

Angiogenesis is a complex process involving extensive connections between vast growth factors, cells, and extracellular matrices (ECMs) [3,7,16–18]. After the bone defect occurs, the local hypoxic microenvironment and acute inflammation stimulate the release of pro-angiogenic growth factors from surrounding cells, which initiate the active proliferation of the endothelial cells (ECs) [8,29]. Afterwards, new blood vessels are formed, and then stabilized and remodeled by pericytes [30,31].

3.1. Cell Sources for Craniofacial Bone Vascularization

Vascularization involves vasculogenesis or angiogenesis; both these approaches rely highly on the functions of ECs and endothelial progenitor cells (EPCs) [32–35]. The craniofacial bone defect region is in need of oxygen and nutrients, and secretes proangiogenic molecules. As illustrated in Figure 2, ECs are triggered to be invasive (referred to as tip cells), lead the sprouts, and protrude filopodia [36]. Then, the protruded filopodia extend in response to the angiogenic signal source [36,37]. Tip cells are followed by stalk cells, which proliferate to elongate the sprout and form the fundamental vessel lumen [35,38,39]. Specification in migratory tip and proliferating stalk cells is dynamic, and ECs continuously compete for the lead position. Eventually, tip cells connect with surrounding tip cells from adjacent sprouts to form a new and stable vessel [35,39]. In addition, ECs have been proven to enhance the anastomosis between the neovessel system and host vasculature [7,40].

Considering that EC sources are limited in the craniofacial bone defect area, the EPCs, which are potentially derived from umbilical cord blood, peripheral blood, bone marrow, or human-induced pluripotent stem cells, are of great importance in vascular engineering because of their pluripotency and outstanding self-proliferation ability [41,42]. Studies have demonstrated that postnatal neovascularization is both directly and indirectly stimulated by EPCs [43,44]. Human EPCs have also been confirmed to be capable of forming a neovasculature in a critical-sized rat bone defect model, indicating that EPCs may be directly involved in the process of angiogenesis via differentiation into lumen-forming cells [45]. Furthermore, the expressions of proangiogenic vascular endothelial growth factors are higher in EPCs or EPCs/MSCs groups compared with those in MSCs alone, as well as the formation of blood vessels, confirming that EPCs are capable of initiating a host angiogenic response through cytokine secretion [44–46].

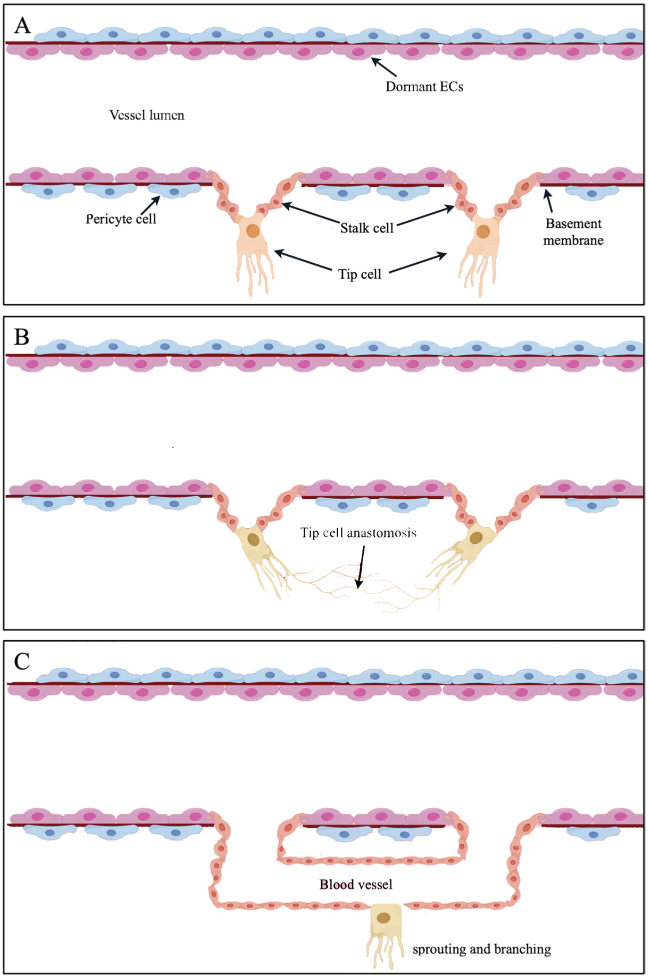

Figure 2. Illustrations of the sprouting and branching steps of blood vessels. (**A**) Sprout initiation and elongation. (**B**) Sprout anastomosis. (**C**) Vessel remodeling.

Except for ECs/EPCs, pericytes are the other composed cells of blood vessels (also referred to as perivascular cells, vascular smooth muscle cells, or mural cells). Pericytes play a crucial role in microvascular function, blood vessel stability, angiogenesis, and blood pressure regulation [30,31]. In addition, 22%~99% of the endothelium in capillaries is covered with pericytes, which are also found in pre-capillary arterioles and post-capillary venules. The high coverage rate seems to correlate positively with endothelial barrier properties. A larger coverage rate of pericyte leads to reduced EC turnover, whereas a lower coverage rate of pericyte results in enhanced proliferation and sprouting capacity of ECs. Furthermore, pericytes exhibit other important functions, such as contractile regulation of blood flow and the formation of ECM. Moreover, pericytes are embedded in the basement membrane of the vasculature and contact with surrounding ECs, resulting in an efficient communication, named pericyte–endothelial interactions, between the two cell types. Pericyte–endothelial interactions are necessary for the development and maintenance of a functional microcirculation in different tissues [47,48]. Currently, there are different views on the pericyte–endothelial interactions in different type of tissues. The most well-accepted view is that pericytes are recruited by stalk cells to support vessels. For example, research in the retinal angiogenesis field shows that the retinal vascular network remains immature and is prone to rarefaction by ineffective stabilization until pericyte recruitment [49].

3.2. Cell Signaling and Angiogenic Growth Factors

The entire angiogenesis process consists of a series of growth factors and mediators of microenvironment components. The current knowledge of angiogenic biology has been widely expanding; one of the most significant factors is the vascular endothelial growth factor (VEGF) family. VEGF and its receptors (VEGFRs) play a prominent role in the activation of ECs in angiogenesis and osteogenesis [50–52]. ECs expressing high VEGFR2 signaling are called tip cells and promote the neighboring ECs' transfer as a stalk cell phenotype by upregulating the signaling of Notch ligand Delta-like 4 (DLL4). The transferring process is initiated by the activation of the NOTCH1 receptor of stalk cell via DLL4. The transferring in turn leads to the suppression of VEGFR2 and the concomitant induction of VEGFR1. The reciprocal regulation of VEGFR expression by Notch signaling reduces sensitivity to VEGF and thereby enforces stalk cell specification. The levels of VEGFRs, DLL4, and NOTCH1 are, however, constantly changing as ECs meet new neighbors. As a result, stalk cells can be relieved from tip cell inhibition and overtake the lead position, resulting in a dynamic position shuffle in the growing sprout [53,54]. The integrated regulation of VEGF and Notch is a prime example of a mechanism that allows ECs to sprout reiteratively in a concerted action, thereby ensuring robust network formation.

Platelet-derived growth factor-BB (PDGF-BB) is a member of the PDGF family, which is capable of improving the migration, proliferation, and differentiation of various mesenchymal cell types, such as EPCs and MSCs. ECs secrete PDGF-BB to recruit platelet-derived growth factor receptor–β positive (PDGFRβ^+) pericytes onto the neovasculature [55,56]. Su et al. demonstrated that bone angiogenesis was weakened when PDGF-BB was selectively knocked out in preosteoclasts. More bone angiogenesis was also obtained in *Pdgfb*-transgenic mice that overexpressed PDGF-BB (Figure 3) [55]. In addition to vessel formation, PDGF-BB–PDGFR signaling was reported to cooperate with DLL4–Notch signaling pathways to prevent excessive vascular sprouting and achieve a balanced and functional vessel network [57,58].

Hypoxia-inducible factor (HIF) is a transcription factor that alters the cell behavior in response to oxygen concentration and further affects angiogenesis [59,60]. HIF-1α is one of the most studied members of the HIF family. Studies have shown that HIF-1α is involved in angiogenesis or vascular remodeling processes through the so-called "HIF-1α-VEGF axis". Under the stimulation of both angiopoietin-1 (Ang-1) and angiopoietin-2 (Ang-2), HIF-1α stimulates MSCs to secrete VEGF and inhibits the expression of the tissue inhibitor of metalloproteinase-3 (TIMP-3), an endogenous competitive inhibitor of the VEGF receptor (which mediates osteogenesis and angiogenesis) [61–64]. Furthermore, the ECs of Type H vessels have been reported to promote vascular growth via the HIF-1α-VEGF axis and further communicate with perivascular osteoblasts through the Notch signal pathway for osteogenesis [26].

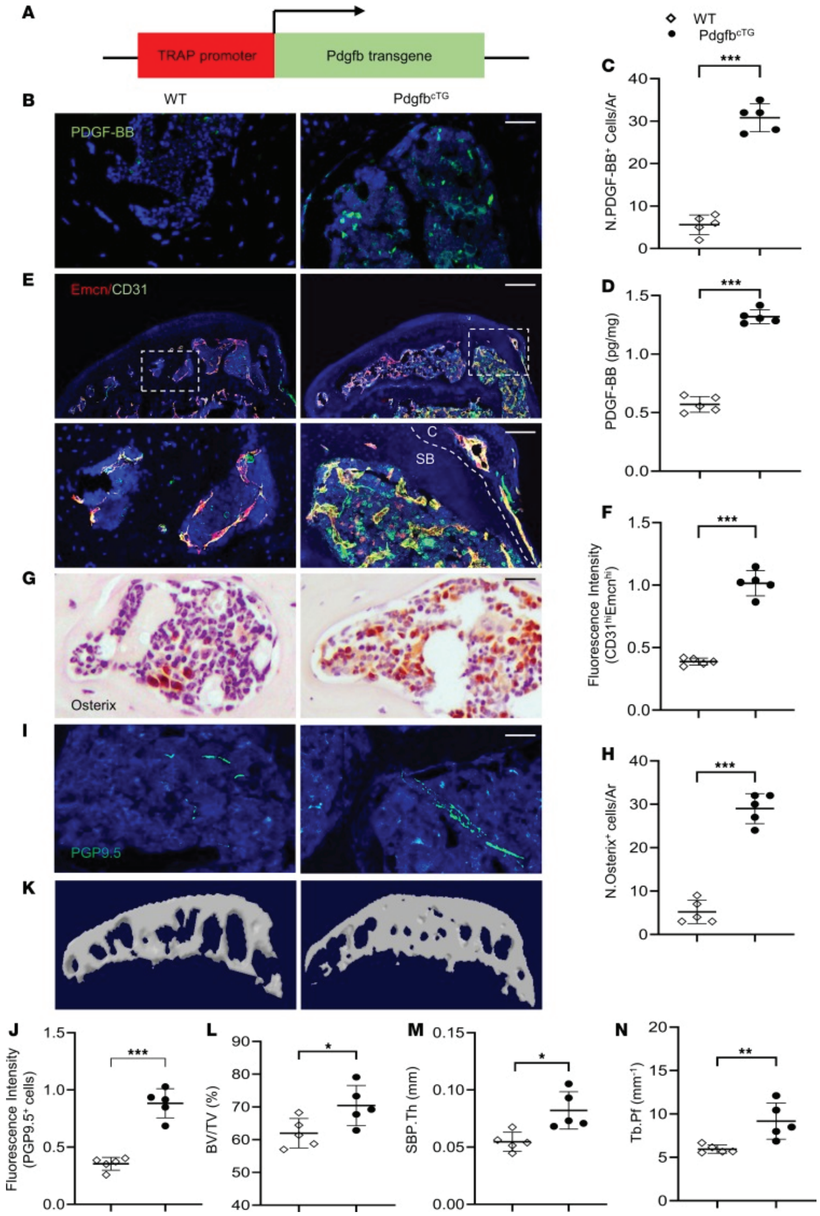

Figure 3. Transgenic mice expressing PDGF-BB in preosteoclasts recapitulate the pathological features of osteoarthritic joint subchondral bone. (**A**) Schematic diagram showing the TRACP5-*Pdgfb* transgene in transgenic mice (PdgfbcTG). (**B**–**N**) Knee joints were harvested from 5-month-old transgenic mice and WT mice. n = 5 mice per group. Immunofluorescence staining of PDGF-BB (green) and quantification of PDGF-BB$^+$ cells in tibial subchondral bone (**B**,**C**). Scale bar: 50 µm. *** $p < 0.001$. ELISA analysis of PDGF-BB concentration in tibial subchondral bone/bone marrow. *** $p < 0.001$ (**D**). Immunofluorescence staining of CD31 (green) and Emcn (red) with quantification of the intensity of CD31^{hi} Emcn^{hi} signal per tissue area in subchondral bone of the tibia (**E**,**F**). C—cartilage; SB—subchondral bone. Scale bars: 200 µm (**top**), 50 µm (**bottom**). *** $p < 0.001$. Immunohistochemical analysis of Osterix (brown) and quantification of Osterix$^+$ cells in tibial subchondral bone (**G**,**H**). Scale

bar: 50 µm. *** $p < 0.001$. Immunofluorescence staining of PGP9.5 (green) with quantification of the intensity of PGP9.5 signal per tissue area in subchondral bone of the tibia (**I**,**J**). Scale bar: 50 µm. *** $p < 0.001$. Three-dimensional µCT images (**K**) and quantitative analysis of structural parameters of subchondral bone: BV/TV (**L**), SBP. Th (mm^{-1}) (**M**) and Tb. Pf (mm^{-1}) (**N**). * $p < 0.05$, and ** $p < 0.01$. All data are shown as means ± standard deviations. Statistical significance was determined by unpaired 2-tailed Student's *t* test. Reprinted with permission from [55], 2020, American Society for Clinical Investigation.

In the context of biomaterials for craniofacial bone regeneration, the use of inorganic cations such as Ca^{2+}, magnesium (Mg^{2+}), and silicon (Si^{4+}) has gained attention due to their influence on mechanical and biological properties crucial for bone regeneration [18,65–68]. These cations do also play significant roles in neovascularization, which are crucial aspects of craniofacial bone regeneration [69–72]. Wang et al. displayed a sustained release of Mg^{2+} from the piezoelectric Whitlockite scaffold and promoted angiogenic differentiation of BMSCs in vitro. Mg^{2+} was further confirmed to remarkably form neobone with rich angiogenic expressions in an in vivo rat calvarial defect model (Figure 4) [73]. Liu et al. also reported the powerful angiogenic property of Mg^{2+}. In their study, MC3T3-E1 cells were treated with different concentrations of Mg^{2+}, and the secretion of PDGF-BB was promoted, which can effectively promote the angiogenic ability of HUVECs [74]. Wan et al. studied the synergistic effect of Mg^{2+} and Si^{4+}. They fabricated hierarchical microspheres named PNM2, which can steadily release Mg^{2+} and Si^{4+} at an optimized ratio of 2:1 to match the process of vascularized bone regeneration at different stages. Then, a high volume and maturity of the vascularized neobone tissue was regenerated with PNM2 microspheres in a rat calvarial defect model [75]. Other cations, like Cu^{2+} and Co^{2+}, also show proangiogenic activity [76,77]. Cu^{2+} affects angiogenesis via regulation of the pERK1/2-foxm1-MMP2/9 axis [78]. Co^{2+} has the capacity to stabilize HIF-1α and subsequently induce the production of VEGF, activating the angiogenic process by creating a hypoxia-mimicking condition [79].

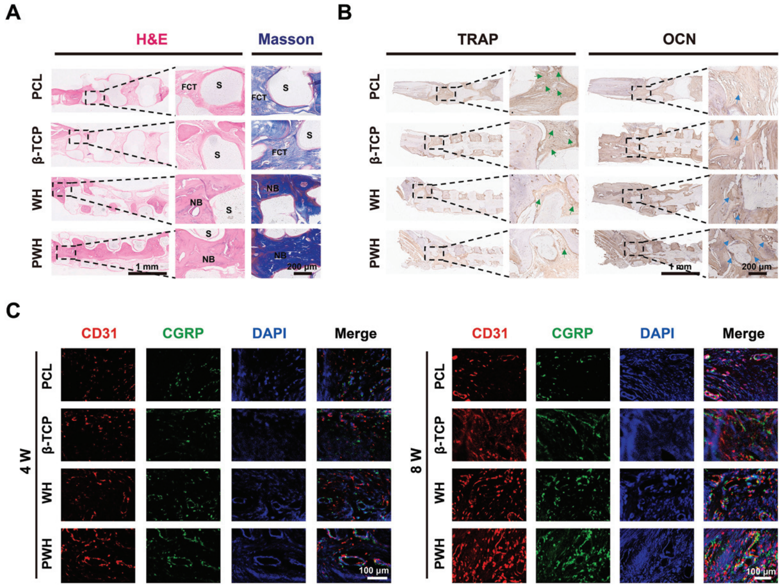

Figure 4. Histological, immunohistological, and immunofluorescence staining for the evaluation of bone regeneration. (**A**) H&E staining and Masson's trichrome staining for sections collected at 8 w

post-operation. (**B**) Immunohistochemical staining of TRAP and OCN expression at 8 w post-operation. (**C**) Immunofluorescence staining of CD31 (red), CGRP (green), and DAPI (blue) expression at 4 w and 8 w post-operation. FCT: fibrous connective tissue. NB: newly formed bone tissue. S: spaces in scaffolds. Reprint from [73].

A breakthrough in the additional application of miRNA in 2006 moved angiogenesis to another level [80]. Zhuang et al. investigated the angiogenic effect of miR-210-3p. They found miR-210-3p can hinder EFNA3 expression and subsequently activate the PI3K/AKT pathway, enhancing the proliferation, migration, and angiogenesis of ECs [81]. Castaño et al. also reported the synergetic effect of dual delivery of two miRNAs. MiR-210 mimics and miR-16 inhibitors were released from a collagen–nanohydroxyapatite scaffold system to enhance angiogenesis and osteogenesis, resulting in accelerated rat calvarial bone defect repair [82]. There are also many other angiogenic miRNAs, such as miR-378, miR-126, and Let-7, that target various signaling molecules. These miRNAs target various aspects of angiogenesis via endothelial cell function, blood vessel formation, and related growth factor signaling (Table 1).

Table 1. Major angiogenesis pathways and potential therapeutic miRNAs.

Target Pathway	miRNA	Target Signaling Pathway
Activation of ECs	miR-210-3p	EFNA3/PI3K/AKT [81,83]
	miR-378	Sufu [84] Fus1 [85]
	miR-126	SPRED1/Ras/Erk [86,87] PIK3R2 [88] VCAM-1 [89]
Sprouting, migration, and tubulogenesis of ECs	miR-17-92	ERK/ELK1 [90]
	Let-7f-5p	DUSP1/Erk1/2 [91]

3.3. Co-Culture Systems with Different Cell Types or Growth Factors

Co-culture strategies involving different cell types and growth factors have indeed found application in the field of craniofacial bone vascularization. These approaches leverage the interactions between various cell types and signals to enhance osteogenesis and angiogenesis. According to previous studies, the co-culture system may strengthen the participating cells isolated from different tissues, showing enhanced cell functions. Co-transplantation of EPCs and osteogenic stem cells has been widely accepted in vascularized bone regeneration due to their respective angiogenic or osteogenic potentials reported in different studies [92–94]. Cells harvested from bone marrow aspirates possess osteogenic ability and can also be induced to form tubelike structures and ECs. Studies have shown that EPCs or MSCs can secrete bone morphogenetic protein–2 (BMP-2), a potent inducer of osteogenesis [95]. In turn, MSCs have secreted angiogenic cytokine to promote the migration of EPCs via PDGF-BB and vessel formation [55,56]. Except for different cells, growth factors are also dually applied within the same system. PDGF-BB co-expression with VEGF can prevent the VEGF-related aberrant angiogenesis. Within the system, the VEGF–VEGFR2 induces vascular sprouting and the PDGF-BB–PDGFRβ system can synchronize with DLL4–Notch signaling to prevent excessive vascular sprouting at the same time, preventing imbalanced expression or activation of each of these signaling components and vascular dysfunctions [96].

3.4. Biological Requirements for Biomimetic Scaffolds Used for Craniofacial Bone Vascularization

Scaffold materials used in the field of craniofacial regeneration serve a critical role beyond simply providing a structural framework; they must also support vascular regeneration in addition to promoting osteo-induction and osteo-conduction (Table 2).

Table 2. In vivo biomaterial scaffold research about vascularization and craniofacial bone regeneration during the last 5 years.

Author and Year	Biomaterial Scaffolds	Bioactive Agent	Implanted Cells	Animal Model	Observation Period	Osteogenesis	Angiogenesis
Yaxi Sun, Dent Mater, 2023 [97]	Calcium phosphate cement scaffold (CPC)	Metformin	hPDLSCs	Critical-sized defect of rat cranium	12 weeks	9 folds by control	3 folds by control
Ruochen Luo, Biomed Mater, 2021 [98]	Poly(lactide-co-glycolide) microspheres	Mg^{2+} and La^{3+}	---	Critical-sized defect of rat cranium	8 weeks	Enhanced	Enhanced
Nurul Aisyah Rizky Putranti Cells, 2022 [99]	Carbonate hydroxyapatite (CAP) granules	BMP-2	SHED	Critical-sized defect of immunodeficient mice cranium	12 weeks	Enhanced	Enhanced
Kun Liu, Regen Biomater, 2020 [100]	Mineralized collagen	BMP-2 and VEGF	---	Mandibular defects of rabbits	12 weeks	Enhanced	Enhanced
[101]	GM/Ac-CD/rGO hydrogel	---	---	Critical-sized defect of rat and mice cranium	8 weeks	Enhanced	Promotes type H vessel formation
Omar Omar, Proc Natl Acad Sci U S A, 2020 [102]	Bioceramic (biocer) implants	---	---	Skull defect of ovine	12 months	Enhanced	Enhanced
Yaohui Tang, Theranostics, 2020 [103]	Injectable gelatin-based µRB hydrogel	BMP-2	ASC	Critical-sized defect of immunodeficient mice cranium	8 weeks	Enhanced	---
Yuanjia He, Stem Cell Res Ther, 2020 [104]	HA/Col scaffold	---	EPCs and ASC	Critical-sized defect of rat cranium	8 weeks	Enhanced	Enhanced
Maxime M Wang, Sci Rep, 2019 [105]	3D-printed bioceramic scaffolds	Dipyridamole	---	Unilateral alveolar defect of rabbits	24 weeks	Enhanced	---
Weibo Zhang, Front Bioeng Biotechnol, 2020 [106]	E1001(1K)/β-TCP scaffolds	Tyrosine-derived polycarbonate	hDPSCs and HUVECs	Mandible defect of rabbits	3 months	Enhanced	Enhanced
Marley J Dewey, Biofabrication, 2021 [107]	Mineralized collagen/PCL composites	---	---	Critical-sized defect of porcine ramus	10 months	Enhanced	Enhanced

Table 2. *Cont.*

Author and Year	**Biomaterial Scaffolds**	**Bioactive Agent**	**Implanted Cells**	**Animal Model**	**Observation Period**	**Osteogenesis**	**Angiogenesis**
Qian-Qian Wan, ACS Appl Mater Interfaces, 2022 [108]	Eggshell membranes	Cerium oxide	---	Critical-sized defect of mice cranium	8 weeks	Enhanced	Enhanced
Yue Kang, Biofabrication, 2023 [109]	Hybrid scaffolds	Exos isolated from hASC	---	Critical-sized defect of immunodeficient mice cranium	10 weeks	Enhanced	Enhanced
Zeqing Zhao, J Dent, 2023 [110]	Calcium phosphate cement (CPC) scaffolds	Human platelet lysate	hPDLSCs and hUVECs	Critical-sized defect of immunodeficient mice cranium	12 weeks	4 folds by control	7.9 folds by control
H Autefage, Biomaterials, 2019 [111]	Bioactive glass-based scaffold	Strontium	---	Femoral condyle defect of ovine	12 weeks	Enhanced	---
Tania Saskianti, Clin Cosmet Investig Dent, 2022 [112]	Hydroxyapatite	---	SHED	Mandibular defect of rats		Downregulation of MMP-8	Upregulation VEGF expressions
W Ma, J Dent Res, 2021 [113]	Col scaffold	Galanin	---	Periodontitis-treated mice	6 weeks	Enhanced	---
Tsuyoshi Kurobane, Acta Biomater, 2019 [114]	Octacalcium phosphate/gelatin composite (OCP/Gel)	---	---	Critical-sized defect of immunodeficient mice cranium	4 weeks	---	Enhanced
Mirali Pandya, Int J Mol Sci, 2021 [115]	Collagen/erythropoietin (EPO) scaffold	EPO		First maxillary molars extracted rats	8 weeks	Enhanced	enhanced
TaichiTenkumo, Regen Ther, 2023 [116]	A triple-functionalized paste of CAP	DNA and siRNA	---	Femoral head defect of rats	21 days	Enhanced	---
Hyeree Park, Mater Sci Eng C Mater Biol Appl, 2021 [117]	DC-S53P4 bioactive glass hybrid gels	---	DPSCs	Critical-sized defect of immunodeficient mice cranium	8 weeks	Enhanced	Enhanced

3.4.1. Surface Morphology

The surface characters of scaffolds are closely related to the cell adhesion, proliferation, and function of blood vessel-forming related cells, which could eventually affect the formation of the functional vessel network. Surface modification includes chemical modification and physical modification, and methods of surface modification usually include immersion [118], coating [119–123], and plasma treatment [124,125]. Porous polyetheretherketone

(PEEK) scaffolds are modified via polydopamine and Mg^{2+} physically deposited on the surface. After surface modification, the hydrophilicity of PEEK scaffolds is significantly enhanced, and bioactive Mg^{2+} could be released, contributing to the reinforced formation of osteogenic H type vessels in a rabbit femoral condyle model [15].

Except for the physical modifications, chemical modifications of the scaffold surface can also facilitate the adhesion and biological behaviors of blood vessel-forming related cells. Among various studies, several amino acid sequences, such as Arg–Gly–Asp (RGD) [126,127], have triggered intensive studies for the enhancement of EC adhesion by the establishment of a ligand-modified surface and established capillary structure. Apart from the well-known amino acids, Hao et al. successfully identified the $\alpha v\beta 3$ integrin ligand LXW7 with the help of unnatural amino acids [128]. The following research found that LXW7 showed a stronger binding affinity to primary EPCs/ECs. In addition, an LXW7-treated surface exhibited proliferation, migration, and tubule formation through increased VEGFR2 phosphorylation [129].

3.4.2. Porous Characters

A porous scaffold is the prerequisite of cell ingrowth, oxygen supply, and nutrient transport. Studies have illustrated that different properties of scaffold pores can affect cell type and behavior. The suggested range of diameters is considered from 200 to 350 μm for bone regeneration [130], while the favored pore size for revascularization is larger than 400 μm [7]. Moreover, large pore sizes have been reported to be beneficial for cell viability but harmful for cell seeding. The above contradiction reminds us that a monomodal scaffold is out of date. A scaffold with multiple pore size is urgently needed in order to fulfill the best osteogenesis and angiogenesis at the same time.

3.4.3. Angiogenic GF Release Property

Sufficient oxygen, enough nutrients, and a large amount of different types of regenerative cells can be supplied to the defect area, allowing the inflammation factors, metabolic wastes, and necrotic tissue to be removed in time in the presence of the dense vascular network. Angiogenic growth factors, including VEGF, have recently attracted much more attention [131]. However, the narrow range of therapeutic windows of VEGF limits clinical promotion. It has been reported that the concentrations of VEGF determine the fate of the tissue regeneration process. Higher concentrations of VEGF are shown to result in unfavorable effects, such as increased permeability and being prone to create malformed and non-functional blood vessels [131,132]. Furthermore, a large proportion of VEGF degraded rapidly because of the short half-life before coming into effect when being released into the biological milieu [131]. Therefore, it is necessary to achieve a spatial and temporal release of VEGF to prolong its activity. Wernike et al. reported that, when VEGF was introduced in the cranial defects of mice and was slowly released via implanted biomimetic BCP ceramics, more dense vessels and more regular vessel morphology could be visualized with intravital microscopy compared with burst-released VEGF [132]. Burger et al. also reported that over-expression of VEGF was associated with paradoxical bone loss. They controlled the distribution of the VEGF dose with factor-decorated matrices and observed both improved vascularization and bone formation in orthotopic critical-size defects compared with burst-released VEGF [133].

3.5. Scaffold-Free Technique

Although biomimetic scaffolds provide the supportive structures for cell ingrowth, ECM depositions, and tissue regeneration, they still bear a non-negligible drawback, i.e., incomplete biodegradability [134]. This may induce chronic inflammation and hinder the complete regeneration of bone defect with neotissue. Under this circumstance, scaffold-free tissue engineering, also referred to as cell sheet engineering (CSE), has been developed in recent years. In scaffold-free tissue engineering, cells are directly assembled or aggregated to form a tissue-like structure. This approach relies on the temperature-responsive cell culture technology and inherent ability of cells to self-organize and interact with one another to create functional tissue structures (Figure 5). Cells are cultured on temperature-responsive culture dishes or surfaces coated with a temperature-responsive polymer, such as poly(N-isopropylacrylamide) (PIPAAm), to form monolayer sheets. These polymers change their properties with temperature, allowing cells to adhere to the surface at 32 °C and detach as a sheet at 37 °C. Thus, the cell–cell junctions can be preserved, avoiding ECM damage caused by proteolytic enzymes [134]. Since the thickness limitation of 3D constructs without vascular networks is no more than 80 µm [135], co-culture cell sheet approaches have been proposed. Human umbilical vein endothelial cells have been reported to be co-cultured within human myoblast sheets to form capillary-like structures within the construct. Then, increased neovascularization and graft survival after transplantation were obtained [136].

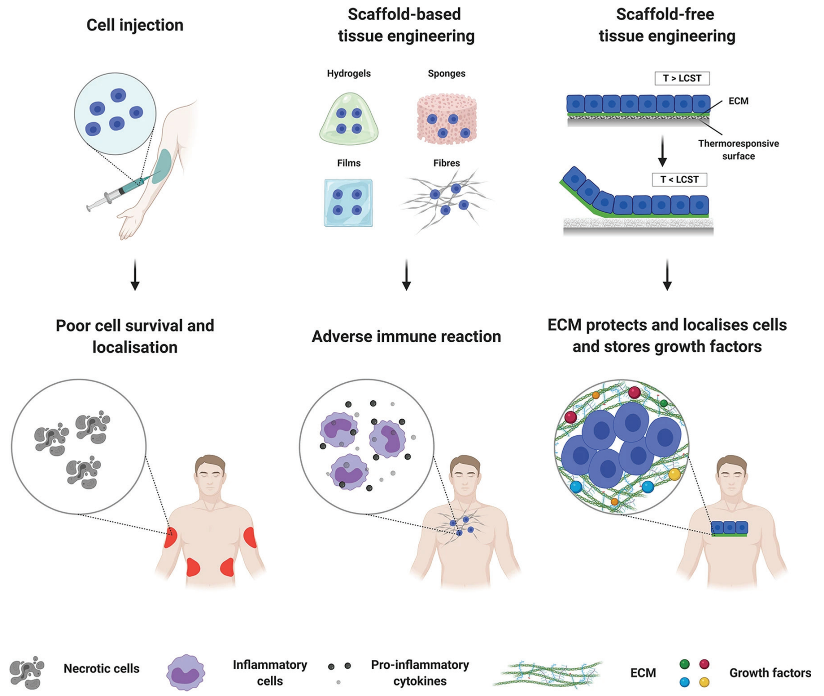

Figure 5. Cell-based tissue engineering therapies. Reprint from [134].

4. Conclusions and Further Expectations

Vascularization in craniofacial bone tissue engineering is a critical aspect of regenerating bone tissue in the craniofacial region. Craniofacial bone defects can result from various causes, including trauma, congenital anomalies, or surgical resection due to disease. To successfully regenerate bone in this region, ensuring the development of a functional vascular network is essential. This review paper therefore focused on the use of angiogenic growth factors, cell-based vascularization strategies, and surface morphology, porous characters, and the angiogenic release property of scaffolds.

Although experiments on neovascularization have shown encouraging results, how to establish the functional neovascular vessel with fast and mature anastomosis between neo and host vasculature and how to increase the osteogenic H type vessel ratio remains challenging. Further studies are required to address these issues and explore angiogenic mechanisms in craniofacial bone reconstruction.

Author Contributions: Conceptualization and supervision, H.Q. and J.C.; writing—original draft preparation, J.C.; writing—review and editing, Y.D., J.Y. and G.Z. All authors have read and agreed to the published version of the manuscript.

Funding: This research received no external funding.

Conflicts of Interest: The author declares no conflicts of interest.

References

1. Zhang, W.; Yelick, P.C. Craniofacial Tissue Engineering. *Cold Spring Harb. Perspect. Med.* **2018**, *8*, a025775. [CrossRef] [PubMed]
2. Hollý, D.; Klein, M.; Mazreku, M.; Zamborský, R.; Polák, Š.; Danišovič, Ľ.; Csöbönyeiová, M. Stem Cells and Their Derivatives-Implications for Alveolar Bone Regeneration: A Comprehensive Review. *Int. J. Mol. Sci.* **2021**, *22*, 11746. [CrossRef] [PubMed]
3. Aghali, A. Craniofacial Bone Tissue Engineering: Current Approaches and Potential Therapy. *Cells* **2021**, *10*, 2993. [CrossRef] [PubMed]
4. Martín-Del-Campo, M.; Rosales-Ibañez, R.; Rojo, L. Biomaterials for Cleft Lip and Palate Regeneration. *Int. J. Mol. Sci.* **2019**, *20*, 2176. [CrossRef]
5. Zhu, M.; Zhao, Z.; Xu, H.H.K.; Dai, Z.; Yu, K.; Xiao, L.; Schneider, A.; Weir, M.D.; Oates, T.W.; Bai, Y.; et al. Effects of Metformin Delivery via Biomaterials on Bone and Dental Tissue Engineering. *Int. J. Mol. Sci.* **2022**, *23*, 15905. [CrossRef]
6. Meijer, E.M.; van Dijk, C.G.M.; Kramann, R.; Verhaar, M.C.; Cheng, C. Implementation of Pericytes in Vascular Regeneration Strategies. *Tissue Eng. Part B Rev.* **2022**, *28*, 1–12. [CrossRef]
7. Tian, T.; Zhang, T.; Lin, Y.; Cai, X. Vascularization in Craniofacial Bone Tissue Engineering. *J. Dent. Res.* **2018**, *97*, 969–976. [CrossRef]
8. Salhotra, A.; Shah, H.N.; Levi, B.; Longaker, M.T. Mechanisms of bone development and repair. *Nat. Rev. Mol. Cell Biol.* **2020**, *21*, 696–711. [CrossRef]
9. Hasani-Sadrabadi, M.M.; Sarrion, P.; Pouraghaei, S.; Chau, Y.; Ansari, S.; Li, S.; Aghaloo, T.; Moshaverinia, A. An engineered cell-laden adhesive hydrogel promotes craniofacial bone tissue regeneration in rats. *Sci. Transl. Med.* **2020**, *12*, eaay6853. [CrossRef]
10. Kasper, F.K.; Melville, J.; Shum, J.; Wong, M.; Young, S. Tissue Engineered Prevascularized Bone and Soft Tissue Flaps. *Oral Maxillofac. Surg. Clin. N. Am.* **2017**, *29*, 63–73. [CrossRef]
11. Weiland, A.J.; Phillips, T.W.; Randolph, M.A. Bone grafts: A radiologic, histologic, and biomechanical model comparing autografts, allografts, and free vascularized bone grafts. *Plast. Reconstr. Surg.* **1984**, *74*, 368–379. [CrossRef]
12. Wu, X.; Zhou, M.; Jiang, F.; Yin, S.; Lin, S.; Yang, G.; Lu, Y.; Zhang, W.; Jiang, X. Marginal sealing around integral bilayer scaffolds for repairing osteochondral defects based on photocurable silk hydrogels. *Bioact. Mater.* **2021**, *6*, 3976–3986. [CrossRef] [PubMed]
13. Diomede, F.; Marconi, G.D.; Fonticoli, L.; Pizzicanella, J.; Merciaro, I.; Bramanti, P.; Mazzon, E.; Trubiani, O. Functional Relationship between Osteogenesis and Angiogenesis in Tissue Regeneration. *Int. J. Mol. Sci.* **2020**, *21*, 3242. [CrossRef] [PubMed]
14. Wu, L.; Liu, Z.; Xiao, L.; Ai, M.; Cao, Y.; Mao, J.; Song, K. The Role of Gli1(+) Mesenchymal Stem Cells in Osteogenesis of Craniofacial Bone. *Biomolecules* **2023**, *13*, 1351. [CrossRef]
15. Wei, X.; Zhou, W.; Tang, Z.; Wu, H.; Liu, Y.; Dong, H.; Wang, N.; Huang, H.; Bao, S.; Shi, L.; et al. Magnesium surface-activated 3D printed porous PEEK scaffolds for in vivo osseointegration by promoting angiogenesis and osteogenesis. *Bioact. Mater.* **2023**, *20*, 16–28. [CrossRef] [PubMed]
16. Noden, D.M. Embryonic origins and assembly of blood vessels. *Am. Rev. Respir. Dis.* **1989**, *140*, 1097–1103. [CrossRef] [PubMed]
17. Díaz Del Moral, S.; Barrena, S.; Muñoz-Chápuli, R.; Carmona, R. Embryonic circulating endothelial progenitor cells. *Angiogenesis* **2020**, *23*, 531–541. [CrossRef]
18. Moccia, F.; Negri, S.; Shekha, M.; Faris, P.; Guerra, G. Endothelial Ca^{2+} Signaling, Angiogenesis and Vasculogenesis: Just What It Takes to Make a Blood Vessel. *Int. J. Mol. Sci.* **2019**, *20*, 3962. [CrossRef]
19. Duan, X.; Bradbury, S.R.; Olsen, B.R.; Berendsen, A.D. VEGF stimulates intramembranous bone formation during craniofacial skeletal development. *Matrix Biol.* **2016**, *52–54*, 127–140. [CrossRef]
20. Hara, E.S.; Nagaoka, N.; Okada, M.; Nakano, T.; Matsumoto, T. Distinct Morphologies of Bone Apatite Clusters in Endochondral and Intramembranous Ossification. *Adv. Biol.* **2022**, *6*, e2200076. [CrossRef]
21. Percival, C.J.; Richtsmeier, J.T. Angiogenesis and intramembranous osteogenesis. *Dev. Dyn.* **2013**, *242*, 909–922. [CrossRef]
22. Ye, X.; He, J.; Wang, S.; Han, Q.; You, D.; Feng, B.; Zhao, F.; Yin, J.; Yu, M.; Wang, H.; et al. A hierarchical vascularized engineered bone inspired by intramembranous ossification for mandibular regeneration. *Int. J. Oral Sci.* **2022**, *14*, 31. [CrossRef]
23. Rouwkema, J.; Koopman, B.; Blitterswijk, C.; Dhert, W.; Malda, J. Supply of nutrients to cells in engineered tissues. *Biotechnol. Genet. Eng. Rev.* **2010**, *26*, 163–178. [CrossRef]
24. Place, T.L.; Domann, F.E.; Case, A.J. Limitations of oxygen delivery to cells in culture: An underappreciated problem in basic and translational research. *Free Radic. Biol. Med.* **2017**, *113*, 311–322. [CrossRef]
25. Owen-Woods, C.; Kusumbe, A. Fundamentals of bone vasculature: Specialization, interactions and functions. *Semin. Cell Dev. Biol.* **2022**, *123*, 36–47. [CrossRef]
26. Ramasamy, S.K.; Kusumbe, A.P.; Wang, L.; Adams, R.H. Endothelial Notch activity promotes angiogenesis and osteogenesis in bone. *Nature* **2014**, *507*, 376–380. [CrossRef]

27. Xu, Z.; Kusumbe, A.P.; Cai, H.; Wan, Q.; Chen, J. Type H blood vessels in coupling angiogenesis-osteogenesis and its application in bone tissue engineering. *J. Biomed. Mater. Res. B Appl. Biomater.* **2023**, *111*, 1434–1446. [CrossRef] [PubMed]
28. Ding, W.; Xu, C.; Zhang, Y.; Chen, H. Advances in the understanding of the role of type-H vessels in the pathogenesis of osteoporosis. *Arch. Osteoporos.* **2020**, *15*, 5. [CrossRef] [PubMed]
29. Huang, Y.; Wang, X.; Lin, H. The hypoxic microenvironment: A driving force for heterotopic ossification progression. *Cell Commun. Signal.* **2020**, *18*, 20. [CrossRef] [PubMed]
30. Dibble, M.; Di Cio, S.; Luo, P.; Balkwill, F.; Gautrot, J.E. The impact of pericytes on the stability of microvascular networks in response to nanoparticles. *Sci. Rep.* **2023**, *13*, 5729. [CrossRef]
31. Sweeney, M.D.; Ayyadurai, S.; Zlokovic, B.V. Pericytes of the neurovascular unit: Key functions and signaling pathways. *Nat. Neurosci.* **2016**, *19*, 771–783. [CrossRef] [PubMed]
32. Hao, D.; Xiao, W.; Liu, R.; Kumar, P.; Li, Y.; Zhou, P.; Guo, F.; Farmer, D.L.; Lam, K.S.; Wang, F.; et al. Discovery and Characterization of a Potent and Specific Peptide Ligand Targeting Endothelial Progenitor Cells and Endothelial Cells for Tissue Regeneration. *ACS Chem. Biol.* **2017**, *12*, 1075–1086. [CrossRef]
33. Shi, H.; Zhao, Z.; Jiang, W.; Zhu, P.; Zhou, N.; Huang, X. A Review Into the Insights of the Role of Endothelial Progenitor Cells on Bone Biology. *Front. Cell Dev. Biol.* **2022**, *10*, 878697. [CrossRef]
34. Zhan, K.; Bai, L.; Xu, J. Role of vascular endothelial progenitor cells in construction of new vascular loop. *Microvasc. Res.* **2013**, *90*, 1–11. [CrossRef] [PubMed]
35. Lopes-Coelho, F.; Silva, F.; Gouveia-Fernandes, S.; Martins, C.; Lopes, N.; Domingues, G.; Brito, C.; Almeida, A.M.; Pereira, S.A.; Serpa, J. Monocytes as Endothelial Progenitor Cells (EPCs), Another Brick in the Wall to Disentangle Tumor Angiogenesis. *Cells* **2020**, *9*, 107. [CrossRef]
36. Figueiredo, A.M.; Barbacena, P.; Russo, A.; Vaccaro, S.; Ramalho, D.; Pena, A.; Lima, A.P.; Ferreira, R.R.; Fidalgo, M.A.; El-Marjou, F.; et al. Endothelial cell invasion is controlled by dactylopodia. *Proc. Natl. Acad. Sci. USA* **2021**, *118*, e2023829118. [CrossRef]
37. Potente, M.; Carmeliet, P. The Link Between Angiogenesis and Endothelial Metabolism. *Annu. Rev. Physiol.* **2017**, *79*, 43–66. [CrossRef]
38. Eldridge, L.; Wagner, E.M. Angiogenesis in the lung. *J. Physiol.* **2019**, *597*, 1023–1032. [CrossRef] [PubMed]
39. Blanco, R.; Gerhardt, H. VEGF and Notch in tip and stalk cell selection. *Cold Spring Harb. Perspect. Med.* **2013**, *3*, a006569. [CrossRef]
40. Ben-Shaul, S.; Landau, S.; Merdler, U.; Levenberg, S. Mature vessel networks in engineered tissue promote graft–host anastomosis and prevent graft thrombosis. *Proc. Natl. Acad. Sci. USA* **2019**, *116*, 2955–2960. [CrossRef]
41. Gao, X.; Yourick, J.J.; Sprando, R.L. Comparative transcriptomic analysis of endothelial progenitor cells derived from umbilical cord blood and adult peripheral blood: Implications for the generation of induced pluripotent stem cells. *Stem Cell Res.* **2017**, *25*, 202–212. [CrossRef]
42. Gao, X.; Yourick, J.J.; Sprando, R.L. Generation of Human Induced Pluripotent Stem Cells Using Endothelial Progenitor Cells Derived from Umbilical Cord Blood and Adult Peripheral Blood. *Methods Mol. Biol.* **2022**, *2454*, 381–396. [CrossRef] [PubMed]
43. Yan, F.; Liu, X.; Ding, H.; Zhang, W. Paracrine mechanisms of endothelial progenitor cells in vascular repair. *Acta Histochem.* **2022**, *124*, 151833. [CrossRef] [PubMed]
44. Yan, F.; Li, J.; Zhang, W. Transplantation of Endothelial Progenitor Cells: Summary and prospect. *Acta Histochem.* **2023**, *125*, 151990. [CrossRef]
45. Seebach, C.; Henrich, D.; Wilhelm, K.; Barker, J.H.; Marzi, I. Endothelial progenitor cells improve directly and indirectly early vascularization of mesenchymal stem cell-driven bone regeneration in a critical bone defect in rats. *Cell Transplant.* **2012**, *21*, 1667–1677. [CrossRef] [PubMed]
46. Shi, W.; Xin, Q.; Yuan, R.; Yuan, Y.; Cong, W.; Chen, K. Neovascularization: The Main Mechanism of MSCs in Ischemic Heart Disease Therapy. *Front. Cardiovasc. Med.* **2021**, *8*, 633300. [CrossRef] [PubMed]
47. Armulik, A.; Abramsson, A.; Betsholtz, C. Endothelial/Pericyte Interactions. *Circ. Res.* **2005**, *97*, 512–523. [CrossRef] [PubMed]
48. Payne, L.B.; Hoque, M.; Houk, C.; Darden, J.; Chappell, J.C. Pericytes in Vascular Development. *Curr. Tissue Microenviron. Rep.* **2020**, *1*, 143–154. [CrossRef]
49. Selvam, S.; Kumar, T.; Fruttiger, M. Retinal vasculature development in health and disease. *Prog. Retin. Eye Res.* **2018**, *63*, 1–19. [CrossRef]
50. Shibuya, M. Vascular Endothelial Growth Factor (VEGF) and Its Receptor (VEGFR) Signaling in Angiogenesis: A Crucial Target for Anti- and Pro-Angiogenic Therapies. *Genes Cancer* **2011**, *2*, 1097–1105. [CrossRef]
51. Abdulkadir, S.; Li, C.; Jiang, W.; Zhao, X.; Sang, P.; Wei, L.; Hu, Y.; Li, Q.; Cai, J. Modulating Angiogenesis by Proteomimetics of Vascular Endothelial Growth Factor. *J. Am. Chem. Soc.* **2022**, *144*, 270–281. [CrossRef]
52. Kivelä, R.; Hemanthakumar, K.A.; Vaparanta, K.; Robciuc, M.; Izumiya, Y.; Kidoya, H.; Takakura, N.; Peng, X.; Sawyer, D.B.; Elenius, K.; et al. Endothelial Cells Regulate Physiological Cardiomyocyte Growth via VEGFR2-Mediated Paracrine Signaling. *Circulation* **2019**, *139*, 2570–2584. [CrossRef]
53. Sawada, N.; Arany, Z. Metabolic Regulation of Angiogenesis in Diabetes and Aging. *Physiology* **2017**, *32*, 290–307. [CrossRef]
54. Tiemeijer, L.A.; Frimat, J.P.; Stassen, O.; Bouten, C.V.C.; Sahlgren, C.M. Spatial patterning of the Notch ligand Dll4 controls endothelial sprouting in vitro. *Sci. Rep.* **2018**, *8*, 6392. [CrossRef]

55. Su, W.; Liu, G.; Liu, X.; Zhou, Y.; Sun, Q.; Zhen, G.; Wang, X.; Hu, Y.; Gao, P.; Demehri, S.; et al. Angiogenesis stimulated by elevated PDGF-BB in subchondral bone contributes to osteoarthritis development. *JCI Insight* **2020**, *5*, e135446. [CrossRef]
56. Hosaka, K.; Yang, Y.; Nakamura, M.; Andersson, P.; Yang, X.; Zhang, Y.; Seki, T.; Scherzer, M.; Dubey, O.; Wang, X.; et al. Dual roles of endothelial FGF-2–FGFR1–PDGF-BB and perivascular FGF-2–FGFR2–PDGFRβ signaling pathways in tumor vascular remodeling. *Cell Discov.* **2018**, *4*, 3. [CrossRef]
57. Hellström, M.; Phng, L.-K.; Hofmann, J.J.; Wallgard, E.; Coultas, L.; Lindblom, P.; Alva, J.; Nilsson, A.-K.; Karlsson, L.; Gaiano, N.; et al. Dll4 signalling through Notch1 regulates formation of tip cells during angiogenesis. *Nature* **2007**, *445*, 776–780. [CrossRef] [PubMed]
58. Noguera-Troise, I.; Daly, C.; Papadopoulos, N.J.; Coetzee, S.; Boland, P.; Gale, N.W.; Lin, H.C.; Yancopoulos, G.D.; Thurston, G. Blockade of Dll4 inhibits tumour growth by promoting non-productive angiogenesis. *Nature* **2006**, *444*, 1032–1037. [CrossRef] [PubMed]
59. Graham, A.M.; Presnell, J.S. Hypoxia Inducible Factor (HIF) transcription factor family expansion, diversification, divergence and selection in eukaryotes. *PLoS ONE* **2017**, *12*, e0179545. [CrossRef] [PubMed]
60. Peng, Y.; Wu, S.; Li, Y.; Crane, J.L. Type H blood vessels in bone modeling and remodeling. *Theranostics* **2020**, *10*, 426–436. [CrossRef] [PubMed]
61. Westra, J.; Molema, G.; Kallenberg, C.G.M. Hypoxia-inducible factor-1 as regulator of angiogenesis in rheumatoid arthritis—Therapeutic implications. *Curr. Med. Chem.* **2010**, *17*, 254–263. [CrossRef]
62. Chen, Y.-Y.; Brown, N.J.; Jones, R.; Lewis, C.E.; Mujamammi, A.H.; Muthana, M.; Seed, M.P.; Barker, M.D. A peptide derived from TIMP-3 inhibits multiple angiogenic growth factor receptors and tumour growth and inflammatory arthritis in mice. *Angiogenesis* **2014**, *17*, 207–219. [CrossRef]
63. Xu, Y.; Lu, X.; Hu, Y.; Yang, B.; Tsui, C.-K.; Yu, S.; Lu, L.; Liang, X. Melatonin attenuated retinal neovascularization and neuroglial dysfunction by inhibition of HIF-1α-VEGF pathway in oxygen-induced retinopathy mice. *J. Pineal Res.* **2018**, *64*, e12473. [CrossRef]
64. Chen, W.; Wu, P.; Yu, F.; Luo, G.; Qing, L.; Tang, J. HIF-1α Regulates Bone Homeostasis and Angiogenesis, Participating in the Occurrence of Bone Metabolic Diseases. *Cells* **2022**, *11*, 3552. [CrossRef] [PubMed]
65. Garbo, C.; Locs, J.; D'Este, M.; Demazeau, G.; Mocanu, A.; Roman, C.; Horovitz, O.; Tomoaia-Cotisel, M. Advanced Mg, Zn, Sr, Si Multi-Substituted Hydroxyapatites for Bone Regeneration. *Int. J. Nanomed.* **2020**, *15*, 1037–1058. [CrossRef]
66. Fiorati, A.; Linciano, C.; Galante, C.; Raucci, M.G.; Altomare, L. Bioactive Hydrogels: Design and Characterization of Cellulose-Derived Injectable Composites. *Materials* **2021**, *14*, 4511. [CrossRef]
67. LeGeros, R.Z. Properties of osteoconductive biomaterials: Calcium phosphates. *Clin. Orthop. Relat. Res.* **2002**, *395*, 81–98. [CrossRef]
68. Hu, D.; Ren, Q.; Li, Z.; Zhang, L. Chitosan-Based Biomimetically Mineralized Composite Materials in Human Hard Tissue Repair. *Molecules* **2020**, *25*, 4785. [CrossRef]
69. Yuan, Z.; Wan, Z.; Gao, C.; Wang, Y.; Huang, J.; Cai, Q. Controlled magnesium ion delivery system for in situ bone tissue engineering. *J. Control Release* **2022**, *350*, 360–376. [CrossRef]
70. Hong, B.Z.; Piao, H.N.; Li, S.F.; Piao, H.; Jin, L.; Cao, P.A. Evidence for a major role of Mg^{2+} in VEGF165-mediated angiogenesis. *Zhonghua Xin Xue Guan Bing Za Zhi* **2007**, *35*, 260–264. [PubMed]
71. Negri, S.; Faris, P.; Berra-Romani, R.; Guerra, G.; Moccia, F. Endothelial Transient Receptor Potential Channels and Vascular Remodeling: Extracellular Ca^{2+} Entry for Angiogenesis, Arteriogenesis and Vasculogenesis. *Front. Physiol.* **2019**, *10*, 1618. [CrossRef]
72. Fan, L.; Körte, F.; Rudt, A.; Jung, O.; Burkhardt, C.; Barbeck, M.; Xiong, X. Encapsulated vaterite-calcite $CaCO_3$ particles loaded with Mg^{2+} and Cu^{2+} ions with sustained release promoting osteogenesis and angiogenesis. *Front. Bioeng. Biotechnol.* **2022**, *10*, 983988. [CrossRef]
73. Wang, L.; Pang, Y.; Tang, Y.; Wang, X.; Zhang, D.; Zhang, X.; Yu, Y.; Yang, X.; Cai, Q. A biomimetic piezoelectric scaffold with sustained Mg^{2+} release promotes neurogenic and angiogenic differentiation for enhanced bone regeneration. *Bioact. Mater.* **2023**, *25*, 399–414. [CrossRef] [PubMed]
74. Liu, W.; Guo, S.; Tang, Z.; Wei, X.; Gao, P.; Wang, N.; Li, X.; Guo, Z. Magnesium promotes bone formation and angiogenesis by enhancing MC3T3-E1 secretion of PDGF-BB. *Biochem. Biophys. Res. Commun.* **2020**, *528*, 664–670. [CrossRef] [PubMed]
75. Wan, Z.; Yuan, Z.; Li, Y.; Zhang, Y.; Wang, Y.; Yu, Y.; Mao, J.; Cai, Q.; Yang, X. Hierarchical Therapeutic Ion-Based Microspheres with Precise Ratio-Controlled Delivery as Microscaffolds for In Situ Vascularized Bone Regeneration. *Adv. Funct. Mater.* **2022**, *32*, 2113280. [CrossRef]
76. Bosch-Rué, E.; Díez-Tercero, L.; Rodríguez-González, R.; Bosch-Canals, B.M.; Perez, R.A. Assessing the potential role of copper and cobalt in stimulating angiogenesis for tissue regeneration. *PLoS ONE* **2021**, *16*, e0259125. [CrossRef] [PubMed]
77. Lin, Z.; Cao, Y.; Zou, J.; Zhu, F.; Gao, Y.; Zheng, X.; Wang, H.; Zhang, T.; Wu, T. Improved osteogenesis and angiogenesis of a novel copper ions doped calcium phosphate cement. *Mater. Sci. Eng. C Mater. Biol. Appl.* **2020**, *114*, 111032. [CrossRef] [PubMed]
78. Tai, Z.; Li, L.; Zhao, G.; Liu, J.X. Copper stress impairs angiogenesis and lymphangiogenesis during zebrafish embryogenesis by down-regulating pERK1/2-foxm1-MMP2/9 axis and epigenetically regulating ccbe1 expression. *Angiogenesis* **2022**, *25*, 241–257. [CrossRef] [PubMed]

79. Zhang, M.; Yao, A.; Ai, F.; Lin, J.; Fu, Q.; Wang, D. Cobalt-containing borate bioactive glass fibers for treatment of diabetic wound. *J. Mater. Sci. Mater. Med.* **2023**, *34*, 42. [CrossRef]
80. Poliseno, L.; Tuccoli, A.; Mariani, L.; Evangelista, M.; Citti, L.; Woods, K.; Mercatanti, A.; Hammond, S.; Rainaldi, G. MicroRNAs modulate the angiogenic properties of HUVECs. *Blood* **2006**, *108*, 3068–3071. [CrossRef]
81. Zhuang, Y.; Cheng, M.; Li, M.; Cui, J.; Huang, J.; Zhang, C.; Si, J.; Lin, K.; Yu, H. Small extracellular vesicles derived from hypoxic mesenchymal stem cells promote vascularized bone regeneration through the miR-210-3p/EFNA3/PI3K pathway. *Acta Biomater.* **2022**, *150*, 413–426. [CrossRef]
82. Castaño, I.M.; Raftery, R.M.; Chen, G.; Cavanagh, B.; Quinn, B.; Duffy, G.P.; Curtin, C.M.; O'Brien, F.J. Dual scaffold delivery of miR-210 mimic and miR-16 inhibitor enhances angiogenesis and osteogenesis to accelerate bone healing. *Acta Biomater.* **2023**, *172*, 480–493. [CrossRef]
83. Besnier, M.; Gasparino, S.; Vono, R.; Sangalli, E.; Facoetti, A.; Bollati, V.; Cantone, L.; Zaccagnini, G.; Maimone, B.; Fuschi, P.; et al. miR-210 Enhances the Therapeutic Potential of Bone-Marrow-Derived Circulating Proangiogenic Cells in the Setting of Limb Ischemia. *Mol. Ther.* **2018**, *26*, 1694–1705. [CrossRef] [PubMed]
84. Nan, K.; Zhang, Y.; Zhang, X.; Li, D.; Zhao, Y.; Jing, Z.; Liu, K.; Shang, D.; Geng, Z.; Fan, L. Exosomes from miRNA-378-modified adipose-derived stem cells prevent glucocorticoid-induced osteonecrosis of the femoral head by enhancing angiogenesis and osteogenesis via targeting miR-378 negatively regulated suppressor of fused (Sufu). *Stem Cell Res. Ther.* **2021**, *12*, 331. [CrossRef] [PubMed]
85. Lee, D.Y.; Deng, Z.; Wang, C.H.; Yang, B.B. MicroRNA-378 promotes cell survival, tumor growth, and angiogenesis by targeting SuFu and Fus-1 expression. *Proc. Natl. Acad. Sci. USA* **2007**, *104*, 20350–20355. [CrossRef] [PubMed]
86. Liu, W.; Li, L.; Rong, Y.; Qian, D.; Chen, J.; Zhou, Z.; Luo, Y.; Jiang, D.; Cheng, L.; Zhao, S.; et al. Hypoxic mesenchymal stem cell-derived exosomes promote bone fracture healing by the transfer of miR-126. *Acta Biomater.* **2020**, *103*, 196–212. [CrossRef] [PubMed]
87. Jia, Y.; Zhu, Y.; Qiu, S.; Xu, J.; Chai, Y. Exosomes secreted by endothelial progenitor cells accelerate bone regeneration during distraction osteogenesis by stimulating angiogenesis. *Stem Cell Res. Ther.* **2019**, *10*, 12. [CrossRef] [PubMed]
88. Qu, Q.; Liu, L.; Cui, Y.; Liu, H.; Yi, J.; Bing, W.; Liu, C.; Jiang, D.; Bi, Y. miR-126-3p containing exosomes derived from human umbilical cord mesenchymal stem cells promote angiogenesis and attenuate ovarian granulosa cell apoptosis in a preclinical rat model of premature ovarian failure. *Stem Cell Res. Ther.* **2022**, *13*, 352. [CrossRef] [PubMed]
89. Tang, Y.; Chen, Y.; Guo, Q.; Zhang, L.; Liu, H.; Wang, S.; Wu, X.; Shen, X.; Tao, L. MiR-126-Loaded Immunoliposomes against Vascular Endothelial Inflammation In Vitro and Vivo Evaluation. *Pharmaceutics* **2023**, *15*, 1379. [CrossRef]
90. Chamorro-Jorganes, A.; Lee, M.Y.; Araldi, E.; Landskroner-Eiger, S.; Fernández-Fuertes, M.; Sahraei, M.; Quiles Del Rey, M.; van Solingen, C.; Yu, J.; Fernández-Hernando, C.; et al. VEGF-Induced Expression of miR-17-92 Cluster in Endothelial Cells Is Mediated by ERK/ELK1 Activation and Regulates Angiogenesis. *Circ. Res.* **2016**, *118*, 38–47. [CrossRef]
91. He, Y.; Li, H.; Yu, Z.; Li, L.; Chen, X.; Yang, A.; Lyu, F.; Dong, Y. Exosomal let-7f-5p derived from mineralized osteoblasts promotes the angiogenesis of endothelial cells via the DUSP1/Erk1/2 signaling pathway. *J. Tissue Eng. Regen. Med.* **2022**, *16*, 1184–1195. [CrossRef]
92. Li, Q.; Yu, T.; Wang, F.; Liu, X.; Wang, Z. Endothelial progenitor cells with stem cells enhance osteogenic efficacy. *Am. J. Transl. Res.* **2020**, *12*, 2409–2424.
93. Zigdon-Giladi, H.; Bick, T.; Lewinson, D.; Machtei, E.E. Co-transplantation of endothelial progenitor cells and mesenchymal stem cells promote neovascularization and bone regeneration. *Clin. Implant Dent. Relat. Res.* **2015**, *17*, 353–359. [CrossRef] [PubMed]
94. Xu, C.; Liu, H.; He, Y.; Li, Y.; He, X. Endothelial progenitor cells promote osteogenic differentiation in co-cultured with mesenchymal stem cells via the MAPK-dependent pathway. *Stem Cell Res. Ther.* **2020**, *11*, 537. [CrossRef]
95. Goerke, S.M.; Obermeyer, J.; Plaha, J.; Stark, G.B.; Finkenzeller, G. Endothelial progenitor cells from peripheral blood support bone regeneration by provoking an angiogenic response. *Microvasc. Res.* **2015**, *98*, 40–47. [CrossRef]
96. Gianni-Barrera, R.; Butschkau, A.; Uccelli, A.; Certelli, A.; Valente, P.; Bartolomeo, M.; Groppa, E.; Burger, M.G.; Hlushchuk, R.; Heberer, M.; et al. PDGF-BB regulates splitting angiogenesis in skeletal muscle by limiting VEGF-induced endothelial proliferation. *Angiogenesis* **2018**, *21*, 883–900. [CrossRef]
97. Sun, Y.; Zhao, Z.; Qiao, Q.; Li, S.; Yu, W.; Guan, X.; Schneider, A.; Weir, M.D.; Xu, H.H.K.; Zhang, K.; et al. Injectable periodontal ligament stem cell-metformin-calcium phosphate scaffold for bone regeneration and vascularization in rats. *Dent. Mater. J.* **2023**, *39*, 872–885. [CrossRef]
98. Luo, R.; Huang, Y.; Yuan, X.; Yuan, Z.; Zhang, L.; Han, J.; Zhao, Y.; Cai, Q. Controlled co-delivery system of magnesium and lanthanum ions for vascularized bone regeneration. *Biomed. Mater.* **2021**, *16*, 065024. [CrossRef] [PubMed]
99. Putranti, N.A.R.; Kunimatsu, R.; Rikitake, K.; Hiraki, T.; Nakajima, K.; Abe, T.; Tsuka, Y.; Sakata, S.; Nakatani, A.; Nikawa, H.; et al. Combination of Carbonate Hydroxyapatite and Stem Cells from Human Deciduous Teeth Promotes Bone Regeneration by Enhancing BMP-2, VEGF and CD31 Expression in Immunodeficient Mice. *Cells* **2022**, *11*, 1914. [CrossRef] [PubMed]
100. Liu, K.; Meng, C.X.; Lv, Z.Y.; Zhang, Y.J.; Li, J.; Li, K.Y.; Liu, F.Z.; Zhang, B.; Cui, F.Z. Enhancement of BMP-2 and VEGF carried by mineralized collagen for mandibular bone regeneration. *Regen. Biomater.* **2020**, *7*, 435–440. [CrossRef]
101. Zhou, J.; Li, Y.; He, J.; Liu, L.; Hu, S.; Guo, M.; Liu, T.; Liu, J.; Wang, J.; Guo, B.; et al. ROS Scavenging Graphene-Based Hydrogel Enhances Type H Vessel Formation and Vascularized Bone Regeneration via ZEB1/Notch1 Mediation. *Macromol. Biosci.* **2023**, *23*, e2200502. [CrossRef]

102. Omar, O.; Engstrand, T.; Kihlström Burenstam Linder, L.; Åberg, J.; Shah, F.A.; Palmquist, A.; Birgersson, U.; Elgali, I.; Pujari-Palmer, M.; Engqvist, H.; et al. In situ bone regeneration of large cranial defects using synthetic ceramic implants with a tailored composition and design. *Proc. Natl. Acad. Sci. USA* **2020**, *117*, 26660–26671. [CrossRef]
103. Tang, Y.; Tong, X.; Conrad, B.; Yang, F. Injectable and in situ crosslinkable gelatin microribbon hydrogels for stem cell delivery and bone regeneration in vivo. *Theranostics* **2020**, *10*, 6035–6047. [CrossRef]
104. He, Y.; Lin, S.; Ao, Q.; He, X. The co-culture of ASCs and EPCs promotes vascularized bone regeneration in critical-sized bone defects of cranial bone in rats. *Stem Cell. Res. Ther.* **2020**, *11*, 338. [CrossRef]
105. Wang, M.M.; Flores, R.L.; Witek, L.; Torroni, A.; Ibrahim, A.; Wang, Z.; Liss, H.A.; Cronstein, B.N.; Lopez, C.D.; Maliha, S.G.; et al. Dipyridamole-loaded 3D-printed bioceramic scaffolds stimulate pediatric bone regeneration in vivo without disruption of craniofacial growth through facial maturity. *Sci. Rep.* **2019**, *9*, 18439. [CrossRef] [PubMed]
106. Zhang, W.; Saxena, S.; Fakhrzadeh, A.; Rudolph, S.; Young, S.; Kohn, J.; Yelick, P.C. Use of Human Dental Pulp and Endothelial Cell Seeded Tyrosine-Derived Polycarbonate Scaffolds for Robust in vivo Alveolar Jaw Bone Regeneration. *Front. Bioeng. Biotechnol.* **2020**, *8*, 796.
107. Dewey, M.J.; Milner, D.J.; Weisgerber, D.; Flanagan, C.L.; Rubessa, M.; Lotti, S.; Polkoff, K.M.; Crotts, S.; Hollister, S.J.; Wheeler, M.B.; et al. Repair of critical-size porcine craniofacial bone defects using a collagen-polycaprolactone composite biomaterial. *Biofabrication* **2021**, *14*, 014102. [CrossRef] [PubMed]
108. Wan, Q.Q.; Jiao, K.; Ma, Y.X.; Gao, B.; Mu, Z.; Wang, Y.R.; Wang, Y.H.; Duan, L.; Xu, K.H.; Gu, J.T.; et al. Smart, Biomimetic Periosteum Created from the Cerium(III, IV) Oxide-Mineralized Eggshell Membrane. *ACS Appl. Mater. Interfaces* **2022**, *14*, 14103–14119. [CrossRef] [PubMed]
109. Kang, Y.; Xu, J.; Meng, L.; Su, Y.; Fang, H.; Liu, J.; Cheng, Y.Y.; Jiang, D.; Nie, Y.; Song, K. 3D bioprinting of dECM/Gel/QCS/nHAp hybrid scaffolds laden with mesenchymal stem cell-derived exosomes to improve angiogenesis and osteogenesis. *Biofabrication* **2023**, *15*, 024103. [CrossRef] [PubMed]
110. Zhao, Z.; Sun, Y.; Qiao, Q.; Weir, M.D.; Schneider, A.; Masri, R.; Lynch, C.D.; Zhang, N.; Zhang, K.; Bai, Y.; et al. Calvaria defect regeneration via human periodontal ligament stem cells and prevascularized scaffolds in athymic rats. *J. Dent.* **2023**, *138*, 104690. [CrossRef]
111. Autefage, H.; Allen, F.; Tang, H.M.; Kallepitis, C.; Gentleman, E.; Reznikov, N.; Nitiputri, K.; Nommeots-Nomm, A.; O'Donnell, M.D.; Lange, C.; et al. Multiscale analyses reveal native-like lamellar bone repair and near perfect bone-contact with porous strontium-loaded bioactive glass. *Biomaterials* **2019**, *209*, 152–162. [CrossRef]
112. Saskianti, T.; Nugraha, A.P.; Prahasanti, C.; Ernawati, D.S.; Tanimoto, K.; Riawan, W.; Kanawa, M.; Kawamoto, T.; Fujimoto, K. Study of Alveolar Bone Remodeling Using Deciduous Tooth Stem Cells and Hydroxyapatite by Vascular Endothelial Growth Factor Enhancement and Inhibition of Matrix Metalloproteinase-8 Expression in vivo. *Clin. Cosmet. Investig. Dent.* **2022**, *14*, 71–78. [CrossRef]
113. Ma, W.; Lyu, H.; Pandya, M.; Gopinathan, G.; Luan, X.; Diekwisch, T.G.H. Successful Application of a Galanin-Coated Scaffold for Periodontal Regeneration. *J. Dent. Res.* **2021**, *100*, 1144–1152. [CrossRef]
114. Kurobane, T.; Shiwaku, Y.; Anada, T.; Hamai, R.; Tsuchiya, K.; Baba, K.; Iikubo, M.; Takahashi, T.; Suzuki, O. Angiogenesis involvement by octacalcium phosphate-gelatin composite-driven bone regeneration in rat calvaria critical-sized defect. *Acta Biomater.* **2019**, *88*, 514–526. [CrossRef]
115. Pandya, M.; Saxon, M.; Bozanich, J.; Tillberg, C.; Luan, X.; Diekwisch, T.G.H. The Glycoprotein/Cytokine Erythropoietin Promotes Rapid Alveolar Ridge Regeneration In Vivo by Promoting New Bone Extracellular Matrix Deposition in Conjunction with Coupled Angiogenesis/Osteogenesis. *Int. J. Mol. Sci.* **2021**, *22*, 2788. [CrossRef]
116. Tenkumo, T.; Kruse, B.; Kostka, K.; Sokolova, V.; Ogawa, T.; Yoda, N.; Prymak, O.; Suzuki, O.; Sasaki, K.; Epple, M. Development of triple-functionalized calcium phosphate nanoparticles as an advanced drug delivery system for bone tissue repair. *Regen. Ther.* **2024**, *25*, 49–60. [CrossRef] [PubMed]
117. Park, H.; Collignon, A.M.; Lepry, W.C.; Ramirez-GarciaLuna, J.L.; Rosenzweig, D.H.; Chaussain, C.; Nazhat, S.N. Acellular dense collagen-S53P4 bioactive glass hybrid gel scaffolds form more bone than stem cell delivered constructs. *Mater. Sci. Eng. C Mater. Biol. Appl.* **2021**, *120*, 111743. [CrossRef] [PubMed]
118. Asri, R.I.M.; Harun, W.S.W.; Hassan, M.A.; Ghani, S.A.C.; Buyong, Z. A review of hydroxyapatite-based coating techniques: Sol–gel and electrochemical depositions on biocompatible metals. *J. Mech. Behav. Biomed. Mater.* **2016**, *57*, 95–108. [CrossRef] [PubMed]
119. Liu, Y.; Huse, R.O.; de Groot, K.; Buser, D.; Hunziker, E.B. Delivery mode and efficacy of BMP-2 in association with implants. *J. Dent. Res.* **2007**, *86*, 84–89. [CrossRef] [PubMed]
120. Yu, X.; Wang, L.; Jiang, X.; Rowe, D.; Wei, M. Biomimetic CaP coating incorporated with parathyroid hormone improves the osseointegration of titanium implant. *J. Mater. Sci. Mater. Med.* **2012**, *23*, 2177–2186. [CrossRef] [PubMed]
121. Hagi, T.T.; Wu, G.; Liu, Y.; Hunziker, E.B. Cell-mediated BMP-2 liberation promotes bone formation in a mechanically unstable implant environment. *Bone* **2010**, *46*, 1322–1327. [CrossRef]
122. Jacobs, E.E.; Gronowicz, G.; Hurley, M.M.; Kuhn, L.T. Biomimetic calcium phosphate/polyelectrolyte multilayer coatings for sequential delivery of multiple biological factors. *J. Biomed. Mater. Res. A* **2017**, *105*, 1500–1509. [CrossRef]
123. Alhamdi, J.R.; Peng, T.; Al-Naggar, I.M.; Hawley, K.L.; Spiller, K.L.; Kuhn, L.T. Controlled M1-to-M2 transition of aged macrophages by calcium phosphate coatings. *Biomaterials* **2019**, *196*, 90–99. [CrossRef]

124. Siebers, M.C.; Walboomers, X.F.; Leeuwenburgh, S.C.; Wolke, J.G.; Jansen, J.A. Electrostatic spray deposition (ESD) of calcium phosphate coatings, an in vitro study with osteoblast-like cells. *Biomaterials* **2004**, *25*, 2019–2027. [CrossRef]
125. Graziani, G.; Bianchi, M.; Sassoni, E.; Russo, A.; Marcacci, M. Ion-substituted calcium phosphate coatings deposited by plasma-assisted techniques: A review. *Mater. Sci. Eng. C Mater. Biol. Appl.* **2017**, *74*, 219–229. [CrossRef]
126. Hadjizadeh, A.; Doillon, C.J. Directional migration of endothelial cells towards angiogenesis using polymer fibres in a 3D co-culture system. *J. Tissue Eng. Regen. Med.* **2010**, *4*, 524–531. [CrossRef]
127. Yu, J.; Gu, Y.; Du, K.T.; Mihardja, S.; Sievers, R.E.; Lee, R.J. The effect of injected RGD modified alginate on angiogenesis and left ventricular function in a chronic rat infarct model. *Biomaterials* **2009**, *30*, 751–756. [CrossRef]
128. Hao, D.; Fan, Y.; Xiao, W.; Liu, R.; Pivetti, C.; Walimbe, T.; Guo, F.; Zhang, X.; Farmer, D.L.; Wang, F.; et al. Rapid endothelialization of small diameter vascular grafts by a bioactive integrin-binding ligand specifically targeting endothelial progenitor cells and endothelial cells. *Acta Biomater.* **2020**, *108*, 178–193. [CrossRef] [PubMed]
129. Walimbe, T.; Dehghani, T.; Casella, A.; Lin, J.; Wang, A.; Panitch, A. Proangiogenic Collagen-Binding Glycan Therapeutic Promotes Endothelial Cell Angiogenesis. *ACS Biomater. Sci. Eng.* **2021**, *7*, 3281–3292. [CrossRef] [PubMed]
130. Abbasi, N.; Hamlet, S.; Love, R.M.; Nguyen, N.-T. Porous scaffolds for bone regeneration. *J. Sci. Adv. Mater. Devices* **2020**, *5*, 1–9. [CrossRef]
131. Dreyer, C.H.; Kjaergaard, K.; Ding, M.; Qin, L. Vascular endothelial growth factor for in vivo bone formation: A systematic review. *J. Orthop. Translat.* **2020**, *24*, 46–57. [CrossRef] [PubMed]
132. Wernike, E.; Montjovent, M.O.; Liu, Y.; Wismeijer, D.; Hunziker, E.B.; Siebenrock, K.A.; Hofstetter, W.; Klenke, F.M. VEGF incorporated into calcium phosphate ceramics promotes vascularisation and bone formation in vivo. *Eur. Cell Mater.* **2010**, *19*, 30–40. [CrossRef] [PubMed]
133. Burger, M.G.; Grosso, A.; Briquez, P.S.; Born, G.M.E.; Lunger, A.; Schrenk, F.; Todorov, A.; Sacchi, V.; Hubbell, J.A.; Schaefer, D.J.; et al. Robust coupling of angiogenesis and osteogenesis by VEGF-decorated matrices for bone regeneration. *Acta Biomater.* **2022**, *149*, 111–125. [CrossRef] [PubMed]
134. De Pieri, A.; Rochev, Y.; Zeugolis, D.I. Scaffold-free cell-based tissue engineering therapies: Advances, shortfalls and forecast. *NPJ Regen. Med.* **2021**, *6*, 18. [CrossRef]
135. Shimizu, T.; Sekine, H.; Yang, J.; Isoi, Y.; Yamato, M.; Kikuchi, A.; Kobayashi, E.; Okano, T. Polysurgery of cell sheet grafts overcomes diffusion limits to produce thick, vascularized myocardial tissues. *FASEB J. Off. Publ. Fed. Am. Soc. Exp. Biol.* **2006**, *20*, 708–710. [CrossRef]
136. Sasagawa, T.; Shimizu, T.; Sekiya, S.; Haraguchi, Y.; Yamato, M.; Sawa, Y.; Okano, T. Design of prevascularized three-dimensional cell-dense tissues using a cell sheet stacking manipulation technology. *Biomaterials* **2010**, *31*, 1646–1654. [CrossRef]

coatings

Review

Advances of Sulfonated Hyaluronic Acid in Biomaterials and Coatings—A Review

Mujahid Iqbal [1], Aqeela Yasin [1], Ambreen Akram [1], Jing-An Li [1,]* and Kun Zhang [2,]*

[1] School of Materials Science and Engineering, Zhengzhou University, Zhengzhou 450001, China; mujahidiqbal@gs.zzu.edu.cn (M.I.); aqeelayasinuaf@gmail.com (A.Y.); ambreenakram2@gmail.com (A.A.)
[2] School of Life Science, Zhengzhou University, Zhengzhou 450001, China
* Correspondence: lijingan@home.swjtu.edu.cn (J.-A.L.); zhangkun@zzu.edu.cn (K.Z.); Tel.: +86-185-3995-6211 (J.-A.L.)

Abstract: Hyaluronic acid (HA) is a non-sulfated glycosaminoglycan (GAG) that is a versatile material whose biological, chemical, and physical characteristics can be deeply tuned to modifications. However, HA is easy to decompose by hyaluronidase in vivo, and this process will reduce its structure and function stability during application. The sulfonation of HA can improve its stability under the action of hyaluronidase. Sulfated hyaluronic acid (S-HA) can be synthesized by many methods, and it shows significantly slower degradation by hyaluronidase compared with HA. In addition, negatively charged S-HA has other advantages such as anti-adhesive activity, anti-inflammatory, macromolecules by electrostatic interactions, stable site absorption of positively charged molecules, and enhancement of growth factor binding ability. It has numerous applications in medical (anti-aging, inflammation, tissue regeneration, cancer therapy, wound healing, and drug delivery) and cosmetics as biomaterials and coatings. In this article, the advances of S-HA for potential application of biomaterials and biomedical coatings will be reviewed and comprehensively discussed.

Keywords: sulfonated hyaluronic acid; hyaluronidase; surface modification; biocompatibility

Citation: Iqbal, M.; Yasin, A.; Akram, A.; Li, J.-A.; Zhang, K. Advances of Sulfonated Hyaluronic Acid in Biomaterials and Coatings—A Review. *Coatings* **2023**, *13*, 1345. https://doi.org/10.3390/coatings13081345

Academic Editor: Petrică Vizureanu

Received: 9 June 2023
Revised: 20 July 2023
Accepted: 28 July 2023
Published: 31 July 2023

1. Introduction

Hyaluronic acid (HA) is a non-sulfated glycosaminoglycan (GAG) [1,2]. It is a versatile material whose biological, chemical, and physical characteristics can be deeply tuned to modifications [3]. Chemically, HA is a negatively linear polysaccharide. Its disaccharide repeating unit contained *N*-acetyl-D-glucosamine and D-glucuronic acid. It exists in various parts of the human body; thus, it is a natural molecule that can be regenerated and decomposed in vivo [4,5]. Numerous studies show that HA and its derivatives with different molecular weights have different effects on cells, CD44 targeting, anti-aging, and retention [6]. HA is widely used to prepare nano-gels for drug delivery and scaffold for tissue engineering, and it is used in cosmetics, wound healing, ophthalmology and cancer treatment [7–9]. HA has good lubricating and anti-inflammatory properties [10]. HA has a large molecular weight that affects its penetration into the skin and its natural activity. A considerable amount of modification to HA was proposed to improve mechanical properties, viscosity, chemical or enzymatic stability, and biocompatibility [11]. It is reported that intra-articular injections of an HA solution give pain relief and enhance joint motion in osteoarthritis (OA) patients [12]. However, retention and localization of injected HA in joints are normally poor because of the non-crosslinked nature of injectants and degradation by enzymes. The main drawback of HA is that it is easy to decompose by hyaluronidase in vivo [13]. Furthermore, due to the lack of negatively charged sulfate groups, HA cannot bind protein with high affinity and with the presence of hyaluronidase (HAase) in humans, which is involved in the fast degradation of HA by cleaving the structure of β-1, 4-glycosidic bonds [14], but the sulfonation of HA can improve its stability under the action of HAase [15]. In addition, Feng et al. reported that adding sulfur to the medicine will endow them with stronger biological activities, including antiviral, antibacterial, antiallergic, antimalarial, and cytotoxic properties [16]. Olivito et al. also demonstrated that synthesizing medicine into unsaturated disulfides will enhance its anticancer activity [17].

1.1. Hyaluronidase Action

Hyaluronidase (HAase) is a class of enzymes that is capable of degrading HA [18]. Hyaluronidases are endoglycosidases that can depolymerize HA and create many effects in tissues [19]. They reduce the lubricating quality of HA; they decrease the normal high viscosity of HA and act as a "spreading factor" that can enable the diffusion of many substances subcutaneously injected such as antiviral vaccines and dyes [20]. It is reported that the action of these proteins was discovered before and categorized the HAase into three groups. With respect to its mechanism of action, every group is different from each other [21]. The first group is the mammalian HAase (testis tube). They are endo-β-nacetlyhexosaminidases that degrade the β-1, 4 glycosidic linkages of HA. The second group is the hookworm/leech HAase. They contained endo-β-D glucuronidases. These HAase degrade the β-1,3 glycosidic bond, resulting in tetra- and hexasaccharides [22]. These enzymes only degrade HA and remain inert toward other GAGs as compared with mammalian glycosidase. The third group is the microbial HAase [23]. They are classified as hyaluroate lyases. They are different from other HAase because they do not use hydrolysis, but at β-1, 4 glycosidic linkages, β-elimination reaction happens [24].

It is reported that HAase is involved in the spread of toxins/infection, cancer progression, and ovum fertilization. It cleaves internal β-*N*-acetyl-D-glucosaminidic linkages in HA. Complete digestion of hyaluronic acid by HAase produces tetrasaccharides, and limited digestion produces angiogenic HA fragments [25]. In humans, six HAase genes group into two tightly linked triplets on chromosomes 3p21.3 (HYAL-1, HYAL-2, and HYAL-3) and 7q31.3 (HYAL-4, HYALPI, and PH20). HYAL-1 HAase is present in human urine and serum, and PH20 is the testicular HAase [26]. It is present on the sperm cell surface and is required for penetration through the follicle cell layer. However, it has been revealed that HYAL-1 is a major tumor-derived HAase that is expressed in the bladder [27], neck, prostate, and head cancer cells [12].

1.2. Effect of S-HA on Hyaluronidase Activity and S-HA Synthetic Techniques

It is reported that sulfation of HA inhibits both testicular and urinary HAases. In a previous study, the effect of sulfonated hyaluronic acid (S-HA) on the activity of HAYAL-1, bee, testicular, and Streptomyces HAases was tested [28]. The study showed that various numbers of sulfation on S-HA affect the ability to inhibit HAase activity. Previously, it was reported that S-HA inhibits urinary HAase activity through noncompetitive and competitive mechanisms. Since S-HA is more effective as an uncompetitive inhibitor than as a competitive inhibitor, it would be more effective in vivo because its efficacy will be liberated of HA [29] concentration present in tissue fluid and target tissues. This is very important for designing anti-HAase treatment for cancer because in several tumor tissues, HA concentration is high. HAase inhibitors exhibiting varied inhibition may prove to be effective in inhibiting HAase activity in many pathophysiologic circumstances [30].

Sulfation is one of the most common modifications of HA, which includes adding sulfate groups to its structure. This modification can enhance the biological activity of HA and change its chemical and physical properties. These numerous methods for sulfating of HA include chemical sulfation, enzymatic sulfation, radiation-induced sulfation, and plasma-induced sulfation [31]. It is reported that in enzymatic sulfation, sulfotransferases are enzymes that are used to transfer the sulfate group to HA. This method is highly specific and allows for the degree and location of sulfation. In the radiation-induced sulfation method, ionizing radiation is carried out to introduce the sulfate group into the HA molecule [32]. This method is highly efficient but can result in the degradation of the HA molecule if not properly controlled [13]. In the plasma-induced sulfation method, plasma is used to introduce the sulfate group into the HA molecule. Moreover, in the chemical sulfation method, sulfur trioxide-pyridine is used to introduce the sulfate group into the HA molecule. This method is highly efficient and also prevents HA from fast degradation [15].

Chemically, S-HA can be synthesized by the modification of hydroxyl groups [33]. S-HA (sulfated) shows significantly slower degradation by HAase as compared with HA (non-sulfated) [34]. In addition, negatively charged S-HA has other advantages such as anti-adhesive activity, anti-inflammatory, macromolecules by electrostatic interactions, stable site absorption of positively charged molecules, and enhancement of growth factor binding ability [35]. Cell adhesion, growth on scaffold surface, and viability can be enhanced by absorption of proteinaceous growth factors of polycationic biomolecules [36]. It prevents cartilage decomposition; osteoarthritis (OA) [37] is categorized by metabolic variations and progressive structure in joint tissues, synovial membrane inflammation, and subchondral sclerosis of the bone [27]. Previous research has shown that sulfation of HA can prevent the degradation of HA. The effect of sulfation on the enzymatic degradation of HA was analytically investigated [38]. Moreover, the study of the regeneration of injured tissues, cell-based repair of scaffold materials, and mainly articular cartilage has been carried out for HA-based hydrogels [29]. Keeping a suitable dosage of transforming growth factor (TGF) in the hMSC-laden hydrogels is important for the stability of subsequent cartilage maturation and chondrogenic phenotype. However, hyaluronic acid hydrogels have limited ability to hold laden proteinaceous growth factors due to the deficiency of the affinity of HA toward these growth factors. S-HA is recognized as a sequester proteinaceous growth factor through electrostatic interaction. It was verified that hydrogels composed of S-HA showed a reduced release rate of the encapsulated stromal-cell-derived factor (SDF). Consequently, in hydrogel, retention of TGF can be improved by sulfated HA hydrogels, thus suppressing the hypertrophy of the encapsulated hMSCs and enhancing chondrogenesis. The summary scheme of sulfation methods, functional advantages, and action pathways of S-HA is displayed in Figure 1.

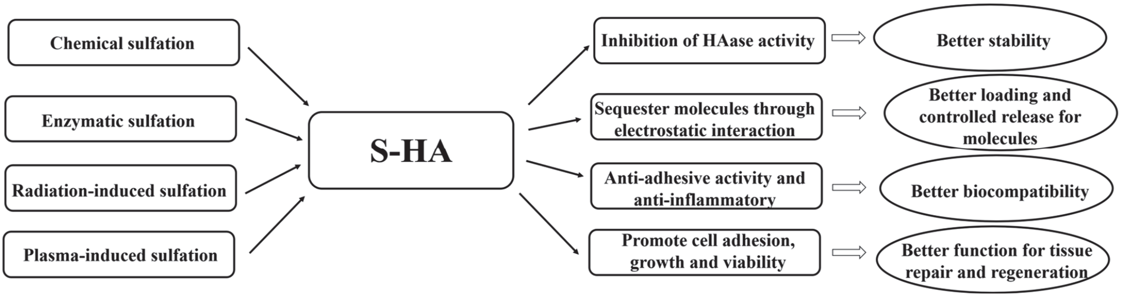

Figure 1. The scheme of sulfation methods, functional advantages, and action pathways of S-HA.

In previous studies, HA macromeres were prepared with various sulfation levels to evaluate the influence of sulfation on HA degradation by HAase treatment. Their results showed that sulfate groups were implanted on the HA backbone, which productively reduced the degradation level of HA in a prescribed amount. The growth factor binding capacity of HA-based hydrogels can be improved by sulfation. Furthermore, studies showed that in sulfated HA hydrogels, chondrogenic differentiation of hMSCs has been summarized [39]. In vivo and in vitro hydrogel sulfation overpowers the chondrogenic hypertrophy of hMSCs and encourages chondrogenesis. Moreover, these sulfation results of osteoarthritis (OA) animal model experiments showed that the sulfated HA hydrogels are able to relieve the OA signs in damaged animal knee joints.

It is also reported that a shortcoming of HA is high-molecular-weight HA polymers [40], which can be easily cleaved by HAase to form low-molecular-weight fragments, and they can promote migration and proliferation of a tumor [13]. In order to prevent these disadvantages and cleavage by HAase, S-HA was synthesized by presenting sulfation to the

–OH groups of HA; thereby, invasion of tumor cells, motility, and inhibiting proliferation was prevented [41]. Furthermore, some researchers proved that S-HA can effectively be reduced in angiogenesis, which can be used to treat solid tumors, retinitis pigmentosa, and wet age-related macular degeneration (wet-AMD) [42]. S-HA has numerous applications such as arthrology, cancer therapy, wound healing, atherosclerosis, tissues regeneration, drug delivery, urology, ophthalmology, pneumology, arthrology, and rhinology [11].

Before 1990, some researchers reported that S-HA was obtained with 3 SO_3^- groups for each disaccharide unit [43]. Mainly, S-HA was synthetized by a sulfur trioxide pyridine complex with HA. It was also synthesized by changing hydroxyl groups into RO-SO_3H with a sulfur pyridine complex in dimethylformamide and synthesized by sulfonation with amidation/oxidation process, and sulfonate groups (R-SO_3H) are combined into the hyaluronic acid backbone because they prevent enzyme activity by steric hindrance [34]. In spite of advanced functionalization, some examples that deal with HA sulfation and sulfonation need the use of toxic solvents [13] and reactants as well as laborious techniques for water organic purification and careful solvent exchange [14]. Synthesis of different types of S-HAs with various sulfation degrees and different molecular weights such as 17 K Dalton, 150 K Dalton, and 1000 K Dalton was reported [44]. The sulfation degrees were controlled by adding various molar ratios of sulfur trioxide (SO_3) to the pyridine (C_5H_5N) complex per repeating unit of HA [13]. The 1:1 ratio of moles of the sulfur trioxide pyridine complex to moles of HA repeat units was reported in S-HA-1 (least sulfated); a 2:1 ratio of moles of the sulfur trioxide pyridine complex to moles of HA repeat units was reported in S-HA-2; a 5:1 ratio of moles of the sulfur trioxide pyridine complex to moles of HA repeat units was reported in S-HA-3; and an 8:1 ratio of moles of the sulfur trioxide pyridine complex to moles of HA repeat units was reported in S-HA-4 (most sulfated). The C-6 position of sulfation is the most reactive hydroxyl in HA [45]. S-HA usually exists in the form of sodium salts in solution; Figure 2 shows the structural diagram of S-HA sodium salt.

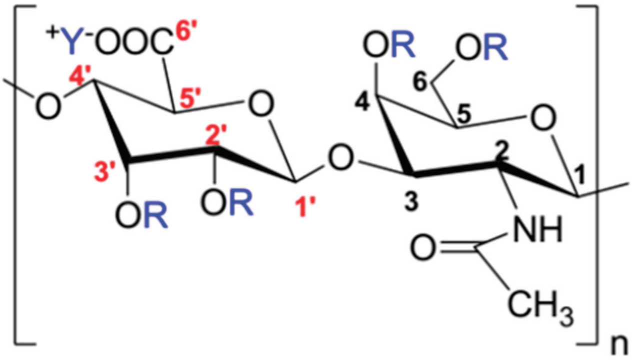

$R = SO_3^-Na^+$ and $Y = Na^+$

Figure 2. Sodium salt of S-HA.

2. Selective Binding Characteristics of S-HA

As a synthetic sulfated polysaccharide, S-HA has the capacity to block the binding of P-selection and, in vivo, the cobra venom factor, which was shown to inhibit P-selection-dependent infiltration of leukocytes in acute lung damage. By inhibiting P-selection-dependent leukocyte infiltration, S-HA exhibits therapeutic and preventive effects in glomeruli [35]. In vitro, S-HA has showed good inhibitory impacts on the binding of L-selection and P-selection. Moreover, S-HA can be produced at low cost due to a huge amount of HA availability from a streptococcal culture medium [46]. For clinical use, S-HA is the best candidate of blocking agents. S-HA is a hyaluronidase (HAase) inhibitor. A previous study showed that S-HA is a strong inhibitor of prostate cancer. It blocked the motility, proliferation, Du145, LNCaP-AI, attack of LNCaP and LAPC-4 prostate cells, and phospho-Bad. It inhibited Akt signaling, nuclear factor kB (NFkB) activation, AR activity, and VEGF expression. Due to their low $pK_a \sim 1.7$, sulfate or sulfonated groups have low pH in anionic forms, while the carboxylic group is completely protonated [47]. Along the HA chain, negatively sulfate or sulfonated groups have shown direct effect on few biological processes such as anti-adhesive activity, anti-inflammatory, and growth on scaffold surfaces [32].

One of the main selective binding properties of S-HA is its high affinity for different cytokines and growth factors, including fibroblast growth factor (FBG), vascular endothelial growth factor (VEGF), and transforming growth factor-beta (TGF-β) [48]. These growth factors perform important roles in wound healing, tissue repair and angiogenesis, and S-HA capability to selectively bind to, and sequestering these factors can improve their bioactivity and support tissue regeneration [49].

Another selective binding property of S-HA is its capability to interact with cell surface receptors, such as RHAMM and CD44. For cell migration and cell adhesion, CD44 is used, and it is called surface receptor. It is also used for HA. Sulfation of HA increases its binding affinity to CD44, and this interaction can control cell signaling pathways and promote cellular responses such as differentiation and proliferation [50].

S-HA was produced by the O-sulfation of HA [32]. Many years ago, it showed to be inhibited with both testicular and urinary HAases. It was shown for cell adhesion, fibroblast motility [51], astrocytes, gene expression in keratinocytes, and proliferation of osteoblasts [25]. Many studies have showed the antitumor activities of S-HA [52]. Sulfated HA supports the variation in osteoblasts from human bone marrow stromal cells. Furthermore, sulfated HA has been recommended to promote basic fibroblast growth factor (bFGF) signaling. Sulfated HA shows that it has the ability to maintain the homogeneous state of hips cells by enabling bFGF signaling [15].

In addition to growth factors and cell surface receptors, S-HA can also selectively bind to extracellular matrix (ECM) components such as fibronectin and collagen [53]. It can interact with these ECM components through its sulfate groups and cell ECM interaction, which are important for tissue organization [54]. The scheme of selective binding characteristics of S-HA is displayed in Figure 3.

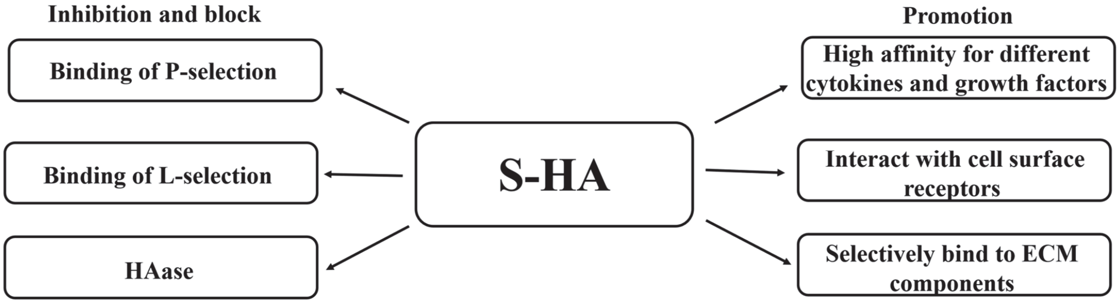

Figure 3. Selective binding characteristics of S-HA.

3. Applications of Sulfonated Hyaluronic Acid (S-HA)

S-HA is a more established form of hyaluronic acid that is designed to last longer in the body, providing more sustainable results [1]. It is usually injected into the skin using a fine needle, and the technique is relatively rapid and painless. The results are visible immediately, and there is little to no downtime after the procedure. On the basis of biocompatibility, biological action, physiochemical, and safety profile, S-HA has numerous applications such as arthrology, cancer therapy [55], wound healing, atherosclerosis, tissue regeneration, drug delivery, urology, ophthalmology, pneumology, arthrology, and rhinology [56] (Figure 4).

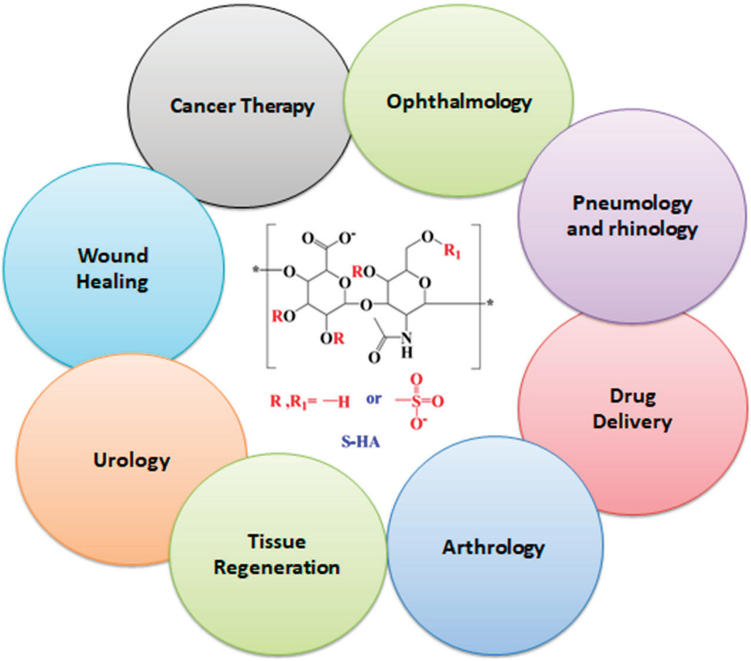

Figure 4. Applications of sulfonated hyaluronic acid (S-HA).

3.1. Drug Delivery

In a drug delivery system, S-HA has taken a growing amount of attention. It has very outstanding tendencies such as biodegradability [57], biocompatibility [58], extremely low toxicity [59], and non-immunogenicity. It has been extensively useful in nano-sized carriers. The surface modification of S-HA can help to improve its drug-loading capacity [60], stability, and controlled release properties, which are important factors for the effective delivery of drug to targeted tissues. To preserve the cellular structure and component of ECM, S-HA is used. Due to its negative charge, it can interact with protein in the ECM [61]. S-HA is used as a reducing and stabilizing agent in drug delivery systems [56]. It is used for prodrug development. For target drug delivery, S-HA and nanoparticles are prepared with other substances. The solubility of drug molecules can be improved by S-HA conjugates during targeted drug delivery in tumor or cancer cells. Due to outstanding hydrophilicity [62] and volume, it can be used to inhibit the unwanted interactions with plasma proteins and cells. Furthermore, due to its hydrophilicity and biocompatibility, it has been used in the progress of nano-carriers to improve target drug delivery for intravenous administration. HA hydrogel is the usually used format for effective drug delivery [63,64], while another usual application of HA for drug delivery is the nanoparticle carrier, which benefits the specific CD44 interaction and nano-effect (Figure 5) [65,66]. Sulfonation will continue to be retained or even strengthen these advantages of HA, and its biggest advantage is to inhibit the degradation effect of HAase on HA and improve molecular stability.

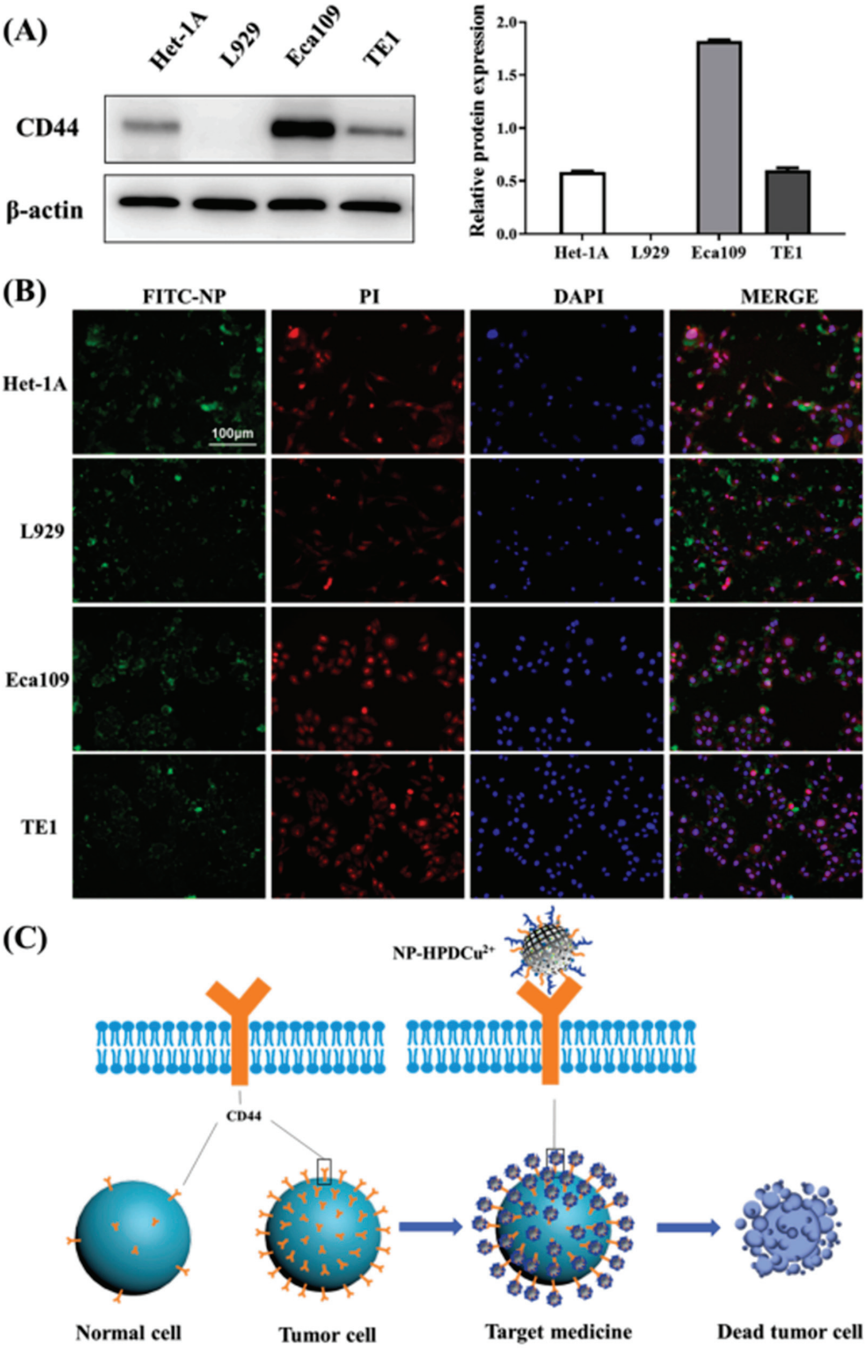

Figure 5. (**A**) Western blot of CD44 expressed on the Het-1A, L929, Eca109, and TE1 (mean ± SD, n = 3). (**B**) Fluorescence images of Het-1A, L929, Eca109, and TE1 stained with FITC labeled HA nanoparticles with drugs (FITC-NP, green color), PI (apoptosis marker, red color), and DAPI (nucleus marker, blue color). (**C**) Mechanism diagram of targeted killing tumor cells by HA nanoparticles with drugs [66].

3.2. Tissue Engineering

Tissue engineering is a very outstanding biomedical application of S-HA. Engineering and biomedical methods are used to find novel biomaterials. These biomaterials are used to replace the injured organ and tissue or to enhance, repair, and maintain its damaged functions. For examples in nerve regeneration, conductive nerve scaffold was used to enhance nerve tissue engineering.

In bone tissue engineering, S-HA can also be used as scaffold materials [67]. The surface modification of S-HA can help improve its mechanical properties, biocompatibility, and bioactivity, which are the most important factors for the successful regeneration of bone tissue [68]. In bladder tissue engineering, collagen-derived hydrogels were used. Furthermore, the basis of bioactivity and biocompatibility of biomaterials can be decided for tissue engineering [69].

Surface modification of cardiovascular implants with S-HA is a feasible strategy to enhance the biocompatibility and stability compared with HA coatings [14]. Sulfonic groups or sulfur content plays an important role in enhancing coating functionality [70]. The use of sulfonated proteoglycan such as S-HA as a coating is mainly inspired by the design and research of chondroitin sulfate coating [71]. This sulfonated molecule endows stainless-steel vascular stent with more powerful anticoagulant, antiproliferative, anti-inflammatory, and pro-endothelialization promoting functions, thus making the vascular patency better [72]. On the basis of S-HA, corresponding nanoparticles can be prepared. S-HA nanoparticles have a smaller particle size and better zeta potential and dispersion coefficient range than HA nanoparticles, which proved that the prepared coatings have stronger functions [41]. Recently, we designed a composite coating with S-HA nanoparticles on the magnesium (Mg) alloy surface for cardiovascular application (Figure 6), and our data indicated that this composite coating significantly improved the corrosion resistance and biocompatibility of the Mg alloy (Figure 7) [73]. The composite coating even showed stronger pro-endothelialization and anti-hyperplasia functions compared with the rapamycin coating prepared by the same method, which suggests a better substitute of rapamycin by S-HA nanoparticles. Carbon quantum dots (CDs) have broad prospects in the field of biomedical diagnosis and treatment [74]. We combine CDs with S-HA to form nanoparticles, which not only endow cardiovascular implant coatings with good biocompatibility but also endow nanoparticles and their composite coatings with novel tracing properties due to the spontaneous fluorescence function of CDs, thereby obtaining diagnostic and therapeutic functions. We have applied for List of Chinese inventions patent for relevant parameters, and the specific method and results will be published in the near future.

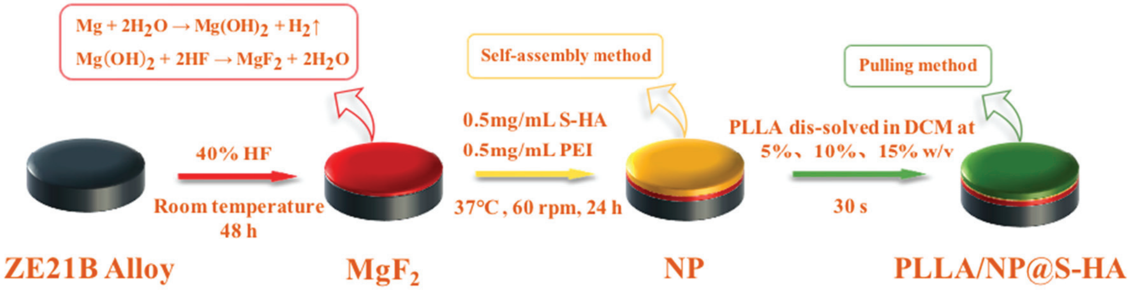

Figure 6. Scheme of preparing PLLA/NP@S-HA coating (S-HA nanoparticle composite coating) on the ZE21B (Mg alloy) surface [73].

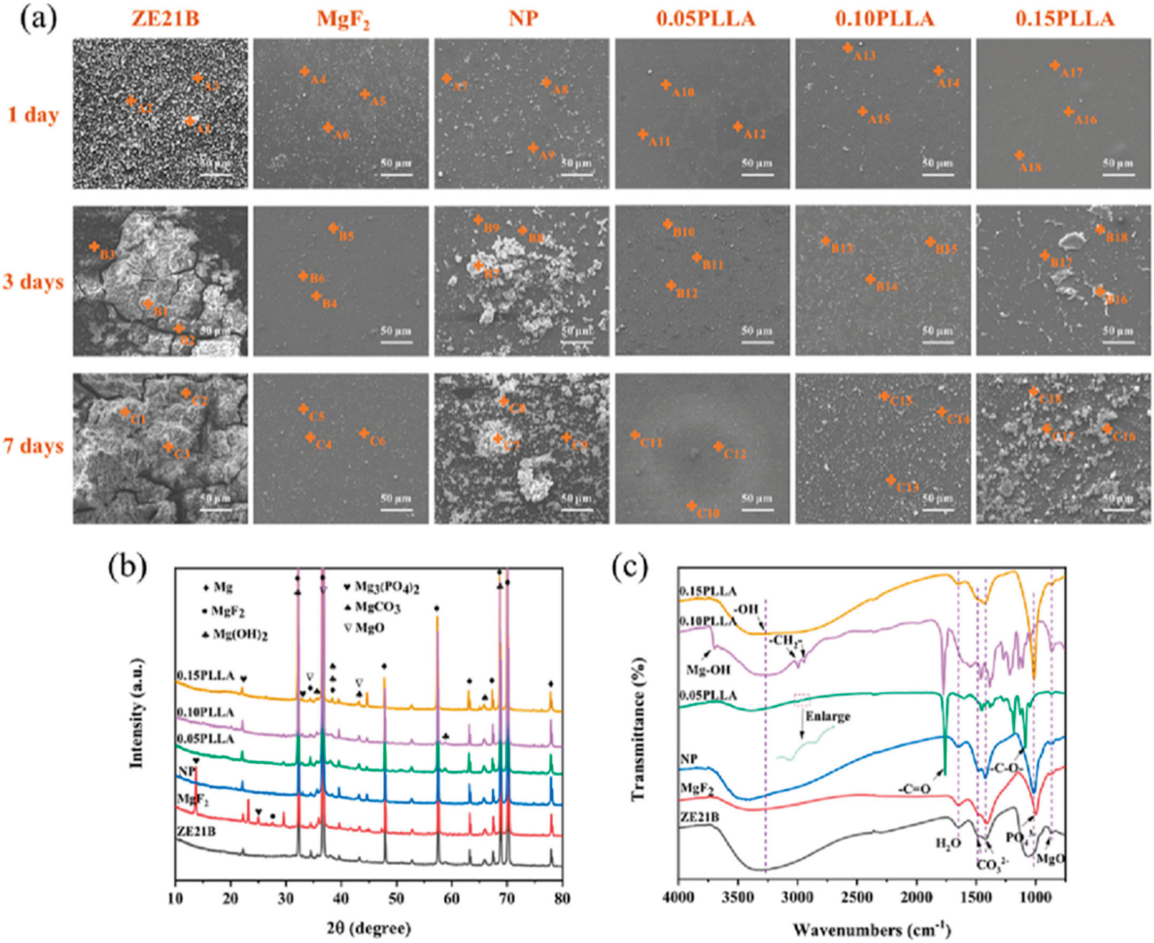

Figure 7. (**a**) SEM images of all samples after soaking in Hanks' solution for 1 day, 3 days, and 7 days; (**b**) XRD spectrum; (**c**) FTIR spectrum of samples after soaking in Hanks' solution for 200 h [73].

3.3. Treatment for Osteoarthritis

Sulfonated hyaluronic acid (S-HA) is most beneficial for the treatment of osteoarthritis. Osteoarthritis is mainly cartilage degradation, inflammation of synovial membrane and joint tissues, and subchondral sclerosis. S-HA is used to prevent and slow down joint degradation [75]. It is used to reduce pain and increases joint mobility. S-HA has been investigated as a potential treatment for osteoarthritis [52], a degenerative joint disease characterized by the breakdown of cartilage and inflammation [76]. Studies have shown that S-HA can have several beneficial effects on osteoarthritic joints. For example, S-HA can reduce inflammation by inhibiting the production of inflammatory cytokines and enzymes. S-HA can also promote the regeneration of cartilage by stimulating the proliferation and differentiation of chondrocytes, the cells that produce cartilage. S-HA injections have been shown to reduce joint pain [77] and inflammation in people with osteoarthritis [78]. It works by cushioning the joints and providing lubrication, which can reduce friction and improve mobility.

One study investigated the use of S-HA as a treatment for knee osteoarthritis [79]. The study found that S-HA injections into the knee joint improved pain and function in patients with osteoarthritis, and that the effects were sustained for up to six months after treatment [4]. Overall, these studies suggest that S-HA has potential as a treatment for osteoarthritis by reducing inflammation and promoting cartilage regeneration. However, more research is needed to fully understand the mechanisms underlying these effects and to determine the optimal conditions for using S-HA in osteoarthritis therapies [80].

One important aspect noticed in the treatment of osteoarthritis is the anti-bacterial function. Thus, how to give consideration to both anti-bacterial and anti-inflammatory Dwifungsi is the key problem of S-HA in the treatment of osteoarthritis. Metal-organic frame structures (MOFs) are effective materials for anti-bacterial and anti-inflammation, even drug delivery. Therefore, combining MOFs and S-HA will endow the treatment of osteoarthritis with stronger anti-bacterial and anti-inflammatory functions. In addition, the S-HA hydrogels or nanoparticles can be prepared as the ink of bioprinting technology, which can also be applied for the precise treatment of osteoarthritis [81,82].

3.4. Treatment for Inflammatory Diseases

Sulfated hyaluronic acid (S-HA) plays an important role in various selection inhibitors that are important for inflammatory diseases. Many selection inhibitors are produced for human inflammatory disease treatment. For example, Efomycin M is proved as a new selection inhibitor, which reduces skin inflammation [83]. The therapeutic and protective effect of TBC-1269 showed a new blocker for a renal ischemia reperfusion injury model. In vitro S-HA exhibits L-selection and P-selection binding with interfaces. Moreover, in vivo S-HA enhanced the rat progressive mesangial proliferative glomerulonephritis, but these properties were not detected by HA [84]. That is why due to inhibitory effects on binding, S-HA was used for the treatment of inflammatory diseases. S-HA is a very beneficial material for the treatment of crescentic glomerulonephritis. Studies demonstrated that in renal tissues, leukocytes have infiltrated, and they create difficulty in the pathogenesis of different glomerulonephritis. An early event in the process of leukocyte infiltration is categorized by selection-mediated leukocyte rolling on the endothelial surface. By inhibiting P-selection-dependent leukocyte infiltration, S-HA exhibits therapeutic and preventive effects in glomeruli.

S-HA injections have also been used to treat rheumatoid arthritis. They can help reduce joint pain and inflammation [85] and improve joint function. It is reported that S-HA is used as potential treatment of inflammatory bowel disease (IBD). It may help to reduce inflammation in the gut and improve symptoms such as abdominal pain and diarrhea. S-HA has shown to reduce inflammation in the skin in people with psoriasis and anti-inflammatory effects. For the potential treatment of asthma patients, S-HA has proved to reduce inflammation and improve breathing.

3.5. Wound Healing

HA is a natural substance found in the body that plays an important role in tissue repair and wound healing [86]. S-HA is a stabilized form of HA that has been modified to enhance its durability and stability. In recent years, S-HA has been used as a wound-healing agent due to its ability to enhance the body’s natural healing process. S-HA can help to reduce inflammation, stimulate collagen production, and promote cell proliferation; all of these factors are important in wound healing [72]. S-HA can be used to treat a variety of wounds [87], including burns [8], surgical incisions, and chronic ulcers [88]. It can be applied as dressing, directly injected into the wound, and it can be topically administered. Previous studies showed that S-HA is used in the healing process and enhances the overall quality of wound healing. It showed the reduction in risk of scarring and infection.

Overall, S-HA is a promising wound-healing agent that has the potential to improve outcomes for patients with a variety of wounds. However, further research is needed to fully understand its effectiveness and optimal use in wound healing.

4. Summary and Perspective

Compared with hyaluronic acid (HA), sulfonated hyaluronic acid (S-HA) presents stronger stability for hyaluronidase, which proved that S-HA will show better in vivo performance as biomedical materials and coating materials. Obtaining benefit from the sulfonic acid group, S-HA has better functions on anticoagulation, antihyperplasia, anti-inflammation, and pro-endothelialization. Even the S-HA nanoparticles may show smaller size and cytocompatibility than HA nanoparticles in equivalent preparation conditions. S-HA hydrogels also presented better drug-controlled delivery compared with HA due to higher stability. S-HA can be combined with more new materials such as CDs, MOFs, etc. to achieve more compatibility functions. It can also be applied as materials of novel technologies, such as the ink of the bioprinting for wider application of biomaterials and coatings. In the future, S-HA will play more important roles in the biomaterial fields as nanoparticles, hydrogels, coatings, and other composite formats.

Author Contributions: Conceptualization, J.-A.L. and K.Z.; writing—original draft preparation, M.I., A.Y., and A.A.; writing—review and editing, J.-A.L. and K.Z.; supervision, J.-A.L.; project administration, J.-A.L.; funding acquisition, J.-A.L. and K.Z. All authors have read and agreed to the published version of the manuscript.

Funding: This research was funded by the National Natural Science Foundation of China, grant number U2004164; the Key Scientific and Technological Research Projects in Henan Province, grant numbers 232102311155 and 232102230106; and the Natural Science Foundation of the Jiangsu Higher Education Institutions of China, grant number 21KJB430013.

Institutional Review Board Statement: Not applicable.

Informed Consent Statement: Not applicable.

Data Availability Statement: Not applicable.

Acknowledgments: Figure 5 reproduced from Ref. [66] with permission from Elsevier B.V. (License Number: 5592850568872); Figures 6 and 7 reproduced from Ref. [73] with permission from Elsevier B.V. (License Number: 5592940983813).

Conflicts of Interest: The authors declare no conflict of interest.

References

1. Larrañeta, E.; Henry, M.; Irwin, N.J.; Trotter, J.; Perminova, A.A.; Donnelly, R.F. Synthesis and characterization of hyaluronic acid hydrogels crosslinked using a solvent-free process for potential biomedical applications. *Carbohydr. Polym.* **2018**, *181*, 1194–1205. [CrossRef] [PubMed]
2. Angello, J.C.; Hauschka, S.D. Hyaluronic acid synthesis and turnover by myotubes in culture. *Dev. Biol.* **1979**, *73*, 322–337. [CrossRef] [PubMed]
3. Feng, Q.; Lin, S.; Zhang, K.; Dong, C.; Wu, T.; Huang, H.; Bian, L. Sulfated hyaluronic acid hydrogels with retarded degradation and enhanced growth factor retention promote hMSC chondrogenesis and articular cartilage integrity with reduced hypertrophy. *Acta Biomater.* **2017**, *53*, 329–342. [CrossRef] [PubMed]
4. Schuurmans, C.C.L.; Mihajlovic, M.; Hiemstra, C.; Ito, K.; Hennink, W.E.; Vermonden, T. Hyaluronic acid and chondroitin sulfate (meth)acrylate-based hydrogels for tissue engineering: Synthesis, characteristics and pre-clinical evaluation. *Biomaterials* **2021**, *268*, 120602. [CrossRef]
5. Della Sala, F.; Fabozzi, A.; di Gennaro, M.; Nuzzo, S.; Makvandi, P.; Solimando, N.; Borzacchiello, A. Advances in Hyaluronic-Acid-Based (Nano)Devices for Cancer Therapy. *Macromol. Biosci.* **2022**, *22*, 2100304. [CrossRef]
6. Ogawa, D.; Shikata, K.; Matsuda, M.; Akima, K.; Iwahashi, M.; Okada, S.; Makino, H. Sulfated hyaluronic acid, a potential selectin inhibitor, ameliorates experimentally induced crescentic glomerulonephritis. *Nephron Exp. Nephrol.* **2005**, *99*, 26–32. [CrossRef]
7. Li, J.; Wang, S.; Sheng, Y.; Liu, C.; Xue, Z.; Tong, P.; Guan, S. Designing HA/PEI nanoparticle composite coating on biodegradable Mg–Zn–Y-Nd alloy to direct cardiovascular cells fate. *Smart Mater. Med.* **2021**, *2*, 124–133. [CrossRef]
8. Magnani, A.; Lamponi, S.; Consumi, M.; Barbucci, R. Biological performance of two materials based on sulfated hyaluronic acid and polyurethane. *J. Mater. Chem.* **1999**, *9*, 2393–2398. [CrossRef]
9. Yu, Y.; Zhu, S.J.; Dong, H.T.; Zhang, X.Q.; Li, J.; Guan, S.K. A novel MgF_2/PDA/S-HA coating on the bio-degradable ZE21B alloy for better multi-functions on cardiovascular application. *J. Magnes. Alloy.* **2023**, *11*, 480–492. [CrossRef]
10. Bhattacharya, D.S.; Svechkarev, D.; Bapat, A.; Patil, P.; Hollingsworth, M.A.; Mohs, A.M. Sulfation Modulates the Targeting Properties of Hyaluronic Acid to P-Selectin and CD44. *ACS Biomater. Sci. Eng.* **2020**, *6*, 3585–3598. [CrossRef]

11. Benitez, A.; Yates, T.J.; Lopez, L.E.; Cerwinka, W.H.; Bakkar, A.; Lokeshwar, V.B. Targeting hyaluronidase for cancer therapy: Antitumor activity of sulfated hyaluronic acid in prostate cancer cells. *Cancer Res.* **2011**, *71*, 4085–4095. [CrossRef]
12. Buhren, B.A.; Schrumpf, H.; Bölke, E.; Kammers, K.; Gerber, P.A. Standardized in vitro analysis of the degradability of hyaluronic acid fillers by hyaluronidase. *Eur. J. Med. Res.* **2018**, *23*, 37. [CrossRef] [PubMed]
13. Sturabotti, E.; Consalvi, S.; Tucciarone, L.; Macrì, E.; Di Lisio, V.; Francolini, I.; Martinelli, A. Synthesis of Novel Hyaluronic Acid Sulfonated Hydrogels Using Safe Reactants: A Chemical and Biological Characterization. *Gels* **2022**, *8*, 480. [CrossRef] [PubMed]
14. Yu, Y.; Zhu, S.; Hou, Y.; Li, J.; Guan, S. Sulfur Contents in Sulfonated Hyaluronic Acid Direct the Cardiovascular Cells Fate. *ACS Appl. Mater. Interfaces* **2020**, *12*, 46827–46836. [CrossRef]
15. Miura, T.; Yuasa, N.; Ota, H.; Habu, M.; Kawano, M.; Nakayama, F.; Nishihara, S. Highly sulfated hyaluronic acid maintains human induced pluripotent stem cells under feeder-free and bFGF-free conditions. *Biochem. Biophys. Res. Commun.* **2019**, *518*, 506–512. [CrossRef]
16. Feng, M.; Tang, B.; Liang, S.H.; Jiang, X. Sulfur Containing Scaffolds in Drugs: Synthesis and Application in Medicinal Chemistry. *Curr Top. Med. Chem.* **2016**, *16*, 1200–1216. [CrossRef]
17. Olivito, F.; Amodio, N.; Di Gioia, M.L.; Nardi, M.; Oliverio, M.; Juli, G.; Tassone, P.; Procopio, A. Synthesis and preliminary evaluation of the anti-cancer activity on A549 lung cancer cells of a series of unsaturated disulfides. *MedChemComm* **2018**, *10*, 116–119. [CrossRef]
18. Rzany, B.; Becker-Wegerich, P.; Bachmann, F.; Erdmann, R.; Wollina, U. Hyaluronidase in the correction of hyaluronic acid-based fillers: A review and a recommendation for use. *J. Cosmet. Dermatol.* **2009**, *8*, 317–323. [CrossRef] [PubMed]
19. Stern, R.; Jedrzejas, M.J. Hyaluronidases: Their genomics, structures, and mechanisms of action. *Chem. Rev.* **2006**, *106*, 818–839. [CrossRef] [PubMed]
20. Cen, L.; Neoh, K.G.; Li, Y.; Kang, E.T. Assessment of in vitro bioactivity of hyaluronic acid and sulfated hyaluronic acid functionalized electroactive polymer. *Biomacromolecules* **2004**, *5*, 2238–2246. [CrossRef]
21. Jones, D.; Tezel, A.; Borrell, M. In vitro resistance to degradation of hyaluronic acid dermal fillers by ovine testicular hyaluronidase. *Dermatol. Surg.* **2010**, *36*, 804–809. [CrossRef]
22. Hintze, V.; Miron, A.; Moeller, S.; Schnabelrauch, M.; Wiesmann, H.P.; Worch, H.; Scharnweber, D. Sulfated hyaluronan and chondroitin sulfate derivatives interact differently with human transforming growth factor-β1 (TGF-β1). *Acta Biomater.* **2012**, *8*, 2144–2152. [CrossRef] [PubMed]
23. Cavallini, M.; Gazzola, R.; Metalla, M.; Vaienti, L. The role of hyaluronidase in the treatment of complications from hyaluronic acid dermal fillers. *Aesthetic Surg. J.* **2013**, *33*, 1167–1174. [CrossRef]
24. Chung, C.; Beecham, M.; Mauck, R.L.; Burdick, J.A. The influence of degradation characteristics of hyaluronic acid hydrogels on in vitro neocartilage formation by mesenchymal stem cells. *Biomaterials* **2009**, *30*, 4287–4296. [CrossRef]
25. Isoyama, T.; Thwaites, D.M.; Selzer, G.; Carey, R.I.; Barbucci, R.; Lokeshwar, V.B. Differential selectivity of hyaluronidase inhibitors toward acidic and basic hyaluronidases. *Glycobiology* **2006**, *16*, 11–21. [CrossRef] [PubMed]
26. Schulz, M.C.; Korn, P.; Stadlinger, B.; Range, U.; Möller, S.; Becher, J.; Hintze, V. Coating with artificial matrices from collagen and sulfated hyaluronan influences the osseointegration of dental implants. *J. Mater. Sci. Mater. Med.* **2014**, *25*, 247–258. [CrossRef]
27. Jordan, A.R.; Lokeshwar, S.D.; Lopez, L.E.; Hennig, M.; Chipollini, J.; Yates, T.; Lokeshwar, V.B. Antitumor activity of sulfated hyaluronic acid fragments in pre-clinical models of bladder cancer. *Oncotarget* **2017**, *8*, 24262–24274. [CrossRef]
28. Kunze, R.; Rösler, M.; Möller, S.; Schnabelrauch, M.; Riemer, T.; Hempel, U.; Dieter, P. Sulfated hyaluronan derivatives reduce the proliferation rate of primary rat calvarial osteoblasts. *Glycoconj. J.* **2010**, *27*, 151–158. [CrossRef]
29. Bayer, I.S. Hyaluronic acid and controlled release: A review. *Molecules* **2020**, *25*, 2649. [CrossRef]
30. Kim, D.W.; Yoon, E.S.; Ji, Y.H.; Park, S.H.; Il Lee, B.; Dhong, E.S. Vascular complications of hyaluronic acid fillers and the role of hyaluronidase in management. *J. Plast. Reconstr. Aesthetic Surg.* **2011**, *64*, 1590–1595. [CrossRef]
31. Li, J.; Qiao, M.; Ji, Y.; Lin, L.; Zhang, X.; Linhardt, R.J. Chemical, enzymatic and biological synthesis of hyaluronic acids. *Int. J. Biol. Macromol.* **2020**, *152*, 199–206. [CrossRef] [PubMed]
32. Miura, T.; Kawano, M.; Takahashi, K.; Yuasa, N.; Habu, M.; Kimura, F.; Nakayama, F. High-Sulfated Hyaluronic Acid Ameliorates Radiation-Induced Intestinal Damage Without Blood Anticoagulation. *Adv. Radiat. Oncol.* **2022**, *7*, 100900. [CrossRef] [PubMed]
33. McCarty, M.F.; Russell, A.L.; Seed, M.P. Sulfated glycosaminsglycan and glucosamine may synergize in promoting synovial hyaluronic acid synthesis. *Med. Hypotheses* **2000**, *54*, 798–802. [CrossRef]
34. Lim, D.K.; Wylie, R.G.; Langer, R.; Kohane, D.S. Selective binding of C-6 OH sulfated hyaluronic acid to the angiogenic isoform of VEGF165. *Biomaterials* **2016**, *77*, 130–138. [CrossRef]
35. Matsuda, M.; Shikata, K.; Shimizu, F.; Suzuki, Y.; Miyasaka, M.; Kawachi, H.; Makino, H. Therapeutic effect of sulphated hyaluronic acid, a potential selectin-blocking agent, on experimental progressive mesangial proliferative glomerulonephritis. *J. Pathol.* **2002**, *198*, 407–414. [CrossRef]
36. Vilela, C.A.; Correia, C.; Oliveira, J.M.; Sousa, R.A.; Espregueira-Mendes, J.; Reis, R.L. Cartilage Repair Using Hydrogels: A Critical Review of in Vivo Experimental Designs. *ACS Biomater. Sci. Eng.* **2015**, *1*, 726–739. [CrossRef]
37. Muzzarelli, R.A.; Greco, A.F.; Busilacchi, A.; Sollazzo, V.; Gigante, A. Chitosan, hyaluronan and chondroitin sulfate in tissue engineering for cartilage regeneration: A review. *Carbohydr. Polym.* **2012**, *89*, 723–739. [CrossRef]

38. Henson, F.M.D.; Getgood, A.M.J.; Caborn, D.M.; Wayne McIlwraith, C.W.; Rushton, N. Effect of a solution of hyaluronic acid-chondroitin sulfate-N-acetyl glucosamine on the repair response of cartilage to single-impact load damage. *Am. J. Vet. Res.* **2012**, *73*, 306–312. [CrossRef] [PubMed]
39. Subramaniam, S.; Fang, Y.H.; Sivasubramanian, S.; Lin, F.H.; Lin, C.P. Hydroxyapatite-calcium sulfate-hyaluronic acid composite encapsulated with collagenase as bone substitute for alveolar bone regeneration. *Biomaterials* **2016**, *74*, 99–108. [CrossRef]
40. Hou, Y.; Zhang, X.; Li, J.; Wang, L.; Guan, S. A multi-functional MgF_2/polydopamine/hyaluronan-astaxanthin coating on the biodegradable ZE21B alloy with better corrosion resistance and biocompatibility for cardiovascular application. *J. Magnes. Alloy.* 2022, *in press*. [CrossRef]
41. Xue, Z.; Sun, X.; Li, H.; Iqbal, M.; Hou, Y.; Jin, Z.; Li, J. Response of cardiovascular environment to sulfonated hyaluronic acid with higher sulfur content. *Colloids Surf. B Biointerfaces* **2023**, *22*, 113046. [CrossRef] [PubMed]
42. Möller, S.; Schmidtke, M.; Weiss, D.; Schiller, J.; Pawlik, K.; Wutzler, P.; Schnabelrauch, M. Synthesis and antiherpetic activity of carboxymethylated and sulfated hyaluronan derivatives. *Carbohydr. Polym.* **2012**, *90*, 608–615. [CrossRef] [PubMed]
43. Albanese, A.; Lamponi, S.; Barbucci, R. Blood-interaction performance of differently sulphated hyaluronic acids. *Thromb. Res.* **1996**, *81*, 383–395.
44. Yeom, J.; Bhang, S.H.; Kim, B.S.; Seo, M.S.; Hwang, E.J.; Cho, I.H.; Hahn, S.K. Effect of cross-linking reagents for hyaluronic acid hydrogel dermal fillers on tissue augmentation and regeneration. *Bioconjug. Chem.* **2010**, *21*, 240–247. [CrossRef] [PubMed]
45. Sall, I.; Férard, G. Comparison of the sensitivity of 11 crosslinked hyaluronic acid gels to bovine testis hyaluronidase. *Polym. Degrad. Stab.* **2007**, *92*, 915–919. [CrossRef]
46. Payan, E.; Jouzeau, J.Y.; Lapicque, F.; Muller, N.; Netter, P. Hyaluronidase degradation of hyaluronic acid from different sources: Influence of the hydrolysis conditions on the production and the relative proportions of tetra- and hexasaccharide produced. *Int. J. Biochem.* **1993**, *25*, 325–329. [CrossRef]
47. Yao, W.; Chen, M.; Dou, X.; Jin, H.; Zhang, X.; Zhu, Y.; Li, Z. Unravel a neuroactive sHA sulfation pattern with neurogenesis activity by a library of defined oligosaccharides. *Eur. J. Med. Chem.* **2019**, *163*, 583–596. [CrossRef]
48. Vogel, S.; Ullm, F.; Müller, C.D.; Pompe, T.; Hempel, U. Impact of binding mode of low-sulfated hyaluronan to 3D collagen matrices on its osteoinductive effect for human bone marrow stromal cells. *Biol. Chem.* **2021**, *402*, 1465–1478. [CrossRef]
49. Zerbinati, N.; Mocchi, R.; Galadari, H.; Maccario, C.; Maggi, M.; Rauso, R.; Sommatis, S. In vitro evaluation of the biological availability of hyaluronic acid polyethylene glycols-cross-linked hydrogels to bovine testes hyaluronidase. *Biomed Res. Int.* **2019**, *2019*, 3196723. [CrossRef]
50. Felz, S.; Neu, T.R.; van Loosdrecht, M.C.M.; Lin, Y. Aerobic granular sludge contains Hyaluronic acid-like and sulfated glycosaminoglycans-like polymers. *Water Res.* **2020**, *169*, 115291. [CrossRef]
51. Hamilton, D.W.; Riehle, M.O.; Rappuoli, R.; Monaghan, W.; Barbucci, R.; Curtis, A.S.G. The response of primary articular chondrocytes to micrometric surface topography and sulphated hyaluronic acid-based matrices. *Cell Biol. Int.* **2005**, *29*, 605–615. [CrossRef] [PubMed]
52. Magnani, A.; Lamponi, S.; Rappuoli, R.; Barbucci, R. Sulphated Hyaluronic Acids: A Chemical and Biological Characterisation. *Polym. Int.* **1998**, *46*, 225–240. [CrossRef]
53. Koehler, L.; Ruiz-Gómez, G.; Balamurugan, K.; Rother, S.; Freyse, J.; Möller, S.; Hintze, V. Dual Action of Sulfated Hyaluronan on Angiogenic Processes in Relation to Vascular Endothelial Growth Factor-A. *Sci. Rep.* **2019**, *9*, 18143. [CrossRef] [PubMed]
54. Satish, L.; Santra, S.; Tsurkan, M.V.; Werner, C.; Jana, M.; Sahoo, H. Conformational changes of GDNF-derived peptide induced by heparin, heparan sulfate, and sulfated hyaluronic acid—Analysis by circular dichroism spectroscopy and molecular dynamics simulation. *Int. J. Biol. Macromol.* **2021**, *82*, 2144–2150. [CrossRef] [PubMed]
55. Burdick, J.A.; Prestwich, G.D. Hyaluronic acid hydrogels for biomedical applications. *Adv. Mater.* **2011**, *23*, 41–56. [CrossRef]
56. Yasin, A.; Ren, Y.; Li, J.; Sheng, Y.; Cao, C.; Zhang, K. Advances in Hyaluronic Acid for Biomedical Applications. *Front. Bioeng. Biotechnol.* **2022**, *10*, 910290. [CrossRef]
57. Manfredi, C.; Spirito, L.; Calace, F.P.; Balsamo, R.; Terribile, M.; Stizzo, M.; Arcaniolo, D. Oral Preparation of Hyaluronic Acid, Chondroitin Sulfate, Curcumin, and Quercetin (Ialuril® Soft Gels) for the Prevention of LUTS after Intravesical Chemotherapy. *Pathophysiology* **2022**, *29*, 365–373. [CrossRef]
58. Kurczewska, J. Recent Reports on Polysaccharide-Based Materials for Drug Delivery. *Polymers* **2022**, *14*, 4189. [CrossRef]
59. Schuiringa, G.H.; Mihajlovic, M.; van Donkelaar, C.C.; Vermonden, T.; Ito, K. Creating a Functional Biomimetic Cartilage Implant Using Hydrogels Based on Methacrylated Chondroitin Sulfate and Hyaluronic Acid. *Gels* **2022**, *8*, 7. [CrossRef]
60. Vázquez, I.; Rodríguez-Amado, J.A.; Montemayor, M.I.; Fraguas, J.; Del González, M.P.; Murado, M.A. Chondroitin sulfate, hyaluronic acid and chitin/chitosan production using marine waste sources: Characteristics, applications and eco-friendly processes: A review. *Mar. Drugs* **2013**, *11*, 747–774. [CrossRef]
61. Nagira, T.; Nagahata-Ishiguro, M.; Tsuchiya, T. Effects of sulfated hyaluronan on keratinocyte differentiation and Wnt and Notch gene expression. *Biomaterials* **2007**, *28*, 844–850. [CrossRef]
62. Amhare, A.F.; Lei, J.; Deng, H.; Lv, Y.; Han, J.; Zhang, L. Biomedical application of chondroitin sulfate with nanoparticles in drug delivery systems: Systematic review. *J. Drug Target.* **2021**, *29*, 259–268. [CrossRef]
63. Cui, L.; Li, J.K.; Guan, S.; Zhang, K.X.; Zhang, K.; Li, J.A. Injectable Multifunctional CMC/HA-DA Hydrogel for Repairing Skin Injury. *Mater. Today Bio* **2022**, *14*, 100257.

64. Wei, S.; Li, J.; He, H.; Shu, C.; Dardik, A.; Bai, H. A three-layered hydrogel patch with hierarchy releasing of PLGA nanoparticle drugs decrease neointimal hyperplasia. *Smart Mater. Med.* **2022**, *3*, 139–147. [CrossRef]
65. Lei, C.; Liu, X.R.; Chen, Q.B.; Li, Y.; Zhou, J.L.; Zhou, L.Y.; Zou, T. Hyaluronic acid and albumin based nanoparticles for drug delivery. *J. Control. Release* **2021**, *331*, 416–433. [CrossRef]
66. Xu, R.; Zhang, K.; Liang, J.; Gao, F.; Li, J.; Guan, F. Hyaluronic acid/polyethyleneimine nanoparticles loaded with copper ion and disulfiram for esophageal cancer. *Carbohydr. Polym.* **2021**, *261*, 117846.
67. Rother, S.; Galiazzo, V.D.; Kilian, D.; Fiebig, K.M.; Becher, J.; Moeller, S.; Hintze, V. Hyaluronan/Collagen Hydrogels with Sulfated Hyaluronan for Improved Repair of Vascularized Tissue Tune the Binding of Proteins and Promote Endothelial Cell Growth. *Macromol. Biosci.* **2017**, *17*, 1700154.
68. Schmidt, J.R.; Vogel, S.; Moeller, S.; Kalkhof, S.; Schubert, K.; von Bergen, M.; Hempel, U. Sulfated hyaluronic acid and dexamethasone possess a synergistic potential in the differentiation of osteoblasts from human bone marrow stromal cells. *J. Cell. Biochem.* **2019**, *120*, 8706–8722.
69. Vogel, S.; Arnoldini, S.; Möller, S.; Schnabelrauch, M.; Hempel, U. Sulfated hyaluronan alters fibronectin matrix assembly and promotes osteogenic differentiation of human bone marrow stromal cells. *Sci. Rep.* **2016**, *6*, 36418.
70. Yao, S.; Cui, J.; Chen, S.; Zhou, X.; Li, J.; Zhang, K. Extracellular matrix coatings on cardiovascular materials—A review. *Coatings* **2022**, *12*, 1039.
71. Zou, D.; Li, J.; Kou, F.; Luo, X.; Yang, P. Reveal crucial subtype of natural chondroitin sulfate on the functionalized coatings for cardiovascular implants. *J. Mater. Sci. Technol.* **2021**, *91*, 67–77. [CrossRef]
72. Li, J.; Li, W.; Zou, D.; Kou, F.; Hou, Y.; Yasin, A.; Zhang, K. Comparison of conjugating chondroitin sulfate A and B on amine-rich surface: For deeper understanding on directing cardiovascular cells fate. *Compos. Part B Eng.* **2022**, *228*, 109430. [CrossRef]
73. Tong, P.; Chen, L.; Sun, X.; Li, H.; Feng, Y.; Li, J.; Guan, S. Surface modification of biodegradable magnesium alloy with Poly (L-lactic acid) and Sulfonated hyaluronic acid nanoparticles for cardiovascular application. *Int. J. Biol. Macromol.* **2023**, *237*, 124191. [CrossRef]
74. Chai, Y.; Feng, Y.; Zhang, K.; Li, J. Preparation of fluorescent carbon dots composites and their potential applications in biomedicine and drug delivery—A review. *Pharmaceutics* **2022**, *14*, 2482. [CrossRef]
75. Cohen, M.M.; Altman, R.D.; Hollstrom, R.; Hollstrom, C.; Sun, C.; Gipson, B. Safety and efficacy of intra-articular sodium hyaluronate (Hyalgan®) in a randomized, double-blind study for osteoarthritis of the ankle. *Foot Ankle Int.* **2008**, *29*, 657–663. [CrossRef]
76. Chen, G.; Ito, Y.; Imanishi, Y.; Magnani, A.; Lamponi, S.; Barbucci, R. Photoimmobilization of sulfated hyaluronic acid for antithrombogenicity. *Bioconjug. Chem.* **1997**, *8*, 730–734. [CrossRef]
77. Shankland, W.E. The effects of glucosamine and chondroitin sulfate on osteoarthritis of the TMJ: A preliminary report of 50 patients. *Cranio—J. Craniomandib. Sleep Pract.* **1998**, *16*, 230–235. [CrossRef]
78. Hempel, U.; Möller, S.; Noack, C.; Hintze, V.; Scharnweber, D.; Schnabelrauch, M.; Dieter, P. Sulfated hyaluronan/collagen I matrices enhance the osteogenic differentiation of human mesenchymal stromal cells in vitro even in the absence of dexamethasone. *Acta Biomater.* **2012**, *8*, 4064–4072. [CrossRef]
79. Vangsness, C.T.; Spiker, W.; Erickson, J. A Review of Evidence-Based Medicine for Glucosamine and Chondroitin Sulfate Use in Knee Osteoarthritis. *Arthrosc.—J. Arthrosc. Relat. Surg.* **2009**, *25*, 86–94. [CrossRef]
80. Zhang, Z.Q.; Yang, Y.X.; Li, J.A.; Zeng, R.C.; Guan, S.K. Advances in coatings on magnesium alloys for cardiovascular stents—A review. *Bioact. Mater.* **2021**, *6*, 4729–4757. [CrossRef]
81. Hou, Y.C.; Cui, X.; Qin, Z.; Su, C.; Zhang, G.; Tang, J.N.; Li, J.A.; Zhang, J.Y. Three-dimensional bioprinting of artificial blood vessel: Process, bio-inks and challenges. *Int. J. Bioprinting* **2023**, *9*, 740.
82. Xie, M.; Su, J.; Zhou, S.; Li, J.; Zhang, K. Application of Hydrogels as Three-dimensional Bioprinting ink for Tissue engineering. *Gels* **2023**, *9*, 88. [CrossRef] [PubMed]
83. Abi Zeid Daou, C.; Bassim, M. Hyaluronic acid in otology: Its uses, advantages and drawbacks—A review. *Am. J. Otolaryngol.—Head Neck Med. Surg.* **2020**, *41*, 102375. [CrossRef] [PubMed]
84. Hong, C.I.; Jung, E.G.; Han, K.I.; Kim, Y.H.; Lee, S.H.; Lee, H.S.; Han, M.D. Structural Characteristics and Anti-inflammatory Activities of Chemically Sulfated-hyaluronic Acid from Streptococcus dysgalactiae. *J. Life Sci.* **2016**, *26*, 545–554. [CrossRef]
85. Lebaudy, E.; Fournel, S.; Lavalle, P.; Vrana, N.E.; Gribova, V. Recent Advances in Antiinflammatory Material Design. *Adv. Healthc. Mater.* **2021**, *10*, 2001373. [CrossRef]
86. Graça, M.F.P.; Miguel, S.P.; Cabral, C.S.D.; Correia, I.J. Hyaluronic acid—Based wound dressings: A review. *Carbohydr. Polym.* **2020**, *241*, 116364. [CrossRef]
87. Nishikawa, H.; Mori, I.; Umemoto, J. Influences of sulfated glycosaminoglycans on biosynthesis of hyaluronic acid in rabbit knee synovial membrane. *Arch. Biochem. Biophys.* **1985**, *240*, 146–153. [CrossRef]
88. Oe, M.; Tashiro, T.; Yoshida, H.; Nishiyama, H.; Masuda, Y.; Maruyama, K.; Fukui, N. Oral hyaluronan relieves knee pain: A review. *Nutr. J.* **2016**, *15*, 11. [CrossRef]

coatings

Review

Extracellular Matrix Coatings on Cardiovascular Materials—A Review

Siyu Yao [1], Jixiang Cui [1], Shuyao Chen [1], Xinglin Zhou [1], Jingan Li [1,]* and Kun Zhang [2,]*

[1] School of Materials Science and Engineering, Zhengzhou University, Zhengzhou 450000, China; yao_siyu226@163.com (S.Y.); 17651973320@163.com (J.C.); 18759373019@163.com (S.C.); z1296260272@163.com (X.Z.)

[2] School of Life Science, Zhengzhou University, Zhengzhou 450000, China

* Correspondence: lijingan@zzu.edu.cn (J.L.); zhangkun@zzu.edu.cn (K.Z.); Tel.: +86-185-3995-6211 (J.L.)

Abstract: Vascular transplantation is an effective and common treatment for cardiovascular disease (CVD). However, the low biocompatibility of implants is a major problem that hinders its clinical application. Surface modification of implants with extracellular matrix (ECM) coatings is an effective approach to improve the biocompatibility of cardiovascular materials. The complete ECM seems to have better biocompatibility, which may give cardiovascular biomaterials a more functional surface. The use of one or several ECM proteins to construct a surface allows customization of coating composition and structure, possibly resulting in some unique functions. ECM is a complex three-dimensional structure composed of a variety of functional biological macromolecules, and changes in the composition will directly affect the function of the coating. Therefore, understanding the chemical composition of the ECM and its interaction with cells is beneficial to provide new approaches for coating surface modification. This article reviews novel ECM coatings, including coatings composed of intact ECM and biomimetic coatings tailored from several ECM proteins, and introduces new advances in coating fabrication. These ECM coatings are effective in improving the biocompatibility of vascular grafts.

Keywords: extracellular matrix; coatings; cardiovascular materials; surface modification; biocompatibility

Citation: Yao, S.; Cui, J.; Chen, S.; Zhou, X.; Li, J.; Zhang, K. Extracellular Matrix Coatings on Cardiovascular Materials—A Review. *Coatings* **2022**, *12*, 1039. https://doi.org/10.3390/coatings12081039

Academic Editor: Marco Laurenti

Received: 8 June 2022
Accepted: 21 July 2022
Published: 22 July 2022

1. Introduction

Cardiovascular disease (CVD) has been the leading cause of morbidity and mortality worldwide for many years, which places a huge burden on health sectors and the economy [1]. Cardiovascular biomaterials can be used in clinical therapeutic devices and implants, such as stents, balloon, artificial heart valve, artificial blood vessel, and occluder, etc. [2–4] (Figure 1), which play an important role in cardiovascular treatment. The clinical use of stents has experienced several stages, such as bare metal stents (BMS, made of stainless steel and cobalt chromium alloys), drug-eluting stents (DES), biodegradable polylactic acid stents and biodegradable magnesium (Mg) alloy stents [5]. At present, iron-based stents, zinc-based stents, and improved biodegradable polylactic acid stents and biodegradable Mg alloy stents are also in the R&D stage [6–9]. In addition, functions related to the biocompatibility of material surfaces, such as anti-coagulation, anti-proliferative, anti-inflammatory and pro-endothelialization, play an important role after implantation. Since endothelialization of cardiovascular prostheses can improve their hemocompatibility, simple surface rapid endothelialization has become a hot spot for cardiovascular device development [10]. At present, the common strategy is to endow the equipment with powerful multi-functions and improve the blood compatibility of the material.

Vascular transplantation is an effective and common method in the treatment of CVD [11]. Tissue engineering techniques are also often applied to the development of vascular materials, with the hope of creating an implant that can support the ingrowth and maintenance of a patient's own tissue, while the implanted scaffold slowly degrades, leaving behind a functional vascular system [12]. Commonly used materials for vascular grafts are synthetic materials, but their biocompatibility still needs improvement [13]. In contrast, the new extracellular matrix (ECM) coating showed a huge performance advantage [14]. ECM-modified scaffolds have the advantage of mimicking tissue specificity and are thought to better mimic the natural cellular microenvironment in vitro [15]. Functional scaffolds modified with cell-derived ECM have been developed, where the ECM components render the scaffold biologically active and confer some unique functions on the scaffold [16]. This ECM coating-modified scaffold has been proved to improve its biocompatibility. Developing a fully biocompatible coating surface that is effective for cell adhesion is one of the goals of tissue engineering [17]. The ideal scaffold coating, alone or in combination, should have multiple functions, such as promoting endothelialization, preventing the adhesion of inflammatory cells, etc.

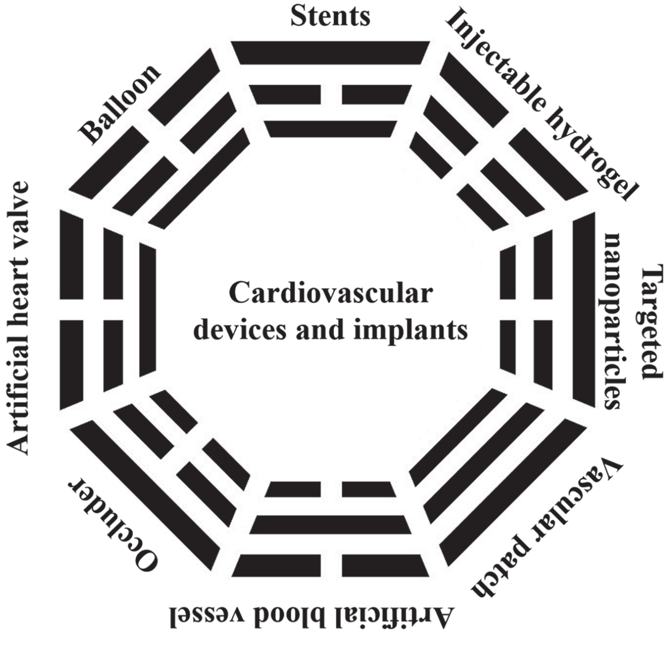

Figure 1. The Chinese eight diagrams to describe the types of artificial cardiovascular devices and implants.

Cardiovascular devices face implant failure, and insufficient endothelialization is one of the main factors. Endothelialization is a process regulated by multiple factors and structures. One method of attracting EC is to precoat the implants with ECM molecules or peptides to promote EC adhesion [18]. An effective approach to improve implant biocompatibility is to functionalize cardiovascular biomaterials with ECM. The ECM is actively involved in various aspects of cardiovascular development and physiology, as well as disease development and progression. The cardiovascular ECM is a complex scaffold of hundreds of proteins that surround the cells of the heart and vascular system and is a key component of the heart and vascular system [19]. The role of the ECM is closely related to its physical and mechanical properties. The ECM coating is closer to the native vascular basement membrane, and the tissue response induced by the implant is milder [20]. As with many other tissues and organs, the application of decellularization methods to obtain acellular ECM scaffolds holds great promise [21,22]. Extensive studies have utilized decellularized ECM from native tissues, or ECM secreted by cultured cells.

ECM-based biomaterials have become mature tools in regenerative engineering, due to their high biocompatibility and biomimetic properties, and bio-scaffolds using ECM materials have become an important medical modality in bioengineering [23–25]. The ECM plays an important role in cardiac repair and regeneration after cardiac injury, and it can be applied as a drug to improve cardiomyocyte proliferation and cardiac regeneration [26]. It has been reported that ECM scaffolds are widely used in medicine, including bone tissue engineering [27], skin tissue engineering [28] and cardiac tissue engineering [29]. ECM-based scaffolds provide a biological matrix with environmental cues that can support the formation of proper vascular tissue. When the scaffold is coated with recombinant human laminin fibers, it supports the attachment and growth of naive stem cells in single-cell suspension [30]. A fibrin-coated pericardial ECM can be used as a material for cardiovascular surgery [31]. The ability of ECM and its components to improve biocompatibility has also been extensively reported [32,33]. Studies have found that ECM coating can improve the adsorption capacity of platelets, reduce EC toxicity, and possibly induce tissue regeneration [34].

There have been numerous experiments investigating new synthetic and naturally isolated coatings. Traditional methods can prepare coatings of corresponding components by separating one or several components from tissue ECM, such as collagen coating, laminin coating. However, the intact ECM appears to be an ideal matrix to promote rapid endothelialization [35]. Coatings with intact ECM components not only mimic the natural cellular environment, but also endow cardiovascular biomaterial surfaces with more functionality. ECM is a kind of biomaterial that can effectively simulate the inherent microenvironment of cells, has good bioactivity, biodegradability and biocompatibility, and has been widely used in vascular grafts. Previous studies have demonstrated that modified ECM coatings can enhance cell attachment and proliferation [35]. The design and modification of ECM coatings have received increasing attention. In this regard, various ECM-related materials have been explored. From tissue-derived ECM 2D coatings, ECM materials have been developed to include recombinant ECM proteins, ECM fragments, and ECM mimetics. Since different components of the ECM play different roles in cellular activities, better characterization of the ECM composition and understanding of its biochemical effects in vivo will help to gain a deep understanding of the research priorities and modification directions of ECM coatings.

2. ECM Materials

2.1. Features and Sources

The ECM is composed of polysaccharides and proteins and it constitutes the microenvironment required by cells. Materials derived from natural ECM are important ingredients of engineered biomaterials designed to mimic cellular and tissue function, and further replace or repair damaged tissue. In some studies, ECM materials have been used in cell culture or injected into vivo for in situ tissue regeneration [36]. For example, several studies have found that ECM-based decellularized myocardial hydrogels can enhance cardiogenesis of cardiac progenitor cells in 3D in vitro culture. In tissues, the ECM offers structural integrity, function, and suitable conditions for cell growth [37]. Mechanical and biochemical cues in the ECM are able to direct many cellular functions. The ECM contains many signaling molecules that are critical for cell behavior, regulating cell growth, polarity, migration, differentiation, and proliferation [38,39]. The ECM plays a crucial role in intercellular signaling, such as tissue regeneration and repair, which are highly affected by proteases and cytokines. Natural ECM has evolved into more complex systems, starting with purified proteins as coatings on the surface of biomaterials, and now there are also cell-derived and whole-tissue-derived constructs. With the advancement of decellularized tissue and isolated cell technology, natural forms of ECM proteins can be better used to create functionally complex biomaterials [40].

ECM can be derived from human or animal organs, tissues or cell cultures. A matrix produced using cells is produced by a single cell type, whereas a tissue-derived ECM is composed of matrices secreted by multiple cell types. At present, from different organs or tissues, a variety of different types of decellularized ECM can be obtained. This decellularized ECM stays close to the natural tissue or organ structure, which contains natural proteins, soluble factors and cell adhesion ligands [36]. In addition, plant material can also serve as a source of ECM. Due to the advantages of plant-derived materials with fast growth rates and availability in almost unlimited quantities, several studies have used acellular plant materials as potential bio-scaffolds [41,42]. Decellularized plant tissue engineering scaffolds can be obtained by applying decellularization technology to different plants and tissues. Modulevsky et al. used plant-derived cellulose biomaterials to produce implantable scaffolds, and this acellular cellulose scaffold showed biocompatibility in immunocompetent mice [43].

2.2. Cell-Derived Matrix (CDM)

A cell-derived matrix (CDM) is the acellular ECM of tissue obtained through laboratory culture procedures. In contrast to dECM, CDM is derived from laboratory cultured cells/tissues, which are derived from actual animals [44]. CDM and dECM derived from the same tissue can have very similar chemical compositions; however, it is difficult for CDM to have the same physical properties as natural tissues, such as structural organization. CDMs represent biologically active and biocompatible materials that are composed of matrix macromolecules, fibrillar proteins, and related growth factors [45]. The advantages of CDM are the availability of human cell sources, increased tunability of matrix properties and conformations (bulk material or scaffold coatings), and the ability to generate matrices with desirable properties using a variety of somatic and stem cells. Therefore, by designing cell sources and culturing methods, the secreted ECM can be tailored for specific functions, which increases the tunability of CDM.

CDMs are interesting alternatives to traditional sources of ECM. A meaningful method would be to investigate the matrix deposition function of specific cell types, providing an in vitro platform to study cell-matrix interface interactions and their mechanisms. As one of the most commonly used strategies to reconstitute ECM, CDMs have broad applications in biomedical research [46]. CDMs contain complex but organized mixtures of macromolecules, which can imitate various aspects of the natural tissue microenvironment and serve as scaffolding materials to modulate stem cell function. ECM produced by adipose derived stromal cells can enhance tissue-engineered myocardial structures in vitro and promote myocardial remodeling after infarction [47]. CDMs can also be used as a coating by simply decellularizing cells on the surface of biomaterials. Biomaterials based on CDMs are primarily used for bone and cardiovascular repair, and have been explored as cell-delivered cardiac patches, as well as for engineered heart valve replacement and vascular transplantation [48,49].

2.3. Preparation of ECM

To obtain tissue-specific biomaterials, decellularization and isolation techniques can be applied to extract ECM from tissues and organs. Decellularization is the process of separating the ECM from cellular and nuclear material, which has minimal impact on the composition, biological activity, and structural integrity of the ECM [50]. Its primary goal is to remove allogeneic or xenogeneic cellular antigens and other immunogenic components, such as DNA, to minimize the risk of adverse immune responses [45]. This process usually uses physical, chemical, enzymatic and thermal methods. Decellularized ECM, obtained by removing cellular components from native tissues, not only preserves major components and structure, but also prevents potential immunogenicity, and it can serve as a template or scaffold for cell culture [17]. Many clinically used ECM-based materials are produced through the decellularization processes. The following takes CDM as an example to briefly introduce the preparation process of ECM materials.

CDM can be obtained from cells in 2D or 3D culture conditions. The production process of CDMs consists of the following four main steps: cell expansion, seeding, matrix generation and decellularization. By expansion, to obtain sufficient cell numbers for production; depending on the application, expanded cells can be seeded on different surfaces, such as 2D surfaces or 3D scaffolds [51]. The most important step in production is the creation of ideal culture conditions, whereby the desired properties of the final ECM product can be achieved by systematically optimizing both intrinsic and extrinsic factors. When sufficient ECM is deposited, cellular components can be destroyed and removed from the ECM by chemical, physical or enzymatic treatment and a specific classification can be found in the work reported by Heath et al. [24]. The obtained ECM also needs some post-processing before application, which is further processed into slurries, coatings, hydrogels, etc. ECM post-processing, such as cross-linking, can further alter ECM stiffness or the overall performance of CDM [45]. A recent study also applied ultrasound to ECM materials [52]. Ultrasound can change ECM protein structure through thermal effects and/or mechanical forces, and can also enhance cell-mediated ECM remodeling behavior. This ultrasound-based approach provides an innovative strategy for the preparation of ECM materials, which facilitates non-invasive fabrication and in situ transformation.

ECM can be produced from different cellular sources. The ECM also varies in composition and function depending on the source of cells [53,54]. A single ECM protein cannot fully mimic the complexity of endogenous ECM, and with the in-depth study of ECM, composite biomimetic coatings prepared using multiple ECM components have been shown to achieve better results. The strategies based on molecular self-assembly have received increasing attention, aiming at producing synthetic matrices with multi-component structures and high-level compositional definition. Work in the field of self-assembly synthesis of ECM has mainly focused on peptides or peptide derivatives, and self-assembly can be used to meet the functional requirements of complex ECM [55]. The combination of ECM materials and 3D printing technology is helpful for the construction of in vitro organ models [56]. The emergence of ECM-based bio-inks shows the great potential of 3D printing to build ECM-mimicking scaffolds [57]. Processing of decellularized ECM into microparticles, which are then reconstituted into hydrogels, also expands the range of potential applications [58,59]. For example, a thin coating of ECM through layer-by-layer (LbL) deposition on the cell surface can enhance cell viability and improve tissue function [60].

The production techniques for ECM coatings on biomaterials depend on the property of the devices and implants. Surface self-assembly was the main method to prepare ECM component coatings on the surface of cardiovascular materials for a long time in the past, especially since the LbL self-assembly technology can make the ECM coating more evenly distributed on the surface, but its disadvantage is that with the increase in different layers, the stability of the coating will gradually decline at a turning point [61]. In comparison, it is simpler and more stable for different ECM components to be blended and self-assembled to the material surface as required [62]. The distribution, morphology and behavior of cells on the surface can be controlled by stamping ECM components onto the surface of materials with polymer stamps. For example, the ECM micro-stripes with the width of 25 μm can regulate the morphology of vascular endothelial cells to grow as ifunder the action of blood flow shear stress in vivo [63]. The above coatings can be prepared by chemical reaction, electrostatic interaction, hydrogen bonding or physical adsorption, according to the binding requirements of membrane base. However, due to the long time-consuming process, it is generally not suitable for the preparation of ECM coatings on the surface of small-scale biodegradable devices, such as Mg-base stents. Facing this situation, the spraying method is a good choice, which can complete the preparation of devices' surface coating in just a few minutes [64]. Generally speaking, 3D printing technology can accurately prepare ECM coatings for the surface of devices. However, for some complex surfaces, it also has certain limitations, such as the inner surface of vascular stents. In addition, 3D printing technology is usually used for precision processing of a small number of devices, which is not suitable for large-scale industrial production.

3. Chemical Composition of ECM

The ECM is composed of complex three-dimensional structures and functional biological macromolecules, and it is a unique tissue-specific microenvironment. The protein components of ECM play the roles of ligands for various signaling receptors, such as integrins [65]. The ECM is an important support for vascular endothelial cells (EC), and in the long-term interaction of cells with materials, the ECM can influence cell behavior. The binding of ECM proteins (such as type I collagen or fibronectin) to topographic factors can have different effects on cell processes [66]. The ECM not only ensures the structural strength and elasticity of blood vessels, but also controls the development and stability of the vascular system. Therefore, the ECM is a very important part of the cardiovascular system.

Most vasculature consists of three layers, including adventitia, tunica, and intima [67]. The adventitia is mainly composed of collagen fibers and fibroblasts. The tunica is composed of elastic fibers and smooth muscle cells (SMC), which are responsible for adapting to different blood pressures by contracting and relaxing. In the inner layer, the intima, consists of a thin non-proliferating (quiescent) monolayer of squamous EC that forms the endothelium, largely leaving blood flow undisturbed. Adjacent layers are separated by elastic layers; the outer and middle layers are separated by an outer elastic layer, and the inner and middle layers are separated by a composite of the inner elastic layer and basement membrane. The intimal layer consists of the innermost basement membrane and the substrate below it. The basement membrane provides dynamic hemostasis regulation and is essential for maintaining a confluent, functional monolayer of EC. Basement membranes and placodes are composed of multiple components that can influence cell phenotype and promote cell adhesion [68]. The vascular basement membrane is a lamellar structure composed of various ECM molecules that controls not only the remodeling of the vascular network but also the mechanical stability of the vascular system [69,70]. It is closely related to the occurrence of diseases [71].

As can be observed from the above, the components of ECM are very complex, and each component protein has different effects on cells [72,73]. Due to the important biochemical role of ECM in cells, understanding the composition of ECM and its interaction with cells is crucial for the preparation, modification, and innovation of ECM coatings, which is conducive to the design of ECM materials that are more suitable for medical needs. Of course, due to the complexity and biochemical properties of ECM components, the proteomic characterization is challenging, and it is still impossible to accurately and exhaustively understand the full picture of its composition and function [74]. Combined with numerous existing research results, we mainly introduce several major components of the ECM.

3.1. Collagen

Collagen is the most important component of ECM, and it provides not only tensile strength and cell adhesion, but also structural properties and elasticity to the tissue, which are involved in the formation of a fibrous network [75]. The rope-like structure of collagen resists tension by bearing stress. Therefore, collagen is critical to the substrate, as it provides significant biochemical signals and mechanical strength for cell adhesion and migration.

Although 28 types of collagens have been identified, collagen type I and IV are the most prevalent types found in the cardiovascular system. Collagen provides a three-dimensional environment for cells to support cell growth and influence the morphology and function. Type I collagen is the most abundant component among the cardiac ECM, with a well-described composition-function relationship, conferring strength and stiffness to heart and vascular tissues [76]. Type IV collagen is a specific ingredient of the basement membrane, and its network bonds to the laminin network through nidogen and perlecan. Depletion of type IV collagen results in increased fibronectin expression and extracellular deposition, followed by rearrangement of long, parallel fibrils. Exogenous type IV collagen can restore basal levels of fibronectin deposition, suggesting that type IV collagen may act as a regulator of fibronectin fibril growth.

3.2. Laminin

Laminins can self-assemble into sheets and are essential components of the basement membrane, and can also bind other ECM components together through cross-linking, so they are an important ECM cross-linker. In addition, laminin also enables the ECM to interact with different types of cells through its binding sites with cell surface receptors. Some studies have found that laminin can play critical roles in a variety of functions, such as cell adhesion, cell differentiation, and phenotypic stability. Laminin exerts multiple important functions in the central nervous system by interacting with integrin and non-integrin receptors [77]. Laminin expressed by EC promotes vascular stability and EC morphogenesis [78]. Some laminin modifications may lead to EC dysfunction, thereby promoting the development of atherosclerosis [79]. The laminin network self-assembles on the EC surface and is thought to trigger basement membrane deposition.

3.3. Fibronectin

Fibronectin is a glycoprotein and it is a dimeric structure formed by two polypeptide chains. There are two forms of fibronectin, soluble fibronectin and insoluble fibronectin. In addition, the fibronectin can bind to cells and promote adhesion to other components. This is primarily through the functional and structural domains of the collagen triple helix denaturation regions, and through specific binding domains that bind to heparin and fibrinogen. In conclusion, fibronectin provides a substrate for complex interactions with EC and their environment.

Previous findings have suggested that fibronectin and its receptors are required for vascular formation, and recent studies have further demonstrated that fibronectin is an important signaling molecule for vascularization and is essential for formation of fenestrae in EC of the fenestrated capillary [69]. The interaction between fibronectin and type I collagen suggests that fibronectin may be involved in the arrangement of collagen fibers as a scaffold [65,80].

3.4. Nidogen

Nidogen accounts for a small proportion in the base membrane, but is a crucial factor for organizing ECM, and it can also cross-link other components, including fibrinogen, perlecan, and fibronectin, etc. Nidogen are divided into two types, nidogen 1 and nidogen 2 [18]. Nidogen 1 is important for the attachment and stabilization of self-assembled layers of laminin and type IV collagen; nidogen 2 can also bind components of the basement membrane. There is also evidence that nidogens may contribute to the maintenance of capillary integrity [81].

3.5. Glycosaminoglycans and Proteoglycans

Glycosaminoglycans (GAGs) not only act as ligands for other ECM macromolecules and cellular integrins, but also retain water and interact with biological mediator proteins [82]. At low concentrations, GAGs form a gel, which allows the ECM to resist compressive forces by hydrating and filling the extracellular space. GAG chains can be covalently linked to core proteins to form proteoglycans. The abundant proteoglycans in the ECM can modulate the activity of the secreted ECM by binding to proteins. In addition, they can also change conformation or block binding sites, thereby controlling the transmission of chemical signals from cell to cell. Several proteoglycans are secreted as transmembrane proteins, while others can also act as a receptor for ECM proteins. In addition to being responsible for hydration, GAGs and proteoglycans also play important roles in other cellular behaviors, such as regulating ECM–EC interactions.

GAG play an essential role in tissue engineering. Since different sources and types of biomacromolecules with different biological roles can be included, the combination of GAGs with other polymers can better mimic the multicomponent and multifunctional configuration of native ECM [83]. GAGs are tunable gel components that can modulate collagen fibril formation, hydrogel properties, and guide cellular behavior. Among them, hyaluronic acid (HA) has a very high molecular weight (MW) GAG, which has been widely applied in various aspects of the biomedical fields (Figure 2) [84]. Collagen hydrogels, containing both modified and unmodified HA, show great promise in tissue engineering. This combined approach of biomaterials could open up new therapeutic approaches for the treatment of complex diseases [85]. As GAGs become more thoroughly understood, it is believed that their use and ubiquity in the field of tissue engineering will continue to expand.

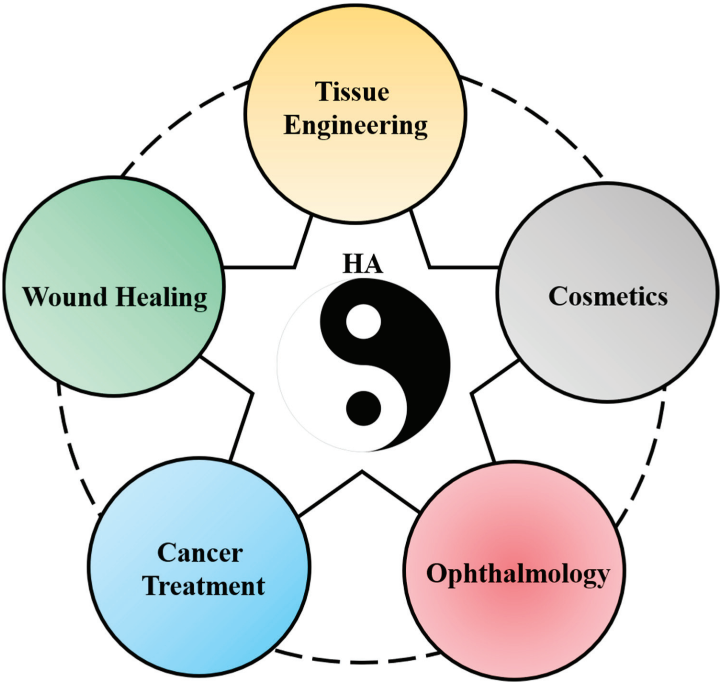

Figure 2. The application of HA, a main component of ECM in biomedical fields [84].

3.6. Elastin

Elastin is one of the main components of the vascular system [86]. It not only provides elastic recovery, but also has crucial influence in mechanical and cellular signaling. The cross-linked network structure of elastin consists of tropoelastin, whose lysine amino acids undergo extensive cross-linking by lysine oxidase immediately after release from cells, followed by condensation to link several side chains. The elasticity of the elastin network comes from its unique structure, and the loose and random coil conformation of the polypeptide chain endows it with good elasticity [87]. Elastin does not form blood clots; thus, the stents and coatings made from it show increased blood compatibility [88]. It interacts with many cell types, and is critical for arterial morphogenesis and controls SMC proliferation. Elastin peptides are chemotactic on EC, and thus have proangiogenic effects [89]. Elastin is a promising candidate for vascular biomaterials or tissue engineering, due to its durable mechanical properties, good association with EC, and inhibition of SMC proliferation.

4. ECM Coatings

ECM coatings are a well-known strategy for improving implant integration. Intact ECM appears to have better biocompatibility and can endow cardiovascular biomaterial surfaces with more functions. Single ECM components have selective, well-defined biological activities and functions [90]. The use of one or a few purified ECM components to construct surfaces allows for customization of coating composition and structure, potentially resulting in unique functionalities. The hemocompatibility of biomaterials mainly depends on the physicochemical properties of its surface; therefore, surface modification is an effective way to improve hemocompatibility. Surface modification of coatings with biomolecules such as HA, peptides, and heparin can effectively improve the performance of coatings [91–93]. Intact ECM or its single component has natural stability and stiffness advantages to promote the adhesion and functional growth of EC on its surface. This is a kind of dynamic stability. The EC on the material surface will continuously secrete new ECM, according to the environmental response and their own needs. The adhesion of the ECM coatings to the surface of the cardiovascular devices depends on the preparation method and interface bonding mode; the chemically bonded coating is usually stronger than electrostatic bonding, hydrogen bonding and van der Waals force bonding, and the combination of the above forces is stronger than that of physical adsorption, but this law is not absolute.

In this section, several ECM-based coating materials are reviewed (Figure 3). The biomimetic endothelial ECM surface was prepared by EC culture and decellularization, which improved the biocompatibility of the substrate. Inspired by the structure and composition of the native vascular basement membrane, the bilayer coating formed by the ECM secreted by EC and SMC exhibits better biocompatibility, which is expected to address the functional limitations of a single ECM and treat more many clinical diseases. Natural ECM derived from Wharton's jelly (WJ) has shown great potential in vascular engineering and it can be used to prepare standardized coatings. In addition, some mimetic coatings made of ECM proteins exhibit unique functions, due to their special composition and structure. A tailored collagen coating through LbL self-assembly can promote in situ endothelialization and inhibit excessive neointimal hyperplasia, providing a novel approach for developing functional coatings for cardiovascular stents. Synthesizing ECM biomimetic peptide coatings with specific structures helps to overcome stent thrombosis, and further immobilizes biomolecules, such as heparin and glycosaminoglycans, to diversify the coating functions [94,95].

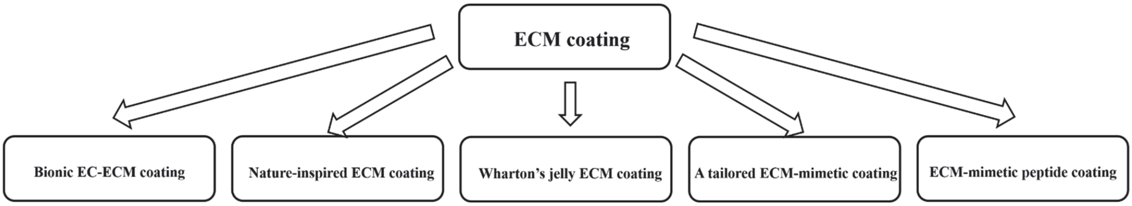

Figure 3. The classification of the types of ECM coatings.

4.1. Bionic EC-ECM Coating

EC play crucial roles in preventing thrombosis; thus, effective re-endothelialization techniques for intravascular implants are important for long-term thrombosis prevention and biocompatibility. A currently recognized and effective method to improve the biocompatibility of cardiovascular biomaterials is the decellularization of the endothelial extracellular matrix (EC-ECM). Li et al. prepared a biomimetic coating composed of endothelial ECM and HA micropatterns (ECM/HAP), which has good blood compatibility and anti-inflammatory properties [96]. In their research, a novel method combining HA micropatterns with EC decellularization was developed; they cultured EC on HA micropatterns and prepared a bionic surface-coated ECM of the elongated and regulated EC by decellularization. The HA microstructure can effectively prolong the cell morphology, induce the secretion of more anticoagulant factors, and limit the contractile phenotype of SMC. Controlling the morphology and ECM secretion of EC by HA micropatterns can significantly improve the biocompatibility of this EC-ECM. The evaluation results further showed that the HA micropatterned endothelial ECM displayed anti-coagulation and endothelialization properties, and inhibited the hyperproliferation of SMC and the attachment of macrophages. This multifunctional ECM/HAP coating can construct biomimetic human endothelial ECM on the surface of biomaterials, and it may provide an efficient method for surface modification of cardiovascular devices. Generally speaking, the immune reactions towards allogenetic or xenogenic cellular antigens are mostly observed in organ or tissue transplantation and above the cellular level, and are relatively rare at the ECM or molecular level. The immune reaction of ECM and molecules to the microenvironment is usually related to the dosage and whether they are antigens. As a coating of cardiovascular materials, a single ECM component is rarely reported as causing an immune reaction. The whole component ECM secreted by cells often causes concern that there may be immunogenicity problems, while HA has the effect of protecting the coating from immune reaction, and the amount of ECM used for surface modification is relatively small. Therefore, immune reaction is not a bottleneck problem that restricts the application of ECM coating on the surface of cardiovascular materials.

On the basis of the above work, by repeating EC culture and decellularization, an idea that could enrich the patterned EC-ECM on the surface of cardiovascular biomaterials came up. Zou et al. prepared a biomimetic EC-ECM surface on polydopamine (PDA)-coated 316L stainless steel by LbL EC culture and decellularization. The surface of this biomimetic ECM was formed by the EC-ECM secreted by patterned EC onto the PDA membrane, and there are fewer platelets and macrophages distributed on the surface of the biomimetic ECM, which indicates that the surface of the new biomimetic ECM has better blood compatibility and anti-inflammatory properties. Compared to surfaces with one and two layers of ECM, surfaces containing three layers of ECM had a more pronounced effect. In addition, the thickness and distribution of macrophages in the new tissues were significantly reduced after PDA modification, and further biomimetic modifications also indicated that more abundant EC-ECM contributes to milder tissue responses. The culture results showed that the three-layer ECM surface demonstrated stronger ability of promoting surface endothelialization. However, in the healthy vascular wall, the ECM of SMC also plays an important role in the adhesion, growth and release of anticoagulant factors of EC. Therefore, the bionic degree of the coating constructed only by patterned EC-ECM is not enough. The vascular basement membrane is composed of ECM secreted by contractile SMC and EC under blood flow shear stress. Therefore, learning from the natural vascular basement membrane structure, building a coating composed of SMC-ECM and EC-ECM may have a better composite function.

4.2. Nature-Inspired ECM Coating

Surface modification with one or more ECM can significantly improve the biological function of the cardiovascular biomaterials. Immobilized proteins or their functional peptides can promote EC growth, while binding mucopolysaccharides confer anti-coagulant, anti-proliferative or anti-inflammatory functions on the surface. On this basis, by modifying the surface of biomaterials with two different ECM components, the surface with a balanced function can be obtained. Inspired by the natural vascular basement membrane composed of ECM secreted by physiological EC and SMC, Han et al. prepared a bilayer ECM coating through successive SMC/EC culture and decellularization, which endowed cardiovascular materials with better biocompatibility [20]. The ECM secreted by EC can make the surface more biocompatible, and the ECM secreted by contractile SMC can better reduce the number of adherent platelets. By controlling physiological SMC and EC by the HA micropattern, followed by sequential culture and decellularization, a nature-inspired bilayer SMC/EC ECM was obtained to modify the material surface. Compared with single-layer SMC-ECM or EC-ECM, the double-layer ECM coating has richer ECM density, larger pore size and different wettability, which contributes to better blood compatibility, anti-proliferative properties, pro-endothelialization, anti-inflammatory function and histocompatibility. In addition, this novel ECM coating can greatly reduce the rate of hemolysis on the material surface, so it has a good inhibitory effect on hemolysis after implantation. The main feature of this ECM coating is that it greatly improves the reproducibility of the function and structure of the vascular basement membrane on the material surface. The phenotype and function of cells can be controlled in a physiological state by the HA micropattern. The functional advantages of this nature-inspired coating are attributed to its excellent biomimetic properties, which will provide new and efficient methods for surface modification of cardiovascular materials. However, the application of this double-layer ECM is limited because it is not easy to be directly prepared onto the biodegradable or uneven materials. To solve this problem, Liu et al. dispersed the double layer ECM into normal saline using the ultrasonic vibration method, and then self-assembled it onto the surface of biodegradable Mg alloy (ZE21B) (Figure 4), thereby improving the corrosion resistance and biocompatibility of ZE21B [97]. It is unknown whether the process of preparing the ECM solution by ultrasonic vibration will cause losses to its components.

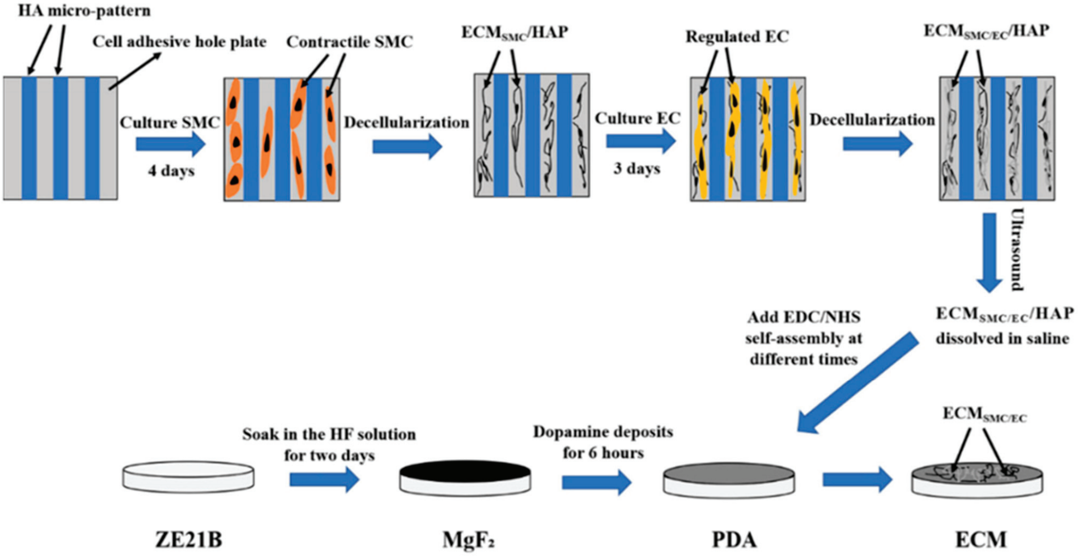

Figure 4. The preparation of the nature-inspired ECM on the biodegradable Mg alloy (ZE21B) surface [97].

Furthermore, heparin is a negatively charged natural polysaccharide that promotes EC proliferation and inhibits SMC expansion. It has been used in the manufacture of vascular grafts, due to its thrombosis-inhibiting properties. The behavior of EC and SMC can be selectively modulated by surface modification of the coating and fixation of an appropriate dose of heparin on its surface. On the basis of the above-mentioned nature-inspired ECM coating prepared from EC and SMC co-culture/decellularization, heparin was immobilized on the ECM coating at an optimized density to selectively promote EC proliferation but inhibit SMC grow and achieve satisfactory blood compatibility [98]. At the same time, the coating also has the characteristics of inhibiting thrombosis, preventing intimal hyperplasia and promoting endothelialization.

Controlling the MW of conjugated HA during surface modification is critical for better biocompatibility. HA, as the main component of the ECM, is a natural biopolymer. This biomolecule has different functions, such as anti-coagulant, anti-proliferative, anti-inflammatory and pro-endothelialization functions, depending on its MW. Low MW (LMW) HA has been reported to be a major player in the thrombosis process, and it also contributes to inflammation [99,100]. High MW (HMW) HA inhibits platelet, SMC, and macrophage adhesion, further conferring anti-coagulant, anti-proliferative, and anti-inflammatory functions on the surface, as well as imparting non-immunogenic properties to the surface, which are critical for implants [101]. However, HA with extremely HMW inhibits endothelial progenitor cell adhesion and EC migration, which is clearly not conducive to rapid endothelialization. Li et al. provided better versatility for cardiovascular biomaterials by preparing HA with gradient MW and controlling the MW of HA on the coating surface [102]. HA with an appropriate MW affects the homeostasis of important pathways in the cardiovascular system, inhibits phenotypic changes in vascular SMC and platelet activation, and promotes the repair and functionalization of endothelial monolayers. This demonstrates the feasibility of coatings with appropriate MW HA for potential applications in the surface modification of cardiovascular implantable devices.

Further research found that a HA nanoparticle less than 200 nm could carry Mg ion into EC, which would inhibit EC apoptosis and promote nitric oxide (NO) release of EC [103]. Our study discovered that the Mg is the main degradation product of biodegradable Mg alloys, which may control the phenotypes of macrophages and the function of EC, further regulating the pro-endothelialization function of the Mg alloy stents (Figure 5) [104]. Thus, a nanocomposite coating was placed onto the Mg alloy to regulate the degradation behavior and the Mg transportation to the EC, SMC and macrophages based on the different requirements of different cells for Mg concentration (Figure 6) [105].

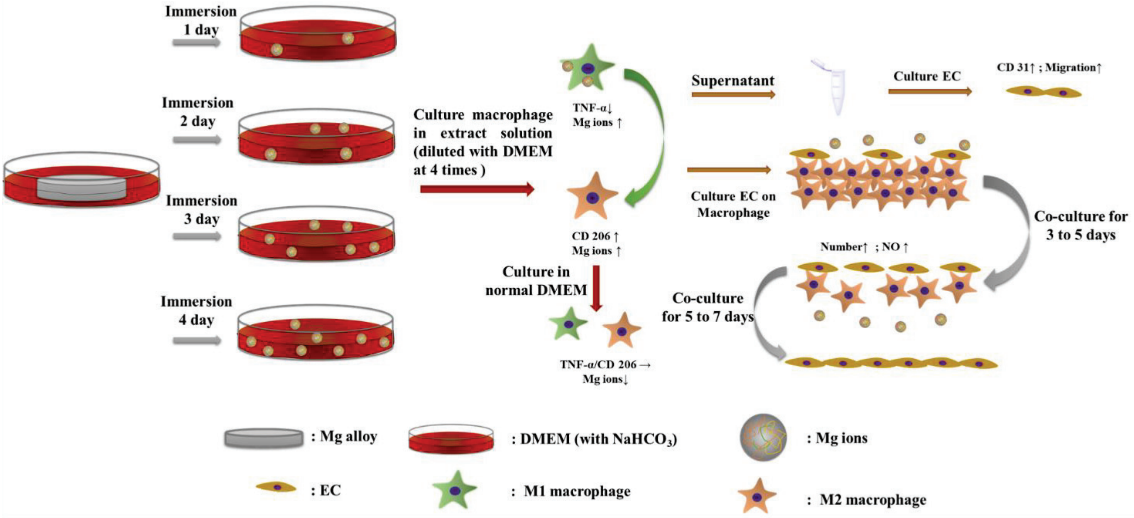

Figure 5. Mg alloy degradation products that regulate macrophages and EC behaviors [104].

4.3. Wharton's Jelly ECM Coating

Human tissue may be a suitable material for the preparation of natural matrices, from which we can extract intact ECM. Hao et al. previously demonstrated that the ECM obtained from Wharton's jelly (WJ) can contribute to MSC culture [106]. Previous studies have also proven that WJ-ECM contains several growth factors, which may promote angiogenesis and vascular cell differentiation [107]. Meanwhile, since WJ-ECM is prepared from human tissue, it does not have any toxicity to cells. In various tissue engineering, WJ-ECM becomes a universal tool to support cell culture. Using native ECM extracted from Wharton's jelly (WJ), Dan et al. report an innovative method for preparing coatings [108]. The mechanical, chemical and enzymatic methods are common methods for ECM isolation. However, simple stirring or chemical dissolution of ECM extracted from WJ tissue is less effective. Here, Dan et al. used trypsin to isolate intact ECM, which not only simplifies the isolation procedure, but also keeps the ECM-containing tissue in a relatively physiological state. Furthermore, WJ-ECM can form a continuous coating on the negatively charged glass surface, and the ECM concentration determines the thickness and stiffness of the coating. Because ECM is derived from human tissue, the coating does not contain chemicals that are harmful to cells, which is the biggest advantage of this coating.

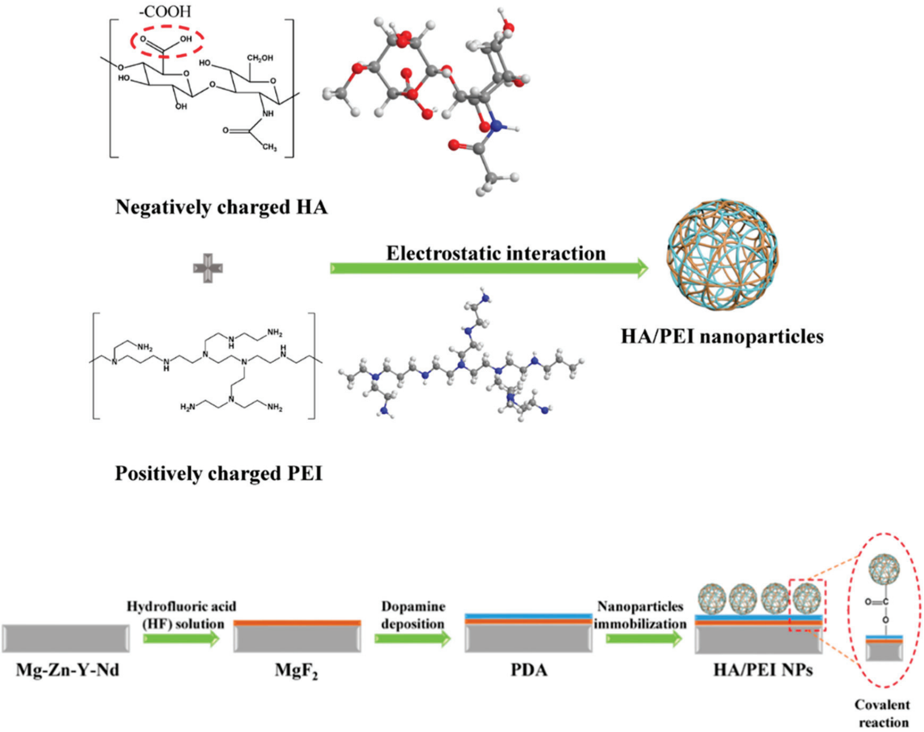

Figure 6. Nanocomposite coating on the Mg–Zn–Y–Nd alloy prepared with HA nanoparticles [105].

The performance of this WJ-ECM coating showed that the WJ-ECM-derived coating could enhance the adhesion and proliferation of EC and human mesenchymal stem cells (hMSCs). Compared to collagen coatings, a higher number of cell adhesions can be observed on WJ-ECM under physiological shear stress. In vascular tissue engineering, biomaterials must provide adequate cellular anchorage against shear stress. In the EC test, the WJ-ECM coating was better than the commercially available collagen I coating for cell anchoring. This suggests that WJ-ECM may promote the endothelium, thereby establishing a suitable continuous layer during vascular tissue engineering. In addition, this new surface shows an interesting phenomenon that the resistance of cells increases under the flow shear stress. Overall, WJ-ECM is a very valuable surface coating, with important applications in the design of biocompatible surfaces in humans.

4.4. A Tailored ECM-Mimetic Coating

As introduced previously in this review, collagen is one of the main components of the ECM. Mixed with other polymers, it is possible to mimic the basic structure of a specific ECM and further obtain the desired function with growth factors [109]. Collagen has been widely used in tissue engineering, but its inherent thrombogenic properties limit its application in vascular devices. The binding affinity to platelets is a major cause of collagen thrombosis, while previous studies have suggested that hydroxyproline (O) may be critical for platelet adhesion and activation. In addition, recombinant collagen not only has better water solubility, but also has a low inflammatory response. Thus, designing recombinant proteins with a large number of cell adhesion motives, but without hydroxyproline, may provide a new method for developing collagen for blood contact. In recent studies, an ECM-mimetic multilayer coating formed by the assembly of collagen and HA has emerged [110].

Yang et al. developed a recombinant human type III collagen protein (hCOLIII), which contains multiple charged residues and has a stable triple-helix conformation. The results of its assessment showed that platelets lacked affinity for hCOLIII [110]. Furthermore, by depositing the hCOLIII LbL assembly together with HA on the amine-rich PDA-coated substrate, they prepared an ECM-mimetic multi-layer coating. The coating has significant thromboprotective properties. Compared to animal-derived collagen, the use of hCOLIII-tailored ECM-mimetic coatings have advantages in inhibiting platelet adhesion and activation. When the coating was prepared with animal-derived collagen, it showed more platelet adhesion. In contrast, hCOLIII-based ECM coatings effectively inhibited platelet adhesion. The coating showed stable performance after implantation, and the experimental results showed that the composite coating had longer and reliable anti-coagulation ability with the higher coverage of hCOLIII and HA. Furthermore, this ECM-mimetic coating provided a favorable microenvironment for EC to promote in situ endothelialization, which showed the properties of enhancing endothelialization. The quantification of adherent platelets also suggested that hCOLIII may be a custom collagen-derived material, showing potential for use as a surface coating for blood-contacting devices. The emergence of this novel ECM-mimetic coating indicates that the hCOLIII-based ECM coating can be used as a blood-contacting material, with promising application prospects in cardiovascular stents. Moreover, the ECM-mimetic coating has the functions of promoting in situ endothelialization and inhibiting excessive intimal hyperplasia, which provides a new method for the use of collagen materials to develop coatings for cardiovascular stents.

In addition, several materials, including gelatin, fibrin, collagen, and silk, have been used for cardiac tissue engineering. A recombinant spider silk protein has been found to be a promising cardiac tissue engineering material, which can be used for coating and 3D printing, offering many of the advantages of silk materials, such as low immunogenicity and biodegradability [15]. This coating made of recombinant spider silk protein is non-cytotoxic, has no apparent pharmacological properties, and does not prevent cardiomyocytes from adequately responding to extracellular stimuli. In terms of cardiomyocyte adhesion and cell viability, this coating was comparable to the fibronectin coating. Because of these intriguing properties, spider silk proteins offer perspectives for future research that could potentially be used to produce cardiac patches for clinical applications.

4.5. ECM-Mimetic Peptide Coating

Insufficient endothelial coverage of cardiovascular implants is a major risk factor for implant failure, due to thrombogenic enhancement. To enhance cell-material interactions, ECM-inspired coatings were developed to provide EC with tissue-specific signaling molecules that modulate cellular activation states for adhesion, proliferation, and survival [94]. Receptors on the cell surface can recognize ECM molecules and trigger signaling pathways that control cell adhesion, migration, and apoptosis. Conjugating certain bioactive peptide sequences may be an available method to direct the cellular activation of implants to the desired wound-healing mechanisms. By mimicking the natural cellular environment, the ECM-derived peptide coating can enhance the interaction of EC with the scaffold material. Peptide-based biomaterial coatings offer a promising toolbox for achieving multifunctionality.

A new peptide coating is presented by Clauder et al., describing a promising approach to stent coating [111]. It contains three proteins of the ECM, namely elastin, fibronectin and laminin. This study used the method of solid-phase peptide synthesis (SPPS) to synthesize carrier peptides. Orthogonal click chemistry reactions provide an efficient method for the functionalization of ECM-derived peptides that can decorate anchor peptides with one or more adhesion motifs. Furthermore, the tunability of anchoring strength and orientation make this method promising. Clauder et al. synthesized three monofunctional peptides and one bifunctional peptide in experiments to study the effect of ECM biomimetic peptide coatings on stent endothelialization and hemocompatibility. This peptide coating was blood compatible, causing neither hemolysis nor platelet adhesion. At the same time, cell–surface interactions were synergistically enhanced when two adhesion peptides were presented in one molecule. The effect of bifunctional peptides on endothelialization was stronger than that of the fibronectin coating, which indicated that the artificial peptide coating had more advantages than non-specific protein adsorption. This cell-adhesive peptide coating is not only suitable for bare metal stents, but also for top layer modification of drug-eluting stents. This provides a feasible method for overcoming late stent thrombosis and improving stent integration.

In further work, Clauder et al. proposed modular assemblies consisting of adhesion peptides, heparin, and pro-angiogenic factors, which could serve as biomimetic coatings that are suitable for cardiovascular devices. Integrins can affect the ability of EC to regulate hemostasis [112]. By equipping them with integrin and proteoglycan binding sites, designing mussel-derived surface-binding peptides can enhance endothelialization. Heparin and heparin-binding angiogenic factors are fixed to peptides using modular assembly. A synergistic effect is proposed due to the tight interaction between cytokines and integrins, which emphasizes the interaction between ECM components. Combining these components in functional biomaterial coatings induces synergy and further enhances the regeneration process. This study also demonstrated that the bifunctional peptide coating was superior to non-specifically adsorbed adhesion proteins. This study shows that a coating that incorporates adhesion peptides, glycosaminoglycans, and modulators is a universal tool that can deliver ECM-inspired versatility to biomaterials and facilitate their integration.

5. Summary and Future Directions

The exploration of ECM coatings has undergone a long research phase, and many different types of surface coatings have been developed. ECM coatings prepared by extracts of organs, tissues or cells exhibit higher biocompatibility and have great potential for application in blood-contacting devices. From collagen or fibronectin coatings formed by single components to coatings made of intact ECM, and furthermore, to bilayer coatings formed by ECM secreted by both cells, ECM coatings show increasingly functional diversification. The increasing availability of ECM-derived biomaterials has broadened the range of potential clinical applications. Although peptide-based self-assembly methods mimic larger partial or entire protein structures that can re-build the structure of the ECM, and these complex ECM mimetics possess microstructural motifs and associated mechanical properties that match innate protein complexes, the function of natural ECM is still irreplaceable. In the future, the biomimetic construction of natural coatings on the surface of cardiovascular materials by using a variety of new technologies in terms of all components and structures will endow the surface with more complex biological properties.

However, based on the complex active components of ECM coatings, during the process of cleaning (usually using a buffer, such as normal saline), sterilization (usually using ultraviolet irradiation sterilization) and storage (4 °C or −20 °C), certain changes will be made to its components or component structure. Some of these changes will not influence the overall stability of the ECM coating, while others will cause serious damage to the stability of the coatings, especially the trace components in bionic ECM coatings. Therefore, in future research, in a sterile environment, the fitting of active ECM coatings with cardiovascular implants over a short time to reduce the stability loss caused by cleaning, sterilization and storage should become a direction of industrialization efforts.

Author Contributions: Conceptualization, J.L.; methodology, S.Y.; software, J.C.; validation, J.C. and S.C.; formal analysis, X.Z.; investigation, S.Y., J.C., S.C. and X.Z.; resources, S.Y.; data curation, S.C.; writing—original draft preparation, S.Y., J.C., S.C.; writing—review and editing, J.L. and K.Z.; visualization, J.L.; supervision, J.L.; project administration, K.Z.; funding acquisition, J.L. and K.Z. All authors have read and agreed to the published version of the manuscript.

Funding: This research was funded by the National Natural Science Foundation of China, grant number U2004164; the Key Scientific and Technological Research Projects in Henan Province, grant number 222102310234.

Institutional Review Board Statement: Not applicable.

Informed Consent Statement: Not applicable.

Data Availability Statement: Not applicable.

Conflicts of Interest: The authors declare no conflict of interest.

References

1. Virani, S.S.; Alonso, A.; Aparicio, H.J.; Benjamin, E.J.; Bittencourt, M.S.; Callaway, C.W.; Carson, A.P.; Chamberlain, A.M.; Cheng, S.S.; Delling, F.N.; et al. Heart Disease and Stroke Statistics-2021 Update A Report From the American Heart Association. *Circulation* **2021**, *143*, e254–e743. [CrossRef] [PubMed]
2. Russ, J.B.; Li, R.L.; Herschman, A.R.; Waisman, H.; Vedula, V.; Kysar, J.W.; Kalfa, D. Design optimization of a cardiovascular stent with application to a balloon expandable prosthetic heart valve. *Mater. Des.* **2021**, *209*, 109977. [CrossRef] [PubMed]
3. Bai, H.; Sun, P.; Wu, H.; Wei, S.; Xie, B.; Wang, W.; Hou, Y.; Li, J.; Dardik, A.; Li, Z. The application of tissue-engineered fish swim bladder vascular graft. *Commun. Biol.* **2021**, *4*, 1153. [CrossRef] [PubMed]
4. Li, B.; Xie, Z.; Wang, Q.; Chen, X.; Liu, Q.; Wang, W.; Shen, Y.; Liu, J.; Li, A.; Li, Y.; et al. Biodegradable polymeric occluder for closure of atrial septal defect with interventional treatment of cardiovascular disease. *Biomaterials* **2021**, *274*, 120851. [CrossRef]
5. Li, J.; Chen, L.; Zhang, X.; Guan, S. Enhancing biocompatibility and corrosion resistance of biodegradable Mg-Zn-Y-Nd alloy by preparing PDA/HA coating for potential application of cardiovascular biomaterials. *Mater. Sci. Eng. C* **2020**, *109*, 110607. [CrossRef]
6. Lin, W.; Zhang, H.; Zhang, W.; Qi, H.; Zhang, G.; Qian, J.; Li, X.; Qin, L.; Li, H.; Wang, X.; et al. In Vivo degradation and endothelialization of an iron bioresorbable scaffold. *Bioact. Mater.* **2021**, *6*, 1028–1039.
7. Jiang, J.; Qian, Y.; Huang, H.; Niu, J.; Yuan, G. Biodegradable Zn-Cu-Mn alloy with suitable mechanical performance and in vitro degradation behavior as a promising candidate for vascular stents. *Biomater. Adv.* **2022**, *133*, 112652. [CrossRef]
8. Sheng, Y.; Li, W.; Chai, Y.; Yin, S.; Li, J.; Guan, S. A compound Schiff base coating on biomedical magnesium alloy for enhanced corrosion resistance and biocompatibility. *Smart Mater. Manuf.* **2022**, 100003. [CrossRef]
9. Wu, H.; He, Q.; Li, L.; Li, L.H.; Zhou, Z.; Chen, N.; Yang, M.; Luo, Q.; Zhang, B.; Luo, R.; et al. A facile and versatile superhydrophilic coating on biodegradable PLA stent with stepwise assembly of metal/phenolic networks for mimicking endothelium function. *Chem. Eng. J.* **2022**, *427*, 130932. [CrossRef]
10. Krueger-Genge, A.; Fuhrmann, R.; Jung, F.; Franke, R.P. Effects of different components of the extracellular matrix on endothelialization. *Clin. Hemorheol. Microcirc.* **2016**, *64*, 867–875. [CrossRef]
11. Tara, S.; Rocco, K.A.; Hibino, N.; Sugiura, T.; Kurobe, H.; Breuer, C.K.; Shinoka, T. Vessel bioengineering- Development of small-diameter arterial grafts. *Circ. J.* **2014**, *78*, 12–19. [CrossRef] [PubMed]
12. Li, J.; Rosa, S.D.; Wang, J.; Zhang, K. Biomaterials Development, Modification, and Potential Application for Interventional Cardiology. *BioMed Res. Int.* **2020**, *2020*, 4890483. [CrossRef]
13. Li, J. Advanced Biomaterials for Drug Delivery and Tissue Regeneration. *Curr. Drug Deliv.* **2021**, *18*, 834–835. [CrossRef] [PubMed]
14. Zou, D.; Li, J.; Kou, F.; Luo, X.; Yang, P. Reveal crucial subtype of natural chondroitin sulfate on the functionalized coatings for cardiovascular implants. *J. Mater. Sci. Technol.* **2021**, *91*, 67–77. [CrossRef]
15. Kramer, J.P.M.; Aigner, T.B.; Petzold, J.; Roshanbinfar, K.; Scheibel, T.; Engel, F.B. Recombinant spider silk protein eADF4(C16)-RGD coatings are suitable for cardiac tissue engineering. *Sci. Rep.* **2020**, *10*, 8789. [CrossRef]
16. Liu, W.; Sun, Y.; Dong, X.; Yin, Q.; Zhu, H.; Li, S.; Zhou, J.; Wang, C. Cell-derived extracellular matrix-coated silk fibroin scaffold for cardiogenesis of brown adipose stem cells through modulation of TGF-β pathway. *Regen. Biomater.* **2020**, *7*, 403–412. [CrossRef]
17. Cheng, H.W.; Yuan, M.T.; Li, C.W.; Chan, B.P. Cell-derived matrices (CDM)-Methods, challenges and applications. *Methods Cell Biol.* **2020**, *156*, 235–258.
18. Lau, S.; Gossen, M.; Lendlein, A. Designing Cardiovascular Implants Taking in View the Endothelial Basement Membrane. *Int. J. Mol. Sci.* **2021**, *22*, 13120. [CrossRef]
19. Bloksgaard, M.; Lindsey, M.; Martinez-Lemus, L.A. Extracellular matrix in cardiovascular pathophysiology. *Am. J. Physiol.-Heart Circ. Physiol.* **2018**, *315*, H1687–H1690. [CrossRef]
20. Han, C.; Luo, X.; Zou, D.; Li, J.; Zhang, K.; Yang, P.; Huang, N. Nature-inspired extracellular matrix coating produced by micro-patterned smooth muscle and endothelial cells endows cardiovascular materials with better biocompatibility. *Biomater. Sci.* **2019**, *7*, 2686–2701. [CrossRef]
21. Nakayama, K.H.; Hou, L.; Huang, N.F. Role of extracellular matrix signaling cues in modulating cell fate commitment for cardiovascular tissue engineering. *Adv. Healthc. Mater.* **2014**, *3*, 628–641. [CrossRef] [PubMed]
22. Cramer, M.C.; Badylak, S.F. Extracellular Matrix-Based Biomaterials and Their Influence Upon Cell Behavior. *Ann. Biomed. Eng.* **2020**, *48*, 2132–2153. [CrossRef] [PubMed]

23. Naba, A.; Clauser, K.R.; Ding, H.; Whittaker, C.A.; Carr, S.A.; Hynes, R.O. The extracellular matrix: Tools and insights for the "omics" era. *Matrix Biol.* **2016**, *49*, 10–24. [CrossRef] [PubMed]
24. Heath, D.E. A Review of Decellularized Extracellular Matrix Biomaterials for Regenerative Engineering Applications. *Regen. Eng. Transl. Med.* **2019**, *5*, 155–166. [CrossRef]
25. Jo, Y.; Hwang, S.H.; Jang, J. Employing Extracellular Matrix-Based Tissue Engineering Strategies for Age-Dependent Tissue Degenerations. *Int. J. Mol. Sci.* **2021**, *22*, 9367. [CrossRef]
26. Li, H.; Bao, M.; Nie, Y. Extracellular matrix–based biomaterials for cardiac regeneration and repair. *Heart Fail. Rev.* **2021**, *26*, 1231–1248. [CrossRef]
27. Sangkert, S.; Kamonmattayakul, S.; Chai, W.L.; Meesane, J. A biofunctional-modified silk fibroin scaffold with mimic reconstructed extracellular matrix of decellularized pulp/collagen/fibronectin for bone tissue engineering in alveolar bone resorption. *Mater. Lett.* **2016**, *166*, 30–34. [CrossRef]
28. Singh, P.; Maparu, A.K.; Shah, S.; Rai, B.; Sivakumar, S. Biomimetic algal polysaccharide coated 3D nanofibrous scaffolds promote skin extracellular matrix formation. *Mater. Sci. Eng. C* **2021**, *119*, 111580. [CrossRef]
29. Maghin, E.; Garbati, P.; Quarto, R.; Piccoli, M.; Bollini, S. Young at Heart: Combining Strategies to Rejuvenate Endogenous Mechanisms of Cardiac Repair. *Front. Bioeng. Biotechnol.* **2020**, *8*, 447. [CrossRef]
30. Leino, M.; Astrand, C.; Hughes-Brittain, N.; Robb, B.; McKean, R.; Chotteau, V. Human embryonic stem cell dispersion in electrospun PCL fiber scaffolds by coating with laminin-521 and E-cadherin-Fc. *J. Biomed. Mater. Res. Part B-Appl. Biomater.* **2018**, *106*, 1226–1236. [CrossRef]
31. Funamoto, S.; Hashimoto, Y.; Kishida, A.; Negishi, J. A fibrin-coated pericardial extracellular matrix prevented heart adhesion in a rat model. *J. Biomed. Mater. Res. Part B-Appl. Biomater.* **2019**, *107*, 1088–1094. [CrossRef] [PubMed]
32. Modi, A.; Verma, S.K.; Bellare, J. Extracellular matrix-coated polyethersulfone-TPGS hollow fiber membranes showing improved biocompatibility and uremic toxins removal for bioartificial kidney application. *Colloids Surf. B Biointerfaces* **2018**, *167*, 457–467. [CrossRef] [PubMed]
33. Liu, L.; Dharmadhikari, S.; Pouliot, R.A.; Li, M.M.; Minneci, P.M.; Tan, Z.; Shontz, K.; Johnson, J.; Reynolds, S.D.; Breuer, C.K.; et al. Modulation of Synthetic Tracheal Grafts with Extracellular Matrix Coatings. *Bioengineering* **2021**, *8*, 116. [CrossRef] [PubMed]
34. Wu, B.; Jin, L.; Ding, K.; Zhou, Y.; Yang, L.; Lei, Y.; Guo, Y.; Wang, Y. Extracellular matrix coating improves the biocompatibility of polymeric heart valves. *J. Mater. Chem. B* **2020**, *8*, 10616–10629. [CrossRef] [PubMed]
35. Coakley, D.N.; Shaikh, F.M.; O'Sullivan, K.; Kavanagh, E.G.; Grace, P.A.; Walsh, S.R.; McGloughlin, T.M. Comparing the endothelialisation of extracellular matrix bioscaffolds with coated synthetic vascular graft materials. *Int. J. Surg.* **2016**, *25*, 31–37. [CrossRef] [PubMed]
36. Huang, G.; Li, F.; Zhao, X.; Ma, Y.; Li, Y.; Lin, M.; Jin, G.; Lu, T.J.; Genin, G.M.; Xu, F. Functional and Biomimetic Materials for Engineering of the Three-Dimensional Cell Microenvironment. *Chem. Rev.* **2017**, *117*, 12764–12850. [CrossRef]
37. Frantz, C.; Stewart, K.M.; Weaver, V.M. The extracellular matrix at a glance. *J. Cell Sci.* **2010**, *123 Pt 24*, 4195–4200. [CrossRef]
38. Bonnans, C.; Chou, J.; Werb, Z. Remodeling the extracellular matrix in development and disease. *Nat. Rev.-Mol. Cell Biol.* **2014**, *15*, 786–801. [CrossRef]
39. Hynes, R.O.; Naba, A. Overview of the Matrisome—An Inventory of Extracellular Matrix Constituents and Functions. *Cold Spring Harb. Perspect. Biol.* **2012**, *4*, a004903. [CrossRef]
40. Xing, H.; Lee, H.; Luo, L.; Kyriakides, T.R. Extracellular matrix-derived biomaterials in engineering cell function. *Biotechnol. Adv. Int. Rev. J.* **2020**, *42*, 107421. [CrossRef]
41. Robbins, E.R.; Pins, G.D.; Laflamme, M.A.; Gaudette, G.R. Creation of a contractile biomaterial from a decellularized spinach leaf without ECM protein coating: An in vitro study. *J. Biomed. Mater. Res. Part A* **2020**, *108*, 2123–2132. [CrossRef] [PubMed]
42. Gershlak, J.R.; Hernandez, S.; Fontana, G.; Perreault, L.R.; Hansen, K.J.; Larson, S.A.; Binder, B.Y.; Dolivo, D.M.; Yang, T.; Dominko, T.; et al. Crossing kingdoms: Using decellularized plants as perfusable tissue engineering scaffolds. *Biomaterials* **2017**, *125*, 13–22. [CrossRef] [PubMed]
43. Modulevsky, D.J.; Cuerrier, C.M.; Pelling, A.E. Biocompatibility of Subcutaneously Implanted Plant-Derived Cellulose Biomaterials. *PLoS ONE* **2017**, *11*, e0157894. [CrossRef]
44. Chan, W.W.; Yu, F.; Le, Q.B.; Chen, S.; Yee, M.; Choudhury, D. Towards Biomanufacturing of Cell-Derived Matrices. *Int. J. Mol. Sci.* **2021**, *22*, 11929. [CrossRef]
45. Assunção, M.; Dehghan-Baniani, D.; Yiu, C.H.K.; Später, T.; Beyer, S.; Blocki, A. Cell-Derived Extracellular Matrix for Tissue Engineering and Regenerative Medicine. *Front. Bioeng. Biotechnol.* **2020**, *8*, 602009. [CrossRef]
46. Fitzpatrick, L.E.; McDevitt, T.C. Cell-derived matrices for tissue engineering and regenerative medicine applications. *Biomater. Sci.* **2015**, *3*, 12–24. [CrossRef]
47. Przybyt, E.; van Luyn, M.J.A.; Harmsen, M.C. Extracellular matrix components of adipose derived stromal cells promote alignment, organization, and maturation of cardiomyocytes in vitro. *J. Biomed. Mater. Res. Part A* **2015**, *103*, 1840–1848. [CrossRef]
48. Kim, I.G.; Hwang, M.P.; Park, J.S.; Kim, S.H.; Kim, J.H.; Kang, H.J.; Subbiah, R.; Ko, U.H.; Shin, J.H.; Kim, C.H.; et al. Stretchable ECM Patch Enhances Stem Cell Delivery for Post-MI Cardiovascular Repair. *Adv. Healthc. Mater.* **2019**, *8*, e1900593. [CrossRef] [PubMed]
49. Junka, R.; Quevada, K.; Yu, X. Acellular polycaprolactone scaffolds laden with fibroblast/endothelial cell-derived extracellular matrix for bone regeneration. *J. Biomed. Mater. Res. Part A* **2020**, *108*, 351–364. [CrossRef] [PubMed]

50. Shakouri-Motlagh, A.; Oconnor, A.J.; Brennecke, S.P.; Kalionis, B.; Heath, D.E. Native and solubilized decellularized extracellular matrix: A critical assessment of their potential for improving the expansion of mesenchymal stem cells. *Acta Biomater.* **2017**, *55*, 1–12. [CrossRef]
51. Jensen, C.; Teng, Y. Is It Time to Start Transitioning From 2D to 3D Cell Culture? *Front. Mol. Biosci.* **2020**, *7*, 33. [CrossRef] [PubMed]
52. Norris, E.G.; Dalecki, D.; Hocking, D.C. Using Acoustic Fields to Fabricate ECM-Based Biomaterials for Regenerative Medicine Applications. *Recent Prog. Mater.* **2020**, *2*, 018. [CrossRef] [PubMed]
53. Lu, J.; Kaestle, K.; Huang, J.; Liu, Q.; Zhang, P.; Gao, L.; Gardiner, J.; Thissen, H.; Yang, H.T. Interactions of human embryonic stem cell-derived cardiovascular progenitor cells with immobilized extracellular matrix proteins. *J. Biomed. Mater. Res. Part A* **2017**, *105*, 1094–1104. [CrossRef]
54. Sung, T.C.; Liu, C.H.; Huang, W.L.; Lee, Y.C.; Kumar, S.S.; Chang, Y.; Ling, Q.D.; Hsu, S.T.; Higuchi, A. Efficient differentiation of human ES and iPS cells into cardiomyocytes on biomaterials under xeno-free conditions. *Biomater. Sci.* **2019**, *7*, 5467–5481. [CrossRef] [PubMed]
55. Collier, J.H.; Rudra, J.S.; Gasiorowski, J.Z.; Jung, J.P. Multi-component extracellular matrices based on peptide self-assembly. *Chem. Soc. Rev.* **2010**, *39*, 3413–3424. [CrossRef]
56. Gu, Z.; Fu, J.; Lin, H.; He, Y. Development of 3D bioprinting: From printing methods to biomedical applications. *Asian J. Pharm. Sci.* **2019**, *15*, 529–557. [CrossRef]
57. Silva, K.D.; Kumar, P.; Choonara, Y.E.; du Toit, L.C.; Pillay, V. Three-dimensional printing of extracellular matrix (ECM)-mimicking scaffolds: A critical review of the current ECM materials. *J. Biomed. Mater. Res. Part A* **2020**, *108*, 2324–2350. [CrossRef]
58. Becker, M.; Maring, J.A.; Schneider, M.; Martin, A.X.H.; Seifert, M.; Klein, O.; Braun, T.; Falk, V.; Stamm, C. Towards a Novel Patch Material for Cardiac Applications: Tissue-Specific Extracellular Matrix Introduces Essential Key Features to Decellularized Amniotic Membrane. *Int. J. Mol. Sci.* **2018**, *19*, 1032. [CrossRef]
59. Baghalishahi, M.; Efthekhar-vaghefi, S.H.; Piryaei, A.; Nematolahi-mahani, S.N.; Mollaei, H.R.; Sadeghi, Y. Cardiac extracellular matrix hydrogel together with or without inducer cocktail improves human adipose tissue-derived stem cells differentiation into cardiomyocyte-like cells. *Biochem. Biophys. Res. Commun.* **2018**, *502*, 215–225. [CrossRef]
60. Guerzoni, L.P.B.; Tsukamoto, Y.; Gehlen, D.B.; Rommel, D.; Haraszti, T.; Akashi, M.; De Laporte, L. A Layer-by-Layer Single-Cell Coating Technique to Produce Injectable Beating Mini Heart Tissues via Microfluidics. *Biomacromolecules* **2019**, *20*, 3746–3754. [CrossRef]
61. Kou, F.; Liu, C.; Wang, L.; Yasin, A.; Li, J.; Guan, S. Fabrication of Citric Acid/RGD Multilayers on Mg-Zn-Y-Nd Alloy via Layer-by-Layer Self-Assembly for Promoting Surface Biocompatibility. *Adv. Mater. Interface* **2021**, *8*, 2002241. [CrossRef]
62. Hou, Y.; Zhang, X.; Li, J.; Wang, L.; Guan, S. A multi-functional MgF_2/Polydopamine/Hyaluronan-astaxanthin coating on the biodegradable ZE21B alloy with better corrosion resistance and biocompatibility for cardiovascular application. *J. Magnes. Alloy.* **2022**. [CrossRef]
63. Li, J.; Zhang, K.; Yang, P.; Qin, W.; Li, G.; Zhao, A.; Huang, N. Human vascular endothelial cell morphology and functional cytokine secretion influenced by different size of HA micro-pattern on titanium substrate. *Colloids Surf. B Biointerfaces* **2013**, *10*, 199–207. [CrossRef] [PubMed]
64. Sheng, Y.; Hou, R.; Liu, C.; Xue, Z.; Zhang, K.; Li, J.; Guan, S. Tailoring of biodegradable magnesium alloy surface with Schiff base coating via electrostatic spraying for better corrosion resistance. *Metals* **2022**, *12*, 471. [CrossRef]
65. Marchand, M.; Monnot, C.; Muller, L.; Germain, S. Extracellular matrix scaffolding in angiogenesis and capillary homeostasis. *Semin. Cell Dev. Biol.* **2019**, *89*, 147–156. [CrossRef] [PubMed]
66. Kukumberg, M.; Yao, Y.; Goh, S.H.; Neo, D.J.; Yao, J.Y.; Yim, E.K. Evaluation of the topographical influence on the cellular behavior of human umbilical vein endothelial cells. *Adv. Biosyst.* **2018**, *2*, 1700217. [CrossRef]
67. Post, A.; Wang, E.; Cosgriff-Hernandez, E. A Review of Integrin-Mediated Endothelial Cell Phenotype in the Design of Cardiovascular Devices. *Ann. Biomed. Eng. J. Biomed. Eng. Soc.* **2019**, *47*, 366–380. [CrossRef]
68. Ozguldez, H.O.; Cha, J.; Hong, Y.; Koh, I.; Kim, P. Nanoengineered cell-derived extracellular matrix influences ECM-related gene expression of mesenchymal stem cells. *Biomater. Res.* **2018**, *22*, 32. [CrossRef]
69. Nakakura, T.; Suzuki, T.; Tanaka, H.; Arisawa, K.; Miyashita, T.; Nekooki-Machida, Y.; Kurosawa, T.; Tega, Y.; Deguchi, Y.; Hagiwara, H. Fibronectin is essential for formation of fenestrae in endothelial cells of the fenestrated capillary. *Cell Tissue Res.* **2021**, *383*, 823–833. [CrossRef]
70. Thomsen, M.S.; Routhe, L.J.; Moos, T. The vascular basement membrane in the healthy and pathological brain. *J. Cereb. Blood Flow Metab.* **2017**, *37*, 3300–3317. [CrossRef]
71. Pozzi, A.; Yurchenco, P.D.; Iozzo, R.D. The nature and biology of basement membranes. *Matrix Biol.* **2017**, *57*, 1–11. [CrossRef] [PubMed]
72. Salzig, D.; Leber, J.; Merkewitz, K.; Lange, M.C.; Köster, N.; Czermak, P. Attachment Growth and Detachment of Human Mesenchymal Stem Cells in a Chemically Defined Medium. *Stem Cells Int.* **2016**, *2016*, 5246584. [CrossRef] [PubMed]
73. Rickel, A.P.; Sanyour, H.J.; Leyda, N.A.; Hong, Z. Extracellular Matrix Proteins and Substrate Stiffness Synergistically Regulate Vascular Smooth Muscle Cell Migration and Cortical Cytoskeleton Organization. *ACS Appl. Bio Mater.* **2020**, *3*, 2360–2369. [CrossRef]

74. Ragelle, H.; Naba, A.; Larson, B.L.; Zhou, F.; Prijic, M.; Whittaker, C.A.; Del Rosario, A.; Langer, R.; Hynes, R.O.; Anderson, D.G. Comprehensive proteomic characterization of stem cell-derived extracellular matrices. *Biomaterials* **2017**, *128*, 147–159. [CrossRef] [PubMed]
75. Silvipriya, K.S.; Krishna, K.K.; Bhat, A.R.; Dinesh, K.B.; Anish, J.; Panayappan, L. Collagen: Animal Sources and Biomedical Application. *J. App. Pharm. Sci.* **2015**, *5*, 123127. [CrossRef]
76. Hall, M.L.; Ogle, B.M. Cardiac Extracellular Matrix Modification as a Therapeutic Approach. *Adv. Exp. Med. Biol.* **2018**, *1098*, 131–150. [PubMed]
77. Nirwane, A.; Yao, Y. Laminins and their receptors in the CNS. *Biol. Rev. Camb. Philos. Soc.* **2018**, *94*, 283–306. [CrossRef]
78. Xu, H.; Pumiglia, K.; LaFlamme, S.E. Laminin-511 and α6 integrins regulate the expression of CXCR4 to promote endothelial morphogenesis. *J. Cell Sci.* **2020**, *133*, jcs246595. [CrossRef]
79. Lorentzen, L.G.; Chuang, C.Y.; Rogowska-Wrzesinska, A.; Davies, M.J. Identification and quantification of sites of nitration and oxidation in the key matrix protein laminin and the structural consequences of these modifications. *Redox Biol.* **2019**, *24*, 101226. [CrossRef]
80. Turner, C.J.; Badu-Nkansah, K.; Hynes, R.O. Endothelium-derived fibronectin regulates neonatal vascular morphogenesis in an autocrine fashion. *Angiogenesis* **2017**, *20*, 519–531. [CrossRef]
81. Zhou, S.; Chen, S.; Pei, Y.A.; Pei, M. Nidogen: A matrix protein with potential roles in musculoskeletal tissue regeneration. *Genes Dis.* **2022**, *9*, 598–609. [CrossRef] [PubMed]
82. Anderegg, U.; Halfter, N.; Schnabelrauch, M.; Hintze, V. Collagen/glycosaminoglycan-based matrices for controlling skin cell responses. *Biol. Chem.* **2021**, *402*, 1325–1335. [CrossRef] [PubMed]
83. Neves, M.I.; Araujo, M.; Moroni, L.; da Silva, R.M.P.; Barrias, C.C. Glycosaminoglycan-Inspired Biomaterials for the Development of Bioactive Hydrogel Networks. *Molecules* **2020**, *25*, 978. [CrossRef] [PubMed]
84. Yasin, A.; Ren, Y.; Li, J.; Sheng, Y.; Cao, C.; Zhang, K. Advances in hyaluronic acid for biomedical application. *Front. Bioeng. Biotechnol.* **2022**, *10*, 910290. [CrossRef]
85. Walimbe, T.; Panitch, A. Best of Both Hydrogel Worlds: Harnessing Bioactivity and Tunability by Incorporating Glycosaminoglycans in Collagen Hydrogels. *Bioengineering* **2020**, *7*, 156. [CrossRef]
86. Wang, Z.; Liu, L.; Mithieux, S.M.; Weiss, A.S. Fabricating Organized Elastin in Vascular Grafts. *Trends Biotechnol.* **2021**, *39*, 505–518. [CrossRef]
87. Jamhawi, N.; Wittebort, R. NMR Study of Elastin's Elasticity Mechanism. *Biophys. J.* **2018**, *114*, 365A. [CrossRef]
88. Waterhouse, A.; Wise, S.G.; Ng, M.K.; Weiss, A.S. Elastin as a nonthrombogenic biomaterial. *Tissue Eng. Part B-Rev.* **2011**, *17*, 93–99. [CrossRef]
89. Long, M.M.; King, V.J.; Prasad, K.U.; Freeman, B.A.; Urry, D.W. Elastin repeat peptides as chemoattractants for bovine aortic endothelial cells. *J. Cell. Physiol.* **1989**, *140*, 512–518. [CrossRef]
90. Sun, X.; Xue, Z.; Yasin, A.; He, Y.; Chai, Y.; Li, J.; Zhang, K. Colorectal Cancer and Adjacent Normal Mucosa Differ in Apoptotic and Inflammatory Protein Expression. *Eng. Regen.* **2022**, *2*, 279–287. [CrossRef]
91. Xu, X.H.; Yang, X.; Zheng, C.G.; Cui, Y. Recent advances in the design of cardiovascular materials for biomedical applications. *Regen. Med.* **2020**, *15*, 1637–1645. [CrossRef] [PubMed]
92. Mi, H.Y.; Jing, X.; Thomsom, J.A.; Turng, L.S. Promoting Endothelial Cell Affinity and Antithrombogenicity of Polytetrafluoroethylene (PTFE) by Mussel-Inspired Modification and RGD/Heparin Grafting. *J. Mater. Chem. B* **2018**, *6*, 3475–3485. [CrossRef] [PubMed]
93. Wu, F.; Li, J.; Zhang, K.; He, Z.; Yang, P.; Zou, D.; Huang, N. Multifunctional Coating Based on Hyaluronic Acid and Dopamine Conjugate for Potential Application on Surface Modification of Cardiovascular Implanted Devices. *ACS Appl. Mater. Interface* **2016**, *8*, 109–121. [CrossRef] [PubMed]
94. Clauder, F.; Zitzmann, F.D.; Friebe, S.; Mayr, S.G.; Robitzki, A.A.; Beck-Sickinger, A.G. Multifunctional coatings combining bioactive peptides and affinity-based cytokine delivery for enhanced integration of degradable vascular grafts. *Biomater. Sci.* **2020**, *8*, 1734–1747. [CrossRef]
95. Qiu, H.; Qi, P.; Liu, J.; Yang, Y.; Tan, X.; Xiao, Y.; Maitz, M.F.; Huang, N.; Yang, Z. Biomimetic engineering endothelium-like coating on cardiovascular stent through heparin and nitric oxide-generating compound synergistic modification strategy. *Biomaterials* **2019**, *207*, 10–22. [CrossRef]
96. Zou, D.; Luo, X.; Han, C.; Li, J.; Yang, P.; Li, Q.; Huang, N. Preparation of a biomimetic ECM surface on cardiovascular biomaterials via a novel layer-by-layer decellularization for better biocompatibility. *Mater. Sci. Eng. C* **2019**, *96*, 509–521. [CrossRef]
97. Liu, C.; Chen, L.; Zhang, K.; Li, J.; Guan, S. Tailoring ZE21B Alloy with Nature-Inspired Extracellular Matrix Secreted by Micro-Patterned Smooth Muscle Cells and Endothelial Cells to Promote Surface Biocompatibility. *Int. J. Mol. Sci.* **2022**, *23*, 3180. [CrossRef]
98. Yu, C.; Yang, H.; Wang, L.; Thomson, J.A.; Turng, L.S.; Guan, G. Surface modification of polytetrafluoroethylene (PTFE) with a heparin-immobilized extracellular matrix (ECM) coating for small-diameter vascular grafts applications. *Mater. Sci. Eng. C* **2021**, *128*, 112301. [CrossRef]
99. Gao, Y.; Sun, Y.; Yang, H.; Qiu, P.; Cong, Z.; Zou, Y.; Song, L.; Guo, J.; Anastassiades, T.P. A Low Molecular Weight Hyaluronic Acid Derivative Accelerates Excisional Wound Healing by Modulating Pro-Inflammation, Promoting Epithelialization and Neovascularization, and Remodeling Collagen. *Int. J. Mol. Sci.* **2019**, *20*, 3722. [CrossRef]

100. Tong, P.; Sheng, Y.; Hou, R.; Iqbal, M.; Chen, L.; Li, J. Recent progress on coatings of biomedical magnesium alloy. *Smart Mater. Med.* **2022**, *3*, 104–116. [CrossRef]
101. Yu, Y.; Zhu, S.J.; Dong, H.T.; Zhang, X.Q.; Li, J.A.; Guan, S.K. A novel MgF_2/PDA/S-HA coating on the biodegradable ZE21B alloy for better multi-functions on cardiovascular application. *J. Magnes. Alloy.* **2021**. [CrossRef]
102. Li, J.; Wu, F.; Zhang, K.; He, Z.; Zou, D.; Luo, X.; Fan, Y.; Yang, P.; Zhao, A.; Huang, N. Controlling Molecular Weight of Hyaluronic Acid Conjugated on Amine-rich Surface: Toward Better Multifunctional Biomaterials for Cardiovascular Implants. *ACS Appl. Mater. Interface.* **2017**, *9*, 30343–30358. [CrossRef] [PubMed]
103. Wang, Z.; Zhu, S.; Wang, L.; Chang, L.; Wang, J.; Li, J.; Guan, S. Preparing a novel magnesium-doped hyaluronan/polyethyleneimine nanoparticle to improve endothelial functionalization. *IET Nanobiotechnol.* **2020**, *14*, 142–147. [CrossRef] [PubMed]
104. Hou, Y.; Witte, F.; Li, J.; Guan, S. The increased ratio of Mg^{2+}/Ca^{2+} from degrading magnesium alloys directs macrophage fate for functionalized growth of endothelial cells. *Smart Mater. Med.* **2022**, *3*, 188–198. [CrossRef]
105. Li, J.; Wang, S.; Sheng, Y.; Liu, C.; Xue, Z.; Tong, P.; Guan, S. Designing HA/PEI nanoparticle composite coating on biodegradable Mg-Zn-Y-Nd alloy to direct cardiovascular cells fate. *Smart Mater. Med.* **2021**, *2*, 124–136. [CrossRef]
106. Hao, H.; Chen, G.; Liu, J.; Ti, D.; Zhao, Y.; Xu, S.; Fu, X.; Han, W. Culturing on Wharton's jelly extract delays mesenchymal stem cell senescence through p53 and p16INK4a/pRb pathways. *PLoS ONE* **2018**, *8*, e58314. [CrossRef]
107. Sobolewski, K.; Malkowski, A.; Bankowski, E.; Jaworski, S. Wharton's jelly as a reservoir of peptide growth factors. *Placenta* **2005**, *26*, 747–752. [CrossRef]
108. Dan, P.; Velot, E.; Francius, G.; Menu, P.; Decot, V. Human-derived extracellular matrix from Wharton's jelly: An untapped substrate to build up a standardized and homogeneous coating for vascular engineering. *Acta Biomater.* **2017**, *48*, 227–237. [CrossRef]
109. Luo, X.; Han, C.; Yang, P.; Zhao, A.; Zou, D.; Jiang, L.; Gao, P.; Yin, B.; Huang, N. The co-deposition coating of collagen IV and laminin on hyaluronic acid pattern for better biocompatibility on cardiovascular biomaterials. *Colloids Surf. B Biointerface.* **2020**, *196*, 111307. [CrossRef]
110. Yang, L.; Wu, H.; Lu, L.; He, Q.; Xi, B.; Yu, H.; Luo, R.; Wang, Y.; Zhang, X. A tailored extracellular matrix (ECM)-Mimetic coating for cardiovascular stents by stepwise assembly of hyaluronic acid and recombinant human type III collagen. *Biomaterials* **2021**, *276*, 121055. [CrossRef]
111. Clauder, F.; Czerniak, A.S.; Friebe, S.; Mayr, S.G.; Scheinert, D.; Beck-Sickinger, A.G. Endothelialization of Titanium Surfaces by Bioinspired Cell Adhesion Peptide Coatings. *Bioconj. Chem.* **2019**, *30*, 2664–2674. [CrossRef] [PubMed]
112. Post, A.; Isgandarova, S.; Martinez-Moczygemba, M.; Hahn, M.; Russell, B.; Hook, M.; Cosgriff-Hernandez, E. Elucidation of Endothelial Cell Hemostatic Regulation with Integrin-Targeting Hydrogels. *Ann. Biomed. Eng.* **2019**, *47*, 866–877. [CrossRef] [PubMed]

coatings

Systematic Review

Potential of Graphene-Functionalized Titanium Surfaces for Dental Implantology: Systematic Review

Angelo Michele Inchingolo †, Giuseppina Malcangi †, Alessio Danilo Inchingolo †, Antonio Mancini, Giulia Palmieri, Chiara Di Pede, Fabio Piras, Francesco Inchingolo *, Gianna Dipalma *,‡ and Assunta Patano ‡

Department of Interdisciplinary Medicine, University of Bari "Aldo Moro", 70124 Bari, Italy; angeloinchingolo@gmail.com (A.M.I.); giuseppinamalcangi@libero.it (G.M.); ad.inchingolo@libero.it (A.D.I.); dr.antonio.mancini@gmail.com (A.M.); giuliapalmieri13@gmail.com (G.P.); c.dipede1@studenti.uniba.it (C.D.P.); dott.fabio.piras@gmail.com (F.P.); assuntapatano@gmail.com (A.P.)

* Correspondence: francesco.inchingolo@uniba.it (F.I.); giannadipalma@tiscali.it (G.D.); Tel.: +39-331-2111-104 (F.I.); +39-339-6989-939 (G.D.)

† These authors contributed equally to this work as first authors.

‡ These authors contributed equally to this work as last authors.

Abstract: Titanium is the most frequently employed material in implantology, because of its high degree of biocompatibility. The properties of materials are crucial for osteointegration; therefore, great effort from researchers has been devoted to improving the capabilities of titanium implant surfaces. In this context, graphene oxide represents a promising nanomaterial because of its exceptional physical and chemical qualities. Many authors in recent years have concentrated their research on the use of graphene in biomedical applications such as tissue engineering, antimicrobial materials, and implants. According to recent studies, graphene coatings may considerably increase osteogenic differentiation of bone marrow mesenchymal stem cells in vitro by the regulation of FAK/P38 signaling pathway, and can encourage the osteointegration of dental implants in vivo. However, further studies, especially on human subjects, are necessary to validate these potential applications. The aim of this work was to evaluate the effects of graphene on bone metabolism and the advantages of its use in implantology. A systematic review of literature was performed on PubMed, Web of Science and Scopus databases, and the articles investigating the role of graphene to functionalize dental implant surfaces and his interactions with the host tissue were analyzed.

Keywords: dental implant; graphene; graphene oxide; osteointegration; osteoblastic differentiation; titanium surface

Citation: Inchingolo, A.M.; Malcangi, G.; Inchingolo, A.D.; Mancini, A.; Palmieri, G.; Di Pede, C.; Piras, F.; Inchingolo, F.; Dipalma, G.; Patano, A. Potential of Graphene-Functionalized Titanium Surfaces for Dental Implantology: Systematic Review. *Coatings* **2023**, *13*, 725. https://doi.org/10.3390/coatings13040725

Academic Editor: Petrică Vizureanu

Received: 23 February 2023
Revised: 29 March 2023
Accepted: 30 March 2023
Published: 2 April 2023

1. Introduction

In recent years, the debate on the implant surface that can be most successfully used has increasingly intensified, replacing the earlier focus of researchers on implant shape [1–3]. One of the main reasons for the dispute is the comparison between the incidence rates of peri-implantitis in implants with a roughneck surface and those with a machined surface [4,5]. In this climate of fervent debate, many studies have been carried out to investigate the properties and outcomes of the various implant surfaces [6–8].

All implants are constituted of three basic components: the body of the implant (fixture), the abutment, and the abutment screw. A schematization of the implant fixture with the coating is presented in Figure 1. Macroscopically, implants can have various geometries, including threaded or tapered forms [7,9].

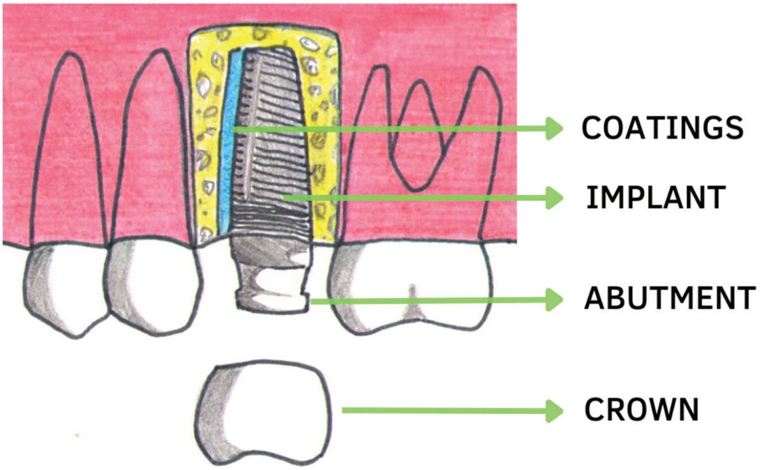

Figure 1. Components of dental implants and a representation of an implant fixture functionalized with coatings.

Osteointegration was defined 60 years ago by Branemark as a direct connection, structural and functional, between new bone and the surface of implant [10]. Current trials on dental implants, however, have as their objective the identification of the best system for enhancing the process of osseointegration, thereby allowing early loading [6]. Two factors are involved in the process of osseointegration: primary and secondary stability [11]. When the implant is inserted into the bone, certain areas of the surface come into direct contact with the bone. This contact determines the primary or mechanical stability, and depends on the shape of the implant, the quality of the bone and the preparation of the implant site [12]. Primary stability gradually decreases during the bone remodeling process and is completely replaced by biological stability (Figure 2). Secondary or biological stability is determined by the amount of new bone development at the bone-to-implant contact [13]. The studies by Osborn and Newesley showed that new bone formation occurs through two phenomena, distant and contact osteogenesis. In the first case, the deposition by osteoblasts and the subsequent mineralization takes place in a direction that goes from the periphery towards the implant, i.e., the bone gradually surrounds the screw [14]. In the second process, osseointegration occurs in the opposite direction, from the implant to the periphery. The apposition of new bone requires a continuous recall of cells from the bone and bloodstream towards the implant, since osteoblasts, after differentiation, are only capable of producing bone by apposition [14]. Once they are polarized, they produce ECM proteins, especially collagen, with the aim of giving a precise structure to the bone–implant interface, which, after calcification, turns into osteoid matrix and finally into bone tissue [14]. It should be noted that osteointegration is also linked to the concepts of osteoinduction and osteoconduction [13]. The former is related to the stimulation of osteoprogenitor cells to osteoblastic differentiation, a phenomenon that initiates osteogenesis, therefore "inducing" it. Osteoconduction, on the other hand, concerns the growth of the bone on a surface, therefore implying the existence of more or less osteoconductive surfaces, i.e., able to favor better or worse the adhesion and adaptation of the cells to the implant site. It can be seen that the direct anchorage (osseointegration) between the implant and the new bone, if maintained successfully and without the interposition of fibrous tissue (conversely, osteofibrointegration involves inflammatory reactions, bone resorption and implant failure), is nothing more than the concrete result of a previous osteoinduction and osteoconduction [13]. The osseointegration process and its quantity depend on the type of implant surface, which can have a geometry that attracts osteoblast cells; therefore, great effort from researchers has been directed towards improving the capabilities of titanium implant surfaces [7,15].

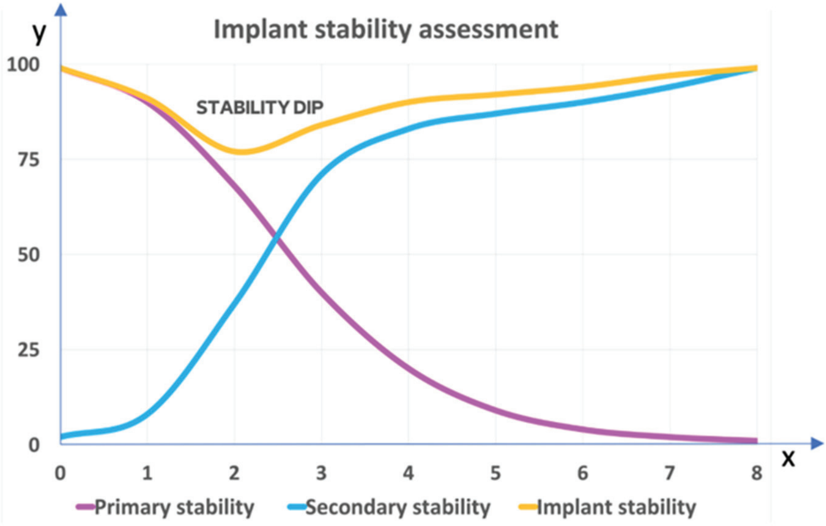

Figure 2. Implant stability assessment. X axis: weeks. Y axis: stability (%). Primary stability (purple) and secondary stability (blue) respectively decrease and increase, according to the curve in the graph. The yellow curve indicates total stability, with a dip after the first two weeks. The bone-to-implant contact (BIC) is a well-established technique to assess the degree of osseointegration and the speed of healing of dental implants.

Certain surface modifications may also include bioactive materials. The contact between the implant and the bone can be influenced by the shape of the implant, such as grooves, ridges, and tool marks [16]. The overall surface area that is available for osseointegration may be increased by the implant shape. Rougher surfaces can encourage bone cells to adhere, differentiate, and proliferate, resulting in an increase in bone formation and mineralization [17]. It has been demonstrated that rougher surfaces with an open structure promote quicker and more efficient osseointegration. Unfortunately, this rougher substrate's surface has a propensity to harboring microorganisms [16–18].

The majority of approaches aim to modify surface roughness. Machine work, blasting, laser etching, 3D printing, acid/alkaline etching, anodizing, and coatings can all cause surface roughness. Implant surfaces that have been machined typically have a roughness of less than 1 m. The roughest surfaces are those that have undergone plasma spraying and blasting. The roughness is determined by the sizes of the blasting particles. Polyelectrolytes do not change the surface roughness of acid-etched or machined titanium surfaces after sandblasting. There is disagreement on the ideal implant surface roughness that will have the optimum benefits on bone [19].

The surface composition has an Impact on hydrophilicity, which adds to the wettability and surface energy of the implant surface. Current surface modification approaches can increase hydrophilicity and surface area. Surface chemistry and wettability can both be changed by electrochemical functionalization [20].

In addition to modifying the surface using physical or chemical methods, it is possible to change its properties by adding other materials to the titanium surface, e.g., bioactive glasses, ceramics, etc. [21].

Different surface treatments have been developed to improve osseointegration, which allow the micro-topography to be roughened, such as machining, sandblasting, acid-etching, anodization, grit-blasting, and various coatings [22]. The surface treatment has the purpose of increasing the contact area of the implant with the biological tissues, improving the osseointegration between the bone tissue and the implant. Already with a single thread, the degree of resistance to tensile and compressive force is greater than that of machined implants; the presence of micro-retention on the surface of the fixture allows for increase the tensile strength and torsion of the implant [22].

Some authors have demonstrated that macrophages, epithelial cells and osteoblasts have a high trophism towards rough surfaces [22–24]. An implant's surface roughness has the capacity to precisely select one population of cells and change their functions [22,25].

Sandblasting the titanium surface improves the biomechanical characteristics of the implant and helps to increase primary stability, enhancing the mechanisms of osseointegration [26].

Acid-etched surfaces are another subtractive technique that can be performed with different acids (sulfuric, hydrochloric) [25]. Following the good results provided by the two subtractive sandblasting and etching techniques, it was decided to combine their advantages in a single treatment, in order to obtain an SLA (sandblasted, large grit, acid-etched) surface: the first sandblasting phase determines a roughness that guarantees a strong mechanical fixation, the acid attack instead perfects the topographical conformation and helps to promote the adhesion of proteins, which is considered essential in the initial stages of bone healing [25,27].

Another method of surface treatment consists of additive techniques, coating the implant via titanium plasma spraying (TPS). This technology is currently used to increase surface roughness [28].

A lot of scientific work has been focused on bioactive surface coatings: these novel methods aim to imitate the metabolic environment and nanostructural organization of human bone (biomimetic effect) [7,29]. Experiments have been performed using a number of substances, medications, growth factors and proteins with the aim of producing innovative coatings [30]. One example of a process that is performed on the surface of dental implants is veneering with hydroxyapatite, which promotes the complete integration of the titanium with human bone tissues [31]. Additionally, bone morphogenetic proteins (BMPs), platelet-derived growth factor (PDGF), insulin-like growth factors (IGF-1 and 2), and a group of transforming growth factors (TGF-β family) could be used as bone-stimulating substances applied to the surface of titanium dental implants [32–35].

Short sequences of amino acids make up the biomolecules known as peptides [35]. Designing new implant surfaces has made use of certain peptides that promote cell adhesion in osseointegration or that have antibacterial properties like RGD peptide or human beta-defensins (HBDs) [29,36].

Implant surfaces can potentially include drugs that regulate the process of bone remodeling. In clinical conditions lacking bone support, such as resorbed alveolar ridges, incorporation of bone antiresorptive medications, such as biphosphonates, may be extremely significant [37]. Recent researches have demonstrated that adding biphosphonate to titanium implants enhances local bone density in the peri-implant area [38–40].

Graphene is a single layer of sp2-hybridized carbon atoms with a honeycomb lattice, and is a key component of fullerenes and carbon nanotubes. It has been attracting considerable interest in the physical, chemical and biomedical fields in recent years due to its mechanical properties, optimal electrical conductivity and very high surface area [41–43]. In particular, this material has been the subject of studies on osteogenesis, neurogenesis and biogenesis, showing strong biocompatibility and good stem cell differentiation in studies [44–46]. In addition, studies have shown graphene oxide (GO) to have antibacterial properties. GO is an oxidized version of graphene with numerous oxygen bonds on both accessible sides, such as carboxyl (-COOH), carbonyl (-C=O), and hydroxyl (OH). The presence of these groups enhances interactions with biomolecules and causes bacterial death without involving the cell. GO's antibacterial activity is linked to a variety of processes, including membrane stress, oxidative stress, entrapment, basal plane, and photothermal impact. The rough edges of GO nanolayers can physically disrupt bacterial membranes, leading to bacterial inactivation owing to internal matrix leaking [47–50].

Porphyromonas gingivalis, *Fusobacterium nucleatum*, *Tannerella forsythia*, and *Treponema denticola* seem to compose the majority of the peri-implant biofilm [51]. He et al. showed that graphene oxide decreased *F. nucleatum* and *P. gingivalis* proliferation [52]. Furthermore, Ghorbanzadeh et al. reported the use of graphene oxide (GO)-coated composites in drastically lowering the metabolic activity of *Streptococcus mutans*, a prominent cariogenic agent [53]. Another GO-CS-HA composite demonstrated lower S. aureus adhesion while also offering strong corrosion resistance and no cell toxicity [54]. GO has also been tested against *Candida albicans* in combination with curcumin and polyethylene glycol [55,56]. Graphene has also been coupled with curcumin for utilization as an antimicrobial photodynamic therapy photosensitizer agent for peri-implantitis treatment. The results showed that there was a great effectiveness in reducing biofilm development [57].

These properties of graphene can be exploited in implant surface design to overcome the problems associated with typical titanium-based dental implants. The aim of this paper is to evaluate the current and future applications of graphene with titanium in implantology by examining its possible advantages.

2. Materials and Methods

2.1. Protocol and Registration

The Preferred Reporting Items for Systematic Reviews and Meta-Analyses (PRISMA) guidelines were used in this systematic review [58].

2.2. Inclusion Criteria

All appropriate trials were assessed by two reviewers using the following inclusion criteria: (1) studies with human subjects; (2) studies in vitro; (3) open-access studies that other researchers can access for free; (4) articles in English language.

2.3. Exclusion Criteria

The exclusion criteria used in the search strategy were as follows: (1) animal studies; (2) systematic reviews; (3) meta-analyses; (4) narrative reviews; (5) letters; (6) books; (7) articles on implants not related to dentistry.

2.4. Search Processing

We searched PubMed, Scopus and Web of Science with a constraint on English-language papers from 8 February 2013 through 8 February 2023 that matched our topic. The following Boolean keywords were utilized in the search strategy: “Graphene Coating” AND “Dental Implant”. These terms were chosen because they best describe the objective of our investigation, which was to evaluate the role of graphene as a material in dentistry useful in the prevention of bacterial infections and in supporting osseointegration.

3. Results

A total of 178 publications were identified from the PubMed (41), Scopus (57) and Web of Science (80) databases, resulting in 145 articles after the removal of duplicates (33). Analysis of the title and abstract resulted in the exclusion of 109 articles as being off topic, because they were not related to the use of graphene in implant dentistry. The writers successfully retrieved the remaining 36 papers and evaluated their eligibility. The approach resulted in the exclusion of 12 articles for being off topic. The evaluation finally resulted in the inclusion of 14 papers for qualitative analysis (Figure 3; Table 1).

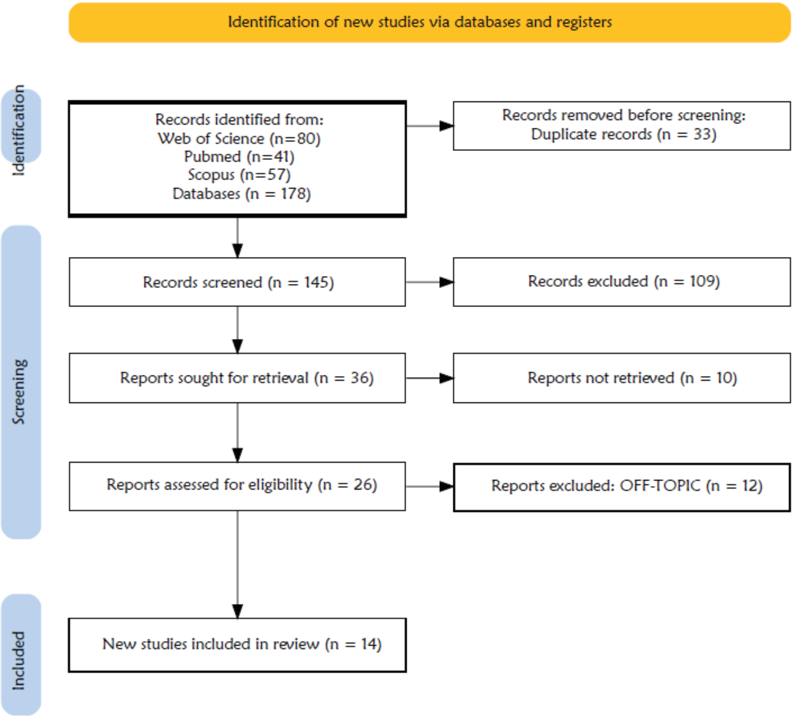

Figure 3. PRISMA flowchart diagram of the inclusion process.

Table 1. Studies included for qualitative analysis.

Authors	**Type of Study**	**Materials and Methods**	**Conclusions**
Kulshrestha, S. et al., 2014 [59]	In vitro study	*S. mutans* MTCC 497 on plates of Graphene Nanocomposite/Zinc Oxide (GZNC)	- GZNC has antibacterial action against *S. mutans* - GZNC treatment inhibits biofilm production - GZNC as an implant coating reduces cytotoxicity
Ren, N. et al., 2017 [60]	In vitro study	Graphene oxide (GO) sheets produced by the modified Hummer's technique were combined with bioactive titanate on titanium implants (GO-Ti) before reduction (rGO-Ti). Cell proliferation of rat bone mesenchymal stem cells (rBMSCs) on them was assessed by mRNA expression and alkaline phosphatase activity.	Results revealed that Dexamethasone loaded surface (DEXdex-GO-Ti) performed superbly in increasing cell proliferation. In RMBSCs on DEX-GO-Ti, osteogenic differentiation-related proteins, mRNA, and calcium were all highly expressed.
Dubey, N. et al., 2018 [61]	In vitro study	- *S. mutans* and *Enterococus faecalis* on titanium plates coated with graphene - Culture of human osteoblastic cells in contact with graphene-coated titanium plates	- Graphene-coated titanium: 1. Is cytocompatible 2. Induced the maturation of human osteoblasts 3. Increased mineralized matrix deposition compared with titanium alone - GO was found to reduce the growth of Streptococcus Mutans and Enterococus Faecalis

Table 1. *Cont.*

Authors	Type of Study	Materials and Methods	Conclusions
Suo, L. et al., 2018 [62]	In vitro and in vivo study	Groups created for in vitro and in vivo evaluation: A. HA-Ti: Titanium + Hydroxyapatite (HA). B. GO/HA-Ti: group A coated with GO. C. CS/HA-Ti: group A coated with chitosan (CS) D. GO/CS/HA-Ti: group D coated by GO	Graphene oxide/chitosan/hydroxyapatite (GO/CS/HA)-coated titanium increases BMSC cell adhesion, proliferation, and differentiation in vitro. In addition, it demonstrated superior osseointegration during in vivo animal tests (rat tibia)
Rho, K. et al., 2019 [63]	In vitro study	Graphene-coated titanium with non-thermal atmospheric pressure plasma treatment	- Argon plasma treatment improves biocompatibility of titanium - Graphene oxide deposition by nonthermal plasma at atmospheric pressure enhances cell differentiation into osteoblasts, ensuring bone growth around the implant
Agarwalla, S.V. et al., 2021 [64]	In vitro study	Growth of C. albicans on graphene-coated grade 4 titanium plates was monitored for seven days. Uncoated titanium was the Control.	Graphene coating on titanium surface inhibits C. albicans biofilm formation due to its hydrophobic properties
Li, Q. and Wang, Z. 2020 [65]	In vitro and in vivo study	Evaluation of the behavior of rBMSC on acid-etched titanium SLA surfaces (control group) and on graphene-coated acid-etched titanium SLA surfaces. In addition, osteogenesis was evaluated in vivo (in rat femur).	The coating of GO: - Made the SLA surface more hydrophilic and capable of protein adsorption - Promoted adhesion, cell proliferation and osteogenic differentiation of BMSCs (activation of FAK/P38 pathway)High bone regeneration capacity was observed around GO-modified implants placed in rat femurs
Agarwalla, S.V. et al., 2019 [66]	In vitro study	*Streptococcus mutans*, *Enterococcus faecalis*, *Pseudomonas aeruginosa*, and *Candida albicans* biofilm development was assessed after 24 h on graphene coating titanium surfaces	For all species, titanium surfaces transferred two times with graphene (TiGD) offered superior quality while reducing the development of biofilm. The production of biofilms was shown to be reduced in correlation with enhanced hydrophobicity of graphene sheets.
Kang, M.S. et al., 2021 [67]	In vitro study	Atomic force microscopy (AFM), water contact angle, and Raman spectroscopy were used to analyze the physicochemical properties of rGO-coated Ti substrates. hMSCs were also cultivated on rGO-Ti, and their cellular characteristics, such as growth and osteogenic differentiation, were assessed.	By applying rGO evenly to Ti substrates the surface roughness and contact angle of Ti substrates could be reduced. After 7 days of incubation, rGO-Ti substrates greatly enhanced cell proliferation.
Lorusso, F. et al., 2021 [68]	In vivo study	Graphene-doped poly methyl methacrylate (PMMA) was compared to PMMA to determine water sorption, water solubility, and tolerance in rabbits using pyrogen test.	The levels of water sorption and solubility were very low in all of the testing samples. After the treatment, unaged graphene-doped PMMA specimens shown a stability in their physical and optical characteristics. Animal tests on the graphene-doped PMMA failed to produce pyrogens, an intradermal and systemic irritant.

Table 1. *Cont.*

Authors	Type of Study	Materials and Methods	Conclusions
Cao, X. et al., 2022 [69]	In vitro study	Anodic oxidation was used to prepare electrodeposition-loaded TiO_2 and GO nanotubes. Pure titanium disks was used as the control group and GO-coated titanium surface was used as the experimental group.	GO can modulate the cellular behavior of HGF on titanium surfaces. It also activates the MAPK signaling pathway to regulate HGF adhesion, spreading and migration, possibly by promoting TGF-β1 expression to promote HGF proliferation.
Shin, Y.C. et al., 2022 [70]	In vitro and in vivo study	Acid-etched SLA Ti (ST) implants were modified with rhBMP-2 and rGO. In vitro cell behaviors, in vivo osseointegration activity were evaluated among different groups, including ST (control), rhBMP-2-immobilized ST (BI-ST), rhBMP-2-treated ST (BT-ST) and rGO-coated ST (R-ST).	The titanium surface coated with rGO - Has high biocompatibility and superior ability to absorb exogenous proteins - Promotes cell growth and osteogenic differentiation without any osteogenic factors - Accelerates osseointegration and dental tissue regeneration in vivo
Kwak, J.M. et al., 2022 [71]	In vitro and in vivo study	In vitro, BMSCs and Human Gingival Fibroblasts (HGFs) were seeded onto titanium discs, the surfaces of which had been treated in four different ways (SLA and/or GO). In vivo, a rabbit tibia model is used to observe the effects of the four surface treatments on the osseointegration of titanium implants.	GO coating of implant surfaces promote cell adhesion, proliferation, osteogenic differentiation and osseointegration. - Expression of ALP, RUNX2 and COL1A1 in titanium disc cells increased after ALS treatment and GO coating - Cell proliferation on GO-coated titanium discs was 25% higher than on non-GO-coated titanium discs - In the rabbit tibia study, it was seen that the GO-coated titanium implant had the highest BIC
Baheti, W. et al., 2023 [72]	In vitro study	Modified Ti implant surfaces were coated with GO, HA, HA-2%GO, and HA-5%GO by electrophoresis deposition and compared with uncoated Ti. Biological characteristics and osteogenic efficacy of in vitro-cultured rBMSCs.	The Ti surface's roughness and hydrophilicity were enhanced by the HA-GO nanocomposite coating. Cell adhesion and diffusion were improved on HA-GO-modified Ti surfaces compared to untreated Ti or Ti modified by HA or GO alone. Moreover, on surfaces treated with HA-GO, the proliferation and osteogenic differentiation of BMSCs in vitro were enhanced.

4. Discussion

Graphene oxide represents a promising nanomaterial because of its exceptional physical and chemical qualities. Considerable research in recent years has concentrated on using graphene in biomedical applications such as tissue engineering, antimicrobial materials, and implants [73]. In this review, we investigated the literature on PubMed, Web of Science and Scopus, regarding the role of graphene to functionalize dental implant surfaces and its interactions with the host tissue.

Graphene is a single atomic sheet of sp2 hybridized carbon atoms arranged in a honeycomb lattice. Is the thinnest and strongest substance presented in nature [74]. It was originally effectively isolated in 2004 by Geim and Novoselov. Due to its exceptional qualities, including mechanical strength, elasticity, and electrical characteristics, graphene has attracted a lot of attention in research [75]. The two primary graphene derivatives are graphene oxide (GO) and reduced graphene oxide (rGO) [76]. Because of its great biocompatibility and low levels of toxicity, its hydro-solubility and reactive oxygen functional groups, studies have shown that graphene and GO may be used as supports in the biomedical sector for tissue regeneration, cell differentiation and proliferation also for enhancing the bioactivity and mechanical performance of biomaterials as well as serving as a carrier for drug and biomolecules [68]. Graphene is a single atomic sheet of sp2 hybridized carbon atoms arranged in a honeycomb lattice. Is the thinnest and strongest substance presented in nature [74]. It was originally effectively isolated in 2004 by Geim and Novoselov. Due to its exceptional qualities, including mechanical strength, elasticity, and electrical characteristics, graphene has attracted a lot of attention in research [75]. The two primary graphene derivatives are graphene oxide (GO) and reduced graphene oxide (rGO) [76]. Because of its great biocompatibility and low levels of toxicity, its idro-solubility and reactive oxygen functional groups, studies have shown that graphene and GO may be used as supports in the biomedical sector for tissue regeneration, cell differentiation and proliferation also for enhancing the bioactivity and mechanical performance of biomaterials as well as serving as a carrier for drug and biomolecules [68].

According to a recent review by Liu et al., graphene has a potential role in oral disease treatment [73]: regarding restorative materials, it may be used for caries filling, since it may enhance the physicochemical and mechanical qualities of dental polymers and exhibit superior biocompatibility. It can be mixed with glass ionomer cements to enhance the composites' mechanical characteristics without having a negative impact on their aesthetic properties or their ability to release fluoride [77]. As shown by other authors, it can also enhance the quality of primer adhesion [78]. According to a recent review by Liu et al. Graphene has a potential role in oral disease treatment [73]: regarding restorative materials, it may be used for caries filling, since it may enhance the physicochemical and mechanical qualities of dental polymers and exhibit superior biocompatibility. It can be mixed with glass ionomer cements to enhance the composites' mechanical characteristics without having a negative impact on their aesthetic properties or their ability to release fluoride [77]. As shown by other authors, it can also enhance the quality of primers' adhesion [78].

Evidence suggests that graphene and GO exert an anticaries effect, preventing the development of *S. mutans* and *P. gingivalis*. In addition, graphene and GO can encourage human dental pulp stem cell (hDPSC) and periodontal ligament stem cell (PDLSC) differentiation and proliferation, which is helpful for the regeneration of dental pulp and periodontal ligament [73]. Graphene and its derivatives have shown considerable potential for the development of drug delivery systems, particularly for the administration of medications for targeted cancer therapy [73].

Unfortunately, there are currently just a few lines of support for the use of GO for this scope.

Graphene improves the antibacterial capabilities of ZnO nanoparticles, with an antibacterial effect that is significantly stronger than that of ZnO nanoparticles alone. The biofilm growth on the teeth was decreased by 85% with the GZNC coating [59]. According to this investigation, GZNC may work well against *S. mutans* as an antibacterial and antibiofilm agent. The nanocomposite also works well as a veneering agent for dental implants due to its low toxicity [59].

Bacterial adhesion must be prevented, since it is difficult to eliminate biofilm in the oral cavity once it has formed. By altering the implant surface, biofilm development can be prevented [79].

The minimal inhibitory concentration (MIC) of graphene nanocomposite/zinc oxide (GZNC) against *S. mutans* was found to be 125 μg mL^{-1} in the study of Kulshrestha et al., whereas the minimum bactericidal concentration (MBC) was found to be 250 μg mL^{-1} [59]. Graphene was found to diminish the growth of Streptococcus Mutans and Enterococcus Faecalis in the study of Dubey et al. [61], and to decrease the growth of Candida albicans in the study of Agarwalla et al. [64]. However, the antibacterial activity in the graphene oxide sample in the investigation ok Rho et al. was quite weak [63]. Moreover, titanium's biocompatibility was improved by argon plasma treatment, and non-thermal plasma deposition of GO at atmospheric pressure encouraged bone development around the implant by promoting osteoblast cell differentiation [63]. According to a study of Shin et al., increasing the concentration of rGO on titanium surfaces results in rougher surfaces that are more able to absorb exogenous proteins, which in turn promotes cell proliferation and osteogenic differentiation [70]. Furthermore, in the study of Kwak et al., the surface roughness of SLA discs was higher than that of titanium discs [71]. After GO coating, the surface roughness decreased slightly, but no significant difference was observed. Furthermore, the expression of alkaline phosphatase (ALP, a marker for osteoblastic differentiation) in cells on titanium discs increased after SLA treatment and GO coating [71]. Cell proliferation on GO-coated titanium discs was 25% higher than that on non-GO coated titanium discs [71]. Notably, the expression of ALP, Runt-related transcription factor 2 (RUNX2) and collagen type I-α1 (COL1A1) is upregulated in cells on GO-SLA-Ti discs [71]. These authors expanded their rabbit tibia study and found that GO-coated titanium implant had the highest bone-to-implant contact ratio (BIC), followed by GO-SLA-Ti, SLA-Ti and Ti [71]. For the GO-Ti and SLA-Ti groups, there were statistically significant variations in BIC ratio. The BIC ratios between the four implant groups were comparable at 4 weeks, though [71]. In the study by Li et al., bone marrow mesenchymal stem cells (BMSCs) grown on the surface of GO-modified material produced higher ALP than those grown on the surface of SLA material. This demonstrates the ability on the part of GO to induce early osteogenic differentiation of BMSCs [65]. The FAK/P38 pathway is activated by GO modification-induced BMSC osteogenic differentiation. Moreover, SLA/GO implants demonstrated outstanding in vivo osseointegration performance, because TGF and BMP2 were expressed at the gene level, the RUNX2 factor was activated, and PGE2 production was increased [65].

Suo et al. observed that titanium coated by graphene oxide/chitosan/hydroxyapatite (GO/CS/HA-Ti) had greater bioactivity in terms of enhanced adhesion, proliferation, and differentiation of BMSCs during in vitro cytological evaluation, and it demonstrated superior osseointegration during in vivo animal testing [62]. On titanium surfaces, GO can alter how human gingival fibroblasts (HGFs) behave cellularly [69]. According to research, GO regulates HGF adhesion, diffusion, migration, and proliferation through activating the MAKP signaling pathway, presumably by encouraging TGF-1 expression [69]. Furthermore, it was mentioned in the study by Kang et al. that rGO-Ti substrates supported hMSC osteogenic differentiation as well as proliferation [67]. These results are primarily explained by the unique properties of rGO, such as its hydrophilic nature and electrical conductivity, thus improving cell adhesion, protein absorption from serum, and cell–cell or cell–matrix signaling [67]. It has been demonstrated in the literature that titanium surfaces coated with hydroxyapatite (HA) and GO increase hydrophilicity and cause mouse bone marrow mesenchymal stem cells to differentiate into osteoblasts (BMSCs) [72]. Even in the research of Agarwalla et al., samples in which the graphene has been transferred dry without the use of risky agents exhibit an increase in titanium's hydrophilicity [66]. Titanium surfaces with GO coatings are more hydrophilic than SLA surfaces, on average [65]. Moreover, the GO-modified surface interacts with proteins through electrostatic interactions and encourages protein adsorption [65].

In the research by Ren et al., GO was applied as a coating to titanium foils as a drug delivery system to promote osteo-differentiation and cell proliferation of rat bone mesenchymal stem cells (rBMSC) [60]. Dexamethasone loaded on GO coupled with bioactive titanate on Ti implants (DEX-GO-Ti) and Dexamethasone loaded on rGO coupled with bioactive titanate on Ti implants (DEX-rGO-Ti) both allowed for improved adsorption and long-lasting release of dexamethasone (DEX) [60]. For DEX-GO-Ti substrates as opposed to DEX-Control and DEX-rGO-Ti substrates, a significantly greater proliferation rate of rBMSCs was attained. Moreover, rBMSCs differentiated more osteogenically on DEX-GO-Ti and DEX-rGO-Ti substrates than on DEX-Control substrates [60]. As a result, the titanium surface's DEX-loaded GO coating controlled the bioactivity of Ti implants, paving the way for new developments in dentistry [60].

Biomaterials derived from polymethylmethacrylate (PMMA), and in particular PMMA doped with graphene (GD-PMMA), were tested by Lorusso et al., who evaluated the osseointegration capacity of GD-PMMA [68]. In their study, 18 PMMA and 18 GD-PMMA implants were placed in the femoral knee joint of male rabbits [68]. All implants integrated well into the bone, but the GD-PMMA titanium surfaces were shown to improve osseointegration in rabbit femurs. Furthermore, the authors suggested that further in vitro and in vivo animal studies are needed to evaluate a potential clinical use for dental implant applications [68,80].

Streptococcus mutans growth has been demonstrated to be inhibited by GZNC [66], while studies by Dubey et al. [61] and Agarwalla et al. [66] indicated that GO also reduced the growth of Streptococcus Mutans and Enterococcus Faecalis and Candida albicans. Rho et al., in contrast, claimed that the antibacterial activity of GO was only moderate [63]. In addition, non-thermal plasma deposition of GO at atmospheric pressure would encourage bone growth around the implant by boosting osteoblastic cell differentiation, which would increase the biocompatibility of titanium [63].

Increased rGO concentration on titanium surfaces produces rougher surfaces that may absorb exogenous proteins, which in turn encourages cell proliferation and osteogenic differentiation, according to research by Shin et al. [70] and Kwak et al. [71]. ALP, RUNX2, and COL1A1 expression also seems to be enhanced by rGO [71]. Several studies have demonstrated the ability of GO to induce early osteogenic differentiation of BMSCs by activating the FAK/P38 pathway and increased adhesion capacity, proliferation of BMSCs [62,65]. In addition, GO can regulate adhesion, migration and proliferation of HGF [69] and hMSCs [66,67,72]. In the research of Ren et al., GO was applied as a titanium sheet coating as a drug delivery system to promote osteodifferentiation and cell proliferation of rBMSCs [60]. Improved DEX adsorption and prolonged DEX release were made possible by DEX-GO-Ti and DEX-rGO-Ti, respectively [60]. A considerably higher rate of rBMSC proliferation was attained for DEX-GO-Ti substrates as compared to DEX-Control and DEX-rGO-Ti substrates. Moreover, on DEX-GO-Ti and DEX-rGO-Ti substrates compared to DEX-Control substrates, rBMSCs differentiated more osteogenically [60]. As a result, the titanium surface's DEX-filled GO covering controlled the bioactivity of Ti implants, opening the door for future advancements in dentistry [60].

Lorusso et al. [68] evaluated implants made of PMMA, specifically GD-PMMA. The study's objective was to assess GD-osseointegration PMMA's capacity before considering it as a possible material for dental implant devices [68]. In their research, male rabbits with femoral knee joints had 18 PMMA and 18 GD-PMMA implants inserted [68]. All implants fused successfully with the bone, although research on rabbit femurs revealed that GD-PMMA titanium surfaces enhanced osseointegration. More in vitro and in vivo animal investigations, according to the authors, are required in order to assess the potential clinical utility of dental implant applications [68,80].

5. Conclusions

Graphene Oxide represents a promising nanomaterial because of its exceptional physical and chemical qualities. From our results graphene coatings may considerably increase osteogenic differentiation of bone marrow mesenchymal stem cells in vitro by the regulation of FAK/P38 signaling pathway and can encourage in vivo the osteointegration of dental implants. However, these potential applications need further studies to be validated, especially in humans. The addition of surface roughness from GO coatings to implant surfaces was found to be stable, non-reactive, and conducive to cell adhesion, diffusion, and proliferation. For addressing several significant issues, the use of GO in implant veneers appears promising. First off, germs found on the tissues surrounding the implant and graphene oxide's antibacterial properties are two of the primary causes of implant failure. Furthermore, several studies have shown that GO can help with osseointegration. Second, GO has the ability to bind biomolecules and active ingredients that may aid further improve osseointegration and quicken the healing process.

Based on the body of research, we draw the conclusion that GO coatings hold significant promise for preserving a healthy balance between a coated dental implant's capacity to prevent biofilm formation and its capacity to incite a positive cellular response.

Author Contributions: Conceptualization, A.M.I., A.D.I., G.M., F.P., A.P. and C.D.P.; methodology, G.P., F.P. and A.M.; software, F.I., G.P. and G.D.; validation, F.P., F.I. and G.D.; formal analysis, A.D.I., F.P., A.P., F.I. and G.D.; resources, A.D.I., A.M.I., G.M., C.D.P. and A.M.; data curation, G.M., G.D., F.I., G.P. and C.D.P.; writing—original draft preparation, A.D.I., A.M.I., F.P., F.I. and G.D.; writing—review and editing, A.P., G.M., G.P. and A.M.; visualization, G.P., C.D.P., A.M. and A.P.; supervision, A.D.I., A.M.I., F.P., G.M., A.P., F.I. and G.D.; project administration, A.P., F.I. and G.D. All authors have read and agreed to the published version of the manuscript.

Funding: This research received no external funding.

Institutional Review Board Statement: Not applicable.

Informed Consent Statement: Not applicable.

Data Availability Statement: Not applicable.

Conflicts of Interest: The authors declare no conflict of interest.

Abbrevations

ALP	Alkaline Phosphatase
BIC	Bone-to-Implant Contact
BMPs	bone morphogenetic proteins
BMSCs	Bone Marrow Mesenchymal Stem Cells
COL1A1	Collagen type 1-α1
DEX	Dexamethasone
DEX-GO-Ti	Dexamethasone loaded on GO coupled with bioactive titanate on Ti implants
DEX-rGO-Ti	Dexamethasone loaded on rGO coupled with bioactive titanate on Ti implants
GD-PMMA	Graphene-doped polymethylmethacrylate
GO	Graphene Oxide
GO/CS/HA-Ti	Titanium coated by graphene oxide/chitosan/hydroxyapatite
GZNC	Graphene Nanocomposite/Zinc Oxide
HA	Hydroxyapatite
HBD	Human beta defensins
hDPSC	human dental pulp stem cell
HGFs	Human Gingival Fibroblasts
hMSCs	human Mesenchymal Stem Cells
IGF	insulin-like growth factors
MBC	Minimum Bactericidal Concentration
MIC	Minimal Inhibitory Concentration
PDGF	platelet-derived growth factor
PDLSC	Periodontal ligament stem cells
PMMA	Polymethylmethacrylate
rBMSC	rat Bone Mesenchymal Stem Cells
rGO	reduced graphene oxide
RUNX2	Runt-related transcription factor 2
SLA	Sandblasted, Large grit, Acid-etched
TPS	Titanium plasma-sprayed

References

1. Esposito, M.; Coulthard, P.; Thomsen, P.; Worthington, H.V. The Role of Implant Surface Modifications, Shape and Material on the Success of Osseointegrated Dental Implants. A Cochrane Systematic Review. *Eur. J. Prosthodont. Restor. Dent.* **2005**, *13*, 15–31. [PubMed]
2. Pellegrini, G.; Francetti, L.; Barbaro, B.; Del Fabbro, M. Novel Surfaces and Osseointegration in Implant Dentistry. *J. Investig. Clin. Dent.* **2018**, *9*, e12349. [CrossRef]
3. Elias, C.N.; Rocha, F.A.; Nascimento, A.L.; Coelho, P.G. Influence of Implant Shape, Surface Morphology, Surgical Technique and Bone Quality on the Primary Stability of Dental Implants. *J. Mech. Behav. Biomed. Mater.* **2012**, *16*, 169–180. [CrossRef] [PubMed]
4. Albrektsson, T.; Sennerby, L. State of the Art in Oral Implants. *J. Clin. Periodontol.* **1991**, *18*, 474–481. [CrossRef]
5. Kligman, S.; Ren, Z.; Chung, C.-H.; Perillo, M.A.; Chang, Y.-C.; Koo, H.; Zheng, Z.; Li, C. The Impact of Dental Implant Surface Modifications on Osseointegration and Biofilm Formation. *J. Clin. Med.* **2021**, *10*, 1641. [CrossRef] [PubMed]

6. Shah, F.A.; Thomsen, P.; Palmquist, A. Osseointegration and Current Interpretations of the Bone-Implant Interface. *Acta Biomater.* **2019**, *84*, 1–15. [CrossRef]
7. Smeets, R.; Stadlinger, B.; Schwarz, F.; Beck-Broichsitter, B.; Jung, O.; Precht, C.; Kloss, F.; Gröbe, A.; Heiland, M.; Ebker, T. Impact of Dental Implant Surface Modifications on Osseointegration. *Biomed. Res. Int.* **2016**, *2016*, 6285620. [CrossRef]
8. Contaldo, M.; De Rosa, A.; Nucci, L.; Ballini, A.; Malacrinò, D.; La Noce, M.; Inchingolo, F.; Xhajanka, E.; Ferati, K.; Bexheti-Ferati, A.; et al. Titanium Functionalized with Polylysine Homopolymers: In Vitro Enhancement of Cells Growth. *Materials* **2021**, *14*, 3735. [CrossRef]
9. Coelho, P.G.; Jimbo, R.; Tovar, N.; Bonfante, E.A. Osseointegration: Hierarchical Designing Encompassing the Macrometer, Micrometer, and Nanometer Length Scales. *Dent. Mater.* **2015**, *31*, 37–52. [CrossRef]
10. Brånemark, P.I.; Adell, R.; Breine, U.; Hansson, B.O.; Lindström, J.; Ohlsson, A. Intra-Osseous Anchorage of Dental Prostheses. I. Experimental Studies. *Scand. J. Plast. Reconstr. Surg.* **1969**, *3*, 81–100. [CrossRef]
11. Brånemark, P.I.; Hansson, B.O.; Adell, R.; Breine, U.; Lindström, J.; Hallén, O.; Ohman, A. Osseointegrated Implants in the Treatment of the Edentulous Jaw. Experience from a 10-Year Period. *Scand. J. Plast. Reconstr. Surg. Suppl.* **1977**, *16*, 1–132. [PubMed]
12. Fanali, S.; Tumedei, M.; Pignatelli, P.; Inchingolo, F.; Pennacchietti, P.; Pace, G.; Piattelli, A. Implant Primary Stability with an Osteocondensation Drilling Protocol in Different Density Polyurethane Blocks. *Comput. Methods Biomech. Biomed. Eng.* **2021**, *24*, 14–20. [CrossRef] [PubMed]
13. Albrektsson, T.; Johansson, C. Osteoinduction, Osteoconduction and Osseointegration. *Eur. Spine J.* **2001**, *10* (Suppl 2), S96–S101. [CrossRef] [PubMed]
14. Osborn, J.F. *Dynamic Aspects of the Implant-Bone Interface. Materials and Systems in Dental Implants*; Hanser: Munich, Germany, 1980; pp. 111–123.
15. Comuzzi, L.; Tumedei, M.; Romasco, T.; Petrini, M.; Afrashtehfar, K.I.; Inchingolo, F.; Piattelli, A.; Di Pietro, N. Insertion Torque, Removal Torque, and Resonance Frequency Analysis Values of Ultrashort, Short, and Standard Dental Implants: An In Vitro Study on Polyurethane Foam Sheets. *J. Funct. Biomater.* **2023**, *14*, 10. [CrossRef] [PubMed]
16. Yang, X.; Wang, D.; Liang, Y.; Yin, H.; Zhang, S.; Jiang, T.; Wang, Y.; Zhou, Y. A New Implant with Solid Core and Porous Surface: The Biocompatability with Bone. *J. Biomed. Mater. Res. A* **2014**, *102*, 2395–2407. [CrossRef]
17. Kaewmanee, R.; Wang, F.; Pan, Y.; Mei, S.; Meesane, J.; Li, F.; Wu, Z.; Wei, J. Microporous Surface Containing Flower-like Molybdenum Disulfide Submicro-Spheres of Sulfonated Polyimide with Antibacterial Effect and Promoting Bone Regeneration and Osteointegration. *Biomater. Sci.* **2022**, *10*, 4243–4256. [CrossRef]
18. Nasatzky, E.; Gultchin, J.; Schwartz, Z. The role of surface roughness in promoting osteointegration. *Refuat Hapeh Vehashinayim (1993)* **2003**, *20*, 8–19, 98.
19. Park, J.H.; Olivares-Navarrete, R.; Wasilewski, C.E.; Boyan, B.D.; Tannenbaum, R.; Schwartz, Z. Use of Polyelectrolyte Thin Films to Modulate Osteoblast Response to Microstructured Titanium Surfaces. *Biomaterials* **2012**, *33*, 5267–5277. [CrossRef]
20. Olivares-Navarrete, R.; Rodil, S.E.; Hyzy, S.L.; Dunn, G.R.; Almaguer-Flores, A.; Schwartz, Z.; Boyan, B.D. Role of Integrin Subunits in Mesenchymal Stem Cell Differentiation and Osteoblast Maturation on Graphitic Carbon-Coated Microstructured Surfaces. *Biomaterials* **2015**, *51*, 69–79. [CrossRef]
21. Raszewski, Z.; Chojnacka, K.; Mikulewicz, M. Preparation and Characterization of Acrylic Resins with Bioactive Glasses. *Sci. Rep.* **2022**, *12*, 16624. [CrossRef]
22. Dohan Ehrenfest, D.M.; Coelho, P.G.; Kang, B.-S.; Sul, Y.-T.; Albrektsson, T. Classification of Osseointegrated Implant Surfaces: Materials, Chemistry and Topography. *Trends Biotechnol.* **2010**, *28*, 198–206. [CrossRef] [PubMed]
23. Brunette, D.M. The Effects of Implant Surface Topography on the Behavior of Cells. *Int. J. Oral Maxillofac. Implants* **1988**, *3*, 231–246. [PubMed]
24. Rovensky, Y.A.; Slavnaja, I.L.; Vasiliev, J.M. Behaviour of Fibroblast-like Cells on Grooved Surfaces. *Exp. Cell Res.* **1971**, *65*, 193–201. [CrossRef] [PubMed]
25. Cervino, G.; Fiorillo, L.; Iannello, G.; Santonocito, D.; Risitano, G.; Cicciù, M. Sandblasted and Acid Etched Titanium Dental Implant Surfaces Systematic Review and Confocal Microscopy Evaluation. *Materials* **2019**, *12*, 1763. [CrossRef] [PubMed]
26. Smith, D.C.; Pilliar, R.M.; Metson, J.B.; McIntyre, N.S. Dental Implant Materials. II. Preparative Procedures and Surface Spectroscopic Studies. *J. Biomed. Mater. Res.* **1991**, *25*, 1069–1084. [CrossRef] [PubMed]
27. Fischer, K.; Stenberg, T. Prospective 10-Year Cohort Study Based on a Randomized Controlled Trial (RCT) on Implant-Supported Full-Arch Maxillary Prostheses. Part 1: Sandblasted and Acid-Etched Implants and Mucosal Tissue. *Clin. Implant Dent. Relat. Res.* **2012**, *14*, 808–815. [CrossRef]
28. Schroeder, A.; van der Zypen, E.; Stich, H.; Sutter, F. The Reactions of Bone, Connective Tissue, and Epithelium to Endosteal Implants with Titanium-Sprayed Surfaces. *J. Maxillofac. Surg.* **1981**, *9*, 15–25. [CrossRef]
29. Schliephake, H.; Scharnweber, D.; Dard, M.; Sewing, A.; Aref, A.; Roessler, S. Functionalization of Dental Implant Surfaces Using Adhesion Molecules. *J. Biomed. Mater. Res. Part B Appl. Biomater.* **2005**, *73B*, 88–96. [CrossRef]
30. Wisniewska, L.M.; Dohan Ehrenfest, D.M.; Galindo-Moreno, P.; Segovia, J.D.; Inchingolo, F.; Wang, H.-L.; Fernandes-Cruz, M. Molecular, Cellular and Pharmaceutical Aspects of Biomaterials in Dentistry and Oral and Maxillofacial Surgery. An Internationalization of Higher Education and Research Perspective. *Curr. Pharm. Biotechnol.* **2017**, *18*, 10–18. [CrossRef]

31. Bessho, K.; Carnes, D.L.; Cavin, R.; Chen, H.Y.; Ong, J.L. BMP Stimulation of Bone Response Adjacent to Titanium Implants in Vivo. *Clin. Oral Implants Res.* **1999**, *10*, 212–218. [CrossRef]
32. Wikesjö, U.M.E.; Sorensen, R.G.; Kinoshita, A.; Wozney, J.M. RhBMP-2/AlphaBSM Induces Significant Vertical Alveolar Ridge Augmentation and Dental Implant Osseointegration. *Clin. Implant Dent. Relat. Res.* **2002**, *4*, 174–182. [CrossRef] [PubMed]
33. Tatakis, D.N.; Koh, A.; Jin, L.; Wozney, J.M.; Rohrer, M.D.; Wikesjö, U.M.E. Peri-Implant Bone Regeneration Using Recombinant Human Bone Morphogenetic Protein-2 in a Canine Model: A Dose-Response Study. *J. Periodontal. Res.* **2002**, *37*, 93–100. [CrossRef] [PubMed]
34. Simonpieri, A.; Del Corso, M.; Vervelle, A.; Jimbo, R.; Inchingolo, F.; Sammartino, G.; Dohan Ehrenfest, D.M. Current Knowledge and Perspectives for the Use of Platelet-Rich Plasma (PRP) and Platelet-Rich Fibrin (PRF) in Oral and Maxillofacial Surgery Part 2: Bone Graft, Implant and Reconstructive Surgery. *Curr. Pharm. Biotechnol.* **2012**, *13*, 1231–1256. [CrossRef]
35. Inchingolo, A.D.; Inchingolo, A.M.; Malcangi, G.; Avantario, P.; Azzollini, D.; Buongiorno, S.; Viapiano, F.; Campanelli, M.; Ciocia, A.M.; De Leonardis, N.; et al. Effects of Resveratrol, Curcumin and Quercetin Supplementation on Bone Metabolism—A Systematic Review. *Nutrients* **2022**, *14*, 3519. [CrossRef] [PubMed]
36. Warnke, P.H.; Voss, E.; Russo, P.A.J.; Stephens, S.; Kleine, M.; Terheyden, H.; Liu, Q. Antimicrobial Peptide Coating of Dental Implants: Biocompatibility Assessment of Recombinant Human Beta Defensin-2 for Human Cells. *Int. J. Oral Maxillofac. Implants* **2013**, *28*, 982–988. [CrossRef] [PubMed]
37. Yifat, M.; Hila, E.; Avraham, H.; Inchingolo, F.; Mortellaro, C.; Peleg, O.; Mijiritsky, E. Histologic and Radiographic Characteristics of Bone Filler Under Bisphosphonates. *J. Craniofacial Surg.* **2019**, *30*, 1085. [CrossRef]
38. Peter, B.; Pioletti, D.P.; Laïb, S.; Bujoli, B.; Pilet, P.; Janvier, P.; Guicheux, J.; Zambelli, P.-Y.; Bouler, J.-M.; Gauthier, O. Calcium Phosphate Drug Delivery System: Influence of Local Zoledronate Release on Bone Implant Osteointegration. *Bone* **2005**, *36*, 52–60. [CrossRef] [PubMed]
39. Yoshinari, M.; Oda, Y.; Ueki, H.; Yokose, S. Immobilization of Bisphosphonates on Surface Modified Titanium. *Biomaterials* **2001**, *22*, 709–715. [CrossRef]
40. Kajiwara, H.; Yamaza, T.; Yoshinari, M.; Goto, T.; Iyama, S.; Atsuta, I.; Kido, M.A.; Tanaka, T. The Bisphosphonate Pamidronate on the Surface of Titanium Stimulates Bone Formation around Tibial Implants in Rats. *Biomaterials* **2005**, *26*, 581–587. [CrossRef]
41. Novoselov, K.S.; Fal'ko, V.I.; Colombo, L.; Gellert, P.R.; Schwab, M.G.; Kim, K. A Roadmap for Graphene. *Nature* **2012**, *490*, 192–200. [CrossRef]
42. Xie, Y.; Li, H.; Ding, C.; Zheng, X.; Li, K. Effects of Graphene Plates' Adoption on the Microstructure, Mechanical Properties, and in Vivo Biocompatibility of Calcium Silicate Coating. *Int. J. Nanomed.* **2015**, *10*, 3855–3863. [CrossRef] [PubMed]
43. Poot, M.; van der Zant, H.S.J. Nanomechanical Properties of Few-Layer Graphene Membranes. *Appl. Phys. Lett.* **2008**, *92*, 063111. [CrossRef]
44. Kim, J.; Kim, Y.-R.; Kim, Y.; Lim, K.T.; Seonwoo, H.; Park, S.; Cho, S.-P.; Hong, B.H.; Choung, P.-H.; Chung, T.D.; et al. Graphene-Incorporated Chitosan Substrata for Adhesion and Differentiation of Human Mesenchymal Stem Cells. *J. Mater. Chem. B* **2013**, *1*, 933–938. [CrossRef] [PubMed]
45. Shin, Y.C.; Lee, J.H.; Jin, L.; Kim, M.J.; Kim, Y.-J.; Hyun, J.K.; Jung, T.-G.; Hong, S.W.; Han, D.-W. Stimulated Myoblast Differentiation on Graphene Oxide-Impregnated PLGA-Collagen Hybrid Fibre Matrices. *J. Nanobiotechnol.* **2015**, *13*, 21. [CrossRef] [PubMed]
46. Park, S.Y.; Park, J.; Sim, S.H.; Sung, M.G.; Kim, K.S.; Hong, B.H.; Hong, S. Enhanced Differentiation of Human Neural Stem Cells into Neurons on Graphene. *Adv. Mater.* **2011**, *23*, H263–H267. [CrossRef] [PubMed]
47. Akhavan, O.; Ghaderi, E. Toxicity of Graphene and Graphene Oxide Nanowalls against Bacteria. *ACS Nano* **2010**, *4*, 5731–5736. [CrossRef]
48. Li, X.; Li, F.; Gao, Z.; Fang, L. Toxicology of Graphene Oxide Nanosheets Against Paecilomyces Catenlannulatus. *Bull. Environ. Contam. Toxicol.* **2015**, *95*, 25–30. [CrossRef]
49. Liu, S.; Zeng, T.H.; Hofmann, M.; Burcombe, E.; Wei, J.; Jiang, R.; Kong, J.; Chen, Y. Antibacterial Activity of Graphite, Graphite Oxide, Graphene Oxide, and Reduced Graphene Oxide: Membrane and Oxidative Stress. *ACS Nano* **2011**, *5*, 6971–6980. [CrossRef]
50. Wang, X.; Liu, X.; Han, H. Evaluation of Antibacterial Effects of Carbon Nanomaterials against Copper-Resistant Ralstonia Solanacearum. *Coll. Surf. B Biointerfaces* **2013**, *103*, 136–142. [CrossRef]
51. Hu, C.; Wang, L.-L.; Lin, Y.-Q.; Liang, H.-M.; Zhou, S.-Y.; Zheng, F.; Feng, X.-L.; Rui, Y.-Y.; Shao, L.-Q. Nanoparticles for the Treatment of Oral Biofilms: Current State, Mechanisms, Influencing Factors, and Prospects. *Adv. Healthc. Mater.* **2019**, *8*, e1901301. [CrossRef]
52. He, J.; Zhu, X.; Qi, Z.; Wang, C.; Mao, X.; Zhu, C.; He, Z.; Li, M.; Tang, Z. Killing Dental Pathogens Using Antibacterial Graphene Oxide. *ACS Appl. Mater. Interfaces* **2015**, *7*, 5605–5611. [CrossRef] [PubMed]
53. Ghorbanzadeh, R.; Hosseinpour Nader, A.; Salehi-Vaziri, A. The Effects of Bimodal Action of Photodynamic and Photothermal Therapy on Antimicrobial and Shear Bond Strength Properties of Orthodontic Composite Containing Nano-Graphene Oxide. *Photodiagn. Photodyn. Ther.* **2021**, *36*, 102589. [CrossRef] [PubMed]
54. Shi, Y.Y.; Li, M.; Liu, Q.; Jia, Z.J.; Xu, X.C.; Cheng, Y.; Zheng, Y.F. Electrophoretic Deposition of Graphene Oxide Reinforced Chitosan-Hydroxyapatite Nanocomposite Coatings on Ti Substrate. *J. Mater. Sci. Mater. Med.* **2016**, *27*, 48. [CrossRef] [PubMed]
55. Vera-González, N.; Shukla, A. Advances in Biomaterials for the Prevention and Disruption of Candida Biofilms. *Front. Microbiol.* **2020**, *11*, 538602. [CrossRef]

56. Palmieri, V.; Bugli, F.; Cacaci, M.; Perini, G.; Maio, F.D.; Delogu, G.; Torelli, R.; Conti, C.; Sanguinetti, M.; Spirito, M.D.; et al. Graphene Oxide Coatings Prevent Candida Albicans Biofilm Formation with a Controlled Release of Curcumin-Loaded Nanocomposites. *Nanomedicine* **2018**, *13*, 2867–2879. [CrossRef]
57. Pourhajibagher, M.; Parker, S.; Chiniforush, N.; Bahador, A. Photoexcitation Triggering via Semiconductor Graphene Quantum Dots by Photochemical Doping with Curcumin versus Perio-Pathogens Mixed Biofilms. *Photodiagn. Photodyn. Ther.* **2019**, *28*, 125–131. [CrossRef]
58. Page, M.J.; McKenzie, J.E.; Bossuyt, P.M.; Boutron, I.; Hoffmann, T.C.; Mulrow, C.D.; Shamseer, L.; Tetzlaff, J.M.; Akl, E.A.; Brennan, S.E.; et al. The PRISMA 2020 Statement: An Updated Guideline for Reporting Systematic Reviews. *BMJ* **2021**, *372*, n71. [CrossRef]
59. Kulshrestha, S.; Khan, S.; Meena, R.; Singh, B.R.; Khan, A.U. A Graphene/Zinc Oxide Nanocomposite Film Protects Dental Implant Surfaces against Cariogenic Streptococcus Mutans. *Biofouling* **2014**, *30*, 1281–1294. [CrossRef]
60. Ren, N.; Li, J.; Qiu, J.; Yan, M.; Liu, H.; Ji, D.; Huang, J.; Yu, J.; Liu, H. Growth and Accelerated Differentiation of Mesenchymal Stem Cells on Graphene-Oxide-Coated Titanate with Dexamethasone on Surface of Titanium Implants. *Dent. Mater.* **2017**, *33*, 525–535. [CrossRef]
61. Dubey, N.; Ellepola, K.; Decroix, F.E.D.; Morin, J.L.P.; Castro Neto, A.H.; Seneviratne, C.J.; Rosa, V. Graphene onto Medical Grade Titanium: An Atom-Thick Multimodal Coating That Promotes Osteoblast Maturation and Inhibits Biofilm Formation from Distinct Species. *Nanotoxicology* **2018**, *12*, 274–289. [CrossRef]
62. Suo, L.; Jiang, N.; Wang, Y.; Wang, P.; Chen, J.; Pei, X.; Wang, J.; Wan, Q. The Enhancement of Osseointegration Using a Graphene Oxide/Chitosan/Hydroxyapatite Composite Coating on Titanium Fabricated by Electrophoretic Deposition. *J. Biomed. Mater. Res. Part B Appl. Biomater.* **2019**, *107*, 635–645. [CrossRef]
63. Rho, K.; Park, C.; Alam, K.; Kim, D.; Ji, M.-K.; Lim, H.-P.; Cho, H. Biological Effects of Plasma-Based Graphene Oxide Deposition on Titanium. *J. Nanomater.* **2019**, *2019*, e9124989. [CrossRef]
64. Agarwalla, S.V.; Ellepola, K.; Silikas, N.; Castro Neto, A.; Seneviratne, C.J.; Rosa, V. Persistent Inhibition of Candida Albicans Biofilm and Hyphae Growth on Titanium by Graphene Nanocoating. *Dent. Mater.* **2021**, *37*, 370–377. [CrossRef] [PubMed]
65. Li, Q.; Wang, Z. Involvement of FAK/P38 Signaling Pathways in Mediating the Enhanced Osteogenesis Induced by Nano-Graphene Oxide Modification on Titanium Implant Surface. *Int. J. Nanomed.* **2020**, *15*, 4659–4676. [CrossRef] [PubMed]
66. Agarwalla, S.V.; Ellepola, K.; da Costa, M.C.F.; Fechine, G.J.M.; Morin, J.L.P.; Castro Neto, A.H.; Seneviratne, C.J.; Rosa, V. Hydrophobicity of Graphene as a Driving Force for Inhibiting Biofilm Formation of Pathogenic Bacteria and Fungi. *Dent. Mater.* **2019**, *35*, 403–413. [CrossRef] [PubMed]
67. Kang, M.S.; Jeong, S.J.; Lee, S.H.; Kim, B.; Hong, S.W.; Lee, J.H.; Han, D.-W. Reduced Graphene Oxide Coating Enhances Osteogenic Differentiation of Human Mesenchymal Stem Cells on Ti Surfaces. *Biomater. Res.* **2021**, *25*, 4. [CrossRef]
68. Lorusso, F.; Inchingolo, F.; Greco Lucchina, A.; Scogna, G.; Scarano, A. Graphene-Doped Poly(Methyl-Methacrylate) as an Enhanced Biopolymer for Medical Device and Dental Implant. *J. Biol. Regul. Homeost. Agents* **2021**, *35*, 195–204. [CrossRef]
69. Cao, X.; Wu, K.; Wang, C.; Guo, Y.; Lu, R.; Wang, X.; Chen, S. Graphene Oxide Loaded on TiO_2-Nanotube-Modified Ti Regulates the Behavior of Human Gingival Fibroblasts. *Int. J. Mol. Sci.* **2022**, *23*, 8723. [CrossRef]
70. Shin, Y.C.; Bae, J.-H.; Lee, J.H.; Raja, I.S.; Kang, M.S.; Kim, B.; Hong, S.W.; Huh, J.-B.; Han, D.-W. Enhanced Osseointegration of Dental Implants with Reduced Graphene Oxide Coating. *Biomater. Res.* **2022**, *26*, 11. [CrossRef]
71. Kwak, J.M.; Kim, J.; Lee, C.-S.; Park, I.-S.; Lee, M.; Min, D.-H.; Yeo, I.-S.L. Graphene Oxide as a Biocompatible and Osteoinductive Agent to Promote Implant Osseointegration in a Rabbit Tibia Model. *Adv. Mater. Interfaces* **2022**, *9*, 2201116. [CrossRef]
72. Baheti, W.; Lv, S.; Mila, M.L.; Amantai, D.; Sun, H.; He, H. Graphene/Hydroxyapatite Coating Deposit on Titanium Alloys for Implant Application. *J. Appl. Biomater. Funct. Mater.* **2023**, *21*, 22808000221148104. [CrossRef] [PubMed]
73. Liu, C.; Tan, D.; Chen, X.; Liao, J.; Wu, L. Research on Graphene and Its Derivatives in Oral Disease Treatment. *Int. J. Mol. Sci.* **2022**, *23*, 4737. [CrossRef]
74. Allen, M.J.; Tung, V.C.; Kaner, R.B. Honeycomb Carbon: A Review of Graphene. *Chem. Rev.* **2010**, *110*, 132–145. [CrossRef] [PubMed]
75. Ghosal, K.; Sarkar, K. Biomedical Applications of Graphene Nanomaterials and Beyond. *ACS Biomater. Sci. Eng.* **2018**, *4*, 2653–2703. [CrossRef] [PubMed]
76. Ferrari, A.C.; Bonaccorso, F.; Fal'ko, V.; Novoselov, K.S.; Roche, S.; Bøggild, P.; Borini, S.; Koppens, F.H.L.; Palermo, V.; Pugno, N.; et al. Science and Technology Roadmap for Graphene, Related Two-Dimensional Crystals, and Hybrid Systems. *Nanoscale* **2015**, *7*, 4598–4810. [CrossRef] [PubMed]
77. Sun, L.; Yan, Z.; Duan, Y.; Zhang, J.; Liu, B. Improvement of the Mechanical, Tribological and Antibacterial Properties of Glass Ionomer Cements by Fluorinated Graphene. *Dent. Mater.* **2018**, *34*, e115–e127. [CrossRef]
78. Alshahrani, A.; Bin-Shuwaish, M.S.; Al-Hamdan, R.S.; Almohareb, T.; Maawadh, A.M.; Al Deeb, M.; Alhenaki, A.M.; Abduljabbar, T.; Vohra, F. Graphene Oxide Nano-Filler Based Experimental Dentine Adhesive. A SEM / EDX, Micro-Raman and Microtensile Bond Strength Analysis. *J. Appl. Biomater. Funct. Mater.* **2020**, *18*, 2280800020966936. [CrossRef]
79. Zhao, L.; Chu, P.K.; Zhang, Y.; Wu, Z. Antibacterial Coatings on Titanium Implants. *J. Biomed. Mater. Res. Part B Appl. Biomater.* **2009**, *91B*, 470–480. [CrossRef]

80. Scarano, A.; Orsini, T.; Di Carlo, F.; Valbonetti, L.; Lorusso, F. Graphene-Doped Poly (Methyl-Methacrylate) (Pmma) Implants: A Micro-CT and Histomorphometrical Study in Rabbits. *Int. J. Mol. Sci.* **2021**, *22*, 1441. [CrossRef]

MDPI
St. Alban-Anlage 66
4052 Basel
Switzerland
www.mdpi.com

Coatings Editorial Office
E-mail: coatings@mdpi.com
www.mdpi.com/journal/coatings

MDPI

Academic Open
Access Publishing

mdpi.com

ISBN 978-3-7258-1114-4